Video Compression and Communications: From Basics to H.261, H.263, H.264, MPEG2, MPEG4 for DVB and HSDPA-Style Adaptive Turbo-Transceivers

by

©L. Hanzo, P.J. Cherriman, J. Streit
Department of Electronics and Computer Science,
University of Southampton, UK

About the Authors

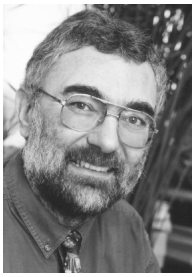

Lajos Hanzo (http://www-mobile.ecs.soton.ac.uk) FREng, FIEEE, FIET, DSc received his degree in electronics in 1976 and his doctorate in 1983. During his 30-year career in telecommunications he has held various research and academic posts in Hungary, Germany and the UK. Since 1986 he has been with the School of Electronics and Computer Science, University of Southampton, UK, where he holds the chair in telecommunications. He has co-authored 15 books on mobile radio communications totalling in excess of 10 000, published about 700 research papers, acted as TPC Chair of IEEE conferences, presented keynote lectures and been awarded a number of distinctions. Currently he is directing an academic research team, working on a range of research projects in the field of wireless multimedia communications sponsored by industry, the Engineering and Physical Sciences Research Council (EPSRC) UK, the European IST Programme and the Mobile Virtual Centre of Excellence (VCE), UK. He is an enthusiastic supporter of industrial and academic liaison and he offers a range of industrial courses. He is also an IEEE Distinguished Lecturer of both the Communications Society and the Vehicular Technology Society (VTS). Since 2005 he has been a Governer of the VTS. For further information on research in progress and associated publications please refer to http://www-mobile.ecs.soton.ac.uk

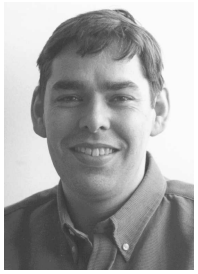

Peter J. Cherriman graduated in 1994 with an M.Eng. degree in Information Engineering from the University of Southampton, UK. Since 1994 he has been with the Department of Electronics and Computer Science at the University of Southampton, UK, working towards a Ph.D. in mobile video networking which was completed in 1999. Currently he is working on projects for the Mobile Virtual Centre of Excellence, UK. His current areas of research include robust video coding, microcellular radio systems, power control, dynamic channel allocation and multiple access protocols. He has published about two dozen conference and journal papers, and holds several patents.

Jürgen Streit received his Dipl.-Ing. Degree in electronic engineering from the Aachen University of Technology in 1993 and his Ph.D. in image coding from the Department of Electronics and Computer Science, University of Southampton, UK, in 1995. From 1992 to 1996 Dr. Streit had been with the Department of Electronics and Computer Science working in the Communications Research Group. His work led to numerous publications. Since then he has joined a management consultancy working as an information technology consultant.

Other Wiley and IEEE Press Books on Related Topics [1]

- R. Steele, L. Hanzo (Ed): *Mobile Radio Communications: Second and Third Generation Cellular and WATM Systems*, John Wiley and IEEE Press, 2nd edition, 1999, ISBN 07 273-1406-8, 1064 pages

- L. Hanzo, F.C.A. Somerville, J.P. Woodard: *Voice Compression and Communications: Principles and Applications for Fixed and Wireless Channels*; IEEE Press and John Wiley, 2001, 642 pages

- L. Hanzo, P. Cherriman, J. Streit: *Wireless Video Communications: Second to Third Generation and Beyond*, IEEE Press and John Wiley, 2001, 1093 pages

- L. Hanzo, T.H. Liew, B.L. Yeap: *Turbo Coding, Turbo Equalisation and Space-Time Coding*, John Wiley and IEEE Press, 2002, 751 pages

- J.S. Blogh, L. Hanzo: *Third-Generation Systems and Intelligent Wireless Networking: Smart Antennas and Adaptive Modulation*, John Wiley and IEEE Press, 2002, 408 pages

- L. Hanzo, C.H. Wong, M.S. Yee: *Adaptive Wireless Transceivers: Turbo-Coded, Turbo-Equalised and Space-Time Coded TDMA, CDMA and OFDM Systems*, John Wiley and IEEE Press, 2002, 737 pages

- L. Hanzo, L-L. Yang, E-L. Kuan, K. Yen: *Single- and Multi-Carrier CDMA: Multi-User Detection, Space-Time Spreading, Synchronisation, Networking and Standards*, John Wiley and IEEE Press, June 2003, 1060 pages

- L. Hanzo, M. Münster, T. Keller, B-J. Choi, *OFDM and MC-CDMA for Broadband Multi-User Communications, WLANs and Broadcasting*, John-Wiley and IEEE Press, 2003, 978 pages

- L. Hanzo, S-X. Ng, T. Keller and W.T. Webb, *Quadrature Amplitude Modulation: From Basics to Adaptive Trellis-Coded, Turbo-Equalised and Space-Time Coded OFDM, CDMA and MC-CDMA Systems*, John Wiley and IEEE Press, 2004, 1105 pages

[1] For detailed contents and sample chapters please refer to http://www-mobile.ecs.soton.ac.uk

- L. Hanzo, T. Keller: *An OFDM and MC-CDMA Primer*, John Wiley and IEEE Press, 2006, 430 pages
- L. Hanzo, F.C.A. Somerville, J.P. Woodard: *Voice and Audio Compression for Wireless Communications*, John Wiley and IEEE Press, 2007, 858 pages
- L. Hanzo, P.J. Cherriman, J. Streit: *Video Compression and Communications: H.261, H.263, H.264, MPEG4 and HSDPA-Style Adaptive Turbo-Transceivers* John Wiley and IEEE Press, 2007, 680 pages
- L. Hanzo, J. Blogh and S. Ni: *HSDPA-Style FDD Versus TDD Networking: Smart Antennas and Adaptive Modulation* John Wiley and IEEE Press, 2007, 650 pages

Contents

Part I

Video Codecs for HSDPA-Style Adaptive Videophones

Part II

High-Resolution Video Coding

Part III

H.261, H.263, H.264, MPEG2 and MPEG 4 for HSDPA-Style Wireless Video Telephony and DVB

Chapter 11

MPEG-4 Video Compression

J-Y. Chung and L. Hanzo

11.1 Introduction

The"Moving Picture Experts Group" (MPEG) was established in 1988 [339], within the International Standard Organisation's (ISO) Steering Group (SG) 29, which was responsible for the encoding of moving pictures and audio. The MPEG group commenced the development of the MPEG-1 standard in 1988, released the MPEG-1 standard in 1993 and embarked on the standardisation of the MPEG-2 scheme in 1990 [340]. The MPEG-1 standard was mainly targeted at CD-ROM applications dedicated to recording video at bit rates of up to 1.5Mbit/s [340, 341]. By contrast, the MPEG-2 standard was designed for substantially higher quality, namely for audiovisual applications such as today's home entertainment systems and digital broadcasting systems requiring video bit rates between 2Mbit/s and 30Mbit/s [342, 343].

The MPEG-4 standardisation process was initiated in 1994 - with the mandate of standardising algorithms for audio-visual coding in multimedia applications, while allowing for interactivity, and supporting high compression as well as universal accessibility and portability of both the audio and video content [344].

The MPEG-4 Visual standard was developed by the ISO/IEC 14496-2 [1], and its Version 1 was released in 1998, which additional tools and profiles were added in two amendments of the standard, culminating in Version 2 during late 2001. The operating bit rates targeted by the MPEG-4 video standard are between 5 and 64kbit/s in the context of mobile or Public Switched Telephone Network (PSTN) based video applications, spanning up to 4 Mbit/s for digital TV broadcast applications, and even to rates in excess of 100Mbit/s in High Definition TV (HDTV) studio applications [345].

The MPEG-4 video coding standard is capable of supporting all functionalities already provided by MPEG-1 and MPEG-2. The MPEG-4 Visual standard improves the popular MPEG-2 standard both in terms of the achievable compression efficiency, at a given visual

[1] This is the project's profile name for the International Organisation for Standardization/International Electrotechnical Commission (ISO/IEC). For example, the profile index 15444 for JPEG, 11172 for MPEG-1, 13818 for MPEG-2, 14496 for MPEG-4, etc.

quality, as well as in terms of the attainable flexibility that facilitates its employment in a wide range of applications. It achieves these substantial advances by making use of more advanced compression algorithms and by providing an extensive set of 'tools' for coding and manipulating digital media. The MPEG-4 Visual standard consists of a 'core' video encoder/decoder model that invoke a number of additional coding tools. The core model is based on the well-established hybrid DPCM/DCT coding algorithm and the basic function of the core is extended by 'tools' supporting an enhanced compression efficiency and reliable transmission. Furthermore, MPEG-4 facilitates an efficient and novel coded representation of the audio and video data that can be "content based", which is a concept to be highlighted in Section 11.3.

To elaborate a little further, the MPEG-4 video standard compresses the video signal with the aid of a compression tool box constituted by a set of encoding tools supporting several classes of functionalities. In short, the most important features supported by the MPEG-4 standard are *a high compression efficiency, content-based interactivity, and universal access*, which are summarised below [340, 346]:

- *Achieving high compression efficiency* has been a core feature of both MPEG-1 and MPEG-2. The storage and transmission of audio visual data requires a high compression efficiency, while reproducing a high-quality video sequence, hence enabling applications such as High Definition Television (HDTV) and Digital Video Disc (DVD) storage.
- *Content-based interactivity* represents video on an 'object-basis', rather than on a video 'frame-basis', which is one of the novel features offered by MPEG-4. The concept of content-based functionality will be elaborated on in more depth in Section 11.3.
- *Universal access* allows audiovisual information to be transmitted and accessed in various network environments such as mobile networks as well as wire line-based systems.

This chapter provides a rudimentary overview of the MPEG-4 video standard. Following the overview of the standard – its approach and features, in Section 11.3, the philosophy of the object oriented coding scheme will be discussed. This is followed by a discussion on the so-called profiles defined for coding of arbitrary-shaped objects and rectangular video frames in Subsection 11.3.3. Then the profiles defined for scalable coding of video objects are highlighted in Section 11.4 and subjective video quality measurement methods as well as our experimental results are discussed in Sections 11.5 and 11.6.

11.2 Overview of MPEG-4

11.2.1 MPEG-4 Profiles

The MPEG-4 standard aims for satisfying the requirements of various visual communications applications using a toolkit-based approach for encoding and decoding of visual information [24, 346]. Below we will describe some of the key features of the MPEG-4 video standard, which are superior in comparison to the previous video coding standards:

- The core compression tools are based on those of the ITU-T H.263 standard, which are more efficient than those of the MPEG-1 [347] and MPEG-2 [348] video compression schemes. Efficient compression of progressive and interlaced video sequences as

well as optional additional tools were introduced for the sake of further improving the attainable compression efficiency.

- Coding of video objects, having both rectangular shapes and irregular-shapes object. This is a new concept in the context of standard-based video coding and enables the independent encoding of both foreground and background objects in a video scene.

- Support for error-resilient transmission over hostile networks. A range of error resilience tools were included in the MPEG-4 codec for the sake of assisting the decoder in recovering from transmission errors and for maintaining a successful video connection in an error-prone network. Furthermore, the scalable coding tools are capable of supporting flexible transmission at a range of desired coded bitrates.

- Coding of still image within the same framework as full-motion video sequences.

- Coding of animated visual objects, such as 2D and 3D computer-generated polygonal meshes, animated objects, etc.

- Coding for specialist applications, such as very high 'studio' quality video. In this application maintaining a high visual quality is more important than attaining a high compression.

Table 11.1 lists the MPEG-4 visual profiles invoked for coding video scenes. These profiles range from the so-called Simple Profile derived for the encoding of rectangular video frames through profiles designed for arbitrary-shaped and scalable object coding to profiles contrived for the encoding of studio-quality video.

MPEG-4 Visual profile	Main features
□ Simple	Low-complexity coding of rectangular video frames
□ Advanced Simple	Coding rectangular frames with improved efficiency and support for interlaces video
□ Advanced Real-Time Simple	Coding rectangular frames for real-time streaming
□ Core	Basic coding of arbitrary-shaped video objects
□ Main	Feature-rich coding of video objects
□ Advanced Coding Efficiency	Highly efficient coding of video objects
□ N-Bit	Coding of video objects with sample resolutions other than 8 bits
□ Simple Scalable	Scalable coding of rectangular video frames
□ Fine Granular Scalability	Advanced scalable coding of rectangular frames
□ Core Scalable	Scalable coding of video objects
□ Scalable Texture	Scalable still texture with improved efficiency and object-based features
□ Advanced Scalable Texture	Scalable still texture with improved efficiency and object-based featured
□ Advanced Core	Combines features of Simple, Core and Advanced Scalable Texture Profiles
□ Simple Studio	Object-based coding of high quality video sequences
□ Core Studio	Object-based coding of high quality video with improved compression efficiency

Table 11.1: MPEG-4 Visual profiles for coding natural video [24, 346]

11.2.2 MPEG-4 Features

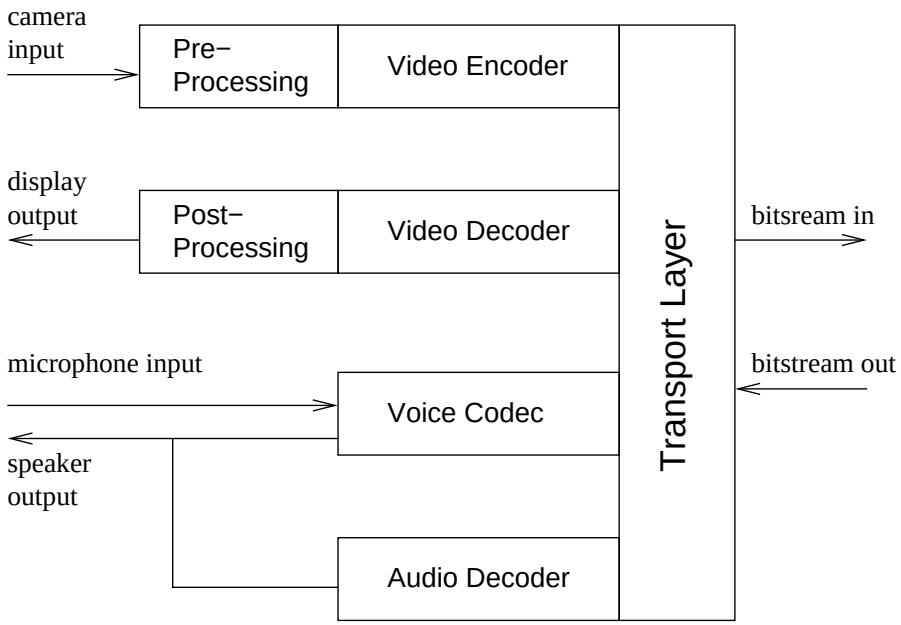

Figure 11.1: Simplified video telephone schematic

Similarly to MPEG-1 [347] and MPEG-2 [348], the MPEG-4 specifications cover both the presentation and transmission of digital audio and video. However, in this thesis we only consider the specifics of the video coding standard. The block diagram of a basic videophone scheme is shown in Figure 11.1. Let us now consider some of the associated operations in slightly more detail.

Pre-processing and video encoding

According to the MPEG ISO standard [349], the MPEG-4 video codec only supports YUV 4:2:0[2] Quarter Common Intermediate Format (QCIF) or Common Intermediate Format (CIF) video representations in the context of compression [32]. Here, the pre-processing block of Figure 11.1 performs all necessary processing of the camera input, in order to create the required 4:2:0 YUV QCIF or CIF based sequences. In order to encode the YUV video sequence into the MPEG-4 bitstream, the MPEG-4 encoder adopts the well-established motion compensation (MC) and Discrete Cosine Transform (DCT) based structure shown in Figure 11.2. The block by block discussion of the MPEG-4 encoder's components is postponed until Sections 11.3.1 and 11.3.2.

Transport-layer

In MPEG-4, the transport of the video stream is divided into four layers, namely the El-

[2] A colour encoding scheme [350] in which the luminance (Y) and the so-called color-difference signals U and V are represented separately. The human eye is less sensitive to colour variations than to intensity variations. Hence, the YUV format allows the encoding of the luminance (Y) information at full resolution and that of the colour-difference information at a lower resolution.

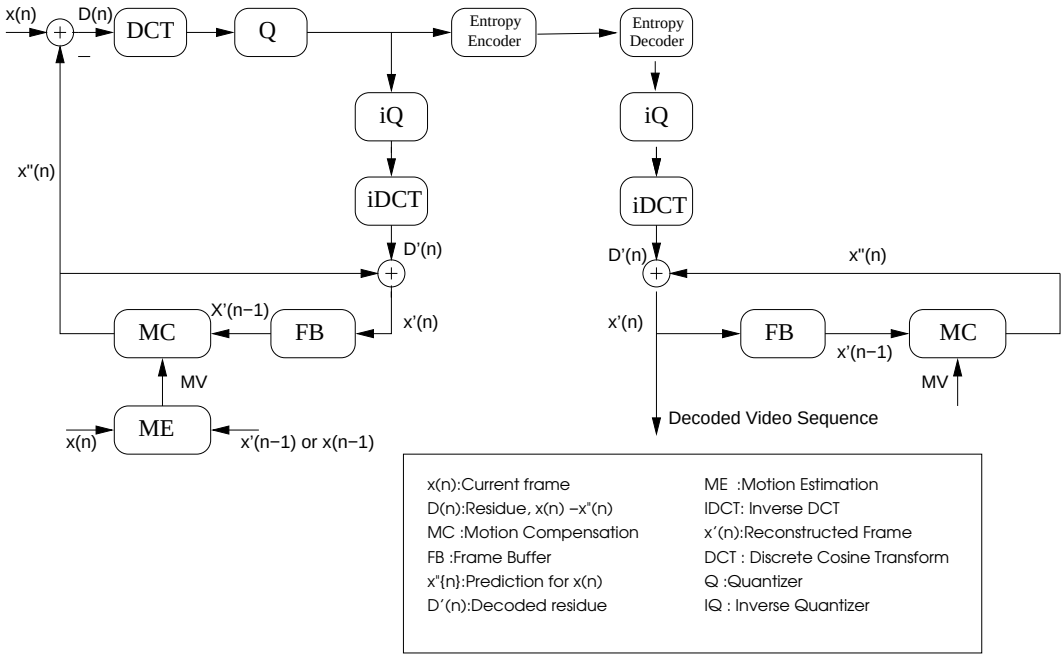

Figure 11.2: Block diagram of the MPEG-4 encoder and decoder.

ementary Stream [351], the Synchronisation Layer, the 'Flexmuxed' [352] stream and the 'Transmux' [353] Stream. The MPEG-4 system's architecture and transport layer have been nicely documented in the literature, for example in [351, 354]. Below we briefly outline these transport layer characteristics:

- The term *Elementary Streams* [351] refers to data that fully or partially contain the encoded representation of a single audio or video object, scene description information or control information.
- The *Synchronisation Layer (SL)* [355] adds the identification of the information sources, such as for example audio or video sources, as well as time stamps.
- *Flexmuxed Streams* [352] convey groups of elementary streams according to a specific set of common attributes, such as for example quality requirements.
- *Transmux Streams* [353] are constituted by streams transmitted over the network using transport protocols, such as the Real-Time Protocol (RTP) [356] used for transmission over the Internet.

Video Decoder and Post Processing
Figure 11.2 portrays the simplified block diagram of the MPEG-4 video decoder. Observe that the structure of the decoding process is identical to that of the encoder's local decoder. Motion compensation, which has been comparatively studied for example in [4], is the most

important process both in the video encoder and decoder in terms of achieving a high video compression. Motion Compensation (MC) generates the Motion Vectors (MV) on the basis of identifying the most likely position within the previous video frame, where the current 8x8-pixel video block has originated from, as it moved along a certain motion trajectory in the consecutive video frames. This motion-compensation process involves allocating a certain search area in the previous frame and then sliding the current block over this search area in an effort to find the position of highest correlation. Once this position has been identified, the motion compensated prediction residual (MCPR) [4] is formed by subtracting the two blocks from each other.

11.2.3 MPEG-4 Object Based Orientation

One of the functionalities defined by the MPEG-4 standard is the audio-visual 'object' based processing, which forms the 'object-based' representation of the audio or video signal [342]. A video object can be exemplified by a person walking against the backdrop of mountains. Both the object and the background can be substituted by another object or by another backdrop and as expected certain encoding techniques perform better for certain objects. This representation supports *'content-based interactivity'*, which will be discussed in more detail in section 11.3.

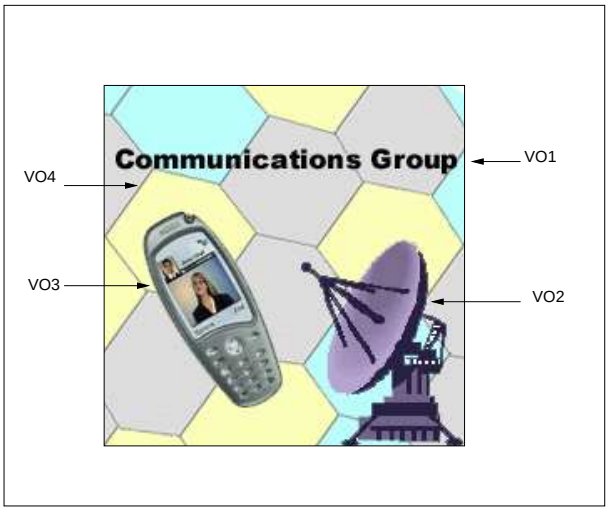

Figure 11.3: Original decoded video scene.

Figure 11.3 shows an example of a video frame extracted from a video scene, which consists of several objects namely text, an antenna, a mobile phone and the background scene. Again, in MPEG-4 based coding [349] these objects are referred to as 'Video Objects' (VO) . The syntax of this representation may be written as (VO1) - text, VO2 - the antenna, VO3 - mobile phone and VO4 - background.

An MPEG-4 video scene may consist of one or more Video Objects (VO) . A video object (VO) is an area of the video scene that may occupy an arbitrarily-shaped region and

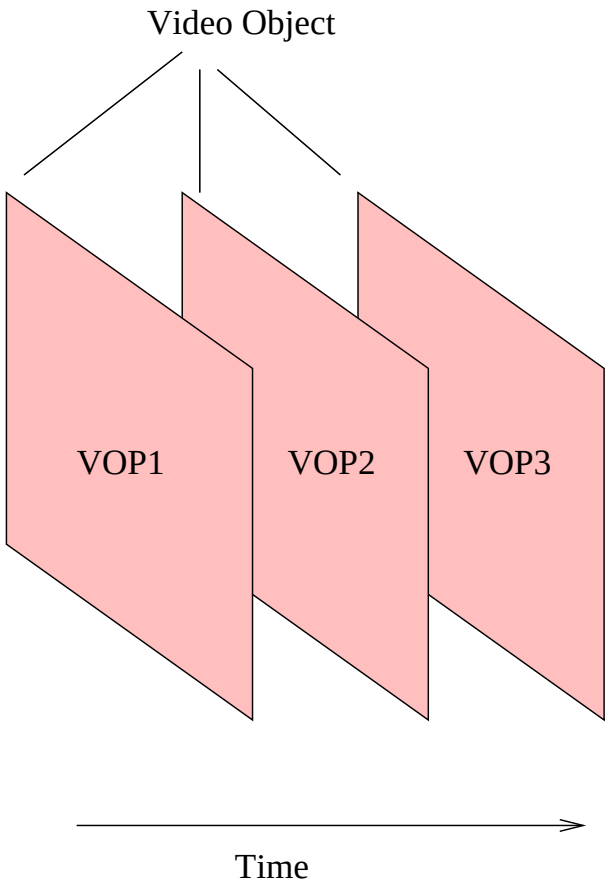

Figure 11.4: VOPs and VO (rectangular)

may be present for an arbitrary length of time. An instance of a VO at a particular point in time is a video object plane (VOP). This definition encompasses the traditional approach of coding complete frames, in which each VOP is a single frame of video and a sequence of frames forms a VO. For example, Figure 11.4 shows a VO consisting of three rectangular VOPs, however in the MPEG-4 video standard, the introduction of the arbitrarily shaped VO concept allows for more flexibility. Figure 11.5 shows a VO that consists of three irregular-shaped VOPs, each one present within a frame and each encoded separately, hence leading to the concept of object-based coding, which will be discussed in more detail in Section 11.3. The VO can be in binary shapes as VO1, VO2, VO3 in Figure 11.6 or in rectangular shape as VO4 in Figure 11.6, which is equivalent to the dimension of the entire video frame's size. For example, if a QCIF video format is used, the dimension would be 176×144 pixels.

In Table 11.2 we summarised some of the important nomenclature, which will be often used, when referring to the MPEG-4 video coding syntax. Let us now consider content-based interactivity in the context of MPEG-4 based coding in more detail.

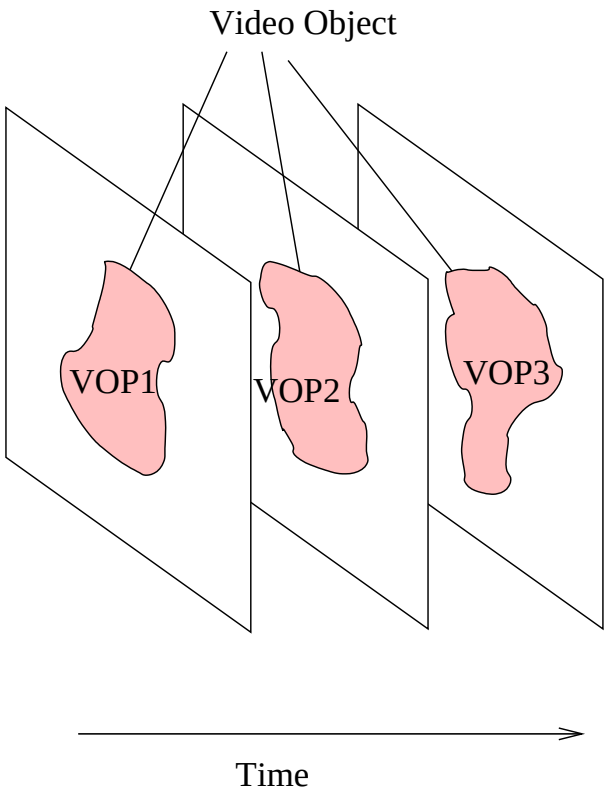

Figure 11.5: VOPs and VO (arbitrary shape)

	Name	Description
□	Visual Object Sequence (VS)	The complete MPEG-4 scene, which may contain 2-D or 3-D natural as well as computer generated objects.
□	Video Object (VO)	A 2D video object. In the simplest case this may be a rectangular frame, or an arbitrarily shaped element of the video frame corresponding to an object or background of the scene.
□	Video Object Layer (VOL)	Every video object can be encoded in a scalable fashion i.e. at different bitrates, using a multi-layer representation constituted by the so-called base-layer and enhancement layer. Alternatively, it may be encoded in a non-scalable, i.e. fixed-bitrate form using a base-layer, but no enhancement layer, depending on the application. These layers are referred to as Video Object Layers (VOL). The VOL facilitates scalable coding, where the video object can be encoded using both spatial and/or temporal scalability.
□	Video Object Plane (VOP)	A VOP is a time-domain sample of a video object. The VOPs can be encoded independently of each other, i.e. using intra-frame coding or inter-frame as well as bidirectional coding techniques employing motion compensation.

Table 11.2: Different MPEG-4 object-oriented representations of various video scenes

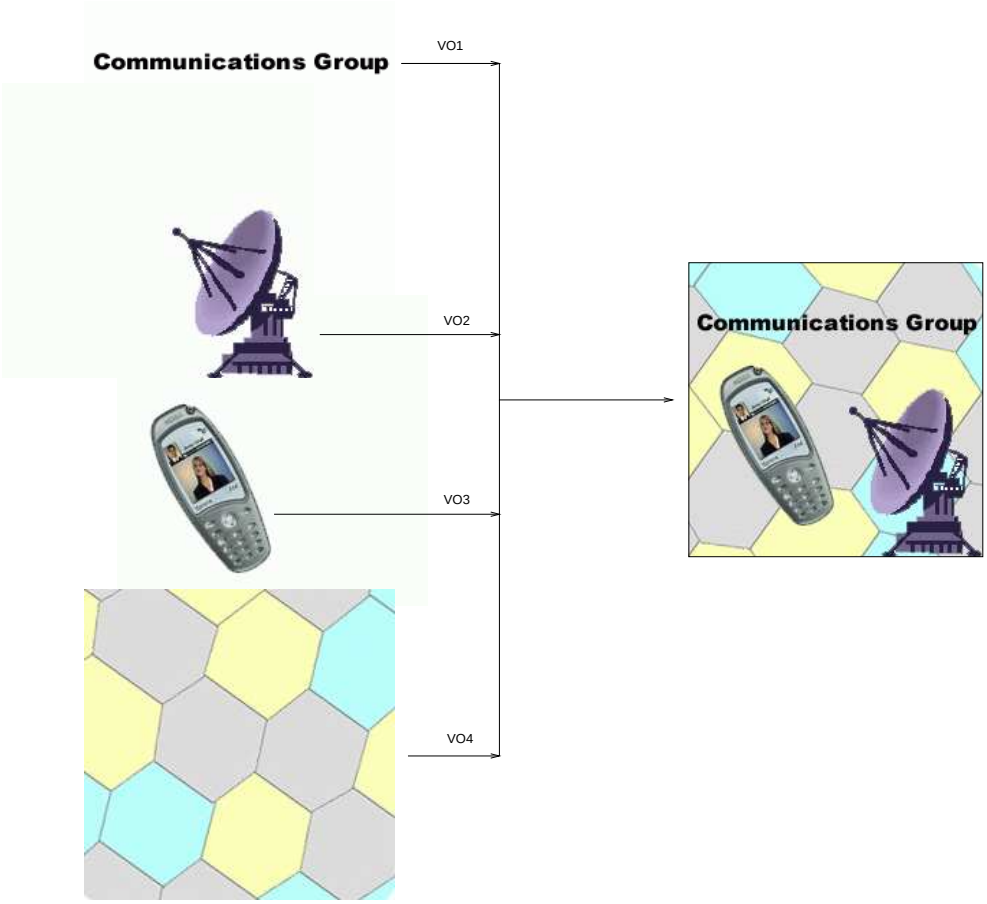

Figure 11.6: Object oriented coding functionality in MPEG-4.

11.3 MPEG-4 : Content-Based Interactivity

'Content-Based Interactivity' attempts to encode an image scene in a way that it will allow the separate decoding and reconstruction of the various objects as well as facilitating the manipulation of the original scene with the aid of simple operations carried out in the form of its bitstream representation [342, 357]. As mentioned in Table 11.2, the MPEG-4 video coding standard provides an "object-layered" bitstream referred to as Video Object Layer (VOL) for supporting this function. Hence, at the encoder the bitstream will be object-layered and the shape, the grade of transparency of each object as well as the spatial coordinates and additional parameters describing object scaling, rotation, etc. are described by the bitstream of each video object layer (VOL) [342]. The received bitstream including all the information bits is decoded and reconstructed by displaying the objects in their original size and at the original location, as depicted in Figure 11.7. Alternatively, it is possible to manipulate the

image sequence according to the user's preference, allowing the scaling shifting and other transformations of the objects, as seen in Figure 11.8.

Figure 11.7: Original decoded video scene.

Figure 11.8: Decoded video scene according to the user's preference. The content-based approach adopted by the MPEG-4 video coding standard allows flexible decoding, representation and manipulation of the video objects in a scene, where for example different-resolution video decoding is facilitated.

As illustrated in Figure 11.8, the mobile phone video object was not decoded, the satellite ground station was decoded and displayed using scaling or rotation. Additionally, a new mobile videophone object defined by the user was included, which did not belong to the original scene. Since the bitstream of the sequence is organised in an "Object Layered" form, the object manipulation is performed at the bitstream level, by adding or deleting the appropriate object bitstreams [358, 359].

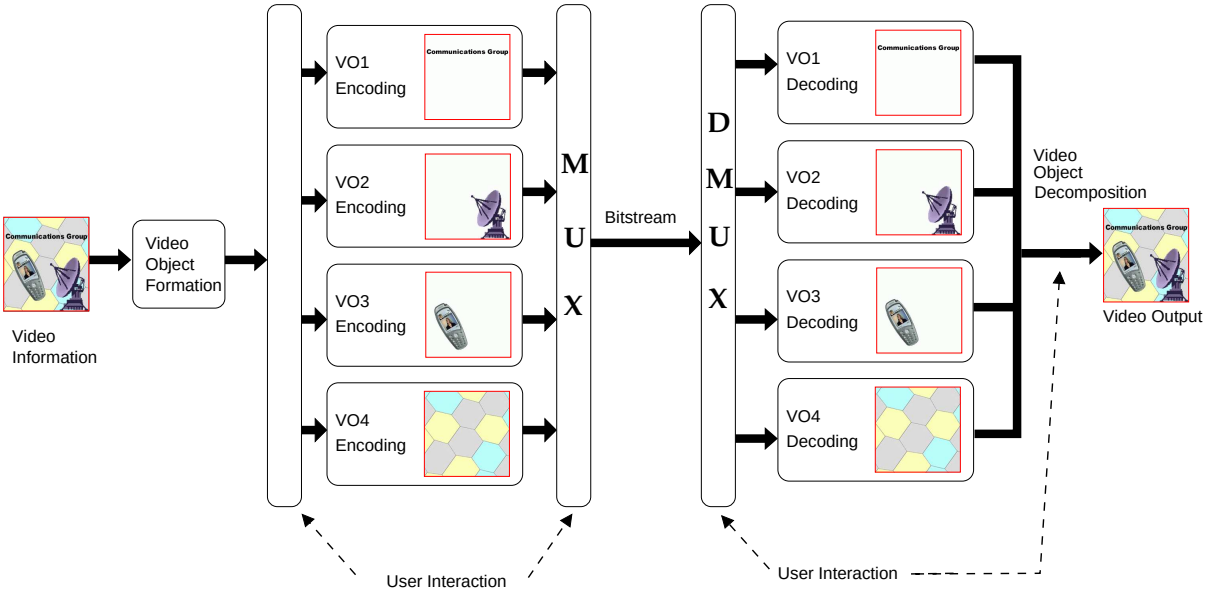

Figure 11.9: The content-based approach adopted by the MPEG-4 video coding standard allows flexible decoding, representation and manipulation of video objects in a scene.

11.3.1 Video Object Plane Based Encoding

Before we may commence the encoding of an object, it must be sampled. Most objects are sampled at regular time intervals corresponding to the frame-scanning rate, and each sample corresponding to the object's spatial representation at an instant in time is known as a Video Object Plane (VOP). Hence each object in the scene is represented by a series of VOPs. In more familiar terms, a camera views a scene and captures the information by sampling the scene (by either canning, or shuttering and scanning). The camera provides its output as a sequence of frames or, in MPEG-4 terminology, the texture part of a sequence of VOPs. A VOP contains texture data and either rectangular shape information or more complex shape data associated with the object. VOPs, like frames in earlier versions of the MPEG codec family [29, 30], may be encoded using intra-frame coding or by using motion compensation.

The MPEG-4 standard introduces the concept of Video Object Planes (VOPs) for supporting the employment of content-based interactive functionalities [340]. The associated concept is illustrated in Figure 11.9. The content of each video input frame is segmented into a number of arbitrarily shaped image regions - i.e. into Video Objects (VO) and each VO is sampled in the time domain by extracting the corresponding area of the consecutive video frames. Each time domain sample of a VO which corresponds to its image in consecutive video frame constitutes a VOP. The shape and location of each VO may vary from frame to frame, which can be visualised by considering the example shown in Figure 11.10. More explicitly, Figure 11.10 shows five consecutive frames of a particular video object, namely that of the paraboloid antenna, which is rotating from the left to the right during the time interval specified by the five consecutive frames spanning the interval of Frame 1 to Frame 5. Hence,

in this case the paraboloid antenna constitutes a VO, while the successive frames portraying the VO constitute VOPs.

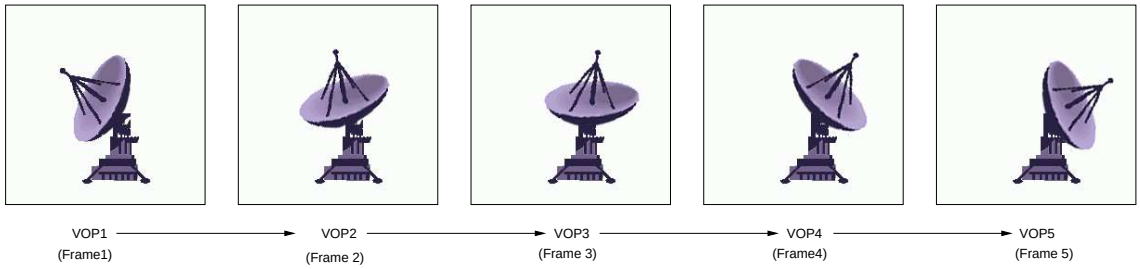

Figure 11.10: The encoding of image sequences using MPEG-4 VOPs enables the employment of content-based functionalities, where the VOP contains five consecutive time domain samples of a VO extracted from five consecutive frames representing a video scene.

In contrast to the MPEG-1 [347] and MPEG-2 [348] standards, the VOP used in MPEG-4 is thus no longer considered to be a rectangular region. Again, the VOP extracted from a video scene contains motion parameters, shape information and texture data. These are encoded using an arrangement similar to a macroblock coding scheme that is reminiscent of the corresponding schemes used the MPEG-1 and MPEG-2 standards, as well as in the ITU H.263 coding standard [31].

11.3.2 Motion and Texture Encoding

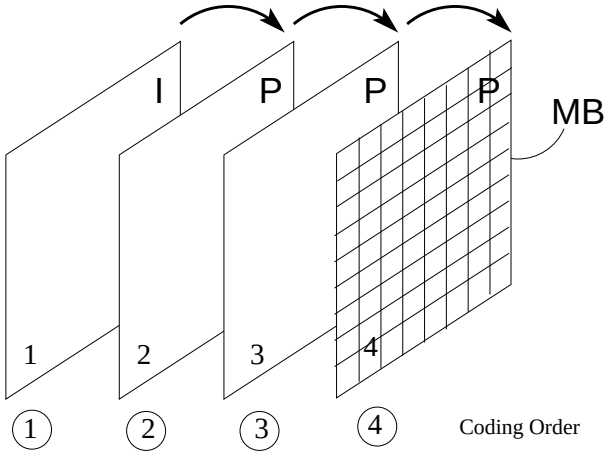

Figure 11.11: I-frames (I-VOP) and P-frame (P-VOP) in a video sequence. The P frames are encoded by using motion compensated prediction based on the nearest previous VOP.

As mentioned earlier, the MPEG-4 video encoding algorithm has a similar structure to that of the well-established MPEG-1/2 and H.263 coding algorithms. Sikora and Schafer

argued in [340] that the MPEG-4 coding algorithm encodes the first VOP in the intra-frame VOP coding mode (I-VOP), while each subsequent frame is encoded using inter-frame coded or predicted VOPs (P-VOP) and only data which accrues from the previous coded VOP frame is used for prediction. As can be seen from Figure 11.11, in this particular case the Video Object is treated in a rectangular form. The first frame is coded as an I-VOP frame, while the second frame-which is the first P-VOP frame-is encoded using the previous I-VOP frame as a reference for temporal coding. Each subsequent P-VOP frame uses the previous P-VOP frame as its reference. Let us now consider how motion and texture encoding is carried out in MPEG-4 [340]. Both the motion and texture encoding of a VOP sequence is block-based. A block in video coding is typically defined as a rectangular array of 8×8 pixels [344]. Since the chrominance of the video signal components is typically sampled at a spatial frequency, which is a factor of two lower, than the spatial sampling frequency of the luminance (Y), each chrominance (C) block carries the colour-difference related information corresponding to four luminance (Y) blocks. The set of these six 8×8-pixel blocks (4Y and 2C) is referred to as a macroblock (MB), as shown in Figures 11.12 and 11.13. A MB is treated as a single encoded unit during the encoding process [360]. Additionally, the MPEG-4 scheme uses Y,U,V coding and a 4:2:0 structure of colour information [350]. This means that the luminance is encoded for every pixel, but the colour difference information is filtered and decimated to half the luminance resolution, both horizontally and vertically. Thus an image area represented by a block of 16×16 luminance pixels requires only 8×8 values for U and 8×8 values for V. Since the standard uses 8×8-pixel blocks for the DCT [349], the macroblock consists of four blocks of luminance samples (Y) and one block U as well as V samples. Figure 11.13 shows the macroblock encoding order for four luminance (Y) and two chronimance (U, V) blocks whereas Figure 11.12 shows the spatial relationship between the luminance and colour difference samples in YUV format.

The block diagram of an idealised video encoder and decoder has been shown earlier in Figure 11.2 of Section 11.2. In this section, we will discuss each individual block of the MPEG-4 video codec in more depth. The MPEG-4 video encoder and decoder are shown in Figure 11.14 and 11.15, respectively. The first frame in a video sequence is encoded in the intra-frame coded mode (I-VOP) without reference to any past or future frames. As seen in Figure 11.2, at the encoder the DCT is applied to each 8×8-pixel luminance and chrominance block. Then each of the 64 DCT coefficients is quantised (Q) in the block. After quantisation, the lowest-frequency DCT coefficient, namely the DC coefficient is treated differently from the remaining coefficients, which are also often referred to as the 'alternating current' (AC) coefficients. The DC coefficient corresponds to the average luminance intensity of the block considered and it is encoded by using a differential DC component encoding method, employing the DC value of the previous frame as reference, when predicting and encoding the current one. The nonzero quantised values of the remaining DCT coefficients and their locations are 'zig-zag'-scanned and run-length or entropy-coded by means of variable-length code (VLC) tables similarly to the techniques shown from the MPEG-1 [29], MPEG-2 [30] and H.263 [27] codecs. More DCT algorithm will be discussed in Subsection **??**. Readers interested in the details of zig-zag scanning are referred to [4], for example.

When considering P-VOP coding, the previous I- or P-VOP frame, namely frame $n-1$ is stored in the reconstructed Frame Buffer (FB) of both the encoder and decoder for frame reference. Motion Compensation (MC) is performed on a macroblock basis. Hence only one Motion Vector (MV) is estimated for the frame VOP-n for a particular macroblock to

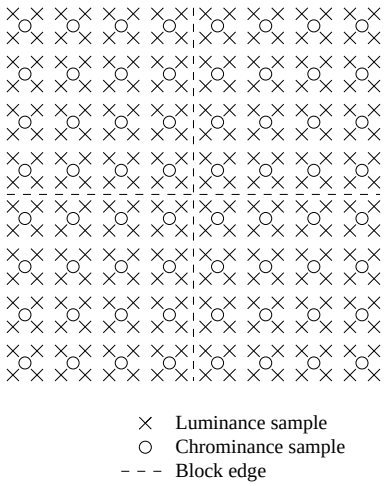

Figure 11.12: Positioning of luminance and chrominance samples in a macroblock containing four 8×8-pixel luminance blocks having a total area of 16×16 pixels in a video frame. Both colour-difference signals separating the chrominance samples are processed at half the spatial resolution.

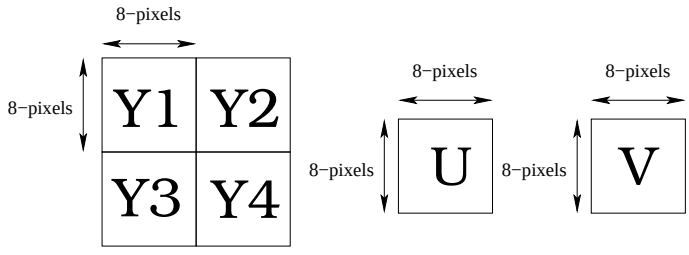

Encoding Order : Y1 , Y2, Y3, Y4, U, V

Figure 11.13: Encoding order of blocks in a macroblock.

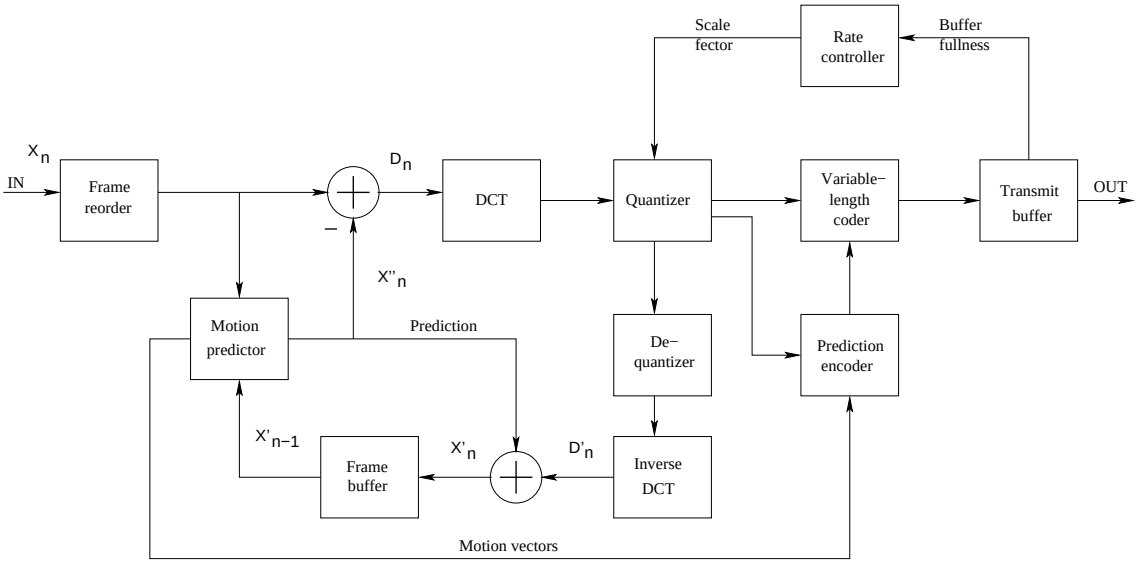

Figure 11.14: Block diagram of the MPEG-4 encoder.

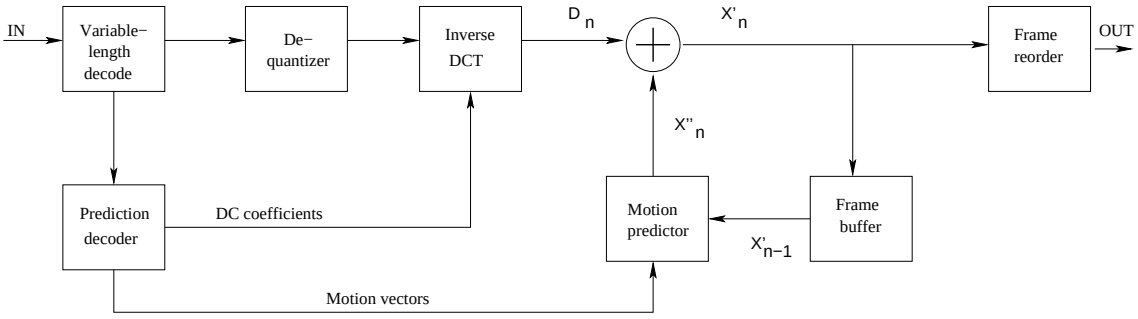

Figure 11.15: Block diagram of the MPEG-4 decoder.

be encoded. These motion vectors are encoded and transmitted to the receiver. The motion-compensated prediction error or block residue $D(n)$ seen in Figure 11.14 is calculated by subtracting each pixel in a macroblock from its motion-shifted counterpart in the previous VOP frame, namely in VOP-$(n-1)$. Then an 8×8-dimensional DCT is applied to each of the 8×8 blocks contained in the macroblock, followed first by quantisation of the DCT coefficients and then by run-length coding and entropy coding, both of which constitute variable-length coding (VLC) techniques.

The decoder of Figure 11.15 uses the 'inverse' routine of the encoder for reproducing a macroblock of the Nth VOP frame at the receiver. After decoding the variable-length words contained in the video decoder's buffer, the pixel values of the motion prediction error or block residue $D(n)$ are reconstructed with the aid of the inverse quantizer (iQ) and inverse DCT blocks of Figure 11.15. The motion-compensated pixels of the previous VOP frame, namely those of VOP-$(n-1)$ are contained in the VOP frame buffer of the decoder, which are added to the motion prediction error $D(n)$ after appropriately positioning them according to the MVs, as seen in Figure 11.15 in order to recover the particular macroblock of VOP-n.

11.3.3 Shape Coding

A VO can be rectangular or of arbitrary shape. For a rectangular VOP, the encoding process is similar to that of the MPEG-1 [347] and MPEG-2 [348] standard. However, if a VO is of arbitrary shape, a further coding step is necessitated prior to motion and texture coding, as illustrated in Figure 11.16 [361]. Specifically, in the MPEG-4 visual standard two types of shape information are considered as inherent characteristics of a VO, binary and gray scale shape information [362].

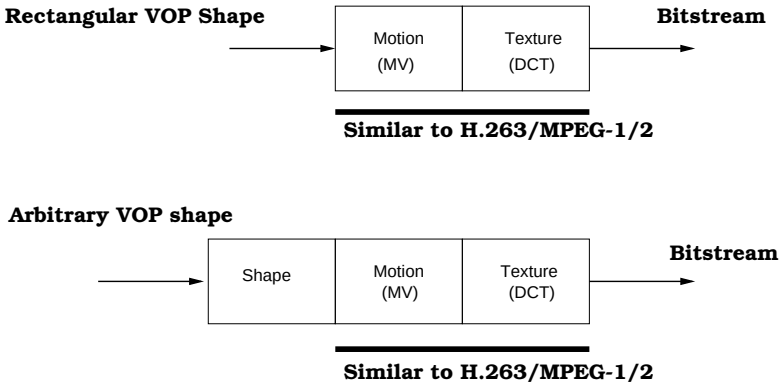

Figure 11.16: MPEG-4 shape coding structures.

11.3.3.1 VOP Shape Encoding

In the MPEG-4 video compression algorithm, the shape of every VOP is coded along with its other parameters, such as its texture and motion vectors. A binary alpha plane defines which pixels within the boundary box belong to the VO at a given instant of time [363]. The VOP

shape information or in this case the binary alpha plane is most commonly represented by a matrix having the same size as the VOP, where each element of the matrix may assume one of two possible values, namely 255 or 0, depending on whether the pixel is inside or outside the video object [362]. If the corresponding pixel belongs to the object, then the element is set to 255, otherwise it is set to 0. This matrix is referred to as a *binary mask* or as a *bitmap*. Figure 11.17 shows the binary alpha plane of the "Miss America" and "Akiyo" VOP.

Figure 11.17: MPEG-4 binary plane of the "Miss America" and "Akiyo" frame.

Before encoding, the binary alpha plane is then partitioned into binary alpha blocks (BAB) of size 16×16-pixels. Each BAB is encoded separately. It is not surprising that a BAB may contain identical values, which are either all 0, in which case the BAB is referred to as a transparent block or 255, when the BAB is said to be an opaque block. The main MPEG-4 tools used for encoding BABs are the Context based Arithmetic Encoding (CAE) algorithm and the motion compensation scheme[3] [362]. Inter-frame CAE (InterCAE) and intra-frame CAE (Intra CAE) are the two variants of the CAE algorithm used in conjunction with P- or I-VOPs, respectively. The InterCAE scenario involves motion vectors, which are based on finding and encoding the best-matching position of the previous VOP frame, whereas the other one is used without motion compensation and is referred to as IntraCAE. A BAB of the current VOP may be encoded in one of the seven possible modes [364]:

[3]Any video sequence can be viewed as a set of consecutive snapshots of still images of a scene. Therefore, the consecutive snapshots are correlated. It is this form of predictability or redundancy that the motion prediction mechanism is exploiting. In a basic form, we can simply use the previous frame for predicting the current frame.

1. If the entire BAB is flagged transparent, no shape encoding is necessary at all and hence texture information is not encoded for this BAB.
2. If the entire BAB is flagged opaque, no shape encoding is necessary at all, but the texture information is encoded for the VOP.
3. The BAB is encoded using IntraCAE without any reference to previous frames and motion compensation.
4. The block is not updated with respect to the same block of the previous frame, if we have zero Motion Vector Difference (MVD) for the block concerned between the previous and current frame.
5. Even if the MVD is zero, the content of the block may be updated. In this case, InterCAE is used for encoding the block update.
6. The MVD is non-zero and no update is necessary, thus neither the texture nor the shape of the block is encoded.
7. The MVD is non-zero and the block has to be updated. In this case, InterCAE is used for encoding both the texture and the shape of the block.

Modes 1 and 2 require no shape coding. For mode 3, shape is encoded using IntraCAE. For modes 4-7, motion estimation and compensation are employed. The motion vector difference (MVD) is the difference between the shape motion vector (MV) and its predicted value (MVP). This predicted value is estimated from either the neighbouring shape motion vectors or from the co-located texture motion vectors. When the mode indicates that no update is required, then the MV is simply used to copy an appropriately displaced 16×16-pixel block from the reference binary alpha plane to the current BAB. If, however, the mode indicates that an update is required, then the update is coded using InterCAE.

11.3.3.2 Gray Scale Shape Coding

Instead of having only 0 and 255 as possible values for the shape encoding matrix, the shape encoding may assume a range of values spanning from 0 to 255, which represent the degree of transparency for each pixel, where 0 corresponds to a transparent pixel and 255 represents an opaque pixel. As regards to the values between 0 and 255, the smaller the value, the more transparent the pixel. Similarly, the larger the value, the more opaque the pixel [363]. This scenario is referred to as gray-scale shape encoding, rather than binary shape encoding. These values may also be stored in a matrix form for representing the shape of VOP. The Gray-scale shape information is also encoded using a block based DCT similar to the conventional approach used in texture coding.

11.4 Scalability of Video Objects

In terms of scalability of the text, images and video to be encoded, the MPEG-4 standard provides a procedure for the supporting complexity-based, spatial, temporal and quality scalability [364] which is the most frequently used parlance for indicating that the MPEG-4 codec

may be configured in a plethora of different coding modes for the sake of striking different trade-offs in terms of the achievable implementation complexity, spatial and temporal resolution, video quality, etc. More specifically:

- Complexity-based scalability of the encoder and decoder facilitates the encoding of images or video at different levels of algorithmic complexity, where the complexity affects the quality of the reconstructed object.

- Spatial scalability makes it possible for the bitstream to be decoded in subsets so that the spatial resolution of the objects would be improved upon decoding each consecutive subset. A maximum of three specific scalability levels are supported for video objects and 11 different levels for still images as well as for text.

- The philosophy of Temporal scalability is similar to that of spatial scalability, except that the video is displayed at a reduced temporal resolution, rather than reduced spatial resolution, for example at lower frame-rate.

- Quality-motivated scalability implies that a bitstream could be separated into several layers, corresponding to different bitrates. When the layers are decoded, the quality is determined by the number of layers that was used.

Important considerations for video coding schemes to be used within future wireless networks are the achievable compression efficiency, the attainable robustness against packet loss, the ability to adapt, to different available bandwidths, different amounts of memory and computational power for different mobile clients, etc. Scalable video coding schemes have been proposed in the literature [72, 108, 118–120, 124], which are capable of producing bit-streams decodable at different bit-rates, requiring different computational power and channel bit-rate.

An example associated with two layers of scalability coding is shown in Figure 11.18. The enhancement layers are encoded by a motion-compensated hybrid codec, where the DCT has been replaced by lattice vector quantisation of the MCER. This approach leads to a coding efficiency attained by the layered coding scheme, which is comparable to that of single-layer codecs [344]. Since the ability to decode an enhancement layer depends on the reception of the base layer and lower enhancement layers, an efficient transmission scheme is expected to ensure that these layers are transmitted such that the associated packet loss is kept as low as possible even for high overall packet loss rates. In addition to the ability to adapt to different clients we can also ensure a sufficiently graceful degradation of the associated video quality in case of packet loss in this scenario.

As mentioned earlier, MPEG-4 provides both spatial and temporal scalability at the object level [24, 364]. In both of these scenarios this technique is invoked for the sake of generating a *base layer*, representing the lowest quality to be supported by the bitstream, and one or more *enhancement layers*. These layers may all be produced in a single encoding step. The scaling can be implemented in two different ways. When there are known bandwidth limitations, the different-rate versions of the bitstream may be used that include only the base layer, or the base layer plus lower-order enhancement layers. Alternatively, all layers may be transmitted and the scaling decision may be left for the decoder's discission. If the display device at the receiver side has a low resolution, or if the available computational resources are insufficient capability, the enhancement layers may be ignored.

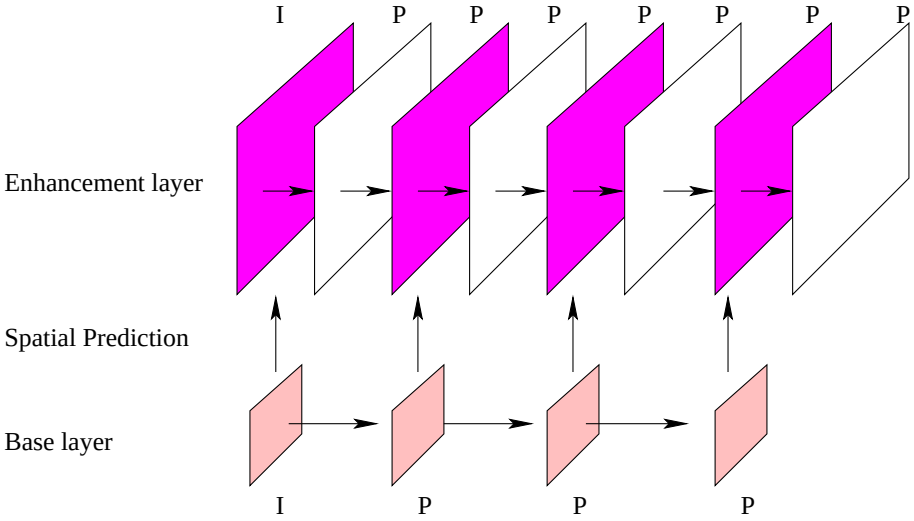

Figure 11.18: Example of a possible configuration of the spatio-temporal resolution pyramid of the scalable video codec. One base layer relying on an intra-frame and three interpolated inter coded frames are shown, supplemented by an enhancement layer having twice the spatial and temporal resolution. The horizontal and vertical arrows denote temporal and spatial prediction, respectively.

Figure 11.19 shows the concept of an encoder exploiting spatial scalability; in this case at just two levels. The input VOP is down-converted to a lower resolution, resulting in the base layer. This layer is encoded and then a decoder reconstructs the base-layer VOP, as it will appear at the decoder's display. This VOP is then up-converted to the same resolution as the input, and a subtraction operation generates the difference in comparison to the original image. These are separately encoded in an enhancement-layer encoder. Note that each stream of the encoded VOPs forms a video object layer. The base-layer VOL uses both Intra- and Inter-frame coding, but the enhancement layer uses only predictive coding. The base-layer VOPs are used as references, as shown in Figure 11.18

11.5 Video Quality Measures

In this section, the objective video quality measure used during our investigations of the various wireless video transceivers is defined. Quantifying the video quality is a challenging task, because numerous factors may affect the results. Video quality is inherently *subjective* and our human perception is influenced by many factors.

11.5.1 Subjective Video Quality Evaluation

Several test procedures designed for subjective video quality evaluation were defined in the ITU-R Recommendation BT.500-11 [365]. A commonly-used procedure outlined in the standard is the so-called Double Stimulus Continuous Quality Scale (DSCQS) method, in which

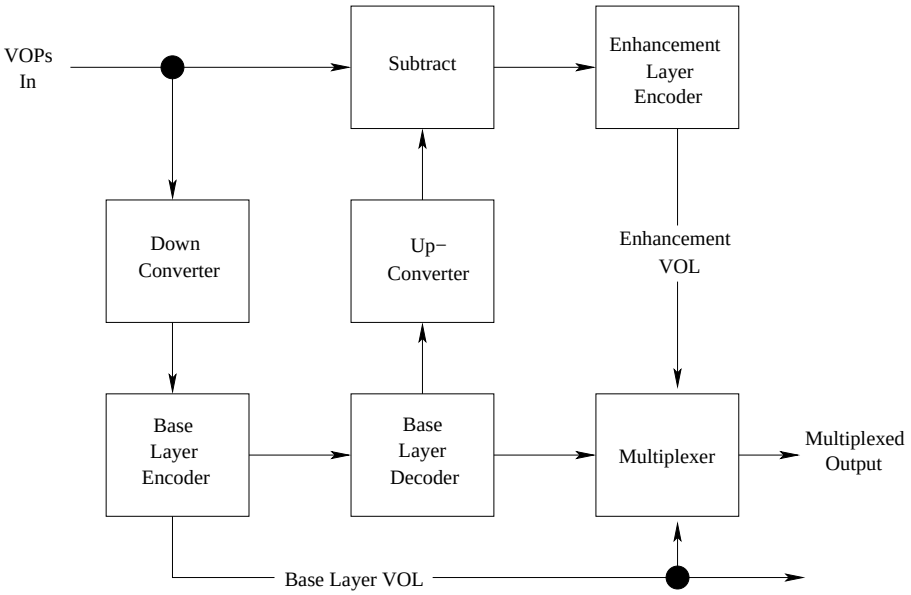

Figure 11.19: Spatially scalable encoder for a single enhancement layer.

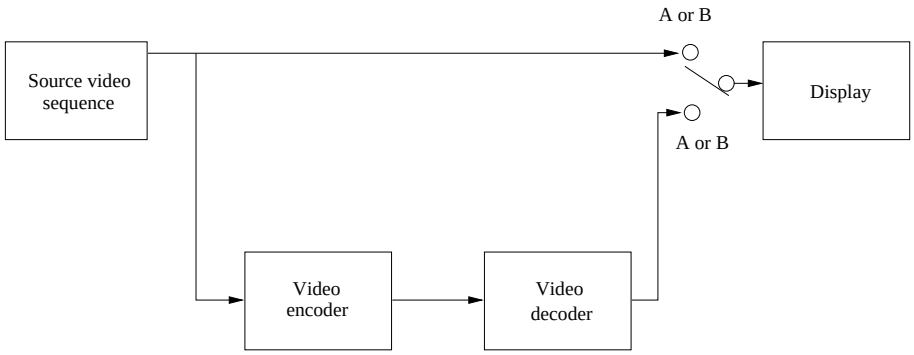

Figure 11.20: DSCQS testing system

an assessor is presented with a pair of images or short video sequences A and B, one after the other, and is asked to assign both A and B a quality score on a continuous scale having five intervals ranging from 'Excellent' to 'Bad'. In a typical test session, the assessor is shown a series of pairs of sequences and is asked to grade each pair. Within each pair of sequences, one sequence is an unimpaired 'reference' sequence and the other is the same sequence, modified by a system or process under test. Figure 11.20 shows an experimental set up for the testing of a video codec, where the original sequence is compared to the same sequence after encoding and decoding. Additionally, the order in which the sequence 'A' and 'B' are presented randomly. The evaluation of subjective measures, such as the DSCQS measure is time consuming and expensive. Hence, contriving an objective video quality measure, which is capable of reliably predicting the subjective quality is desirable.

11.5.2 Objective Video Quality

The designers and developers of video compression and processing systems rely heavily on objective quality measures. The most widely used measure is the Peak Signal to Noise Ratio (PSNR). The PSNR is measured on a logarithmic scale and depends on the normalised mean squared error (MSE) between the original and the reconstructed as well as potentially channel-impaired image or video frame, relative to $(2^n - 1)^2$, namely normalised by the square of the highest possible pixel value in the image, where n is the number of bits per image sample, yielding:

$$PSNR = 10log_{10}\frac{(2^n - 1)^2}{MSE}. \tag{11.1}$$

The PSNR may be conveniently calculated. However, its evaluation requires the availability of the unimpaired original image or video signal for comparison, which may not be available.

Unfortunately the PSNR defined above does not always constitute a reliable image quality measure. For example, if the received image is shifted by one pixel compared to the original image, the human eye would hardly notice any difference, while the PSNR objective measures would indicate a more substantial degradation in quality.

Nonetheless, owing to its appealing implicity, in this thesis, the PSNR will be used as the predominant image quality measure.

11.6 Effect of Coding Parameters

The previous sections described the MPEG-4 encoding and decoding process with the aid of block diagrams shown in Figures 11.14 and 11.15. In video compression, some of the encoding parameters seen in the context of Figures 11.14 and 11.15 may directly affect the resultant reconstructed video quality. Therefore in this section, we will briefly demonstrate how these parameters may affect the encoded/decoded video quality.

The MPEG-4 source code used in our simulations was a modified version of the software implementation provided by the Mobile Multimedia Systems (MoMuSys) Pan-European project. Simulations were carried out for the sake of characterising the achievable performance of the MPEG-4 codec. Most of our simulations used the popular "Akiyo", "Miss America", "Suzi"

or "Foreman" (144×176)-pixel resolution QCIF video sequence at a transmission frame scanning rate of 10 or 30 frames/s. Additionally, the length of the video sequence used in our simulations was 100 frames and apart from the first frame, no Intra-Frame coded update was used, unless otherwise stated. Our results will be shown in graphical form in Figure 11.25 to Figure 11.28.

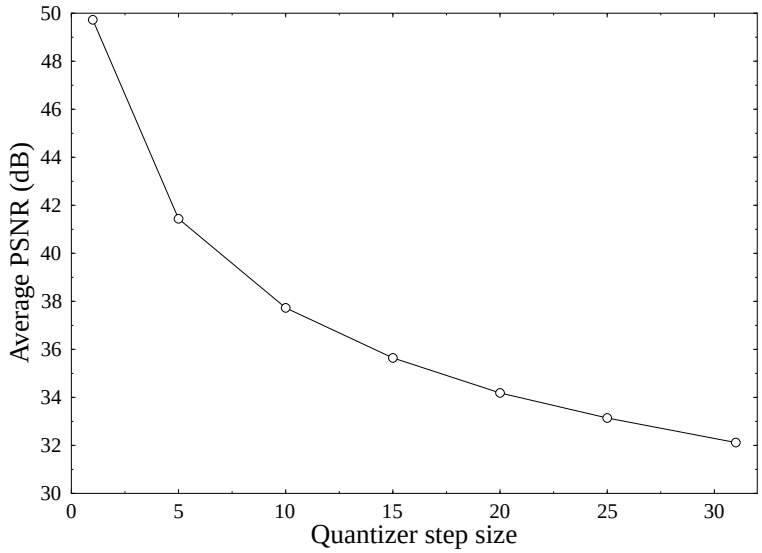

Figure 11.21: MPEG-4 average video quality (PSNR) versus quantiser step size ranging from 1 to 31 using the (144×176)-pixel QCIF "Miss America" sequence.

Our investigations commenced by demonstrating the effect of the quantiser index employed in the MPEG-4 encoder. In video compression, the quantisation operation is typically constituted by a 'forward quantiser' in the encoder and an 'inverse quantiser' in the decoder. A critical parameter is the quantiser step size. If the step size is large, typically a highly compressed bit stream is generated. However, the reconstructed values provide a crude approximation of the original signal. If the step size is small, the reconstructed values match the original signal more closely at the cost of a reduced compression efficiency. The effect of different quantiser step sizes is demonstrated in Figure 11.21 in terms of the video PSNR, while the associated subjective video quality is illustrated in Figure 11.22.

Let us now consider the effect of different bit-rates, although the effects of the video bit-rate and quantiser step size are highly correlated. In order to achieve a given target bit-rate, the encoded video frame buffer is used for adjusting the quantiser step size. More explicitly, the encoder produces a variable-rate stream and the buffer may be emptied at a near-constant transmission rate. If the encoder produces bits at a low rate, the buffer may become empty.

Fine

Quantizer step size 1

Quantizer step size 5

Quantizer step size 15

Coarse

Quantizer step size 20

Quantizer step size 25

Quantizer step size 31

Figure 11.22: The effect of quantisation step size on the MPEG-4 encoder in the 2nd frame of the 144x176 pixel QCIF “Miss America” sequence.

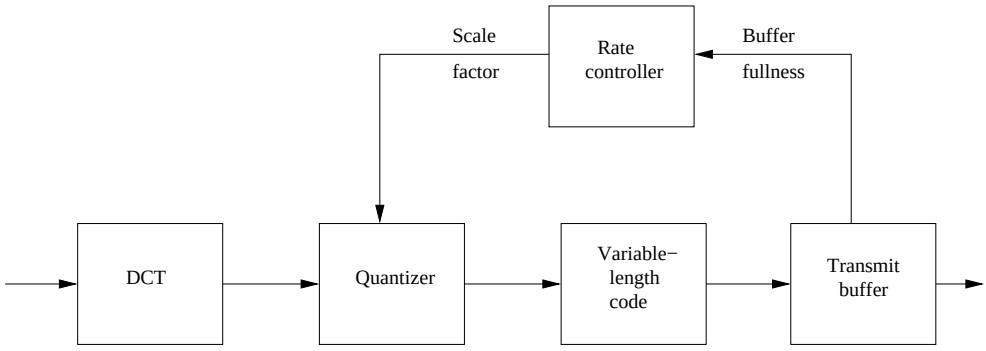

Figure 11.23: Rate control in MPEG-4.

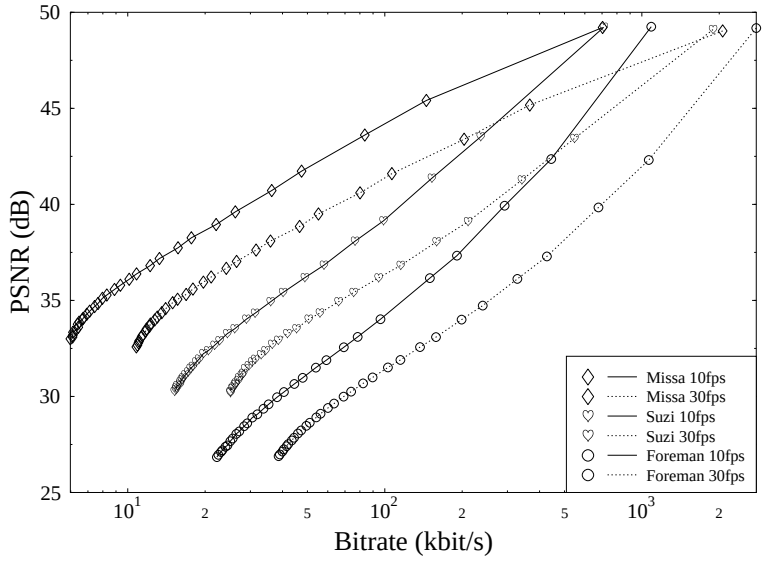

Figure 11.24: Image quality (PSNR) versus coded bit-rate performance of the MPEG-4 codec for various QCIF- resolution video sequences scanned at 10 and 30 frames/s.

By contrast, if the encoded bitrate is too high, the buffer may overflow and the data may become irretrievably lost. For the sake of avoiding these two problems, we typically feed a measure of buffer fullness to the rate controller, which reacts by appropriately adjusting the quantisation step size of the DCT coefficients of the video blocks that have not yet been encoded. Figure 11.23 shows the rate control mechanism of the basic MPEG-4 encoder. The actions of the rate-controller are characterised in Figures 11.24 and 11.25. More specifically, Figure 11.24 characterises the average PSNR versus bit-rate performance, while Figure 11.25 shows the PSNR versus the video frame index. The bit rate range used in these simulations spanned between 10 kbit/s (kbps) and 1000 kbps. As expected, it can be seen from the graphs that the video quality increases upon increasing the video bit-rate. Figure 11.25 plots the PSNR versus frame index performance for the "Akiyo" sequence scanning at the video frame rate of 10 fps in bit-rate range spanning from 10 kbps to 100 kbps.

So far, our experiments were carried out in an error-free environment for various encoding parameters. The next experiments were carried by transmitting the MPEG-4 bitstream over an Additive White Gaussian Noise (AWGN) channels using a simple BPSK modem. Note that the system used in this experiment employed no channel coding. Figure 11.26 portrays the PSNR versus video frame index performance for transmission over the AWGN channel for the channel SNR range spanning from 9 dB to 14 dB. Figure 11.27 shows the average luminance (Y) PSNR versus Bit Error Ratio (BER). Observe in Figures 11.26 and 11.27 that

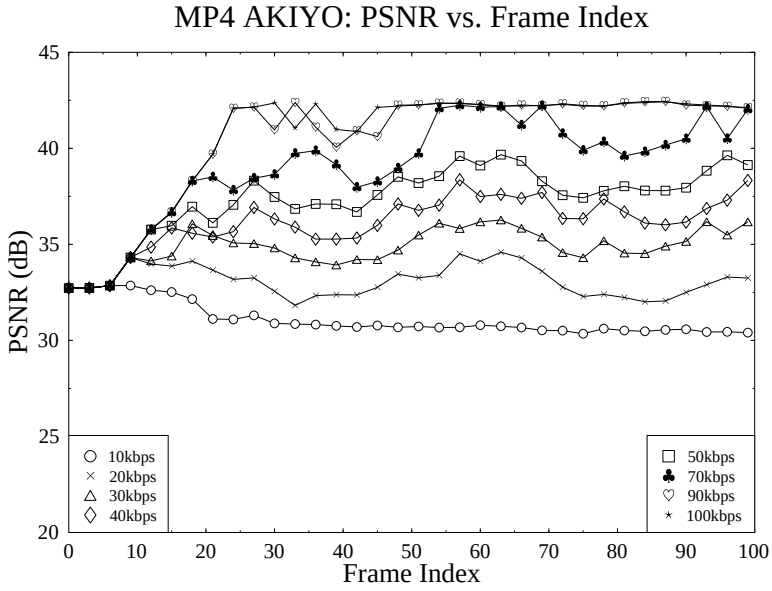

Figure 11.25: MPEG-4 video quality (PSNR) versus frame index performance for the bit rate range spanning from 10kbps to 100kbps using the (144x176)-pixel QCIF "Akiyo" sequence.

as expected, the decoded picture quality increases as the channel SNR increases. At low channel SNRs, the channel inflicts a high BER, hence the decoded video frame sequence will be highly degraded. This is demonstrated in Figure 11.29. Viewing the codec's performance from a different perspective, Figure 11.28 shows the average PSNR degradation versus BER.

11.7 Summary and Conclusion

In Section 11.1, we commenced our discourse by a brief historical perspective on the development of the MPEG-4 visual standard, the MPEG-4 visual profiles and features. These include the diverse set of coding tools described in the standard that are capable of supporting a wide range of applications, such as efficient coding of video frames, video coding for error-prone transmission networks, object-based coding and manipulation, as well as the interactive visual applications.

In Section 11.3, we introduced the MPEG-4 visual encoding standard that supports an object-based representation of the video sequence. This allows convenient access to and manipulation of arbitrarily shaped regions in the frames of the video sequence.

Scalable coding is another of the feature supported by the MPEG-4 codec. Scalability is supported in terms of generating several layers of information. In addition to the base layer, enhancement layers may be decoded, which will improve the resultant image quality either

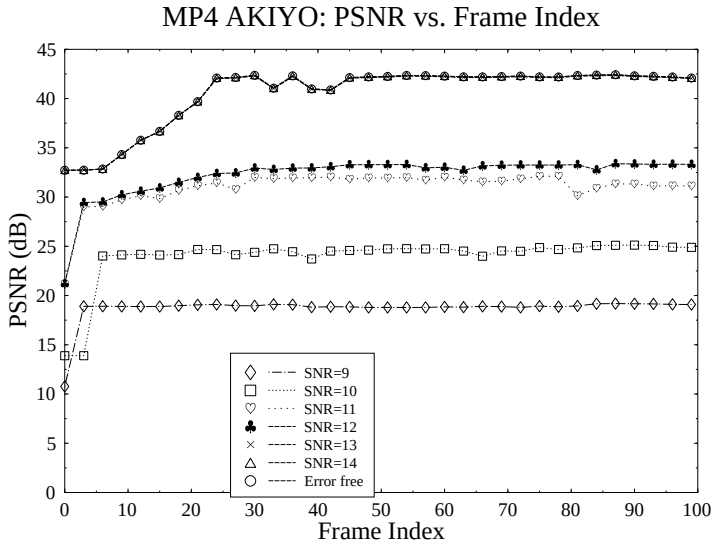

Figure 11.26: Decoded video quality (PSNR) versus frame index when transmitting over an AWGN channel using a BPSK modem. These results were recorded for the 'Akiyo' video sequence at a resolution of (144x176)-pixels and 100kbps video bitrate. The 81st decoded video frame was shown in Figure 11.29

in terms of the achievable temporal or spatial resolution.

In Section 11.5 the PSNR objective measure was introduced for quantifying the video quality. Finally, the effect of certain important video encoding parameters were discussed in Section 11.6, commencing with an emphasis on the *quantiser step size* parameter, which also affects the resultant video *target bitrate*.

The specifications of MPEG-4 standard continue to evolve with the addition of new tools, such as the recently introduced profile supporting video streaming [24]. However, amongst developers and manufacturers, the most popular elements of the MPEG-4 Visual standard to date have been the simple and the advanced simple profile tools, which were summarised in Table 11.1. Having studied the MPEG-4 codec, let us know focus our attention on one it relative, namely on the H.264 [26] codec in the next Chapter.

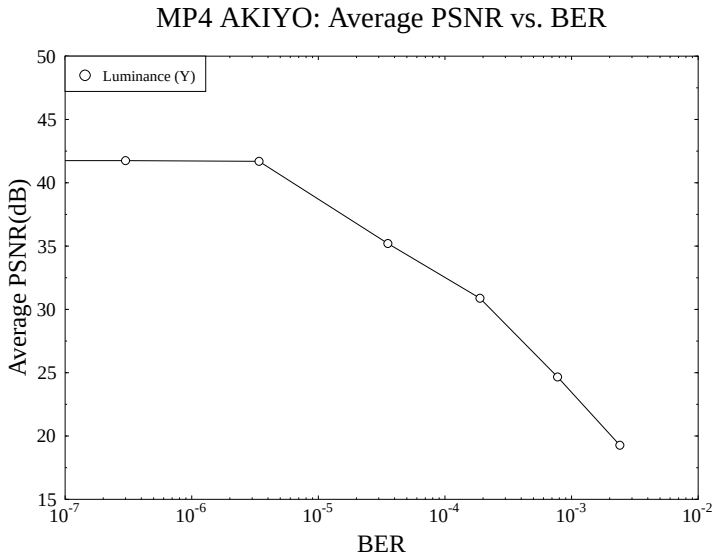

Figure 11.27: Average video quality (PSNR) versus BER for transmission over an AWGN channel using BPSK modulation and the (144x176)-pixel QCIF 'Akiyo' sequence.

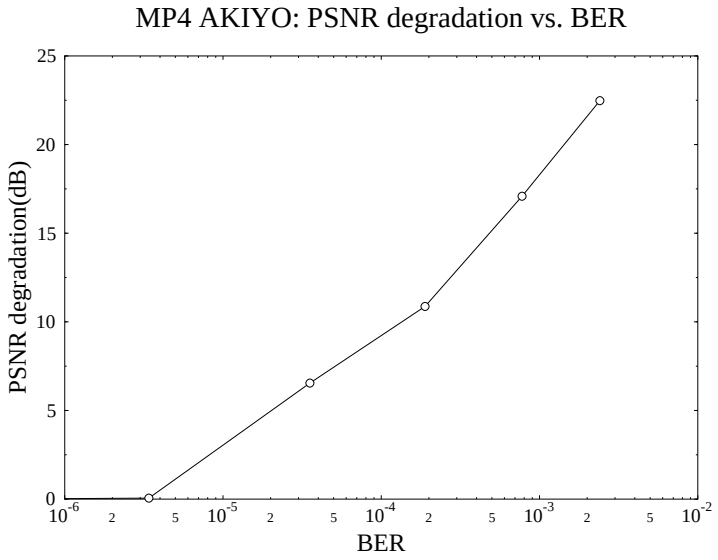

Figure 11.28: Decoded video quality degradation in terms of PSNR versus Bit Error Rate (BER) for transmission over an AWGN channel using BPSK modulation due to corruption of the MPEG-4 bit stream during transmission. The results were recorded for the QCIF resolution "Akiyo" video sequence.

SNR = 9dB SNR = 10dB SNR = 11dB

SNR = 12dB SNR = 13dB SNR = 14dB

Figure 11.29: Image degradation due to corruption of the MPEG-4 bitstream over AWGN channels using a BPSK modem in the 81st frame of the (144x176)-pixel QCIF "Akiyo" sequence. The BER within this frame at the above SNRs were between 10^{-7} to 10^{-3} respectively, while the PSNR ranged from 41.74dB to 19.27dB.

Chapter 12

HSDPA-Like and Turbo-Style Adaptive Single- and Multi-Carrier Video Systems

P.J. Cherriman, J-Y. Chung, L. Hanzo, T. Keller, E-L. Kuan, C.S. Lee, R. Maunder, S.X. Ng, S. Vlahoyiannatos, J. Wang, B.L. Yeap

12.1 Turbo-Equalized H.263-Based Videophony for GSM/GPRS[1] [2]

12.1.1 Motivation and Background

The operational second-generation (2G) wireless systems [389] constitute a mature technology. In the context of 2G systems, and, with the advent of videotelephony, attractive value-added services can be offered to a plethora of existing users. Although the 2G systems have not been designed with video communications in mind, with the aid of the specially designed error-resilient, fixed-rate video codecs proposed in Chapters 3–5 it is nonetheless realistic to provide videophone services over these low-rate schemes. Specifically, in this chapter we designed a suite of fixed-rate, proprietary video codecs capable of operating at a video scanning or refreshment rate of 10 frames/s over an additional speech channel of the 2G systems. These video codecs were capable of maintaining sufficiently low bit rates for the provision of videophony over an additional speech channel in the context of the operational 2G wireless systems [389] provided that low-dynamic head-and-shoulders video sequences of the 176 $\times$

[1] This section is based on **P. Cherriman, B. L. Yeap, and L. Hanzo**: Turbo-Equalised H.263-based video telephony for GSM/GPRS; submitted to IEEE Tr. on CSVT, 2000.

Simulation Parameters	
Channel model	COST-207 hilly terrain
Carrier frequency	900 MHz
Vehicular speed	30 mph
Doppler frequency	40.3 Hz
Modulation	GMSK, $B_n = 0.3$
Channel coding	Convol.(n,k,K) = (2,1,5)
Octal generator polynomials	23, 33
Channel interleavers	Random (232, 928)
Turbo-coding interleavers	Random (116, 464)
Max turbo-equalizer iterations	10
No. of TDMA frame per packet	2
No. of slots per TDMA frame	1, 4
Convolutional decoder algorithm	LOG-MAP
Equalizer algorithm	LOG-MAP

Table 12.1: System parameters

144-pixel Quarter Common Intermediate Format (QCIF) or 128 $\times$ 96-pixel sub-QCIF video resolution are employed. We note, however, that for high-dynamic sequences the 32 kbps typical speech bit rate of the cordless telephone systems [389], such as the Japanese PHS, the Digital European Cordless Telephone (DECT), or the British CT2 system, is more adequate in terms of video quality. Furthermore, the proposed programmable video codecs are capable of multirate operation in the third generation (3G) Universal Mobile Telecommunications System (UMTS) or in the IMT2000 and cdma2000 systems, which were summarized in [82].

Chapters 3–5 used constant video rate proprietary video codecs and reconfigureable Quadrature Amplitude Modulation (QAM)-based [390] transceivers. In this chapter we advocate constant-envelope Gaussian Minimum Shift Keying (GMSK) [389]. Specifically, we investigated the feasibility of H.263-based videotelephony in the context of an enhanced turbo-equalized GSM-like system, which can rely on power-efficient class-C amplification. The associated speech compression and transmission aspects are beyond the scope of this book [391].

The outline of this section is as follows. Section 12.1.2 summarizes the associated system parameters and system's schematic, while Section 12.1.3 provides a brief overview of turbo equalization. Section 12.1.4 characterizes the system both in terms of turbo equalization performance and video performance. Lastly, Section 12.1.5 provides our conclusions. Let us now consider the outline of the system.

12.1.2 System Parameters

The associated video system parameters for the GSM system are summarized in Table 12.1, and the system's schematic is portrayed in Figure 12.1. An advanced feature of the system is its employment of joint channel decoding and channel equalization, which is referred to as turbo equalization. The fundamental principles and motivation for using turbo equalization are described in Section 12.1.3.

The system uses the GSM frame structure of Chapter 8 in [389] and the COST-207 Hilly Terrain (HT) channel model, whose impulse response is shown in Figure 12.2. Each trans-

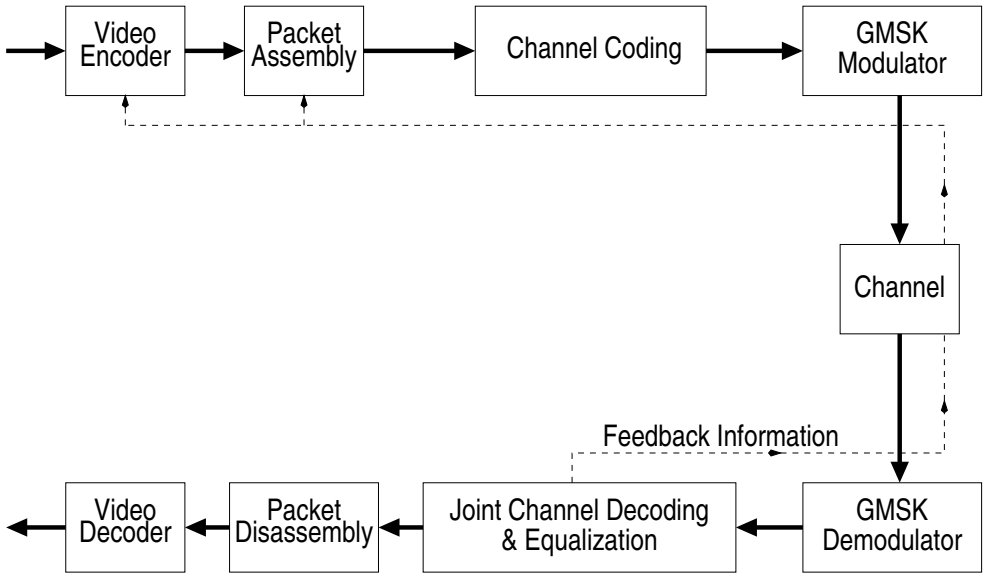

Figure 12.1: System schematic for turbo-equalized video system.

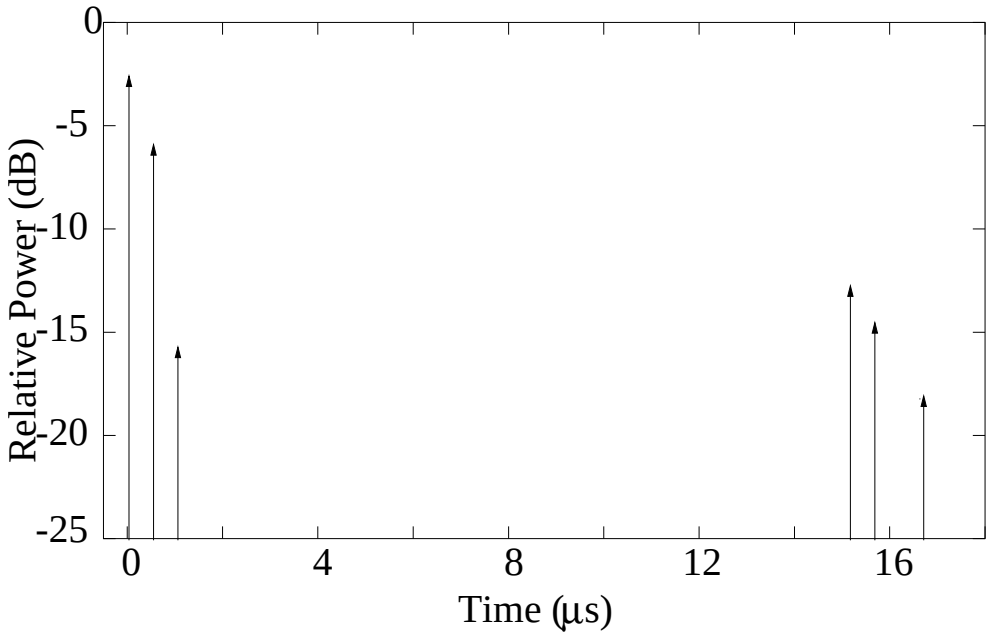

Figure 12.2: COST207-Hilly terrain channel model.

Bit rates, etc.		
Slots/TDMA frame	1	4
Coded bits/TDMA slot	116	116
Data bits/TDMA slot	58	58
Data bits/TDMA frame	58	232
TDMA frame/packet	2	2
Data bits/packet	116	464
Packet header (bits)	8	10
CRC (bits)	16	16
Video bits/packet	92	438
TDMA frame length	4.615 ms	4.615 ms
TDMA frames/s	216.68	216.68
Video packets per sec	108.34	108.34
Video bit rate (kbps)	10.0	47.5
Video frame rate (fps)	10	10

Table 12.2: Summary of System-Specific Bit Rates

mitted packet is interleaved over two GSM TDMA frames in order to disperse bursty errors.

The GPRS system allows the employment of multiple time-slots per user. We studied both a GSM-like system using 1 slot per TDMA frame and a GPRS-like arrangement with four slots per TDMA frame. In this scenario, the user is assigned half the maximum capacity of an eight-slot GPRS/GSM carrier. The bit rates associated with one and four slots per TDMA frame are shown in Table 12.2.

The effective video bit rates that can be obtained in conjunction with half-rate convolutional coding are 10 and 47.5 Kbit/s for the one and four slots per TDMA frame scenario, respectively. Again, the system's schematic is shown in Figure 12.1. The basic prerequisite for the duplex video system's operation (as seen in Figure 12.1) is use of the channel decoder's output is used for assessing whether the received packet contains any transmission errors. If it does, the remote transmitter is instructed (by superimposing a strongly protected packet acknowledgment flag on the reverse-direction message) to drop the corresponding video packet following the philosophy of [392]. This prevents the local and remote video reconstructed frame buffers from being contaminated by channel errors.

12.1.3 Turbo Equalization

Turbo equalization [393] was proposed by Douillard, Picart, Jézéquel, Didier, Berrou, and Glavieux in 1995 for a serially concatenated rate $R = \frac{1}{2}$, convolutional-coded Binary Phase Shift Keying (BPSK) system. Specifically, Douillard *et al.* demonstrated that the turbo equalizer could mitigate the effects of intersymbol interference (ISI), provided that the channel impulse response (CIR) is known. Instead of performing the equalization and error correction decoding independently, better performance can be achieved by considering the channel's memory, when performing joint equalization and decoding iteratively. Gertsman and Lodge [394] then showed that the iterative process of turbo equalizers can compensate for the degradations caused by imperfect channel estimation. In the context of noncoherent detection, Marsland *et al.* [395] demonstrated that turbo equalization offered better performance

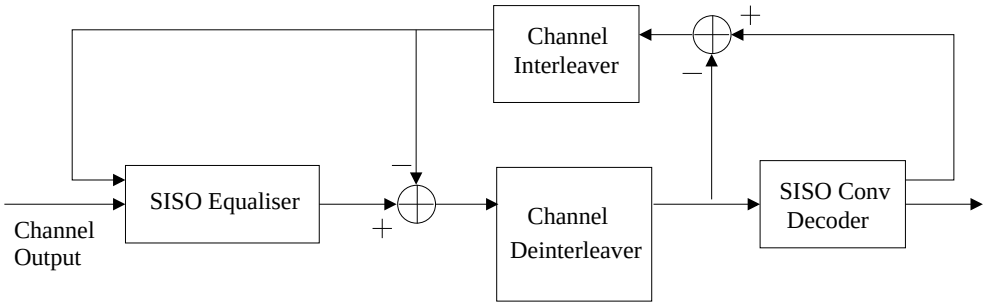

Figure 12.3: Structure of original turbo equalizer introduced by Douillard *et al.* [393].

than Dai's and Shwedyk's noncoherent, hard-decision-based receiver using a bank of Kalman filters [396]. Different iteration termination criteria [397], such as cross-entropy [398], were also investigated in order to minimize the number of iteration steps for the turbo equalizer. A turbo-equalization scheme for the Global System of Mobile Communications (GSM) was also proposed by Bauch and Franz [399], who investigated different approaches for overcoming the dispersion of the *a priori* information due to the interburst interleaving scheme used in GSM. Further research into combined turbo coding using convolutional constituent codes and turbo equalization has been conducted by Raphaeli and Zarai [400].

The basic philosophy of the original turbo-equalization technique derives from the iterative turbo-decoding algorithm consisting of two Soft-In/Soft-Out (SISO) decoders. This structure was proposed by Berrou *et al.* [401, 402]. Before proceeding with our in-depth discussion, let us briefly define the terms *a priori*, *a posteriori*, and extrinsic information, which we employ throughout this section.

A priori The *a priori* information associated with a bit v_m is the information known before equalization or decoding commences, from a source other than the received sequence or the code constraints. *A priori* information is also often referred to as intrinsic information to contrast it with extrinsic information.

Extrinsic The extrinsic information associated with a bit v_m is the information provided by the equalizer or decoder based on the received sequence and on the *a priori* information of all bits with the exception of the received and *a priori* information explicitly related to that particular bit v_m.

A posteriori The *a posteriori* information associated with a bit is the information that the SISO algorithm provides taking into account all available sources of information about the bit u_k.

The turbo equalizer of Figure 12.3 consists of a SISO equalizer and a SISO decoder. The SISO equalizer in the figure generates the *a posteriori* probability upon receiving the corrupted transmitted signal sequence and the *a priori* probability provided by the SISO decoder. However, at the initial iteration stages (i.e., at the first turbo-equalization iteration) no *a priori* information is supplied by the channel decoder. Therefore, the *a priori* probability is set to $\frac{1}{2}$, since the transmitted bits are assumed to be equiprobable. Before passing the *a posteriori*

information generated by the SISO equalizer to the SISO decoder of Figure 12.3, the contribution of the decoder in the form of — *a priori* information — accruing from the previous iteration must be removed in order to yield the combined channel and extrinsic information. This also minimizes the correlation between the *a priori* information supplied by the decoder and the *a posteriori* information generated by the equalizer. The term "combined channel and extrinsic information" indicates that they are inherently linked. In fact, they are typically induced by mechanisms, which exhibit memory. Hence, they cannot be separated. The removal of the *a priori* information is necessary, to prevent the decoder from "reprocessing" its own information, which would result in the positive feedback phenomenon, overwhelming the decoder's current reliability-estimation of the coded bits, that is, the extrinsic information.

The combined channel and extrinsic information is channel-deinterleaved and directed to the SISO decoder, as depicted in Figure 12.3. Subsequently, the SISO decoder computes the *a posteriori* probability of the coded bits. Note that the latter steps are different from those in turbo decoding, which only produces the *a posteriori* probability of the source bits rather than those of all channel-coded bits. The combined deinterleaved channel and extrinsic information are then removed from the *a posteriori* information provided by the decoder in Figure 12.3 before channel interleaving in order to yield the extrinsic information. This approach prevents the channel equalizer from receiving information based on its own decisions, which was generated in the previous turbo-equalization iteration. The extrinsic information computed is then employed as the *a priori* input information of the equalizer in the next channel equalization process. This constitutes the first turbo-equalization iteration. The iterative process is repeated until the required termination criteria are met [397]. At this stage, the *a posteriori* information of the source bits, which has been generated by the decoder, is utilized to estimate the transmitted bits.

Recent work by Narayanan and Stüber [403] demonstrates the advantage of employing turbo equalization in the context of coded systems invoking recursive modulators, such as Differential Phase Shift Keying (DPSK). Narayanan and Stüber emphasized the importance of a recursive modulator and show that high-iteration gains can be achieved, even when there is no ISI in the channel (i.e., for transmission over the nondispersive Gaussian channel). The advantages of turbo equalization as well as the importance of a recursive modulator motivated our research on turbo equalization of coded partial response GMSK systems [389], since GMSK is also recursive in its nature. In our investigations, we have employed convolutional coding for the proposed turbo-equalized GSM-like video system as it has been shown in reference [404] that convolutional-coded GMSK systems are capable of providing large iteration gains — that is, gains in SNR performance with respect to the first iteration — with successive turbo-equalization iterations. We also observed that the convolutional-coded GMSK system employing turbo equalization outperformed the convolutional-coding based turbo-coded GMSK scheme, as demonstrated by Figure 12.4. Specifically, over a nondispersive Gaussian channel the convolutional-coded GMSK system had an approximately 0.8 dB better E_b/N_o performance than the corresponding convolutional-coding based turbo-coded GMSK scheme at $\mathrm{BER} = 10^{-4}$. Although not explicitly shown here, similar findings were valid for dispersive Rayleigh-fading channels, where the advantage of the convolutional-coded system over the convolutional-coding-based turbo-coded scheme was approximately 1.0 dB.

These results were surprising since the more complex turbo-coded system was expected to form a more powerful encoded system compared to the convolutional-coded scheme. Be-

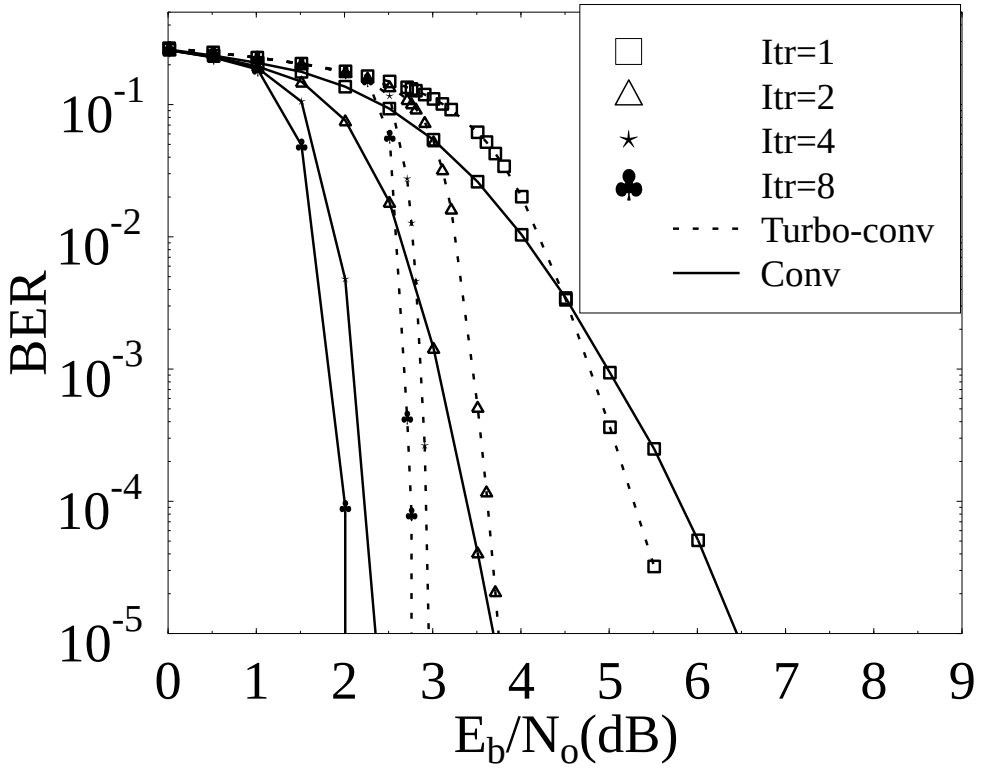

Figure 12.4: Comparison of the $R = 0.5$ convolutional-coded GMSK system with $R = 0.5$ convolutional-coding-based turbo-coded GMSK scheme, transmitting over the nondispersive Gaussian channel employing convolutional and turbo-coding-based turbo equalization, which performs eight turbo equalization iterations at the receiver.

low, we offer an interpretation of this phenomenon by considering the performance of both codes after the first turbo-equalization iteration. Specifically, over the nondispersive Gaussian channel in Figure 12.4, the convolutional-coded scheme yielded a lower BER than that of the turbo-coded system at E_b/N_o values below 4.5 dB, indicating that the *a posteriori* LLRs of the bits produced by the convolutional decoder had a higher reliability than that of the corresponding turbo-coded scheme. Consequently, upon receiving the higher-confidence LLR values from the decoder, the equalizer in the convolutional-coded scheme was capable of producing significantly more reliable LLR values in the subsequent turbo-equalization iteration, when compared to the turbo-coded system. After receiving these more reliable LLR values, the decoder of the convolutional-coded system will generate even more reliable LLR values. Hence, the convolutional-coded system outperformed the turbo-coded scheme after performing eight turbo-equalization iterations. Motivated by these trends — which were also confirmed in the context of dispersive Rayleigh-fading channels [404] — we opted for a convolutional-coded rather than turbo-coded GSM-like videophone system, which employs turbo equalization in order to enhance the video performance of the system.

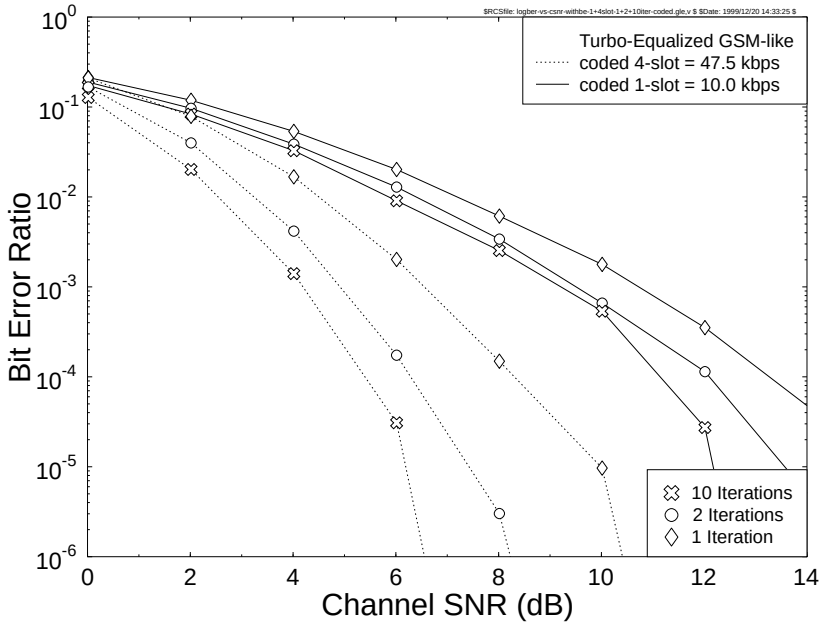

Figure 12.5: BER versus channel SNR for one and four slots per TDMA frame, and for 1, 2, and 10 turbo-equalizer iterations, over the channel of Figure 12.2.

12.1.4 Turbo-equalization Performance

Let us now characterize the performance of our video system. Figure 12.5 shows the bit error ratio (BER) versus channel SNR for the one- and four-slot scenarios, after one, two and ten iterations of the turbo equalizer. The figure shows the BER performance improvement upon each iteration of the turbo equalizer, although there is only a limited extra performance improvement after five iterations. The figure also shows that the four-slot scenario has a lower bit error ratio than the one-slot scenario. This is because the four-slot scenario has a longer interleaver, which renders the turbo-equalization process more effective due to its increased time diversity.

Let us now consider the associated packet-loss ratio (PLR) versus channel SNR performance in Figure 12.6. The PLR is a more pertinent measure of the expected video performance, since — based on the philosophy of [392] and on the previous two chapters — our video scheme discards all video packets, which are not error-free. Hence, our goal is to maintain as low a PLR as possible. Observe in Figure 12.6 that the associated iteration gains are more pronounced in terms of the packet-loss ratio than in bit error ratio.

It should also be noted that for low SNRs the packet-loss performance of the four-slot system is inferior to that of the one-slot system, while the bit error ratio is similar or better at the same SNRs. This is because the probability of having a single-bit error in the four-slot video packet is higher due to its quadruple length. This phenomenon is further detailed in Section 12.1.4.2.

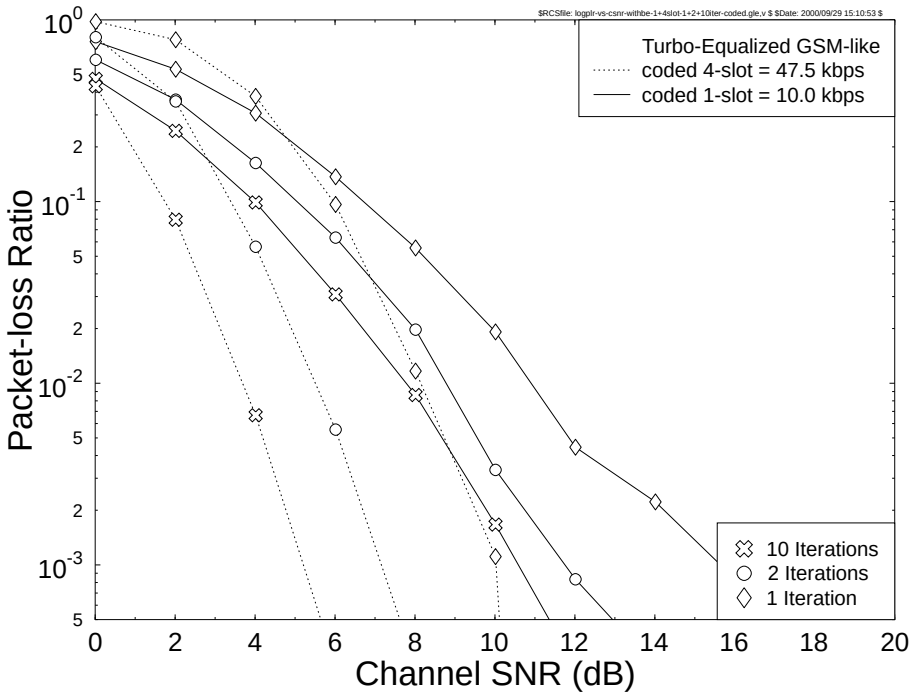

Figure 12.6: Video packet-loss ratio versus channel SNR for one and four slots per TDMA frame, and for 1, 2, and 10 turbo-equalizer iterations, over the channel of Figure 12.2 using convolutional coding.

12.1.4.1 Video Performance

The PLR performance is directly related to the video quality of our video system. Figure 12.7 shows the associated average PSNR versus channel SNR performance, demonstrating that an improved video quality can be maintained at lower SNRs as the number of iterations increases. In addition, the higher bit rate of the four-slot system corresponds to a higher overall video quality. Up to 6 dB SNR-gain can be achieved after 10 turbo-equalization iterations, as seen in Figure 12.7.

Figure 12.7 characterizes the performance of the highly motion-active "Carphone" sequence. However, the performance improvements are similar for the low-activity "Miss America" video sequence, as seen in Figure 12.8. Observe that the lower-activity "Miss America" video sequence is represented at a higher video quality at the same video bit rate. A deeper insight into the achievable video-quality improvement in conjunction with turbo equalization can be provided by plotting the video quality measured in PSNR (dB) versus time, as seen in Figure 12.9 for the "Miss America" video sequence using the four-slot system at a channel SNR of 6 dB for one, two, and ten iterations of the turbo equalizer.

Specifically, the bottom-trace of the figure shows how the video quality varies in the one-iteration scenario, which is equivalent to conventional equalization. The sudden reductions

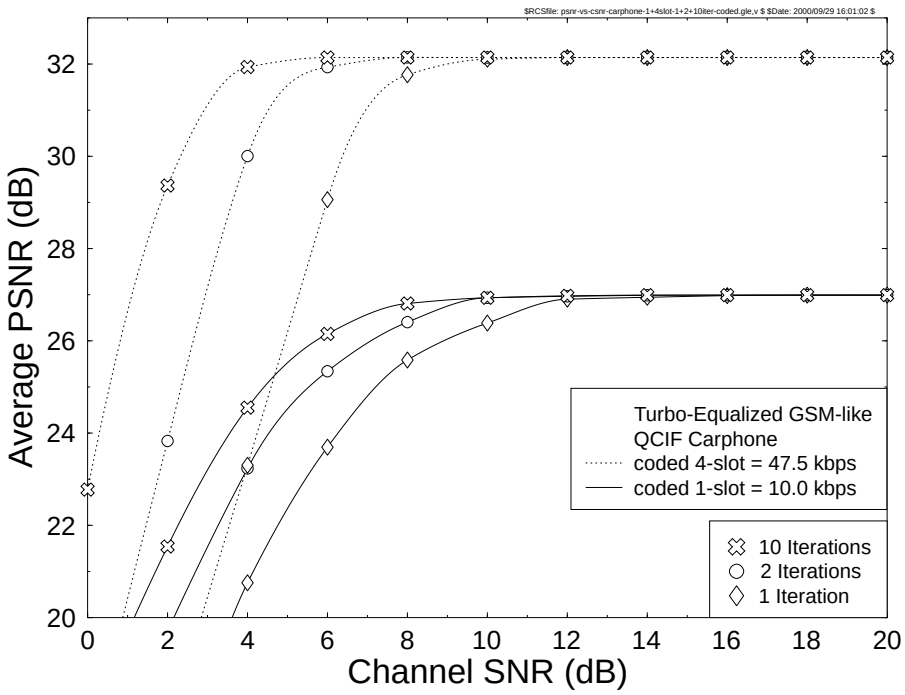

Figure 12.7: Video quality in PSNR (dB) versus channel SNR for one and four slots per TDMA frame, and for 1, 2, and 10 iterations of the turbo-equalizer upon using the highly motion active "Carphone" video sequence over the channel of Figure 12.2 using convolutional coding.

in video quality are caused by packet-loss events, which result in parts of the picture being "frozen" for one or possibly several consecutive video frames. The sudden increases in video quality are achieved when the system updates the "frozen" part of the video picture in subsequent video frames. The packet-loss ratio for this scenario was 10% at the stipulated SNR of 6dB.

The video quality improved significantly with the aid of two turbo-equalizer iterations, while the packet-loss ratio was reduced from 10% to 0.7%. In the time interval shown in Figure 12.9, there are eight lost video packets, six of which can be seen as sudden reductions in video quality. However, in each case the video quality recovered with the update of the "frozen" picture areas in the next video frame.

We have found that the maximum acceptable PSNR video-quality degradation with respect to the perfect-channel scenario was about 1 dB, which was associated with nearly unimpaired video quality. In Table 12.3 we tabulated the corresponding minimum required channel SNRs that the system can operate at for a variety of scenarios, extracted from Figure 12.7. As the table shows, the minimum operating channel SNR for the one- and four-slot system using one iteration is 9 dB and 7.5 dB, respectively. This corresponds to a system using conventional equalization. A system using two turbo-equalization iterations can reduce these operating SNRs to 7.2 dB and 5.2 dB, respectively. The minimum operating SNRs can be

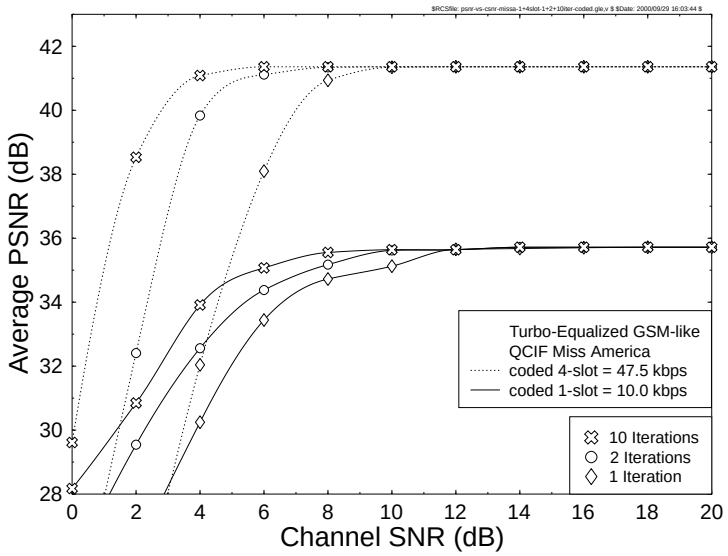

Figure 12.8: Video quality in PSNR (dB) versus channel SNR for one and four slots per TDMA frame, and for 1, 2, and 10 turbo-equalizer iterations, using the low-activity "Miss America" video sequence over the channel of Figure 12.2 using convolutional coding.

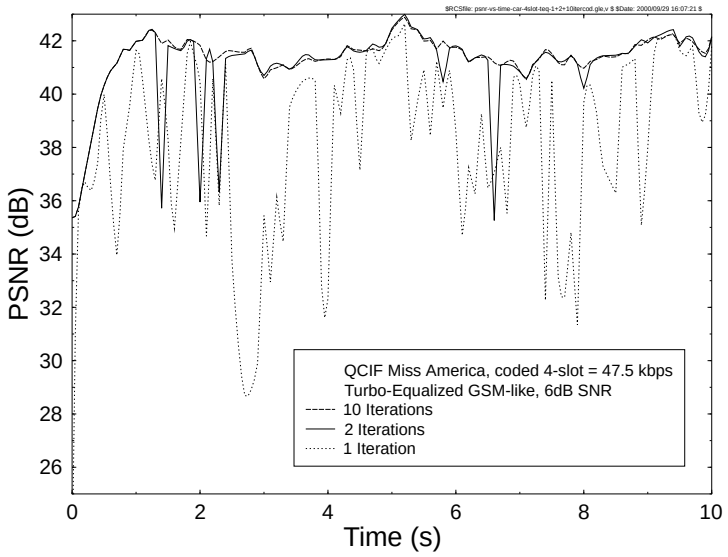

Figure 12.9: Video quality in PSNR (dB) versus time using four slots per TDMA frame, and for 1, 2, and 10 iterations of the turbo-equalizer for the low-activity "Miss America" video sequence using convolutional coding.

Channel SNR for 1 dB Loss of PSNR		
Slots/TDMA Frame	1	4
1 Iteration	9.0 dB	7.5 dB
2 Iterations	7.2 dB	5.2 dB
3 Iterations	6.44 dB	3.9 dB
4 Iterations	6.37 dB	3.7 dB
10 Iterations	5.8 dB	3.4 dB

Table 12.3: Minimum Required Operating Channel SNR for the QCIF "Carphone" Sequence over the Channel of Figure 12.2

reduced to as low as 5.8 dB and 3.4 dB for the one- and four-slot systems, respectively, when invoking ten iterations.

12.1.4.2 Bit Error Statistics

In order to demonstrate the benefits of turbo equalization more explicitly, we investigated the mechanism of how turbo equalization reduces the bit error and packet-loss ratios. We found that the distribution of the bit errors in video packets after each iteration provided interesting insights. Hence, the CDF of the number of bit errors per video packet was evaluated. In order to allow a fair comparison between the one- and four-slot system, we normalized the number of bit errors per packet to the video packet size, thereby producing the CDF of "in-packet" BER.

Figure 12.10 shows the CDF of the "in-packet" BER for a channel SNR of 2 dB and for one, two, five, and ten iterations for both the one- and four-slot systems. The value of the CDF for an "in-packet" BER of zero is the probability that a packet is error-free and so can be interpreted as the packet success ratio (PSR). The packet-loss ratio is equal to 1 minus the PSR. For example, the four-slot system in Figure 12.10 at one iteration has a packet success ratio of 0.22, which corresponds to a packet-loss ratio of 78%.

Both the one- and four-slot systems increase the PSR as the number of iterations increases. For example, the four-slot system increases the PSR from 22% to 92% as the number of iterations is increased from one to ten. This corresponds to a reduction in the packet-loss ratio from 78% to 8%. However, the CDF of "in-packet" BER can provide further insight into the system's operation. It can be seen in Figure 12.10 that the turbo-equalizer iterations reduce the number of packets having "in-packet" BERs of less than 30%. However, the probability of a packet having an "in-packet" BER higher than 35% is hardly affected by the number of iterations, since the number of bit errors is excessive, hence overwhelming even the powerful turbo equalization.

Figures 12.5 and 12.6, show that the four-slot system always has a lower BER than the one-slot system, although at low SNRs the PLR is higher for the four-slot system. The CDF in Figure 12.10 can assist in interpreting this further. The CDF shows that the PSR improves more significantly for the four-slot system than for the one-slot system as the number of iterations increases. This is because the four-slot system allows the employment of a longer interleaver, thereby improving the efficiency of the turbo equalizer. However, the CDF also underlines a reason for the lower BER of the four-slot system across the whole range of SNRs, demonstrating that the probability of packets having a high "in-packet" bit error rate is lower

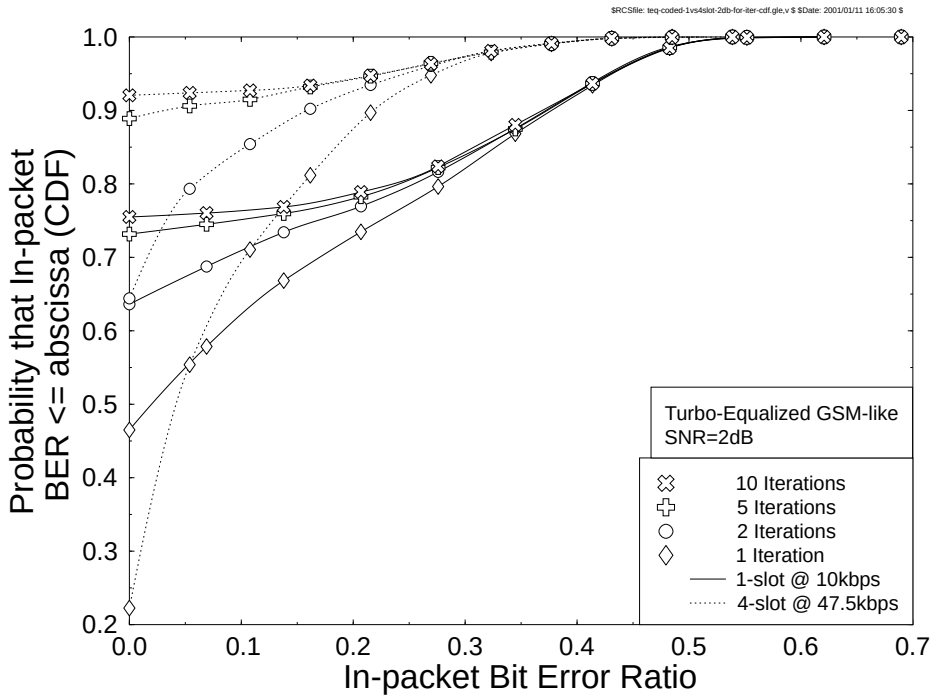

Figure 12.10: CDF of the "in-packet" BER at a channel SNR of 2 dB over the channel of Figure 12.2, and for various numbers of iterations for the turbo-equalized one- and four-slot systems using convolutional coding.

for the four-slot system. Since packets having a high "in-packet" BER have a more grave effect on the overall BER than those packets having a low "in-packet" BER, this explains the inferior overall BER performance of the one-slot system.

Figure 12.11 shows the CDF of "in-packet" BER for conventional equalization and with the aid of ten turbo-equalizer iterations for 0 dB, 2 dB, and 4 dB channel SNRs. Figure 12.11(a) represents a one-slot system, and Figure 12.11(b) a four-slot system. The figures also show the packet-loss ratio performance improvement with the aid of turbo equalization.

12.1.5 Summary and Conclusions

In this section the performance of turbo-equalized GSM/GPRS-like videophone transceivers was studied over dispersive fading channels as a function of the number of turbo-equalization iterations. Iteration gains in excess of 4 dB were attained, although the highest per iteration gain was achieved for iteration indices below 5. As expected, the longer the associated interleaver, the better the BER and PLR performance. In contrast to our expectations, the turbo-coded, turbo-equalized system was outperformed by the less complex convolutional coded turbo-equalized system. In conclusion, GPRS/GSM are amenable to videotelephony, and turbo equalization is a powerful means of improving the system's performance. Our fu-

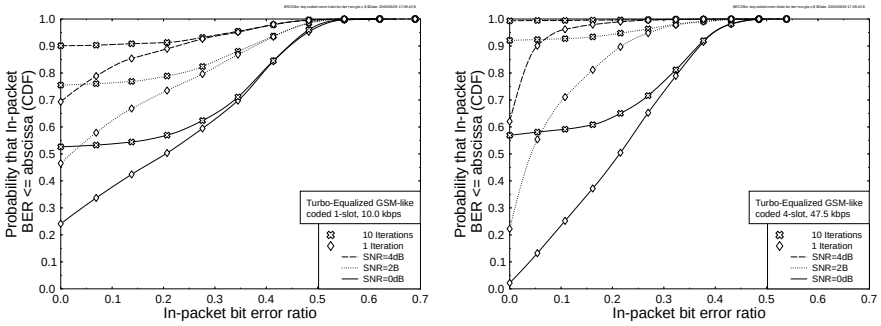

(a) 1-slot (b) 4-slot

Figure 12.11: CDF of "in-packet" BER performance over the channel of Figure 12.2 for the turbo-equalized one- and four-slot system for channel SNRs of 0 dB, 2 dB, and 4 dB and 1 and 10 iterations using convolutional coding.

ture work will improve the system's performance invoking the forthcoming MPEG4 video codec, using space-time coding and burst-by-burst adaptive turbo equalization.

12.2 HSDPA-Style Burst-by-burst Adaptive CDMA Videophony: Turbo-Coded Burst-by-Burst Adaptive Joint Detection CDMA and H.263-Based Videophony[3] [4]

12.2.1 Motivation and Video Transceiver Overview

While the third-generation wireless communications standards are still evolving, they have become sufficiently mature for the equipment designers and manufacturers to complete the design of prototype equipment. One of the most important services tested in the field trials of virtually all dominant players in the field is interactive videotelephony at various bit rates and video qualities. Motivated by these events, the goal of this section is to quantify the expected video performance of a UMTS-like videophone scheme, while also providing an outlook on the more powerful burst-by-burst adaptive transceivers of the near future.

In this study, we transmitted 176 $\times$ 144 pixel Quarter Common Intermediate Format (QCIF) and 128 $\times$ 96 pixel Sub-QCIF (SQCIF) video sequences at 10 frames/s using a reconfigurable Time Division Multiple Access/Code Division Multiple Access (TDMA/CDMA) transceiver, which can be configured as a 1-, 2-, or 4-bit/symbol scheme. The H.263 video

[3]This section is based on P. Cherriman, E.L. Kuan, and L. Hanzo: Burst-by-burst Adaptive Joint-detection CDMA/H.263 Based Video Telephony, submitted to IEEE Transactions on Cicuits and Systems for Video Technology, 1999.

[4]

Parameter	
Multiple access	TDMA/CDMA
Channel type	C0ST 207 Bad Urban
Number of paths in channel	7
Normalized Doppler frequency	3.7×10^{-5}
CDMA spreading factor	16
Spreading sequence	Random
Frame duration	4.615 ms
Burst duration	577 μs
Joint-detection CDMA receiver	Whitening matched filter (WMF) or minimum mean square error block decision feedback equalizer (MMSE-BDFE)
No. of slots/frame	8
TDMA frame length	4.615ms
TDMA slot length	577μs
TDMA slots/video packet	3
Chip periods/TDMA slot	1250
Data symbols/TDMA slot	68
User data symbol rate (kBd)	14.7
System data symbol rate (kBd)	117.9

Table 12.4: Generic System Parameters Using the Frames Spread Speech/Data Mode 2 Proposal [405]

codec [258] exhibits an impressive compression ratio, although this is achieved at the cost of a high vulnerability to transmission errors, since a run-length coded stream is rendered undecodable by a single-bit error. In order to mitigate this problem, when the channel codec protecting the video stream is overwhelmed by the transmission errors, we refrain from decoding the corrupted video packet in order to prevent error propagation through the reconstructed video frame buffer [392]. We found that it was more beneficial in video-quality terms, if these corrupted video packets were dropped and the reconstructed frame buffer was not updated, until the next video packet replenishing the specific video frame area was received. The associated video performance degradation was found to be perceptually unobjectionable for packet-dropping or transmission frame error rates (FER) below about 5%. These packet dropping events were signaled to the remote decoder by superimposing a strongly protected 1-bit packet acknowledgment flag on the reverse-direction packet, as outlined in [392]. Bose-Chaudhuri-Hocquenghem (BCH) [321] and turbo error correction codes [401] were used, and again, the CDMA transceiver was capable of transmitting 1, 2, and 4 bits per symbol, where each symbol was spread using a low spreading factor (SF) of 16, as seen in Table 12.4. The associated parameters will be addressed in more depth during our later discourse. Employing a low spreading factor of 16 allowed us to improve the system's multi-user performance with the aid of joint-detection techniques [406]. We also note that the implementation of the joint-detection receivers is independent of the number of bits per symbol associated with the modulation mode used, since the receiver simply inverts the associated system matrix and invokes a decision concerning the received symbol, regardless of how many bits per symbol were used. **Therefore, joint-detection receivers are amenable to amalgamation with the**

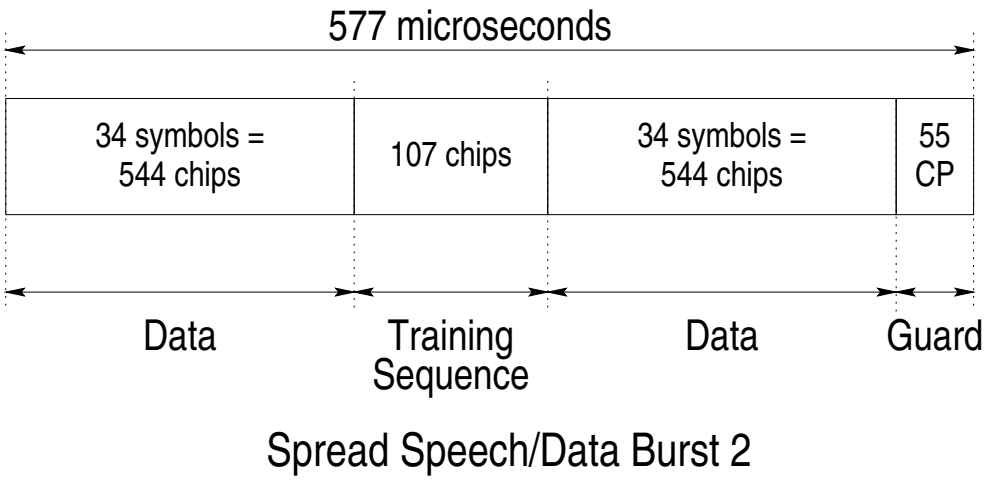

Figure 12.12: Transmission burst structure of the FMA1 spread speech/data mode 2 of the FRAMES proposal [405].

Features	BCH coding	Turbo Coding
Modulation	4QAM	
Transmission bit rate (kbit/s)	29.5	
Video rate (kbit/s)	13.7	11.1
Video frame rate (Hz)	10	

Table 12.5: FEC-protected and Unprotected BCH and Turbo-Coded Bit Rates for the 4QAM Transceiver Mode

above 1-, 2-, and 4-bit/symbol modem, since they do not have to be reconfigured each time the modulation mode is switched.

In this performance study, we used the Pan-European FRAMES proposal [405] as the basis for our CDMA system. The associated transmission frame structure is shown in Figure 12.12, while a range of generic system parameters is summarized in Table 12.4. In our performance studies, we used the COST207 [407] seven-path bad urban (BU) channel model, whose impulse response is portrayed in Figure 12.13.

Our initial experiments compared the performance of a whitening matched filter (WMF) for single-user detection and the minimum mean square error block decision feedback equalizer (MMSE-BDFE) for joint multi-user detection. These simulations were performed using four-level Quadrature Amplitude Modulation (4QAM), invoking both binary BCH [321] and turbo-coded [401] video packets. The associated bit rates are summarized in Table 12.5. The transmission bit rate of the 4QAM modem mode was 29.5 Kbps, which was reduced due to the approximately half-rate BCH or turbo coding, plus the associated video packet acknowledgment feedback flag error control [160] and video packetization overhead to produce effective video bit rates of 13.7 Kbps and 11.1 Kbps, respectively. A more detailed discussion on the video packet acknowledgment feedback error control and video packetization overhead will be provided in Section 12.2.2 with reference to the convolutionally coded

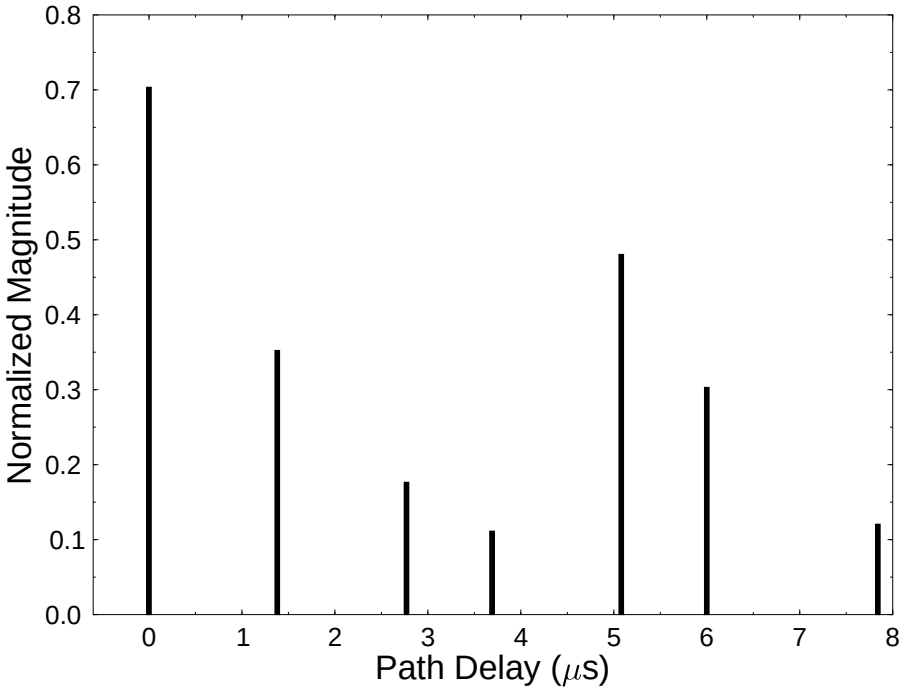

Figure 12.13: Normalized channel impulse response for the COST 207 [407] seven-path Bad Urban channel.

multimode investigations.

Figure 12.14 portrays the bit error ratio (BER) performance of the BCH coded video transceiver using both matched filtering and joint detection for two to eight users. The bit error ratio is shown to increase as the number of users increases, even upon employing the MMSE-BDFE multi-user detector (MUD). However, while the matched filtering receiver exhibits an unacceptably high BER for supporting perceptually unimpaired video communications, the MUD exhibits a far superior BER performance.

When the BCH codec was replaced by the turbo-codec, the bit error ratio performance of both matched filtering and the MUD receiver improved, as shown in Figure 12.15. However, as expected, matched filtering was still outperformed by the joint-detection scheme for the same number of users. Furthermore, the matched filtering performance degraded rapidly for more than two users.

Figure 12.16 shows the video packet-loss ratio (PLR) for the turbo-coded video stream using matched filtering and joint detection for two to eight users. The figure clearly shows that the matched filter was only capable of meeting the target packet-loss ratio of 5% for up to four users, when the channel SNR was in excess of 11 dB. However, the joint detection algorithm guaranteed the required video packet loss ratio performance for two to eight users in the entire range of channel SNRs shown. Furthermore, the two-user matched-filtered PLR performance was close to the eight-user MUD PLR.

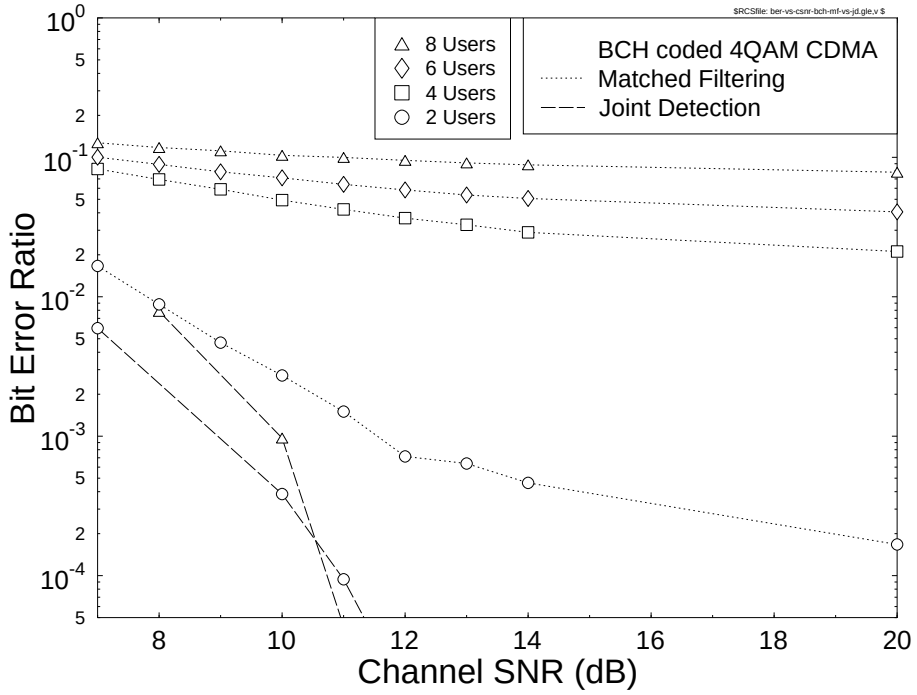

Figure 12.14: BER versus channel SNR 4QAM performance using BCH-coded, 13.7 Kbps video, comparing the performance of matched filtering and joint detection for two to eight users.

12.2.2 Multimode Video System Performance

Having shown that joint detection can substantially improve our system's performance, we investigated the performance of a multimode convolutionally coded video system employing joint detection, while supporting two users. The associated convolutional codec parameters are summarized in Table 12.6.

We now detail the video packetization method employed. The reader is reminded that the number of symbols per TDMA frame was 68 according to Table 12.4. In the 4QAM mode this would give 136 bits per TDMA frame. However, if we transmitted one video packet per TDMA frame, then the packetization overhead would absorb a large percentage of the available bit rate. Hence we assembled larger video packets, thereby reducing the packetization overhead and arranged for transmitting the contents of a video packet over three consecutive TDMA frames, as indicated in Table 12.4. Therefore, each protected video packet consists of $68 \times 3 = 204$ modulation symbols, yielding a transmission bit rate of between 14.7 and 38.9 Kbps for BPSK and 16QAM, respectively. However, in order to protect the video data, we employed half-rate, constraint-length nine convolutional coding, using octal generator polynomials of 561 and 753. The useful video bit rate was further reduced due to the 16-bit Cyclic Redundancy Checking (CRC) used for error detection and the 9-bit repetition-coded feedback error flag for the reverse link. This results in video packet

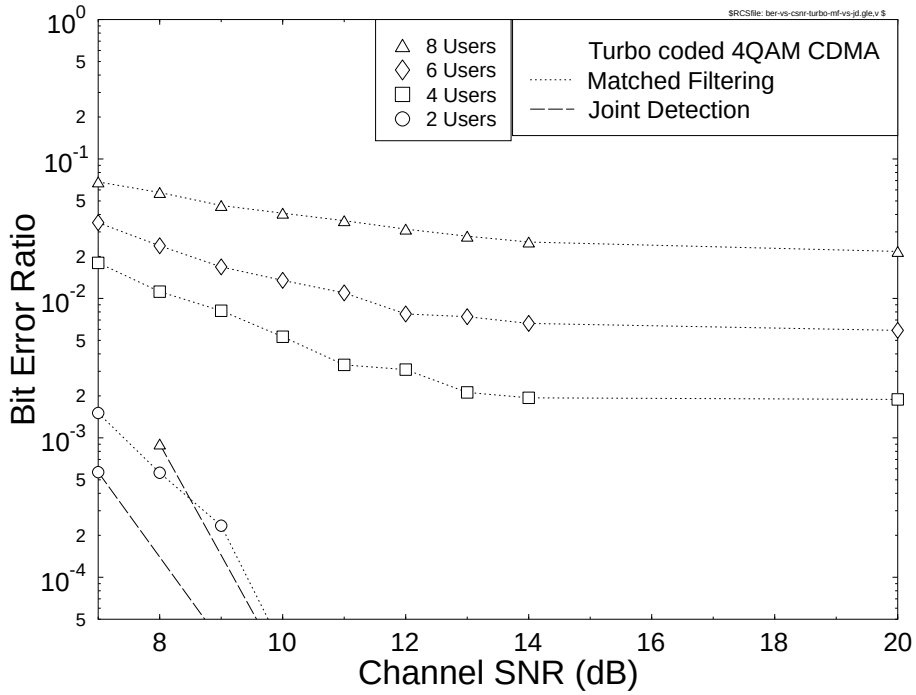

Figure 12.15: BER versus channel SNR 4QAM performance using turbo-coded 11.1 Kbps video, comparing the performance of matched filtering and joint detection for two to eight users.

Features	Multirate System		
Mode	BPSK	4QAM	16QAM
Bits/symbol	1	2	4
FEC	Convolutional Coding		
Transmitted bits/packet	204	408	816
Total bit rate (kbit/s)	14.7	29.5	58.9
FEC-coded bits/packet	102	204	408
Assigned to FEC-coding (kbit/s)	7.4	14.7	29.5
Error detection per packet	16 bit CRC		
Feedback bits/packet	9		
Video packet size	77	179	383
Packet header bits	8	9	10
Video bits/packet	69	170	373
Unprotected video rate (kbit/s)	5.0	12.3	26.9
Video frame rate (Hz)	10		

Table 12.6: Operational-Mode Specific Transceiver Parameters for the Proposed Multimode System

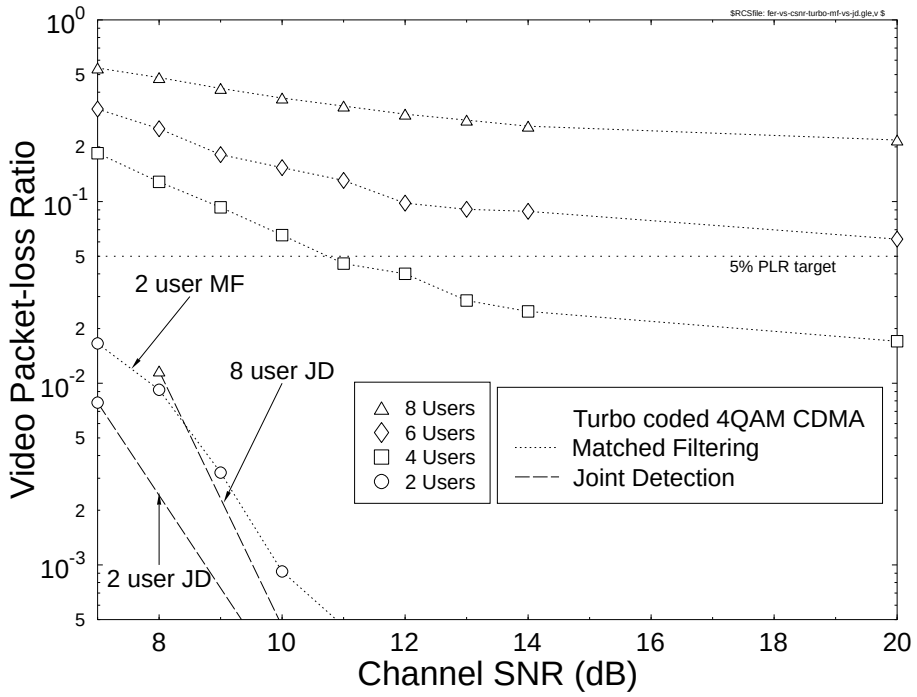

Figure 12.16: Video packet-loss ratio versus channel SNR for the turbo-coded 11.1 Kbps video stream, comparing the performance of matched filtering and joint detection for two to eight users.

sizes of 77, 179, and 383 bits for each of the three modulation modes. The useful video capacity was reduced further by the video packet header of between 8 and 10 bits, resulting in useful or effective video bit rates ranging from 5 to 26.9 Kbps in the BPSK and 16QAM modes, respectively.

The proposed multimode system can switch among the 1-, 2-, and 4-bit/symbol modulation schemes under network control, based on the prevailing channel conditions. As seen in Table 12.6, when the channel is benign, the unprotected video bit rate will be approximately 26.9 Kbps in the 16QAM mode. However, as the channel quality degrades, the modem will switch to the BPSK mode of operation, where the video bit rate drops to 5 Kbps, and for maintaining a reasonable video quality, the video resolution has to be reduced to SQCIF (128 x 96 pels).

Figure 12.17 portrays the packet loss ratio for the multimode system in each of its modulation modes for a range of channel SNRs. The figure shows that above a channel SNR of 14 dB the 16QAM mode offers an acceptable packet-loss ratio of less than 5%, while providing an unprotected video rate of about 26.9 Kbps. If the channel SNR drops below 14 dB, the multimode system is switched to 4QAM and eventually to BPSK, when the channel SNR is below 9 dB, in order to maintain the required quality of service, which is dictated by the packet-loss ratio. The figure also shows the acknowledgment feedback error ratio (FBER)

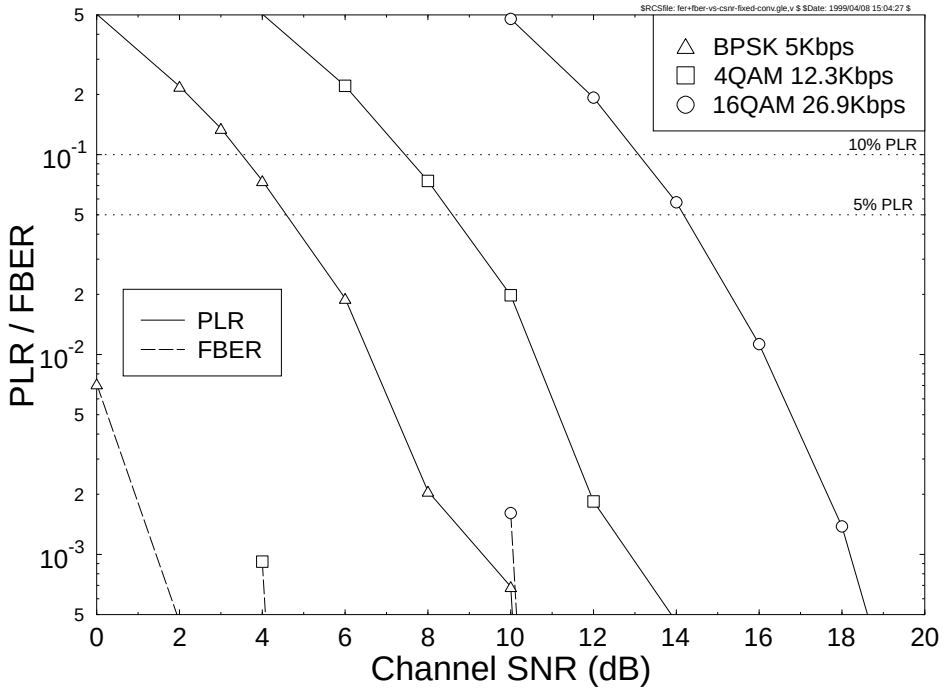

Figure 12.17: Video packet-loss ratio (PLR) and feedback error ratio (FBER) versus channel SNR for the three modulation schemes of the two-user multimode system using joint detection.

for a range of channel SNRs, which has to be substantially lower than the video PLR itself. This requirement is satisfied in the figure, since the feedback errors only occur at extremely low-channel SNRs, where the packet-loss ratio is approximately 50%. It is therefore assumed that the multimode system would have switched to a more robust modulation mode, before the feedback acknowledgment flag can become corrupted.

The video quality is commonly measured in terms of the peak signal-to-noise-ratio (PSNR). Figure 12.18 shows the video quality in terms of the PSNR versus the channel SNRs for each of the modulation modes. As expected, the higher throughput bit rate of the 16QAM mode provides a better video quality. However, as the channel quality degrades, the video quality of the 16QAM mode is reduced. Hence, it becomes beneficial to switch from the 16QAM mode to 4QAM at an SNR of about 14 dB, as suggested by the packet-loss ratio performance of Figure 12.17. Although the video quality expressed in terms of PSNR is superior for the 16QAM mode in comparison to the 4QAM mode at channel SNRs in excess of 12 dB, because of the excessive PLR the perceived video quality appears inferior to that of the 4QAM mode, even though the 16QAM PSNR is higher for channel SNRs in the range of 12–14 dB. More specifically, we found that it was beneficial to switch to a more robust modulation scheme when the PSNR was reduced by about 1 dB with respect to its unimpaired PSNR value. This ensured that the packet losses did not become subjectively obvious, resulting in a

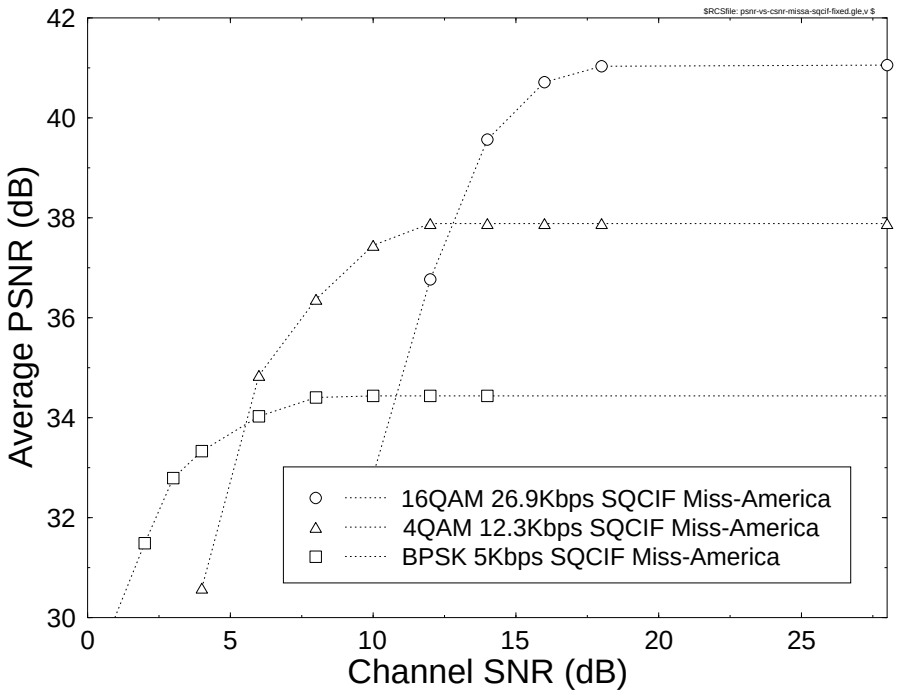

Figure 12.18: Decoded video quality (PSNR) versus channel SNR for the modulation modes of BPSK, 4QAM, and 16QAM supporting two users with the aid of joint detection. These results were recorded for the "Miss America" video sequence at SQCIF resolution (128 $\times$ 96 pels).

higher perceived video quality and smoother degradation, as the channel quality deteriorated.

The effect of packet losses on the video quality quantified in terms of PSNR is portrayed in Figure 12.19. The figure shows that the video quality degrades as the PLR increases. In order to ensure a seamless degradation of video quality as the channel SNR is reduced, it is best to switch to a more robust modulation scheme when the PLR exceeded 5%. The figure shows that a 5% packet-loss ratio results in a loss of PSNR when switching to a more robust modulation scheme. However, if the system did not switch until the PSNR of the more robust modulation mode was similar, the perceived video quality associated with the originally higher rate, but channel-impaired, stream became inferior.

12.2.3 Burst-by-Burst Adaptive Videophone System

A burst-by-burst adaptive modem maximizes the system's throughput by using the most appropriate modulation mode for the current instantaneous channel conditions. Figure 12.20 exemplifies how a burst-by-burst adaptive modem changes its modulation modes based on the fluctuating channel conditions. The adaptive modem uses the SINR estimate at the output of the joint detector to estimate the instantaneous channel quality and therefore to set the

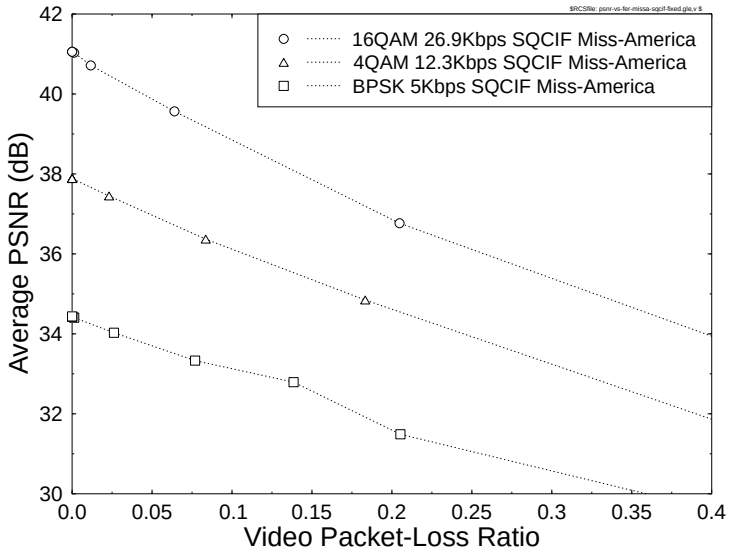

Figure 12.19: Decoded video quality (PSNR) versus video packet-loss ratio for the modulation modes of BPSK, 4QAM, and 16QAM, supporting two users with the aid of joint detection. The results were recorded for the "Miss America" video sequence at SQCIF resolution (128 $\times$ 96 pels).

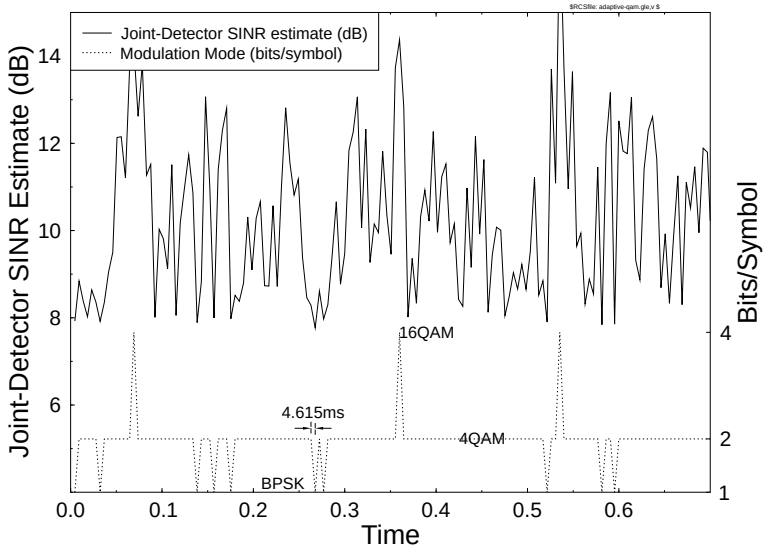

Figure 12.20: Example of modem mode switching in a dynamically reconfigured burst-by-burst modem in operation, where the modulation mode switching is based on the SINR estimate at the output of the joint detector.

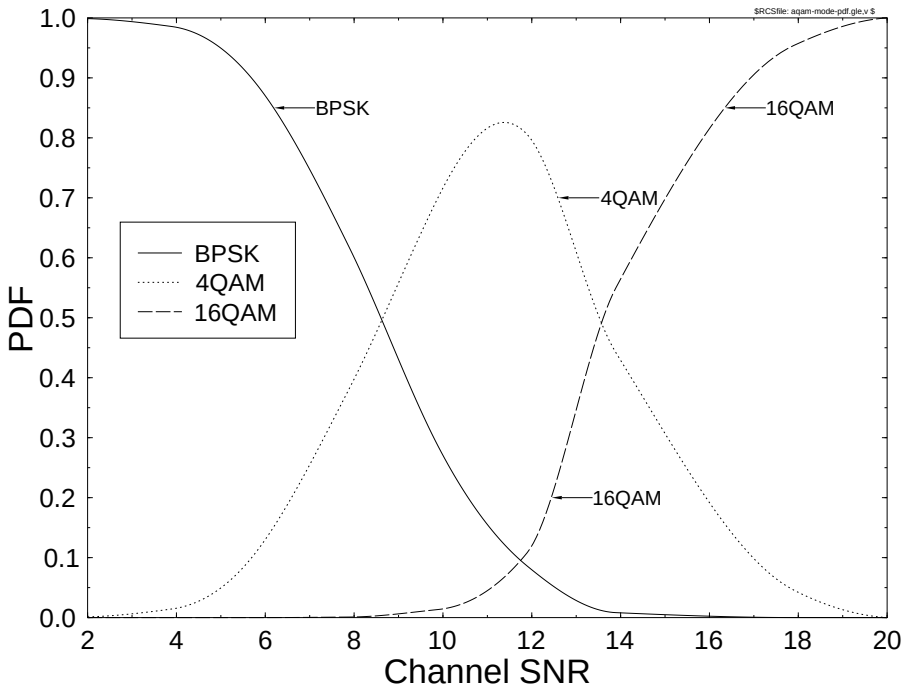

Figure 12.21: PDF of the various adaptive modem modes versus channel SNR.

modulation mode.

The probability of the adaptive modem using each modulation mode for a particular channel SNRs is portrayed in Figure 12.21. At high-channel SNRs, the modem mainly uses the 16QAM modulation mode, while at low-channel SNRs the BPSK mode is most prevalent.

The advantage of dynamically reconfigured burst-by-burst adaptive modem over the statically switched multimode system previously described is that the video quality is smoothly degraded as the channel conditions deteriorate. The switched multimode system results in more sudden reductions in video quality, when the modem switches to a more robust modulation mode. Figure 12.22 shows the throughput bit rate of the dynamically reconfigured burst-by-burst adaptive modem, compared to the three modes of the statically switched multimode system. The reduction of the fixed modem modes' effective throughput at low SNRs is due to the fact that under such channel conditions an increased fraction of the transmitted packets have to be dropped, reducing the effective throughput. The figure shows the smooth reduction of the throughput bit rate, as the channel quality deteriorates. The burst-by-burst modem matches the BPSK mode's bit rate at low-channel SNRs and the 16QAM mode's bit rate at high SNRs. The dynamically reconfigured HSDPA-style burst-by-burst adaptive modem characterized in the figure perfectly estimates the prevalent channel conditions, although in practice the estimate of channel quality is imperfect and it is inherently delayed, which results in a slightly reduced performance when compared to perfect channel estimation [82, 84].

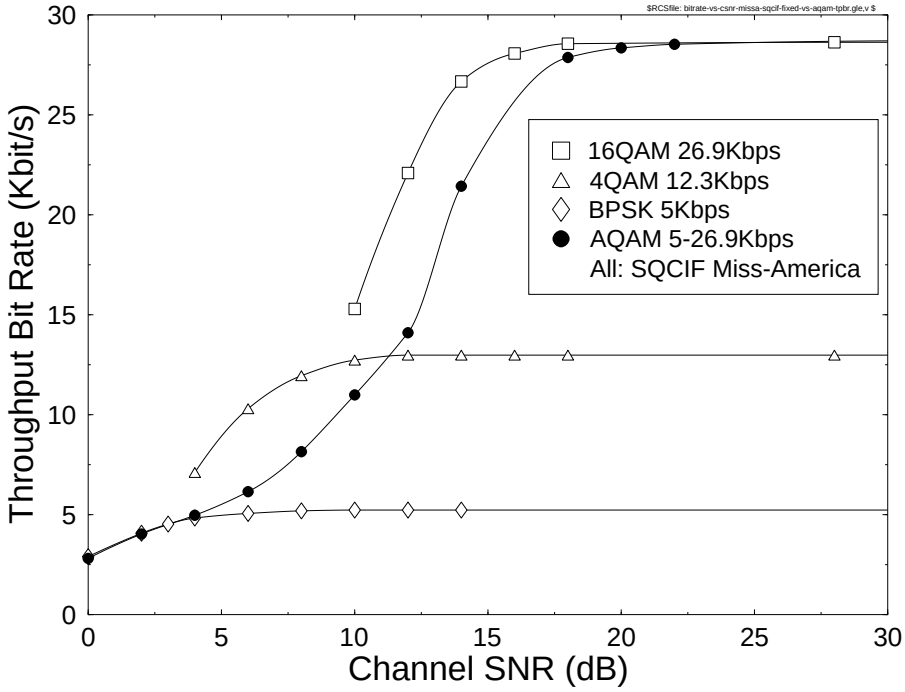

Figure 12.22: Throughput bit rate versus channel SNR comparison of the three fixed modulation modes (BPSK, 4QAM, 16QAM) and the adaptive burst-by-burst modem (AQAM), both supporting two users with the aid of joint detection.

The smoothly varying throughput bit rate of the burst-by-burst adaptive modem translates into a smoothly varying video quality as the channel conditions change. The video quality measured in terms of the average peak signal-to-noise ratio (PSNR) is shown versus the channel SNR in Figure 12.23 in contrast to that of the individual modem modes. The figure demonstrates that the burst-by-burst adaptive modem provides equal or better video quality over a large proportion of the SNR range shown than the individual modes. However, even at channel SNRs, where the adaptive modem has a slightly reduced PSNR, the perceived video quality of the adaptive modem is better since the video packet-loss rate is far lower than that of the fixed modem modes.

Figure 12.24 shows the video packet-loss ratio versus channel SNR for the three fixed modulation modes and the burst-by-burst adaptive modem with perfect channel estimation. Again, the figure demonstrates that the video packet-loss ratio of the adaptive modem is similar to that of the fixed BPSK modem mode. However, the adaptive modem has a far higher bit-rate throughput, as the channel SNR increases. The burst-by-burst adaptive modem gives an error performance similar to that of the BPSK mode, but with the flexibity to increase the bit-rate throughput of the modem, when the channel conditions improve. If imperfect channel estimation is used, the bit rate throughput of the adaptive modem is reduced slightly. Furthermore, the video packet-loss ratio seen in Figure 12.24 is slightly higher for the AQAM

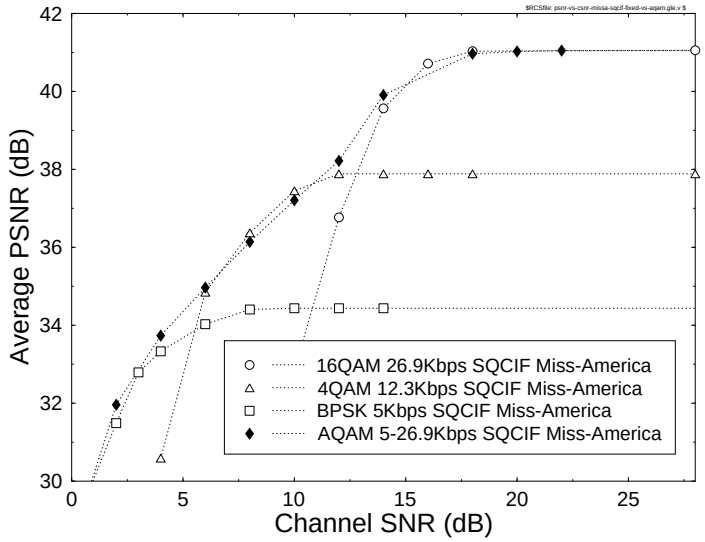

Figure 12.23: Average decoded video quality (PSNR) versus channel SNR comparision of the fixed modulation modes of BPSK, 4QAM and 16QAM, and the burst-by-burst adaptive modem — both supporting two users with the aid of joint detection. These results were recorded for the "Miss America" video sequence at SQCIF resolution (128×96 pels).

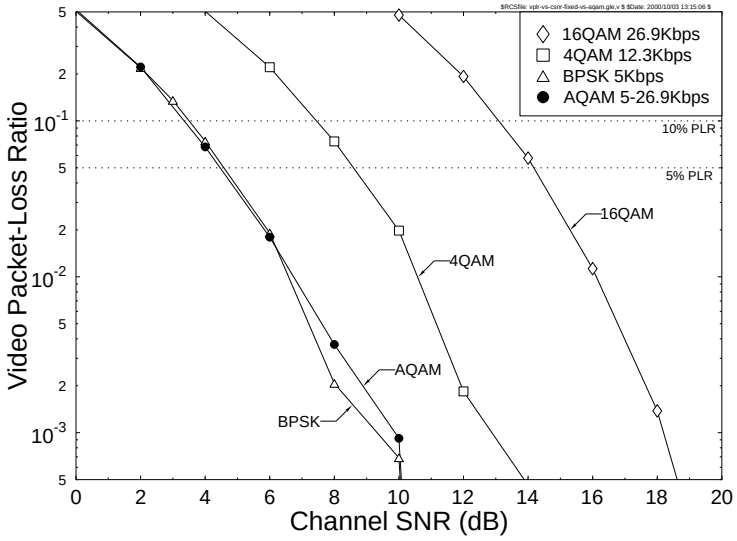

Figure 12.24: Video packet-loss ratio (PLR) versus channel SNR for the three modulation schemes of the multimode system, compared to the burst-by-burst adaptive modem. Both systems substain two users using joint detection.

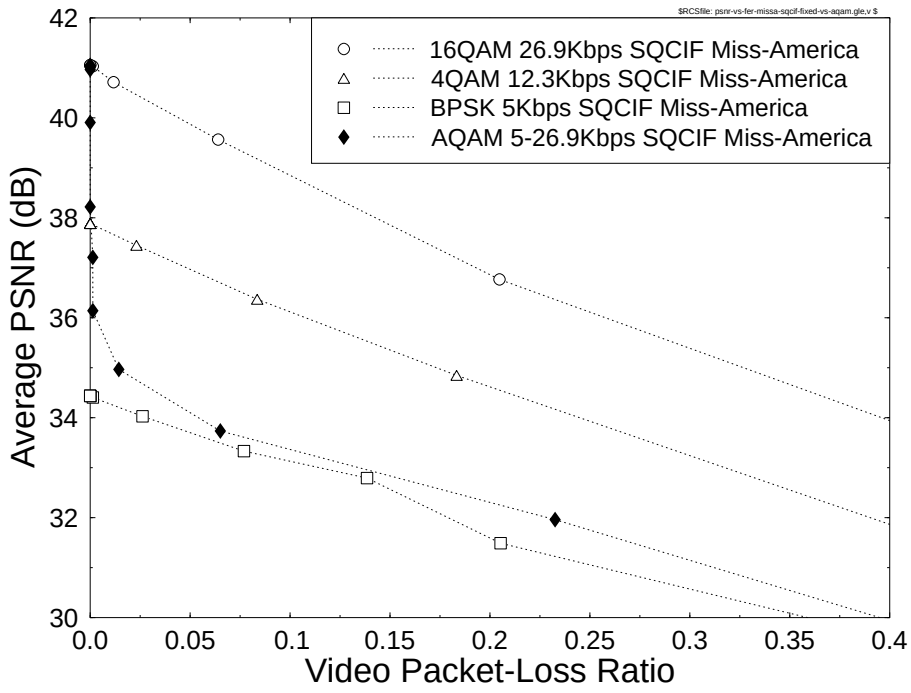

Figure 12.25: Decoded video quality (PSNR) versus video packet-loss ratio comparison of the fixed modulation modes of BPSK, 4QAM, and 16QAM, and the burst-by-burst adaptive modem. Both supporting two users with the aid of joint detection. These results were recorded for the "Miss America" video sequence at SQCIF resolution (128×96 pels).

scheme due to invoking higher-order modem modes, as the channel quality increases. However, we have shown in the context of wideband video transmission [160] that it is possible to maintain the video packet-loss ratio within tolerable limits for the range of channel SNRs considered.

The interaction between the video quality measured in terms of PSNR and the video packet loss ratio can be seen more clearly in Figure 12.25. The figure shows that the adaptive modem slowly degrades the decoded video quality from that of the error-free 16QAM fixed modulation mode, as the channel conditions deteriorate. The video quality degrades from the error-free 41 dB PSNR, while maintaining a near-zero video packet-loss ratio, until the PSNR drops below about 36 dB PSNR. At this point, the further reduced channel quality inflicts an increased video packet-loss rate, and the video quality degrades more slowly. The PSNR versus packet-loss ratio performance then tends toward that achieved by the fixed BPSK modulation mode. However, the adaptive modem achieved better video quality than the fixed BPSK modem even at high packet-loss rates.

12.2.4 Summary and Conclusions

In conclusion, the proposed joint-detection assisted burst-by-burst adaptive CDMA-based video transceiver substantially outperformed the matched-filtering based transceiver. The transceiver guaranteed a near-unimpaired video quality for channel SNRs in excess of about 5 dB over the COST207 dispersive Rayleigh-faded channel. The benefits of the multimode video transceiver clearly manifest themselves in terms of supporting unimpaired video quality under time-variant channel conditions, where a single-mode transceiver's quality would become severely degraded by channel effects. The dynamically reconfigured burst-by-burst adaptive modem gave better perceived video quality due to its more graceful reduction in video quality, as the channel conditions degraded, than a statically switched multimode system.

Following our discussions on joint-detection assisted CDMA-based burst-by-burst adaptive interactive videotelephony, in the next two sections we concentrate on a range of multicarrier modems. The last section of the chapter considers distributive broadcast video transmission, based also on multicarrier modems.

12.3 Subband-Adaptive Turbo-Coded OFDM-Based Interactive Videotelephony[5] [6] [7]

12.3.1 Motivation and Background

In Section 12.2 a CDMA-based video system was proposed, while the previous section considered the transmission of interactive video using OFDM transceivers in various propagation environments. In this section, burst-by-burst adaptive OFDM is proposed and investigated in the context of interactive videotelephony.

As mentioned earlier, burst-by-burst adaptive quadrature amplitude modulation [221] (AQAM) was devised by Steele and Webb [221, 320] in order to enable the transceiver to cope with the time-variant channel quality of narrowband fading channels. Further related research was conducted at the University of Osaka by Sampei and his colleagues, investigating variable coding rate concatenated coded schemes [408]; at the University of Stanford by Goldsmith and her team, studying the effects of variable-rate, variable-power arrangements [409]; and at the University of Southampton in the United Kingdom, investigating a variety of practical aspects of AQAM [410, 411]. The channel's quality is estimated on a burst-by-burst basis, and the most appropriate modulation mode is selected in order to maintain the required target bit error rate (BER) performance, while maximizing the system's Bit Per Symbol (BPS) throughput. Though use of this reconfiguration regime, the distribution of channel errors becomes typically less bursty, than in conjunction with nonadaptive

[5] This section is based on P.J. Cherriman, T. Keller, and L. Hanzo: Subband-adaptive Turbo-coded OFDM-based Interactive Video Telephony, submitted to IEEE Transactions on Circuits and Systems for Video Technology, July 1999.

[6] Acknowledgment: The financial support of the Mobile VCE, EPSRC, UK and that of the European Commission is gratefully acknowledged.

modems, which potentially increases the channel coding gains [412]. Furthermore, the soft-decision channel codec metrics can also be invoked in estimating the instantaneous channel quality [412], regardless of the type of channel impairments.

A range of coded AQAM schemes was analyzed by Matsuoka *et al.* [408], Lau *et al.* [413] and Goldsmith *et al.* [414]. For data transmission systems, which do not necessarily require a low transmission delay, variable-throughput adaptive schemes can be devised, which operate efficiently in conjunction with powerful error correction codecs, such as long block length turbo codes [401]. However, the acceptable turbo interleaving delay is rather low in the context of low-delay interactive speech. Video communications systems typically require a higher bit rate than speech systems, and hence they can afford a higher interleaving delay.

The above principles — which were typically investigated in the context of narrow-band modems — were further advanced in conjunction with wideband modems, employing powerful block turbo-coded, wideband Decision Feedback Equalizer (DFE) assisted AQAM transceivers [412, 415]. A neural-network Radial Basis Function (RBF) DFE-based AQAM modem design was proposed in [416], where the RBF DFE provided the channel-quality estimates for the modem mode switching regime. This modem was capable of removing the residual BER of conventional DFEs, when linearly nonseparable received phasor constellations were encountered.

These burst-by-burst adaptive principles can also be extended to Adaptive Orthogonal Frequency Division Multiplexing (AOFDM) schemes [417] and to adaptive joint-detection-based Code Division Multiple Access (JD-ACDMA) arrangements [418]. The associated AQAM principles were invoked in the context of parallel AOFDM modems by Czylwik *et al.* [419], Fischer [420], and Chow *et al.* [421]. Adaptive subcarrier selection has also been advocated by Rohling *et al.* [422] in order to achieve BER performance improvements. Due to lack of space without completeness, further significant advances over benign, slowly varying dispersive Gaussian fixed links — rather than over hostile wireless links — are due to Chow, Cioffi, and Bingham [421] from the United States, rendering OFDM the dominant solution for asymmetric digital subscriber loop (ADSL) applications, potentially up to bit rates of 54 Mbps. In Europe OFDM has been favored for both Digital Audio Broadcasting (DAB) and Digital Video Broadcasting [423, 424] (DVB) as well as for high-rate Wireless Asynchronous Transfer Mode (WATM) systems due to its ability to combat the effects of highly dispersive channels [425]. The idea of "water-filling" — as allocating different modem modes to different subcarriers was referred to — was proposed for OFDM by Kalet [426] and later further advanced by Chow *et al.* [421]. This approach was adapted later in the context of time-variant mobile channels for duplex wireless links, for example, in [417]. Finally, various OFDM-based speech and video systems were proposed in [427, 428], while the co-channel interference sensitivity of OFDM can be mitigated with the aid of adaptive beam-forming [429, 430] in multi-user scenarios.

The remainder of this section is structured as follows. Section 12.3.1 outlines the architecture of the proposed video transceiver, while Section 12.3.5 quantifies the performance benefits of AOFDM transceivers in comparison to conventional fixed transceivers. Section 12.3.6 endeavors to highlight the effects of more "aggressive" loading of the subcarriers in both BER and video quality terms, while Section 12.3.7 proposed time-variant rather than constant rate AOFDM as a means of more accurately matching the transceiver to the time-variant channel quality fluctuations, before concluding in Section 12.3.8.

12.3.2 AOFDM Modem Mode Adaptation and Signaling

The proposed duplex AOFDM scheme operates on the following basis:

- *Channel quality estimation* is invoked upon receiving an AOFDM symbol in order to select the modem mode allocation of the next AOFDM symbol.
- *The decision concerning the modem modes for the next AOFDM symbol* is based on the prediction of the expected channel conditions. Then the transmitter has to select the appropriate modem modes for the groups or subbands of OFDM subcarriers, where the subcarriers were grouped into subbands of identical modem modes in order to reduce the required number of signaling bits.
- *Explicit signaling or blind detection of the modem modes* is used to inform the receiver as to what type of demodulation to invoke.

If the channel quality of the up-link and down-link can be considered similar, then the channel-quality estimate for the up-link can be extracted from the down-link and vice versa. We refer to this regime as open-loop adaptation. In this case, the transmitter has to convey the modem modes to the receiver, or the receiver can attempt blind detection of the transmission parameters employed. By contrast, if the channel cannot be considered reciprocal, then the channel-quality estimation has to be performed at the receiver, and the receiver has to instruct the transmitter as to what modem modes have to be used at the transmitter, in order to satisfy the target integrity requirements of the receiver. We refer to this mode as closed-loop adaptation. Blind modem mode recognition was invoked, for example, in [417] — a technique that results in bit rate savings due to refraining from dedicating bits to explicit modem mode signaling at the cost of increased complexity. Let us address the issues of channel quality estimation on a subband-by-subband basis in the next subsection.

12.3.3 AOFDM Subband BER Estimation

A reliable channel-quality metric can be devised by calculating the expected overall bit error probability for all available modulation schemes M_n in each subband, which is denoted by $\bar{p}_e(n) = 1/N_s \sum_j p_e(\gamma_j, M_n)$. For each AOFDM subband, the modem mode having the highest throughput, while exhibiting an estimated BER below the target value is then chosen. Although the adaptation granularity is limited to the subband width, the channel-quality estimation is quite reliable, even in interference-impaired environments.

Against this background in our forthcoming discussions, the design tradeoffs of turbo-coded Adaptive Orthogonal Frequency Division Multiplex (AOFDM) wideband video transceivers are presented. We will demonstrate that AOFDM provides a convenient framework for adjusting the required target integrity and throughput both with and without turbo channel coding and lends itself to attractive video system construction, provided that a near-instantaneously programmable rate video codec — such as the H.263 scheme highlighted in the next section — can be invoked.

12.3.4 Video Compression and Transmission Aspects

In this study we investigate the transmission of 704 x 576 pixel Four-times Common Intermediate Format (4CIF) high-resolution video sequences at 30 frames/s using subband-adaptive

turbo-coded Orthogonal Frequency Division Multiplex (AOFDM) transceivers. The transceiver can modulate 1, 2, or 4 bits onto each AOFDM subcarrier, or simply disable transmissions for subcarriers that exhibit a high attenuation or phase distortion due to channel effects.

The H.263 video codec [160] exhibits an impressive compression ratio, although this is achieved at the cost of a high vulnerability to transmission errors, since a run-length coded bit stream is rendered undecodable by a single bit error. In order to mitigate this problem, when the channel codec protecting the video stream is overwhelmed by the transmission errors, we refrain from decoding the corrupted video packet in order to prevent error propagation through the reconstructed video frame buffer [392]. We found that it was more beneficial in video-quality terms if these corrupted video packets were dropped and the reconstructed frame buffer was not updated, until the next video packet replenishing the specific video frame area was received. The associated video performance degradation was found perceptually unobjectionable for packet dropping- or transmission frame error rates (FER) below about 5%. These packet dropping events were signaled to the remote video decoder by superimposing a strongly protected one-bit packet acknowledgment flag on the reverse-direction packet, as outlined in [392]. Turbo error correction codes [401] were used.

12.3.5 Comparison of Subband-Adaptive OFDM and Fixed Mode OFDM Transceivers

In order to show the benefits of the proposed subband-adaptive OFDM transceiver, we compare its performance to that of a fixed modulation mode transceiver under identical propagation conditions, while having the same transmission bit rate. The subband-adaptive modem is capable of achieving a low bit error ratio (BER), since it can disable transmissions over low-quality subcarriers and compensate for the lost throughput by invoking a higher modulation mode than that of the fixed-mode transceiver over the high-quality subcarriers.

Table 12.7 shows the system parameters for the fixed BPSK and QPSK transceivers, as well as for the corresponding subband-adaptive OFDM (AOFDM) transceivers. The system employs constraint length three, half-rate turbo coding, using octal generator polynomials of 5 and 7 as well as random turbo interleavers. Therefore, the unprotected bit rate is approximately half the channel-coded bit rate. The protected to unprotected video bit rate ratio is not exactly half, since two tailing bits are required to reset the convolutional encoders' memory to their default state in each transmission burst. In both modes, a 16-bit Cyclic Redundancy Checking (CRC) is used for error detection, and 9 bits are used to encode the reverse link feedback acknowledgment information by simple repetition coding. The feedback flag decoding ensues using majority logic decisions. The packetization requires a small amount of header information added to each transmitted packet, which is 11 and 12 bits per packet for BPSK and QPSK, respectively. The effective or useful video bit rates for the BPSK and QPSK modes are then 3.4 and 7.0 Mbps.

The fixed-mode BPSK and QPSK transceivers are limited to 1 and 2 bits per symbol, respectively. By contrast, the proposed AOFDM transceivers operate at the same bit rate, as their corresponding fixed modem mode counterparts, although they can vary their modulation mode on a subcarrier- by-subcarrier basis between 0, 1, 2, and 4 bits per symbol. Zero bits per symbol implies that transmissions are disabled for the subcarrier concerned.

The "micro-adaptive" nature of the subband-adaptive modem is characterized by Fig-

	BPSK mode	QPSK mode
Packet rate	4687.5 packets/s	
FFT length	512	
OFDM symbols/packet	3	
OFDM symbol duration	2.6667μs	
OFDM time frame	80 timeslots = 213 μs	
Normalized Doppler frequency, f'_d	1.235×10^{-4}	
OFDM symbol normalised Doppler frequency, F_D	7.41×10^{-2}	
FEC coded bits/packet	1536	3072
FEC-coded video bit rate	7.2 Mbps	14.4 Mbps
Unprotected bits/packet	766	1534
Unprotected bit rate	3.6 Mbps	7.2 Mbps
Error detection CRC (bits)	16	16
Feedback error flag bits	9	9
Packet header bits/packet	11	12
Effective video bits/packet	730	1497
Effective video bit rate	3.4 Mbps	7.0 Mbps

Table 12.7: System Parameters for the Fixed QPSK and BPSK Transceivers, as well as for the Corresponding Subband-adaptive OFDM (AOFDM) Transceivers for Wireless Local Area Networks (WLANs)

ure 12.26, portraying at the top a contour plot of the channel signal-to-noise ratio (SNR) for each subcarrier versus time. At the center and bottom of the figure, the modulation mode chosen for each 32-subcarrier subband is shown versus time for the 3.4 and 7.0 Mbps target-rate subband-adaptive modems, respectively. The channel SNR variation versus both time and frequency is also shown in three-dimensional form in Figure 12.27, which may be more convenient to visualize. This was recorded for the channel impulse response of Figure 12.28. It can be seen that when the channel is of high quality — as for example, at about frame 1080 — the subband-adaptive modem used the same modulation mode, as the equivalent fixed-rate modem in all subcarriers. When the channel is hostile — for example, around frame 1060 — the subband-adaptive modem used a lower-order modulation mode in some subbands than the equivalent fixed-mode scheme, or in extreme cases disabled transmission for that subband. In order to compensate for the loss of throughput in this subband, a higher-order modulation mode was used in the higher quality subbands.

One video packet is transmitted per OFDM symbol; therefore, the video packet-loss ratio is the same as the OFDM symbol error ratio. The video packet-loss ratio is plotted against the channel SNR in Figure 12.29. It is shown in the graph that the subband-adaptive transceivers — or synonymously termed as microscopic-adaptive (μAOFDM), in contrast to OFDM symbol-by-symbol adaptive transceivers — have a lower packet-loss ratio (PLR) at the same SNR compared to the fixed modulation mode transceiver. Note in Figure 12.29 that the subband-adaptive transceivers can operate at lower channel SNRs than the fixed modem mode transceivers, while maintaining the same required video packet-loss ratio. Again, the figure labels the subband-adaptive OFDM transceivers as μAOFDM, implying that the adaption is not noticeable from the upper layers of the system. A macro-adaption could

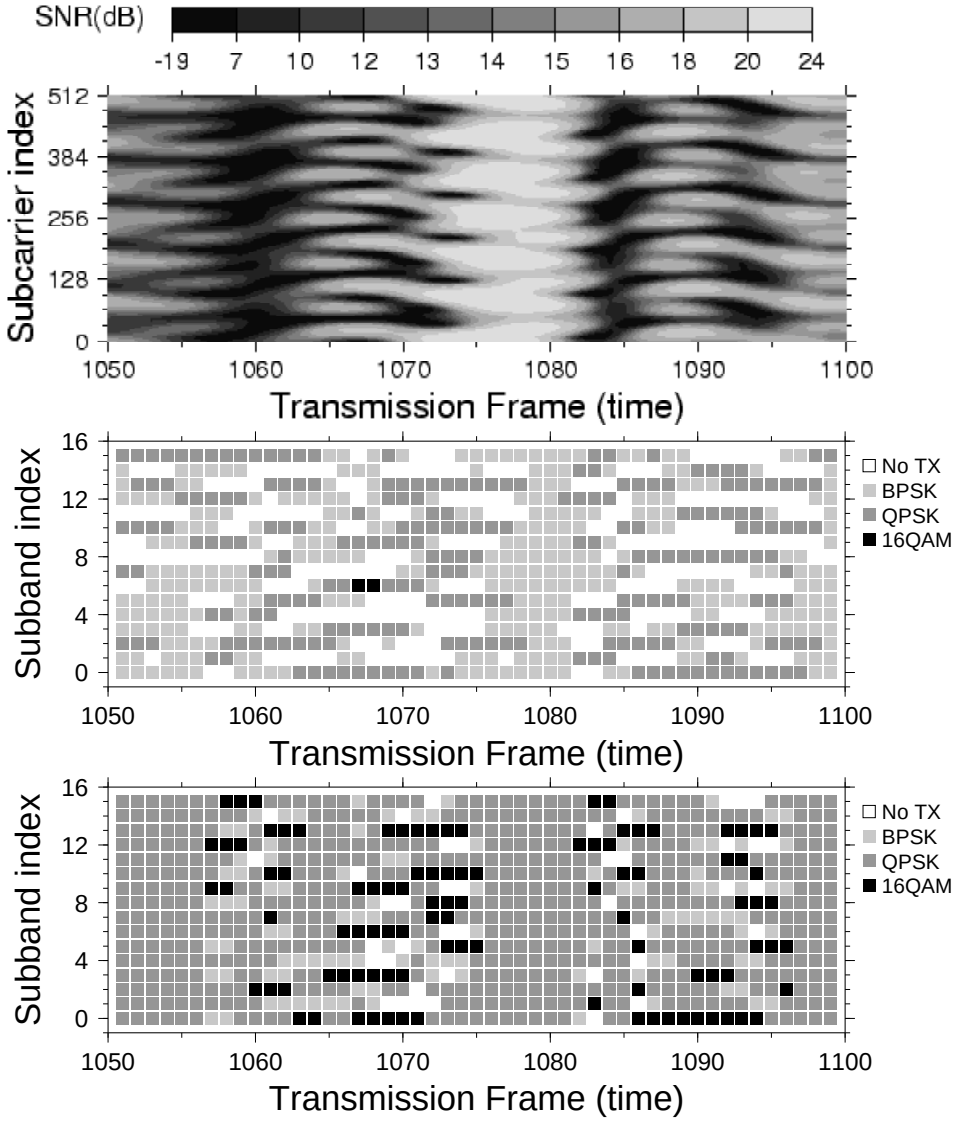

Figure 12.26: The micro-adaptive nature of the subband-adaptive OFDM modem. The top graph is a contour plot of the channel SNR for all 512 subcarriers versus time. The bottom two graphs show the modulation modes chosen for all 16 32-subcarrier subbands for the same period of time. The middle graph shows the performance of the 3.4 Mbps subband-adaptive modem, which operates at the same bit rate as a fixed BPSK modem. The bottom graph represents the 7.0 Mbps subband-adaptive modem, which operated at the same bit rate as a fixed QPSK modem. The average channel SNR was 16 dB.

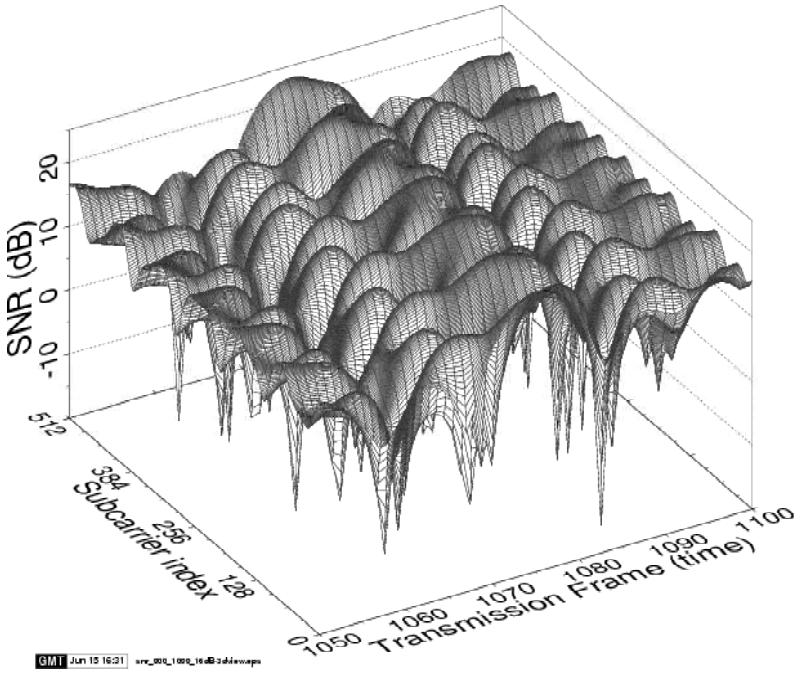

Figure 12.27: Instantaneous channel SNR for all 512 subcarriers versus time, for an average channel SNR of 16 dB over the channel characterized by the channel impulse response (CIR) of Figure 12.28.

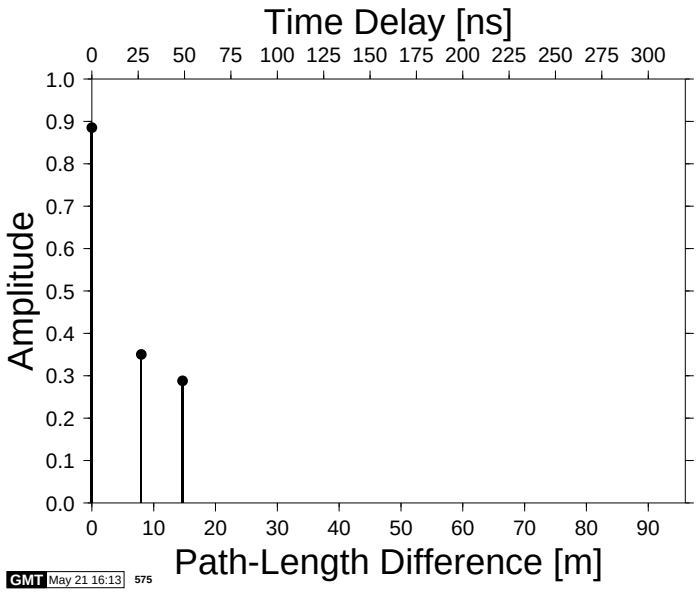

Figure 12.28: Indoor three-path WATM channel impulse response.

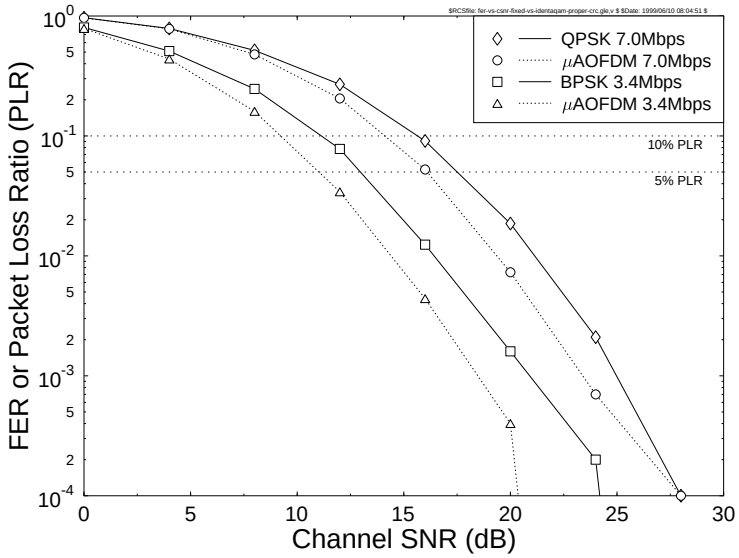

Figure 12.29: Frame Error Rate (FER) or video packet-loss ratio (PLR) versus channel SNR for the BPSK and QPSK fixed modulation mode OFDM transceivers and for the corresponding subband-adaptive μAOFDM transceiver, operating at identical effective video bit rates, namely, at 3.4 and 7.0 Mbps, over the channel model of Figure 12.28 at a normalized Doppler frequency of $F_D = 7.41 \times 10^{-2}$.

be applied in addition to the microscopic adaption by switching between different target bit rates, as the longer-term channel quality improves and degrades. This issue is the subject of Section 12.3.7.

Having shown that the subband-adaptive OFDM transceiver achieved a reduced video packet loss in comparison to fixed modulation mode transceivers under identical channel conditions, we now compare the effective throughput bit rate of the fixed and adaptive OFDM transceivers in Figure 12.30. The figure shows that when the channel quality is high, the throughput bit rates of the fixed and adaptive transceivers are identical. However, as the channel degrades, the loss of packets results in a lower throughput bit rate. The lower packet-loss ratio of the subband-adaptive transceiver results in a higher throughput bit rate than that of the fixed modulation mode transceiver.

The throughput bit rate performance results translate to the decoded video-quality performance results evaluated in terms of PSNR in Figure 12.31. Again, for high-channel SNRs the performance of the fixed and adaptive OFDM transceivers is identical. However, as the channel quality degrades, the video quality of the subband-adaptive transceiver degrades less dramatically than that of the corresponding fixed modulation mode transceiver.

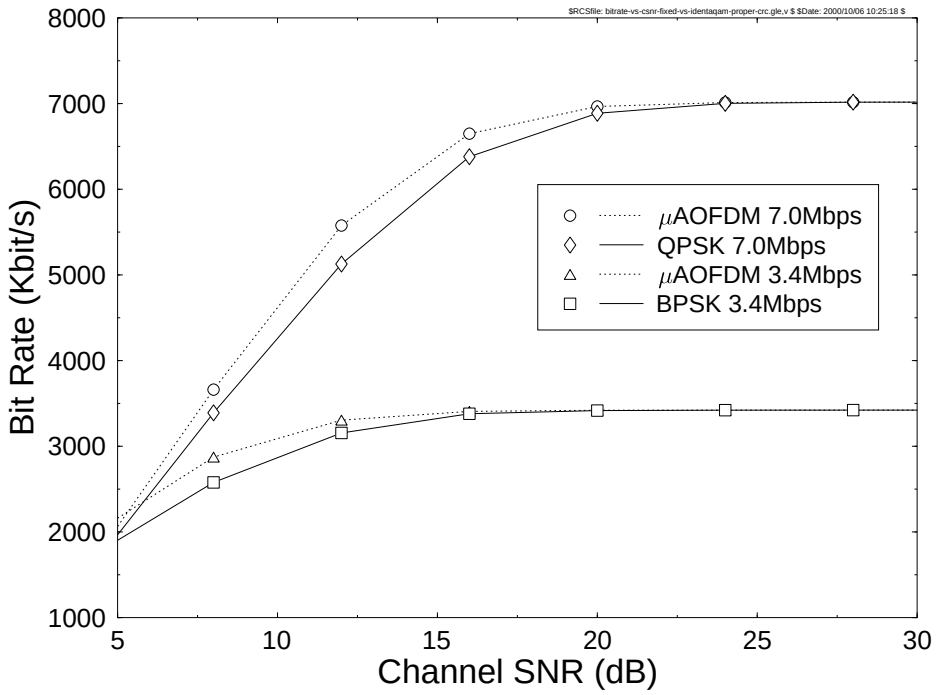

Figure 12.30: Effective throughput bit rate versus channel SNR for the BPSK and QPSK fixed modulation mode OFDM transceivers and that of the corresponding subband-adaptive or μAOFDM transceiver operating at identical effective video bit rates of 3.4 and 7.0 Mbps, over the channel of Figure 12.28 at a normalized Doppler frequency of $F_D = 7.41 \times 10^{-2}$.

12.3.6 Subband-Adaptive OFDM Transceivers Having Different Target Bit Rates

As mentioned earlier, the subband-adaptive modems employ different modulation modes for different subcarriers in order to meet the target bit rate requirement at the lowest possible channel SNR. This is achieved by using a more robust modulation mode or eventually by disabling transmissions over subcarriers having a low channel quality. By contrast, the adaptive system can invoke less robust, but higher throughput, modulation modes over subcarriers exhibiting a high-channel quality. In the examples we have previously considered, we chose the AOFDM target bit rate to be identical to that of a fixed modulation mode transceiver. In this section, we comparatively study the performance of various μAOFDM systems having different target bit rates.

The previously described μAOFDM transceiver of Table 12.7 exhibited a FEC-coded bit rate of 7.2 Mbps, which provided an effective video bit rate of 3.4 Mbps. If the video target bit rate is lower than 3.4 Mbps, then the system can disable transmission in more of the subcarriers, where the channel quality is low. Such a transceiver would have a lower bit error

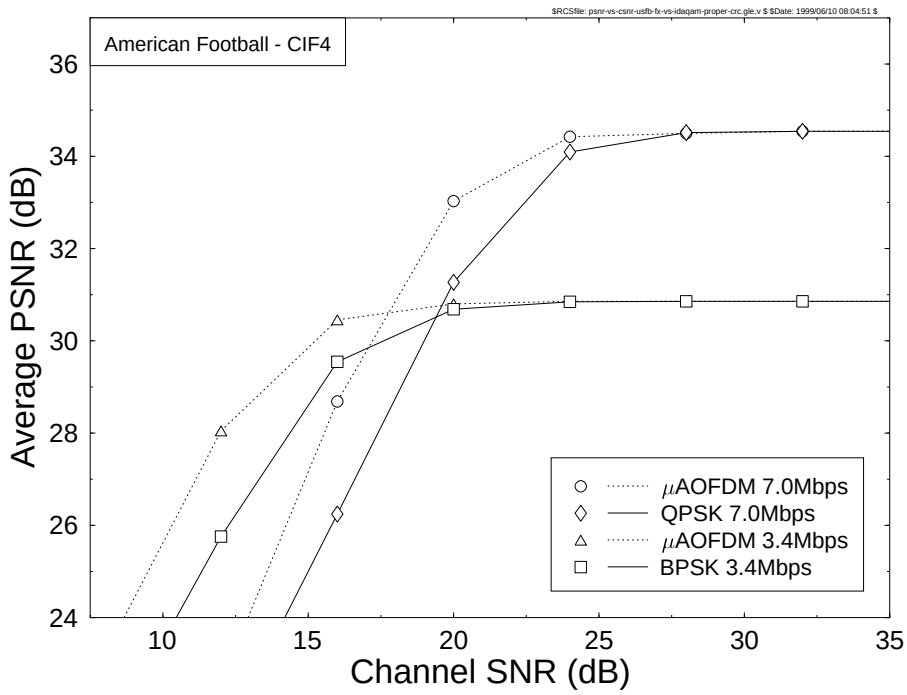

Figure 12.31: Average video quality expressed in PSNR versus channel SNR for the BPSK and QPSK fixed modulation mode OFDM transceivers and for the corresponding μAOFDM transceiver operating at identical channel SNRs over the channel model of Figure 12.28 at a normalized Doppler frequency of $F_D = 7.41 \times 10^{-2}$.

rate than the previous BPSK-equivalent μAOFDM transceiver and therefore could be used at lower average channel SNRs, while maintaining the same bit error ratio target. By contrast, as the target bit rate is increased, the system has to employ higher-order modulation modes in more subcarriers at the cost of an increased bit error ratio. Therefore, high target bit-rate μAOFDM transceivers can only perform within the required bit error ratio constraints at high-channel SNRs, while low target bit-rate μAOFDM systems can operate at low-channel SNRs without causing excessive BERs. Therefore, a system that can adjust its target bit rate as the channel SNR changes would operate over a wide range of channel SNRs, providing the maximum possible average throughput bit rate, while maintaining the required bit error ratio.

Hence, below we provide a performance comparison of various μAOFDM transceivers that have four different target bit rates, of which two are equivalent to that of the BPSK and QPSK fixed modulation mode transceivers of Table 12.7. The system parameters for all four different bit-rate modes are summarized in Table 12.8. The modes having effective video bit rates of 3.4 and 7.0 Mbps are equivalent to the bit rates of a fixed BPSK and QPSK mode transceiver, respectively.

Figure 12.32 shows the Frame Error Rate (FER) or video packet-loss ratio (PLR) perfor-

Packet rate	4687.5 Packets/s			
FFT length	512			
OFDM symbols/packet	3			
OFDM symbol duration	2.6667μs			
OFDM time frame	80 time-slots $=$ 213μs			
Normalized Doppler frequency, f'_d	1.235×10^{-4}			
OFDM symbol normalized Doppler frequency, F_D	7.41×10^{-2}			
FEC-coded bits/packet	858	1536	3072	4272
FEC-coded video bit rate	4.0 Mbps	7.2 Mbps	14.4 Mbps	20.0 Mbps
No. of unprotected bits/packet	427	766	1534	2134
Unprotected bit rate	2.0 Mbps	3.6 Mbps	7.2 Mbps	10.0 Mbps
No. of CRC bits	16	16	16	16
No. of feedback error flag bits	9	9	9	9
No. of packet header bits/packet	10	11	12	13
Effective video bits/packet	392	730	1497	2096
Effective video bit rate	1.8 Mbps	3.4 Mbps	7.0 Mbps	9.8 Mbps
Equivalent modulation mode		BPSK	QPSK	
Minimum channel SNR for 5% PLR (dB)	8.8	11.0	16.1	19.2
Minimum channel SNR for 10% PLR (dB)	7.1	9.2	14.1	17.3

Table 12.8: System Parameters for the Four Different Target Bit Rates of the Various Subband-adaptive OFDM (μAOFDM) Transceivers

mance versus channel SNR for the four different target bit rates of Table 12.8, demonstrating, as expected, that the higher target bit-rate modes require higher channel SNRs in order to operate within given PLR constraints. For example, the mode having an effective video bit rate of 9.8 Mbps can only operate for channel SNRs in excess of 19 dB under the constraint of a maximum PLR of 5%. However, the mode that has an effective video bit rate of 3.4 Mbps can operate at channel SNRs of 11 dB and above, while maintaining the same 5% PLR constraint, albeit at about half the throughput bit rate and so at a lower video quality.

The trade-offs between video quality and channel SNR for the various target bit rates can be judged from Figure 12.33, suggesting, as expected, that the higher target bit rates result in a higher video quality, provided that channel conditions are favorable. However, as the channel quality degrades, the video packet-loss ratio increases, thereby reducing the throughput bit rate and hence the associated video quality. The lower target bit-rate transceivers operate at an inherently lower video quality, but they are more robust to the prevailing channel conditions and so can operate at lower channel SNRs, while guaranteeing a video quality, which is essentially unaffected by channel errors. It was found that the perceived video quality became impaired for packet-loss ratios in excess of about 5%.

The trade-offs between video quality, packet-loss ratio, and target bit rate are further augmented with reference to Figure 12.34. The figure shows the video quality measured in PSNR versus video frame index at a channel SNR of 16 dB as well as for an error-free situation. At the bottom of each graph, the packet-loss ratio per video frame is shown. The three figures indicate the trade-offs to be made in choosing the target bit rate for the specific channel conditions experienced — in this specific example for a channel SNR of 16dB. Note that under error-free conditions the video quality improved upon increasing the bit rate.

Specifically, video PSNRs of about 40, 41.5, and 43 dB were observed for the effective video bit rates of 1.8, 3.4, and 7.0 Mbps. The figure shows that for the target bit rate of

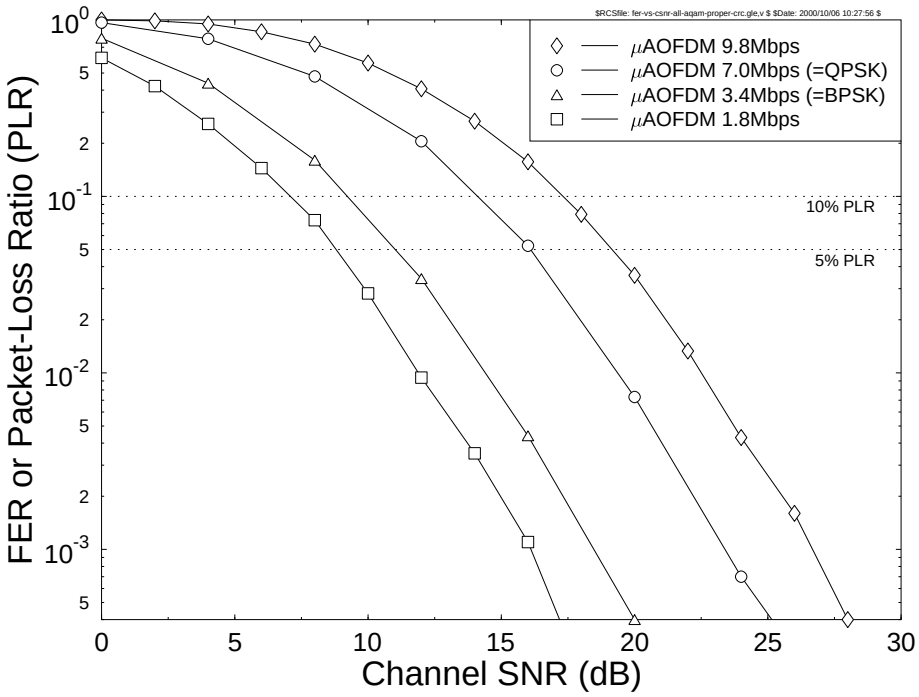

Figure 12.32: FER or video packet-loss ratio (PLR) versus channel SNR for the subband adaptive OFDM transceivers of Table 12.8 operating at four different target bit rates, over the channel model of Figure 12.28 at a normalized Doppler frequency of $F_D = 7.41 \times 10^{-2}$.

1.8 Mbps, the system has a high grade of freedom in choosing which subcarriers to invoke. Therefore, it is capable of reducing the number of packets that are lost. The packet-loss ratio remains low, and the video quality remains similar to that of the error-free situation. The two instances where the PSNR is significantly different from the error-free performance correspond to video frames in which video packets were lost. However, in both instances the system recovers in the following video frame.

As the target bit rate of the subband-adaptive OFDM transceiver is increased to 3.4 Mbps, the subband modulation mode selection process has to be more "aggressive," resulting in increased video packet loss. Observe in the figure that the transceiver having an effective video bit rate of 3.4 Mbps exhibits increased packet loss. In one frame as much as 5% of the packets transmitted for that video frame were lost, although the average PLR was only 0.4%. Because of the increased packet loss, the video PSNR curve diverges from the error-free performance curve more often. However, in almost all cases the effects of the packet losses are masked in the next video frame, indicated by the re-merging PSNR curves in the figure, maintaining a close to error-free PSNR. The subjective effect of this level of packet loss is almost imperceivable.

When the target bit rate is further increased to 7.0 Mbps, the average PLR is about 5% under the same channel conditions, and the effects of this packet-loss ratio are becoming ob-

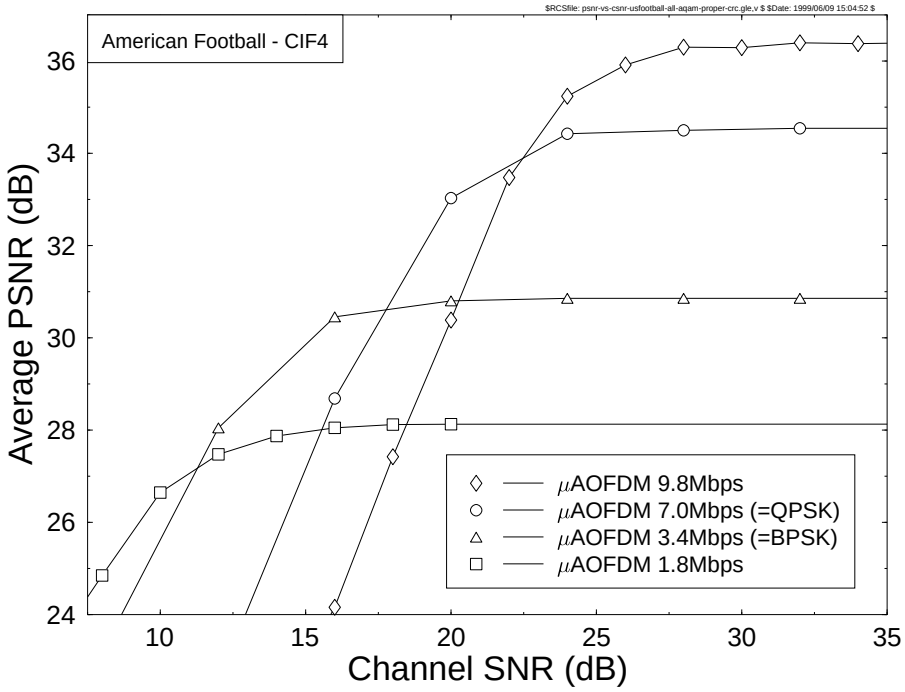

Figure 12.33: Average video quality expressed in PSNR versus channel SNR for the subband-adaptive OFDM transceivers of Table 12.8, operating at four different target bit rates, over the channel model of Figure 12.28 at a normalized Doppler frequency of $F_D = 7.41 \times 10^{-2}$.

jectionable in perceived video-quality terms. At this target bit rate, there are several video frames where at least 10% of the video packets have been lost. The video quality measured in PSNR terms rarely reaches its error-free level, because every video frame contains at least one lost packet. The perceived video quality remains virtually unimpaired until the head movement in the "Suzie" video sequence around frames 40–50, where the effect of lost packets becomes obvious, and the PSNR drops to about 30 dB.

12.3.7 Time-Variant Target Bit Rate OFDM Transceivers

By using a high target bit rate, when the channel quality is high, and employing a reduced target bit rate, when the channel quality is poor, an adaptive system is capable of maximizing the average throughput bit rate over a wide range of channel SNRs, while satisfying a given quality constraint. This quality constraint for our video system could be a maximum packet-loss ratio.

Because a substantial processing delay is associated with evaluating the packet-loss information, modem mode switching based on this metric is less efficient due to this latency. Therefore, we decided to invoke an estimate of the bit error ratio (BER) for mode switching, as follows. Since the noise energy in each subcarrier is independent of the channel's

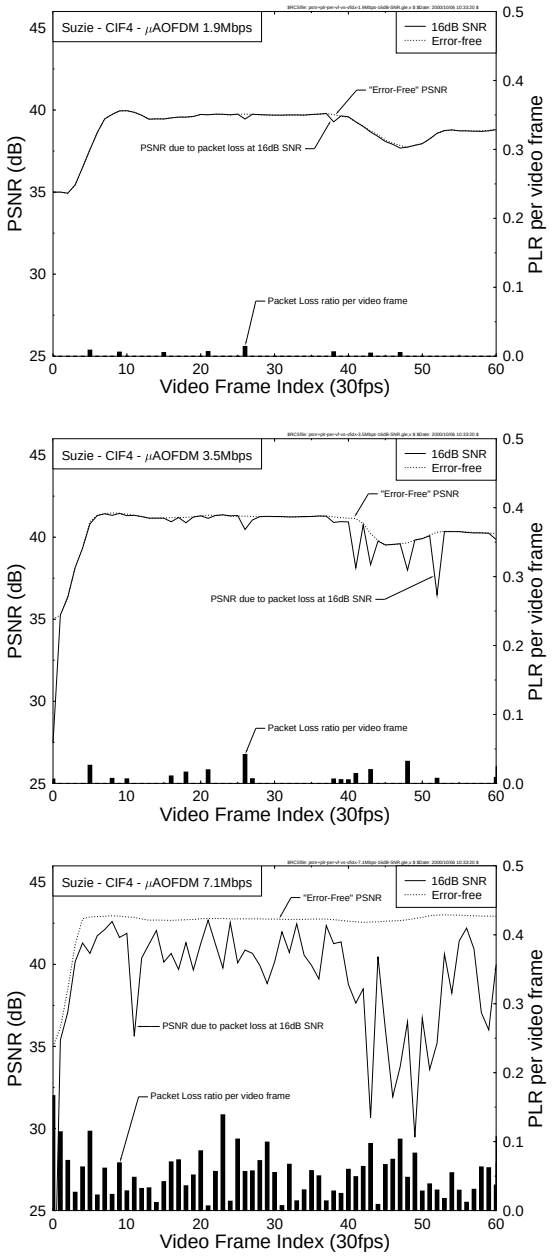

Figure 12.34: Video-quality and packet-loss ratio (PLR) performance versus video-frame index (time) comparison of subband-adaptive OFDM transceivers having target bit rates of 1.8, 3.4, and 7.0 Mbps, under the same channel conditions, at 16 dB SNR over the channel of Figure 12.28 at a normalized Doppler frequency of $F_D = 7.41 \times 10^{-2}$.

frequency domain transfer function H_n, the local signal-to-noise ratio (SNR) in subcarrier n can be expressed as

$$\gamma_n = |H_n|^2 \cdot \gamma, \tag{12.1}$$

where γ is the overall SNR. If no signal degradation due to Inter–Subcarrier Interference (ISI) or interference from other sources appears, then the value of γ_n determines the bit error probability for the transmission of data symbols over the subcarrier n. Given γ_j across the N_s subcarriers in the jth subband, the expected overall BER for all available modulation schemes M_n in each subband can be estimated, which is denoted by $\bar{p}_e(n) = 1/N_s \sum_j p_e(\gamma_j, M_n)$. For each subband, the scheme with the highest throughput, whose estimated BER is lower than a given threshold, is then chosen.

We decided to use a quadruple-mode switched subband-adaptive modem using the four target bit rates of Table 12.8. The channel estimator can then estimate the expected bit error ratio of the four possible modem modes. Our switching scheme opted for the modem mode, whose estimated BER was below the required threshold. This threshold could be varied in order to tune the behavior of the switched subband-adaptive modem for a high or a low throughput. The advantage of a higher throughput was a higher error-free video quality at the expense of increased video packet losses, which could reduce the perceived video quality.

Figure 12.35 demonstrates how the switching algorithm operates for a 1% estimated BER threshold. Specifically, the figure portrays the estimate of the bit error ratio for the four possible modem modes versus time. The large square and the dotted line indicate the mode chosen for each time interval by the mode switching algorithm. The algorithm attempts to use the highest bit-rate mode, whose BER estimate is less than the target threshold, namely, 1% in this case. However, if all the four modes' estimate of the BER is above the 1% threshold, then the lowest bit-rate mode is chosen, since this will be the most robust to channel errors. An example of this is shown around frames 1035–1040. At the bottom of the graph a bar chart specifies the bit rate of the switched subband adaptive modem versus time in order to emphasize when the switching occurs.

An example of the algorithm, when switching among the target bit rates of 1.8, 3.4, 7, and 9.8 Mbps, is shown in Figure 12.36. The upper part of the figure portrays the contour plot of the channel SNR for each subcarrier versus time. The lower part of the figure displays the modulation mode chosen for each 32-subcarrier subband versus time for the time-variant target bit-rate (TVTBR) subband adaptive modem. It can be seen at frames 1051–1055 that all the subbands employ QPSK modulation. Therefore, the TVTBR-AOFDM modem has an instantaneous target bit rate of 7 Mbps. As the channel degrades around frame 1060, the modem has switched to the more robust 1.8 Mbps mode. When the channel quality is high around frames 1074–1081, the highest bit-rate 9.8 Mbps mode is used. This demonstrates that the TVTBR-AOFDM modem can reduce the number of lost video packets by using reduced bit-rate but more robust modulation modes, when the channel quality is poor. However, this is at the expense of a slightly reduced average throughput bit rate. Usually, a higher throughput bit rate results in a higher video quality. However, a high bit rate is also associated with a high packet-loss ratio, which is usually less attractive in terms of perceived video quality than a lower bit-rate, lower packet-loss ratio mode.

Having highlighted how the time-domain mode switching algorithm operates, we will now characterize its performance for a range of different BER switching thresholds. A low BER switching threshold implies that the switching algorithm is cautious about switching to the higher bit-rate modes. Therefore the system performance is characterized by a low video

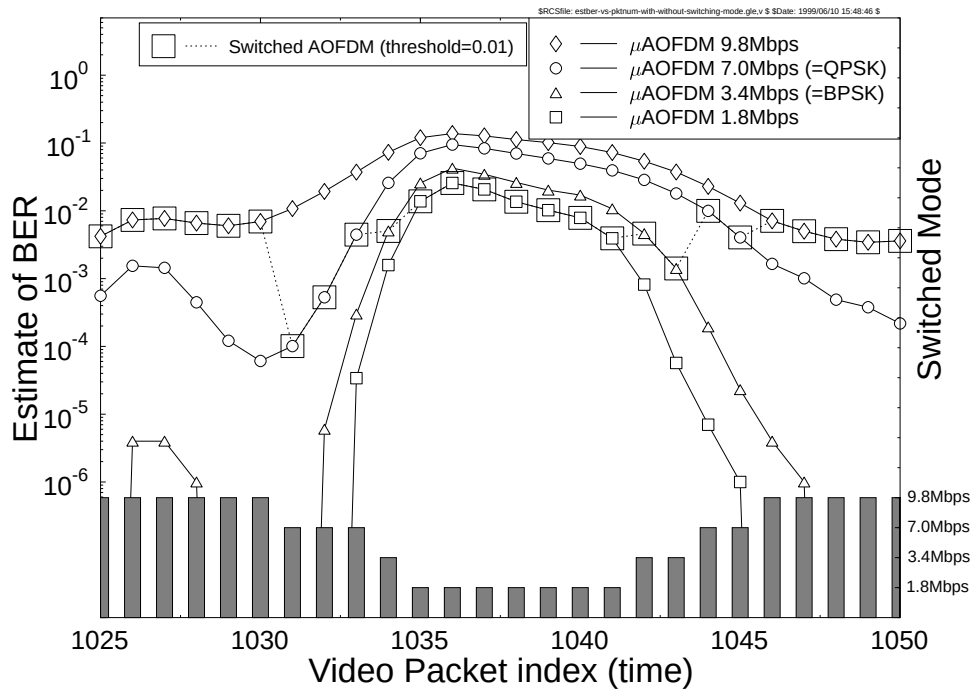

Figure 12.35: Illustration of mode switching for the switched subband adaptive modem. The figure shows the estimate of the bit error ratio for the four possible modes. The large square and the dotted line indicate the modem mode chosen for each time interval by the mode switching algorithm. At the bottom of the graph, the bar chart specifies the bit rate of the switched subband adaptive modem on the right-hand axis versus time when using the channel model of Figure 12.28 at a normalized Doppler frequency of $F_D = 7.41 \times 10^{-2}$.

packet-loss ratio and a low throughput bit rate. A high BER switching threshold results in the switching algorithm attempting to use the highest bit-rate modes in all but the worst channel conditions. This results in a higher video packet-loss ratio. However, if the packet-loss ratio is not excessively high, a higher video throughput is achieved.

Figure 12.37 portrays the video packet-loss ratio or FER performance of the TVTBR-AOFDM modem for a variety of BER thresholds, compared to the minimum and maximum rate unswitched modes. For a conservative BER switching threshold of 0.1%, the time-variant target bit-rate subband adaptive (TVTBR-AOFDM) modem has a similar packet-loss ratio performance to that of the 1.8 Mbps nonswitched or constant target bit-rate (CTBR) subband adaptive modem. However, as we will show, the throughput of the switched modem is always better than or equal to that of the unswitched modem and becomes far superior, as the channel quality improves. Observe in the figure that the "aggressive" switching threshold of 10% has a similar packet-loss ratio performance to that of the 9.8 Mbps CTBR-AOFDM modem. We found that in order to maintain a packet-loss ratio of below 5%, the BER switching thresholds of 2 and 3% offered the best overall performance, since the packet-loss ratio was fairly low,

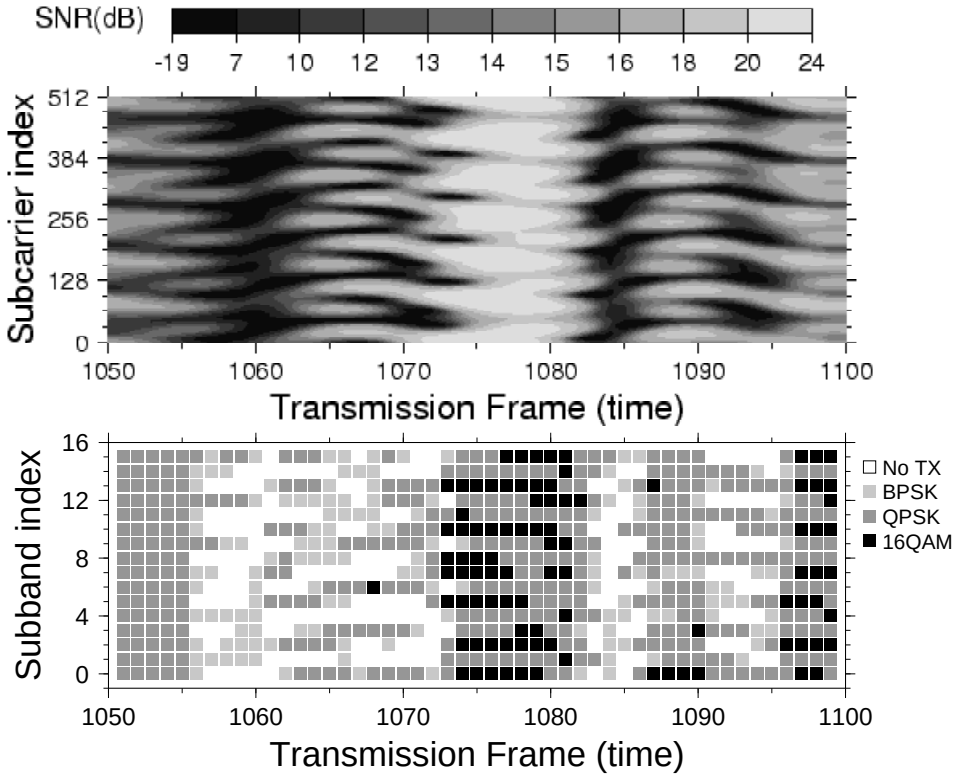

Figure 12.36: The micro-adaptive nature of the time-variant target bit-rate subband adaptive (TVTBR-AOFDM) modem. The top graph is a contour plot of the channel SNR for all 512 subcarriers versus time. The bottom graph shows the modulation mode chosen for all 16 subbands for the same period of time. Each subband is composed of 32 subcarriers. The TVTBR AOFDM modem switches between target bit rates of 2, 3.4, 7, and 9.8 Mbps, while attempting to maintain an estimated BER of 0.1% before channel coding. Average Channel SNR is 16 dB over the channel of Figure 12.28 at a normalized Doppler frequency of $F_D = 7.41 \times 10^{-2}$.

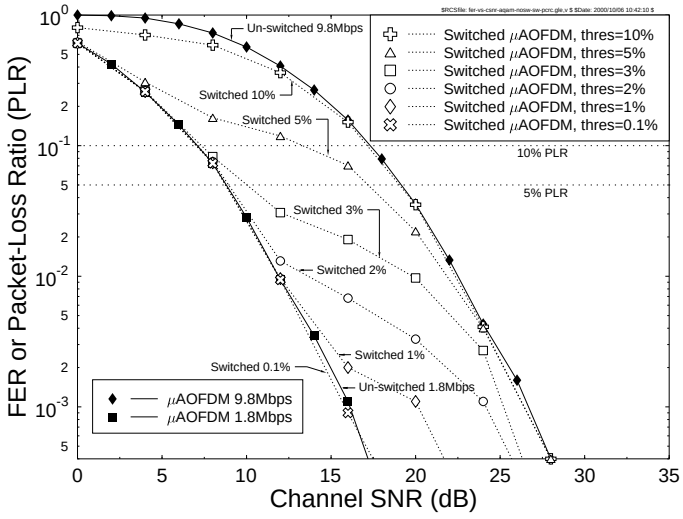

Figure 12.37: FER or video packet-loss ratio versus channel SNR for the TVTBR-AOFDM modem for a variety of BER switching thresholds. The switched modem uses four modes, with target bit rates of 1.8, 3.4, 7, and 9.8 Mbps. The unswitched 1.8 and 9.8 Mbps results are also shown in the graph as solid markers using the channel model of Figure 12.28 at a normalized Doppler frequency of $F_D = 7.41 \times 10^{-2}$.

while the throughput bit rate was higher than that of an unswitched CTBR-AOFDM modem.

A high BER switching threshold results in the switched subband adaptive modem transmitting at a high average bit rate. However, we have shown in Figure 12.37 how the packet-loss ratio increases as the BER switching threshold increases. Therefore, the overall useful or effective throughput bit rate — that is, the bit rate excluding lost packets — may in fact be reduced in conjunction with high BER switching thresholds. Figure 12.38 demonstrates how the transmitted bit rate of the switched TVTBR-AOFDM modem increases with higher BER switching thresholds. However, when this is compared to the effective throughput bit rate, where the effects of packet loss are taken into account, the tradeoff between the BER switching threshold and the effective bit rate is less obvious. Figure 12.39 portrays the corresponding effective throughput bit rate versus channel SNR for a range of BER switching thresholds. The figure demonstrates that for a BER switching threshold of 10% the effective throughput bit-rate performance was reduced in comparison to some of the lower BER switching threshold scenarios. Therefore, the BER = 10% switching threshold is obviously too aggressive, resulting in a high packet-loss ratio and a reduced effective throughput bit rate. For the switching thresholds considered, the BER = 5% threshold achieved the highest effective throughput bit rate. However, even though the BER = 5% switching threshold produces the highest effective throughput bit rate, this is at the expense of a relatively high video packet-loss ratio, which, as we will show, has a detrimental effect on the perceived video quality.

We will now demonstrate the effects associated with different BER switching thresholds on the video quality represented by the peak-signal-to-noise ratio (PSNR). Figure 12.40

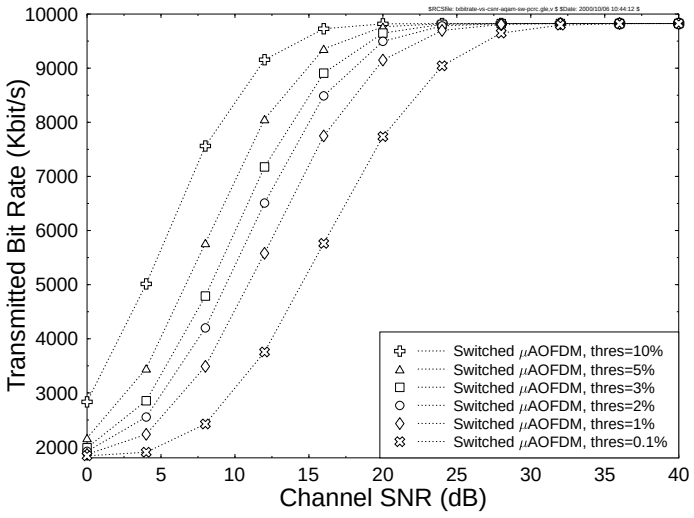

Figure 12.38: Transmitted bit rate of the switched TVTBR-AOFDM modem for a variety of BER switching thresholds. The switched modem uses four modes, having target bit rates of 1.8, 3.4, 7, and 9.8 Mbps, over the channel model of Figure 12.28 at a normalized Doppler frequency of $F_D = 7.41 \times 10^{-2}$.

portrays the PSNR and packet-loss performance versus time for a range of BER switching thresholds. The top graph in the figure indicates that for a BER switching threshold of 1% the PSNR performance is very similar to the corresponding error-free video quality. However, the PSNR performance diverges from the error-free curve when video packets are lost, although the highest PSNR degradation is limited to 2 dB. Furthermore, the PSNR curve typically reverts to the error-free PSNR performance curve in the next frame. In this example, about 80% of the video frames have no video packet loss. When the BER switching threshold is increased to 2%, as shown in the center graph of Figure 12.40, the video-packet loss ratio has increased, such that now only 41% of video frames have no packet loss. The result of the increased packet loss is a PSNR curve, which diverges from the error-free PSNR performance curve more regularly, with PSNR degradations of up to 7 dB. When there are video frames with no packet losses, the PSNR typically recovers, achieving a similar PSNR performance to the error-free case. When the BER switching threshold was further increased to 3% — which is not shown in the figure — the maximum PSNR degradation increased to 10.5 dB, and the number of video frames without packet losses was reduced to 6%.

The bottom graph of Figure 12.40 depicts the PSNR and packet loss performance for a BER switching threshold of 5%. The PSNR degradation in this case ranges from 1.8 to 13 dB and all video frames contain at least one lost video packet. Even though the BER = 5% switching threshold provides the highest effective throughput bit rate, the associated video quality is poor. The PSNR degradation in most video frames is about 10 dB. Clearly, the highest effective throughput bit rate does not guarantee the best video quality. We will now demonstrate that the switching threshold of BER = 1% provides the best video quality, when using the average PSNR as our performance metric.

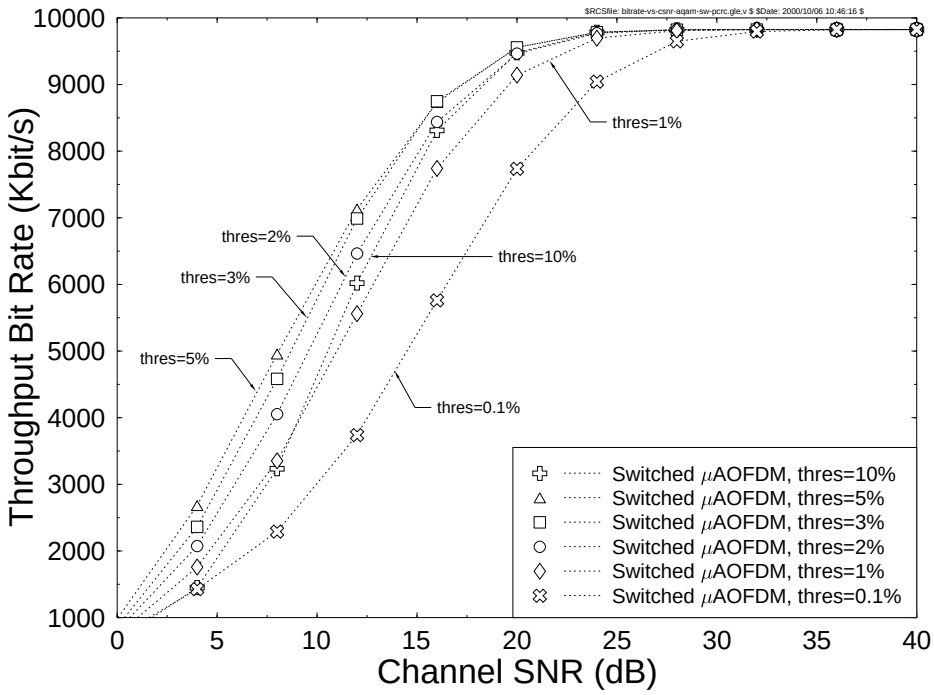

Figure 12.39: Effective throughput bit rate of the switched TVTBR-AOFDM modem for a variety of BER switching thresholds. The switched modem uses four modes, with target bit rates of 1.8, 3.4, 7, and 9.8 Mbps. The channel model of Figure 12.28 is used at a normalized Doppler frequency of $F_D = 7.41 \times 10^{-2}$.

Figure 12.41(a) compares the average PSNR versus channel SNR performance for a range of switched (TVTBR) and unswitched (CTBR) AOFDM modems. The figure compares the four unswitched (i.e., CTBR subband adaptive modems) with switching (i.e., TVTBR subband adaptive modems), which switch between the four fixed-rate modes, depending on the BER switching threshold. The figure indicates that the switched TVTBR subband adaptive modem having a switching threshold of BER = 10% results in similar PSNR performance to the unswitched CTBR 9.8 Mbps subband adaptive modem. When the switching threshold is reduced to BER = 3%, the switched TVTBR AOFDM modem outperforms all of the unswitched CTBR AOFDM modems. A switching threshold of BER = 5% achieves a PSNR performance, which is better than the unswitched 9.8 Mbps CTBR AOFDM modem, but worse than that of the unswitched 7.0 Mbps modem, at low- and medium-channel SNRs.

A comparison of the switched TVTBR AOFDM modem employing all six switching thresholds that we have used previously is shown in Figure 12.41(b). This figure suggests that switching thresholds of BER = 0.1, 1, and 2% perform better than the BER = 3% threshold, which outperformed all of the unswitched CTBR subband adaptive modems. The best average PSNR performance was achieved by a switching threshold of BER = 1%. The more conservative BER = 0.1% switching threshold results in a lower PSNR performance, since its

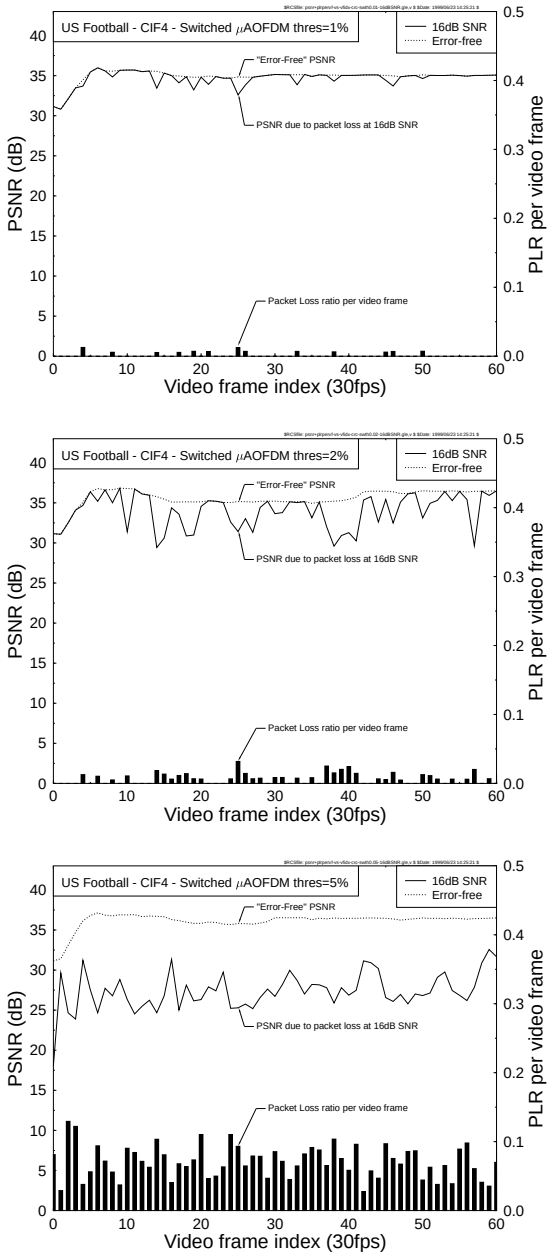

Figure 12.40: Video-quality and packet-loss ratio performance versus video-frame index (time) comparison between switched TVTBR-AOFDM transceivers with different BER switching thresholds, at an average of 16dB SNR, using the channel model of Figure 12.28 at a normalized Doppler frequency of $F_D = 7.41 \times 10^{-2}$.

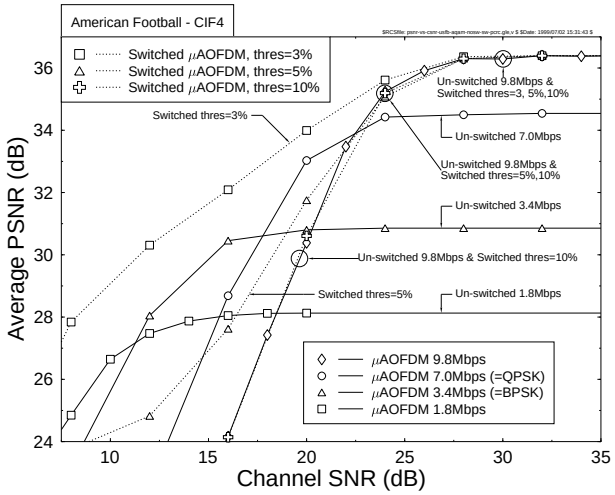

(a)

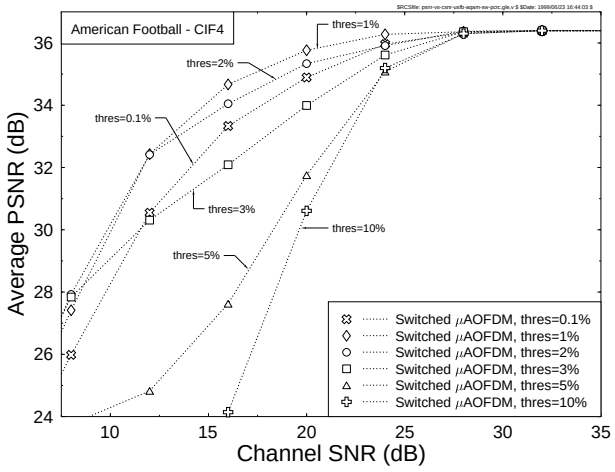

(b)

Figure 12.41: Average PSNR versus channel SNR performance for switched and unswitched subband adaptive modems. Figure (a) compares the four unswitched CTBR subband adaptive modems with switched TVTBR subband adaptive modems (using the same four modem modes) for switching thresholds of BER = 3, 5, and 10%. Figure (b) compares the switched TVTBR subband adaptive modems for switching thresholds of BER = 0.1, 1, 2, 3, 5, and 10%.

throughput bit rate was significantly reduced. Therefore, the best trade-off in terms of PSNR, throughput bit rate, and video packet-loss ratio was achieved with a switching threshold of about BER = 1%.

12.3.8 Summary and Conclusions

A range of AOFDM video transceivers has been proposed for robust, flexible, and low-delay interactive videotelephony. In order to minimize the amount of signaling required, we divided the OFDM subcarriers into subbands and controlled the modulation modes on a subband-by-subband basis. The proposed constant target bit-rate AOFDM modems provided a lower BER than the corresponding conventional OFDM modems. The slightly more complex switched TVTBR-AOFDM modems can provide a balanced video-quality performance, across a wider range of channel SNRs than the other schemes investigated.

12.4 Burst-by-Burst Adaptive Decision Feedback Equalised TCM, TTCM and BICM for H.263-Assisted Wireless Video Telephony[8]

12.4.1 Introduction

$\mathcal{M}$-ary Coded Modulation (CM) schemes such as Trellis Coded Modulation (TCM) [431] and Bit-Interleaved Coded Modulation (BICM) [432,433] constitute powerful and bandwidth efficient forward error correction schemes, which combine the functions of coding and modulation. It was found in [432, 433] that BICM is superior to TCM when communicating over narrowband Rayleigh fading channels, but inferior to TCM in Gaussian channels. In 1993, power efficient binary Turbo Convolutional Codes (TCCs) were introduced in [401], which are capable of achieving a low bit error rate at low Signal-to-Noise Ratios (SNR). However, TCCs typically operate at a fixed coding rate of 1/2 and they were originally designed for Binary-Phase-Shift-Keying (BPSK) modulation, hence they require doubling the bandwidth. In order to lend TCCs a higher spectral efficiency, BICM using TCCs was first proposed in [434], where it was also referred to as Turbo Coded Modulation (TuCM). As another design alternative, Turbo Trellis Coded Modulation (TTCM) was proposed in [435], which has a structure similar to that of the family of TCCs, but employs TCM codes as component codes. It was shown in [435] that TTCM performs better than TCM and TuCM at a comparable complexity. Many other bandwidth efficient schemes using turbo codes, such as multilevel coding employing turbo codes [436], have been proposed in the literature [437], but here we focus our study on the family of TCM, BICM and TTCM schemes in the context of a wireless video telephony system.

In general, fixed-mode transceivers fail to adequately accommodate and counteract the time varying nature of the mobile radio channel. Hence their error distribution becomes bursty and this would degrade the performance of most channel coding schemes, unless long-delay channel interleavers are invoked. However, the disadvantage of long-delay interleavers is that owing to their increased latency they impair 'lip-synchronisation' between the voice

[8]Ng, Chung, Cherriman and Hanzo: CSVT

and video signals. By contrast, in Burst-by-Burst (BbB) Adaptive Quadrature Amplitude (or Phase Shift Keying) Modulation (AQAM) schemes [410, 411, 414, 438–447] a higher-order modulation mode is employed, when the instantaneous estimated channel quality is high for the sake of increasing the number of Bits Per Symbol (BPS) transmitted. Conversely, a more robust but lower-throughput modulation mode is used, when the instantaneous channel quality is low, in order to improve the mean Bit Error Ratio (BER) performance. Uncoded AQAM schemes [410, 411, 414, 439] and channel coded AQAM schemes [440–446] have been lavishly investigated in the context of narrowband fading channels. In particular, adaptive trellis-coded $\mathcal{M}$-ary PSK was considered in [440] and coset codes were applied to adaptive trellis-coded $\mathcal{M}$-ary QAM in [442]. *However, these contributions were based on a number of ideal assumptions, such as perfect channel estimation and zero modulation mode feedback delay.* Hence, in [443], adaptive TCM using more realistic outdated fading estimates was investigated. Recently, the performance of adaptive TCM based on realistic practical considerations such as imperfect channel estimation, modem mode signalling errors and modem mode feedback delay was evaluated in [444], where the adaptive TCM scheme was found to be robust in most practical situations, when communicating over narrowband fading channels. In an effort to increasing the so-called time-diversity order of the TCM codes, adaptive BICM schemes have been proposed in [445], although their employment was still limited to communications over narrowband fading channels.

On the other hand, for communications over wideband fading channels, a BbB adaptive transceiver employing separate channel coding and modulation schemes was proposed in [448]. The main advantage of this wideband BbB adaptive scheme is that regardless of the prevailing channel conditions, the transceiver achieves always the best possible source-signal representation quality such as video, speech, or audio quality by automatically adjusting the achievable bitrate and the associated multimedia source-signal representation quality in order to match the channel quality experienced. Specifically, this wideband BbB adaptive scheme employs the adaptive video rate control and packetisation algorithm of [392], which generates exactly the required number of video bits for the channel-quality-controlled burst-by-burst adaptive transceiver, depending on the instantaneous modem-mode-dependent payload of the current packet, as determined by the current modem mode. Hence, a channel-quality-dependent variable-sized video packet is transmitted in each Time Division Multiple Access (TDMA) frame constituted by a fixed number of AQAM symbols and hence the best possible source-signal representation quality is achieved on a near-instantaneous basis under given propagation conditions in order to cater for the effects of path-loss, fast-fading, slow-fading, dispersion, co-channel interference, etc. More explicitly, a half-rate BCH block code and a half-rate TCC were employed and the modulation modes were adapted according to the channel conditions. However, due to the fixed coding rate of the system the range of the effective video bitrates was limited. **Hence in this section our objective is to further develop the wireless video telephone system of [448] by increasing its bandwidth efficiency up to a factor of two upon rendering not only the modulation-mode selection, but also the choice of the channel coding rate near instantaneously adaptive with the advent of the aforementioned bandwidth efficient coded modulation schemes. As a second objective, we extend this adaptive coded modulation philosophy to multiuser scenarios in the context of a UMTS Terrestrial Radio Access (UTRA) [160, 449] system.**

This section is organised as follows. In Section 12.4.2 the system's architecture is outlined. In Section 12.4.3, the performance of various fixed-mode coded modulation schemes is

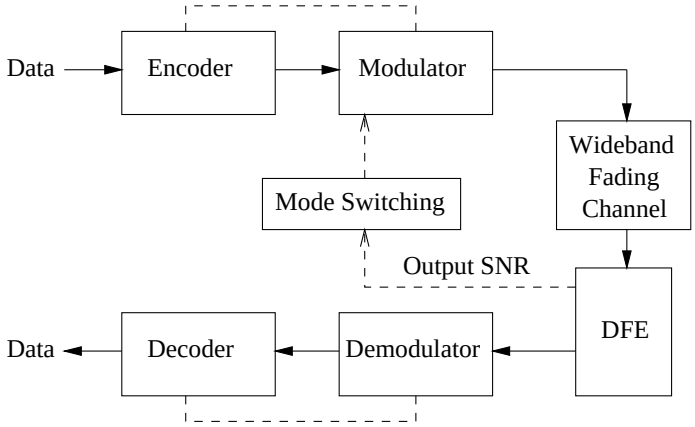

Figure 12.42: The block diagram of the BbB adaptive coded modulation scheme.

characterised, while in Section 12.4.4 the performance of adaptive coded modulation schemes is evaluated. In Section 12.4.5 the performance of the adaptive TTCM based video system is studied in the UTRA CDMA environment. Finally, we will conclude in Section 12.4.6.

12.4.2 System Overview

The simplified block diagram of the BbB adaptive coded modulation scheme is shown in Figure 12.42, where channel interleaving spanning one transmission burst is used. The length of the CM codeword is one transmission burst.

We invoke four CM encoders for our quadruple-mode adaptive coded modulation scheme, each attaching one parity bit to each information symbol generated by the video encoder, yielding a channel coding rate of $1/2$ in conjunction with the modulation modes of 4QAM, a rate of $2/3$ for 8PSK, $3/4$ for 16QAM and $5/6$ for 64QAM. The complexity of the CM schemes is compared in terms of the number of decoding states and the number of decoding iterations. For a TCM or BICM code of memory M, the corresponding complexity is proportional to the number of decoding states $S = 2^M$. Since TTCM schemes invoke two component TCM codes, a TTCM code employing t iterations and using an S-state component code exhibits a complexity proportional to $2.t.S$ or $t.2^{M+1}$.

Over wideband fading channels, the employed Minimum Mean Squared Error (MMSE) based Decision Feedback Equaliser (DFE) eliminates most of the channel-induced InterSymbol Interference (ISI). Consequently, the mean-squared error at the output of the DFE can be calculated and used as the channel quality metric invoked for switching the modulation modes. More explicitly, the residual signal deviation from the error-free transmitted phasors at the DFE's output reflects the instantaneous channel quality of the time varying wideband fading channel. Hence, given a certain instantaneous channel quality, the most appropriate modulation mode can be chosen according to this residual signal deviation from the error-free transmitted phasors at the DFE's output. Specifically, the SNR at the output of the DFE, γ_{dfe},

can be computed as [439]:

$$\begin{aligned}\gamma_{dfe} &= \frac{\text{Wanted Signal Power}}{\text{Residual ISI Power + Effective Noise Power}}. \\ &= \frac{E\left[\left|s_k \sum_{m=0}^{N_f} C_m h_m\right|^2\right]}{\sum_{q=-(N_f-1)}^{-1} E\left[\left|\sum_{m=0}^{N_f-1} C_m h_{m+q} s_{k-q}\right|^2\right] + N_0 \sum_{m=0}^{N_f} |C_m|^2},\end{aligned} \quad (12.2)$$

where C_m and h_m denotes the DFE's feed-forward coefficients and the Channel Impulse Response (CIR), respectively. The transmitted signal is represented by s_k and N_0 denotes the noise spectral density. Finally, the number of DFE feed-forward coefficients is denoted by N_f. The equaliser's output SNR, γ_{dfe}, in Equation 12.2, is then compared against a set of adaptive modem mode switching thresholds f_n, and subsequently the appropriate modulation mode is selected [439].

In the adaptive transmission schemes the outdated channel quality estimates arriving after a feedback delay inevitably inflict performance degradations, which can be mitigated using powerful channel quality prediction techniques [450,451]. However, in our proposed adaptive video system we adopted the practical approach of employing outdated, rather than perfect channel quality estimates. Specifically, a practical modem mode switching regime adapted to the specific requirements of wireless video telephony is employed, where a suitable modulation mode is chosen at the receiver on a BbB basis and it is then communicated to the transmitter by superimposing the requested modulation mode identifier code onto the terminal's reverse-direction transmission burst. Hence, the actual channel condition is outdated by one TDMA/TDD frame duration.

At the receiver, the DFE's symbol estimate $\hat{s}_k$ is passed to the channel decoder and the log-domain branch metric is computed for the sake of maximum-likelihood decoding at time instant k as:

$$m_k(s_i) = -\frac{|\hat{s}_k - s_i|^2}{2\sigma^2}, \ i = \{0, \ldots, \mathcal{M}-1\}, \quad (12.3)$$

where s_i is the ith legitimate symbol of the $\mathcal{M}$-ary modulation scheme and σ^2 is the variance of the Additive White Gaussian Noise (AWGN). Note that the equaliser output $\hat{s}_k$ is near-Gaussian, since the channel has been equalised [439]. In other words, the DFE has 'converted' the dispersive Rayleigh fading channels into an 'AWGN-like' channel. Hence, the TCM and TTCM codes that have been designed for AWGN channels will outperform the BICM scheme, as we will demonstrate in Figure 12.44.

The following assumptions are stipulated. Firstly, we assume that the equaliser is capable of estimating the CIR perfectly with the aid of the equaliser training sequence hosted by the transmission burst of Figure 12.43. Secondly, the CIR is time-invariant for the duration of a transmission burst, but varies from burst to burst according to the Doppler frequency, which corresponds to assuming that the CIR is slowly varying.

12.4.2.1 System Parameters and Channel Model

For the sake of direct comparisons we used the same H.263 video codec, as in [448]. Hence we refer the interested readers to [160] for a detailed description of the H.263 video codec.

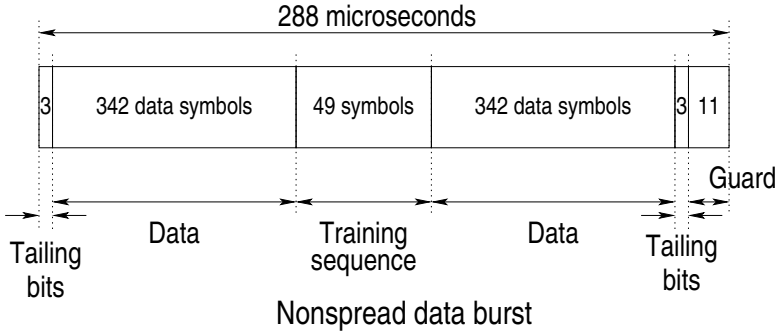

Figure 12.43: Transmission burst structure of the FMA1 non-spread data as specified in the FRAMES proposal [405].

Features	Multi-rate System			
Mode	4QAM	8PSK	16QAM	64QAM
Transmission Symbols/TDMA slot	684			
Bits/Symbol	2	3	4	6
Transmission bits/TDMA slot	1368	2052	2736	4104
Packet Rate	216.7/s			
Transmission bitrate (kbit/s)	296.4	444.6	592.8	889.3
Code Termination Symbols	6			
Data Symbols/TDMA slot	678			
Coding Rate	1/2	2/3	3/4	5/6
Information Bits/Symbol	1	2	3	5
Unprotected bits/TDMA slot	678	1356	2034	3390
Unprotected bitrate (kbit/s)	146.9	293.8	440.7	734.6
Video packet CRC (bits)	16			
Feedback protection (bits)	9			
Video packet header (bits)	11	12	12	13
Video bits/packet	642	1319	1997	3352
Effective Video-rate (kbit/s)	139.1	285.8	432.7	726.3
Video framerate (Hz)	30			

Table 12.9: Operational-mode specific transceiver parameters for TTCM.

The transmitted bitrate of all four modes of operation is shown in Table 12.9 for the TTCM coding scheme. The associated bitrates are similar for the other coded modulation schemes. The slight difference is caused by using different numbers of code termination symbols. The unprotected bitrate before channel coding is also shown in the table. The actual useful bitrate available for video encoding is slightly lower, than the unprotected bitrate due to the useful bitrate reduction required by the transmission of the strongly protected packet acknowledgement information and packetisation overhead information. The effective video bitrate is also shown in the table, which varies from 139 to 726 kbit/s. We have investigated the video system concerned using a wide range of video sequences having different resolutions. However for conciseness we will only show results for the Common Intermediate Format (CIF)

Parameter	Value
Carrier Frequency	1.9GHz
Vehicular Speed	30mph
Doppler frequency	85Hz
Normalised Doppler frequency	3.3×10^{-5}
Channel type	C0ST 207 Typical Urban [407]
Number of paths in channel	4
Data modulation	Adaptive Coded Modulation (4-QAM, 8-PSK, 16-QAM, 64-QAM)
Receiver type	Decision Feedback Equaliser Number of Forward Filter Taps = 35 Number of Backward Filter Taps = 7

Table 12.10: Modulation and channel parameters.

Features	Value
Multiple access	TDMA
No. of Slots/Frame	16
TDMA frame length	4.615ms
TDMA slot length	288μs
Data Symbols/TDMA slot	684
User Data Symbol Rate (kBd)	148.2
System Data Symbol Rate (MBd)	2.37
Symbols/TDMA slot	750
User Symbol Rate (kBd)	162.5
System Symbol Rate (MBd)	2.6
System Bandwidth (MHz)	3.9
Eff. User Bandwidth (kHz)	244

Table 12.11: Generic system features of the reconfigurable multi-mode video transceiver, using the non-spread data burst mode of the FRAMES proposal [405] shown in Figure 12.43.

resolution (352x288 pixels) 'Salesman' sequence at 30 frames per second.

Table 12.10 shows the modulation and channel parameters employed. Again, similar to [448], the COST 207 [407] channel models, which are widely used in the community, were employed. Specifically, a 4-path Typical Urban COST 207 channel [407] was used. The multi-path channel model is characterised by its discretized symbol-spaced CIR, where each path is faded independently according to a Rayleigh distribution. The non-spread data transmission burst structure FMA1 specified in the FRAMES proposal [405] was used, which is shown in Figure 12.43. Nyquist signalling was employed and the remaining system parameters are shown in Table 12.11.

A component TCM having a code memory of $M = 3$ was used for the TTCM scheme. The number of iterations for TTCM was fixed to $t = 4$ and hence the iterative scheme exhibited a similar decoding complexity to that of the TCM having a code memory $M = 6$ in terms of the number of coding states. The fixed-mode CM schemes that we invoked in our BbB AQAM schemes are Ungerböck's TCM [85, 431], Robertson's TTCM [85, 435] and Zehavi's BICM [85, 432]. Soft decision trellis decoding utilising the Log-Maximum A

Posteriori algorithm [452] was invoked for decoding.

Note that the parameters of the DFE employed, which are the same as that of [448], as well as that of the Joint Detection (JD) receiver in Section 12.4.5 were adjusted such that they achieve their best attainable performance in terms of removing the effect of channel induced multipath interference as well as the multiuser interference, respectively. Hence, opting for a more complex DFE or JD design would not improve the overall achievable performance. Furthermore, since the video quality expressed in terms of the luminance Peak Signal to Noise Ratio (PSNR) is a direct function of the system's effective throughput, we will use the PSNR value as the ultimate evaluation metric of the system's performance. Since the same video system and channel model are employed, the complexity difference between the various CM-assisted video schemes is directly dependent on the decoding complexity of the CM schemes. Hence, the complexity of the proposed video system is estimated in terms of the number of trellis states of the CM decoders.

12.4.3 Employing Fixed Modulation Modes

Initial simulations of the videophone transceiver were performed with the transceiver configured in one of the four fixed modulation modes of Table 12.9. We commence by comparing the performance of TTCM in conjunction with a code memory of $M = 3$ and using $t = 4$ iterations, to that of non-iterative TCM along with a code memory of $M = 6$, since the associated computational complexity is similar. We then also compare these results to that of TCM using a code memory of $M = 3$ and to BICM employing a code memory $M = 3$. Again, one video packet is transmitted in each TDMA frame and the receiver checks, whether the received packet has any bit-errors using the associated Cyclic Redundancy Check (CRC). If the received packet has been corrupted, a negative acknowledgement flag is transmitted to the video encoder in order to prevent it from using the packet just transmitted for updating the encoder's reconstruction frame buffer. This allows the video encoder's and decoder's reconstruction frame buffer to use the same contents for motion compensation. This acknowledgement message is strongly protected using repetition codes and superimposed on the reverse link transmission. In these investigations a transmission frame error resulted in a video packet error. We shall characterise the relative frequency of these packet corruption events by the Packet Loss Ratio (PLR). The PLR of the CM schemes is shown in Figure 12.44. We emphasise again that the video packets are either error-free or discarded. Hence the PLR is a more meaningful modem performance metric in this scenario, than the BER.

From Figure 12.44, it is found that the BICM scheme has the worst PLR performance and the TCM6 scheme using a code memory $M = 6$ has a significant PLR performance advantage over the TCM3 scheme employing a code memory of $M = 3$. Furthermore, the TTCM scheme provides the best PLR performance, requiring an approximately 2.5 dBs lower channel SNR than the BICM scheme. This is because turbo decoding of the TTCM scheme is very effective in reducing the number of bit errors to zero in all the received packets exhibiting a moderate or low number of bit errors before channel decoding. By contrast, the gravely error-infected received packets are simply dropped and the corresponding video frame segment is replaced by the same segment of the previous frame. The performance of BICM is worse, than that of TCM due to the associated limited channel interleaving depth [432, 433] of the BICM scheme in our slow-fading wideband channels.

Figure 12.45 shows the error-free decoded video quality, measured in terms of the PSNR

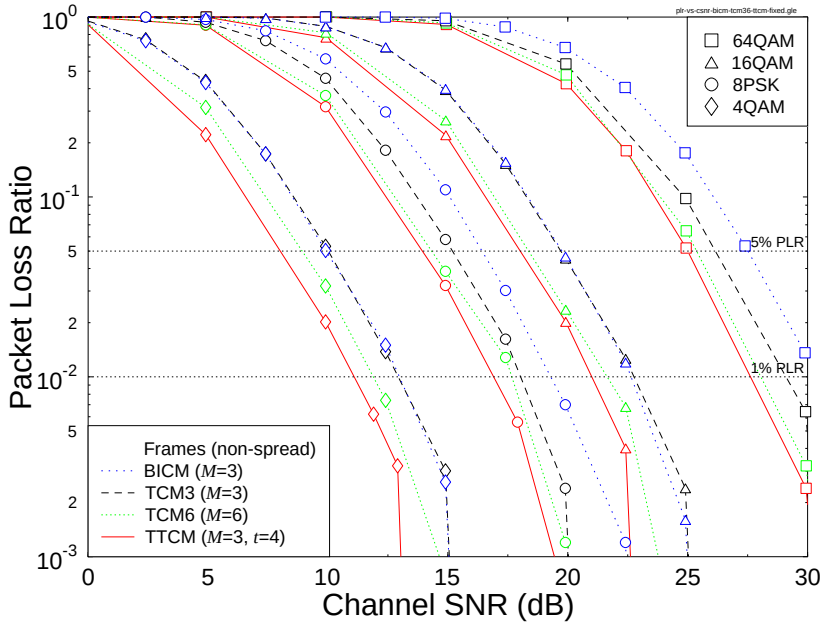

Figure 12.44: Packet loss ratio versus channel SNR for the four fixed modem modes, using the four joint coding/modulation schemes considered, namely BICM, TCM3, TCM6 and TTCM when communicating over the COST 207 channel [407].

versus time for the CIF-resolution "Salesman" sequence for each of the four fixed modulation modes using the TTCM scheme. The figure demonstrates that the higher order modulation modes, which have a higher associated bitrate provide a better video quality. However, in an error-impaired situation a high error-free PSNR does not always guarantee achieving a better subjective video quality. In order to reduce the detrimental effects of channel-induced errors on the video quality, we refrain from decoding the error-infested video packets and hence avoid error propagation through the reconstructed video frame buffer [392, 448]. Instead, these originally high-bitrate and high-quality but error-infested video packets are dropped and hence the reconstructed video frame buffer will not be updated, until the next packet replenishing the specific video frame area arrives. As a result, the associated video performance degradation becomes fairly minor for PLR values below 5% [448], which is significantly lower than in case of replenishing the corresponding video frame area with the error-infested video packet.

12.4.4 Employing Adaptive Modulation

The BbB AQAM mode switching mechanism is characterised by a set of switching thresholds, by the corresponding random TTCM symbol-interleavers and the component codes, as

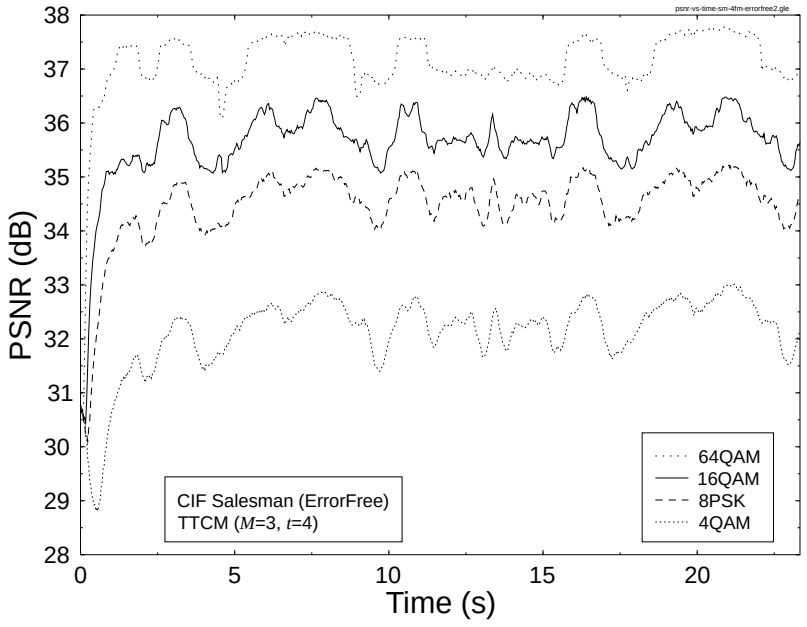

Figure 12.45: PSNR (video quality) versus time for the four fixed modulation modes, under error-free channel conditions using the CIF resolution "Salesman" video sequence at 30 frame/s. TTCM scheme using a code memory of $M = 3$ and $t = 4$ iterations was employed.

follows:

$$\text{Modulation Mode} = \begin{cases} 4QAM, I_0 = I_s, R_0 = 1/2 & \text{if } \gamma_{DFE} \leq f_1 \\ 8PSK, I_1 = 2I_s, R_1 = 2/3 & \text{if } f_1 < \gamma_{DFE} \leq f_2 \\ 16QAM, I_2 = 3I_s, R_2 = 3/4 & \text{if } f_2 < \gamma_{DFE} \leq f_3 \\ 64QAM, I_3 = 5I_s, R_3 = 5/6 & \text{if } \gamma_{DFE} > f_3, \end{cases} \tag{12.4}$$

where $f_n, n = 1...3$ are the AQAM switching thresholds, which were set according to the target PLR requirements, while $I_s = 684$ is the number of data symbols in a transmission burst and I_n represents the random TTCM symbol-interleaver size expressed in terms of the number of bits, which is not used for the TCM and BICM schemes.

The video encoder/decoder pair discards all corrupted video packets in an effort to avoid error propagation effects in the video decoder. Therefore in this section the AQAM switching thresholds f_n were chosen using an experimental procedure in order to maintain the required target PLR, rather than the BER. More specifically, we defined a set of "normal" thresholds for each adaptive coded modulation scheme depending on their fixed modem mode's performance in terms of PLR versus average equaliser SNR. Explicitly, the "normal" threshold was set to maintain a PLR around 3%. We also defined a "conservative" threshold, for a PLR around 0.5%, and an "aggressive" threshold, for a PLR around 20% for the adaptive TTCM scheme. These modem mode switching thresholds are listed in Table 12.12.

The probability of each of the modulation modes versus channel SNR is shown in Fig-

No.	Scheme	M	Type	Thresholds (dB)		
				f_1	f_2	f_3
1.	TTCM	3	N	13.07	17.48	24.77
2.	TTCM	3	C	16.00	20.00	27.25
3.	TTCM	3	A	10.05	12.92	20.67
4.	TCM	3	N	14.48	18.86	26.24
5.	TCM	6	N	13.98	17.59	25.37
6.	BICM	3	N	15.29	18.88	26.49

Table 12.12: Switching thresholds according to Equation 12.4 at the output of the equaliser required for each modulation mode of the BbB adaptive modem. The threshold types are Normal (N), Conservative (C) and Aggressive (A). M denotes the code memory of the encoder.

ure 12.46 for the BbB adaptive TTCM scheme using the "normal" switching thresholds. The graph shows that the 4QAM mode is the most probable one at low channel SNRs, and the 64QAM mode is predominant at high channel SNRs. In addition, for example at 20 dB, the 4QAM mode is being used about 8% of the time and 64QAM only 1% of the time, since most of the time the AQAM modem is operating in its 8PSK or 16QAM mode with an associated probability of 40% and 51%, respectively.

12.4.4.1 Performance of TTCM AQAM

In this section we compare the performance of the four fixed modulation modes with that of the quadruple-mode TTCM AQAM scheme using the "normal" switching thresholds of Table 12.12. The code memory is $M = 3$ and the number of turbo iterations is $t = 4$.

Specifically, in Figure 12.47 we compare the PLR performance of the four fixed modulation modes with that of the quadruple-mode TTCM AQAM arrangement using the "normal" switching thresholds. The figure shows that the performance at low channel SNRs is similar to that of the fixed TTCM 4QAM mode, while at high channel SNRs the performance is similar to that of the fixed 64QAM mode. At medium SNR values the PLR performance is near-constant, ranging from 1% to 5%. More explicitly, the TTCM AQAM modem maintains this near-constant PLR, which is higher than that of the fixed 4QAM modem, while achieving a higher throughput bitrate, than the 2 bit/symbol rate of 4QAM. Since our BbB AQAM videophone system's video performance is closely related to the PLR, the TTCM AQAM scheme provides a near-constant video performance across a wide range of channel SNRs. Additionally, the BbB TTCM AQAM modem allows the throughput bitrate to increase, as the channel SNR increases, thereby supporting an improved video quality, as the channel SNR improves, which is explicitly shown in Figure 12.48.

The effective throughput bitrate of the fixed-mode modems drops rapidly due to the increased PLR, which is a consequence of discarding the 'payload' of the corrupted video packets, as the channel SNR reduces. The TTCM AQAM throughput bitrate matches that achieved by the fixed modem modes at both low and high channel SNRs. At a channel SNR of 25 dB the fixed-mode 64QAM modem achieves an approximately 700kbps throughput, while the TTCM AQAM modem transmits at approximately 500kbps. However, by referring to Figure 6 it can be seen that the 700kbps video throughput bitrate is achieved by 64QAM at a concomitant PLR of slightly over 5%, while the AQAM modem experiences a reduced

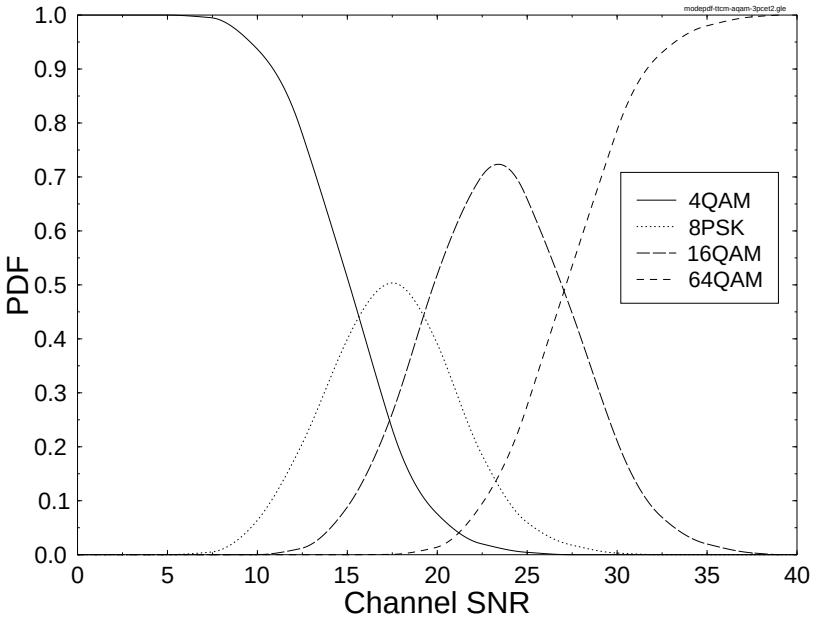

Figure 12.46: PDF of the various active mode versus channel SNR for the quadruple-mode BbB adaptive TTCM scheme using the "normal" thresholds employing a code memory of $M = 3$ and $t = 4$ iterations when communicating over the COST 207 channel [407].

PLR of 2%. As mentioned earlier, the associated video performance degradation becomes noticeable at a PLR in excess of 5%. Hence, the fixed-mode 64QAM modem results in a subjectively inferior video quality in comparison to the TTCM AQAM scheme at a channel SNR of 25 dB. The video quality expressed in terms of the average PSNR is closely related to the effective video throughput bitrate. Hence the trends observed in terms of PSNR in Figure 12.49 are similar to those seen in Figure 12.48.

Note that the channel-quality related AQAM mode feedback is outdated by one TDMA transmission burst of 4.615 ms for the sake of providing realistic results. As shown in [448], in the idealistic zero-delay-feedback AQAM scheme, the resultant PSNR curve follows the envelope of the fixed-mode schemes. However, a suboptimum modulation modes may be chosen due to the one-frame-feedback delay, which may inflict an increased video packet loss. Since the effective throughput is quantified in terms of the average bitrate provided by all the successful transmitted video packets but excluding the erroneous and hence dropped packets, the throughput and hence the PSNR of the realistic AQAM scheme using outdated channel quality estimates is lower than that of the ideal AQAM scheme. Furthermore, the AQAM system's effective throughput is slightly reduced by allocating some of the useful payload to the AQAM mode signalling information, which is protected by strong repetition coding. Therefore, the throughput or PSNR curve of the AQAM scheme plotted in Figure 12.48 or Figure 12.49 does not strictly follow the throughput or PSNR envelope of the fixed-mode schemes. However, at lower vehicular speeds the switching latency is less crucial and the

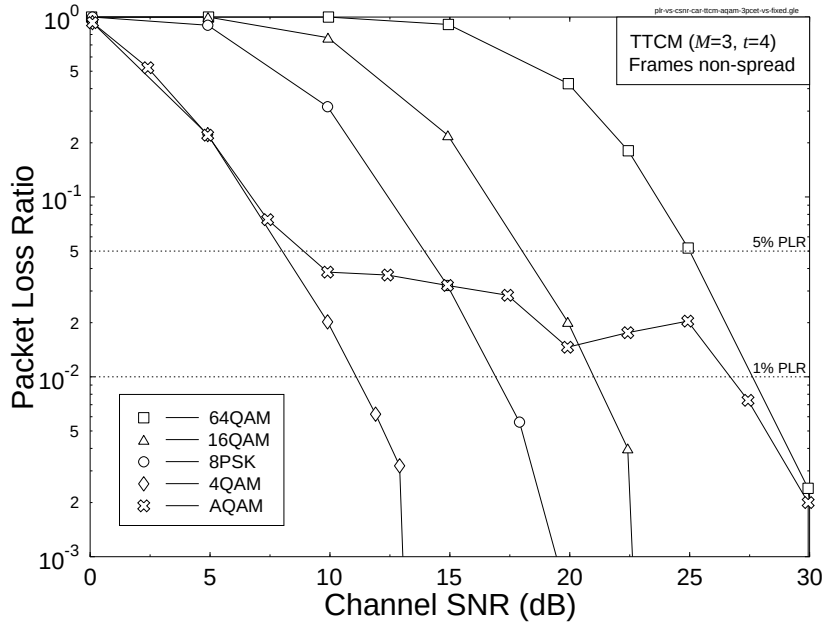

Figure 12.47: Packet loss ratio versus channel SNR for the four fixed TTCM modes and for the quadruple-mode AQAM scheme using the "normal" thresholds of Table 12.12, employing a code memory of $M = 3$ and $t = 4$ iterations when communicating over the COST 207 channel [407].

practical one-frame delay AQAM can achieve a performance that is closer to that of the ideal zero-delay AQAM.

Figure 12.49 portrays that the AQAM modem's video performance degrades gracefully, as the channel SNR degrades, while the fixed-mode modems' video performance degrades more rapidly, when the channel SNR becomes insufficient for the reliable operation of the specific modem mode concerned. As we have shown in Figure 12.45, the higher-order modulation modes, which have a higher associated bitrate provide a higher PSNR in an error-free scenario. However, in the presence of channel errors, the channel-induced PSNR drops and the associated perceptual video quality degradations imposed by transmission errors are more dramatic when higher-order modulation modes are employed. Therefore, annoying video artefacts and a low subjective video perception will be observed when employing higher-order modulation modes such as 64QAM during instances of low channel quality. *However, these subjective video quality degradations and the associated artefacts are eliminated by the advocated AQAM/TTCM regime, because it operates as a 'safety-net' mechanism, which drops the instantaneous AQAM/TTCM throughput in an effort to avoid the dramatic PSNR degradations of the fixed modes during instances of low channel quality, instead of dropping the entire received packet.*

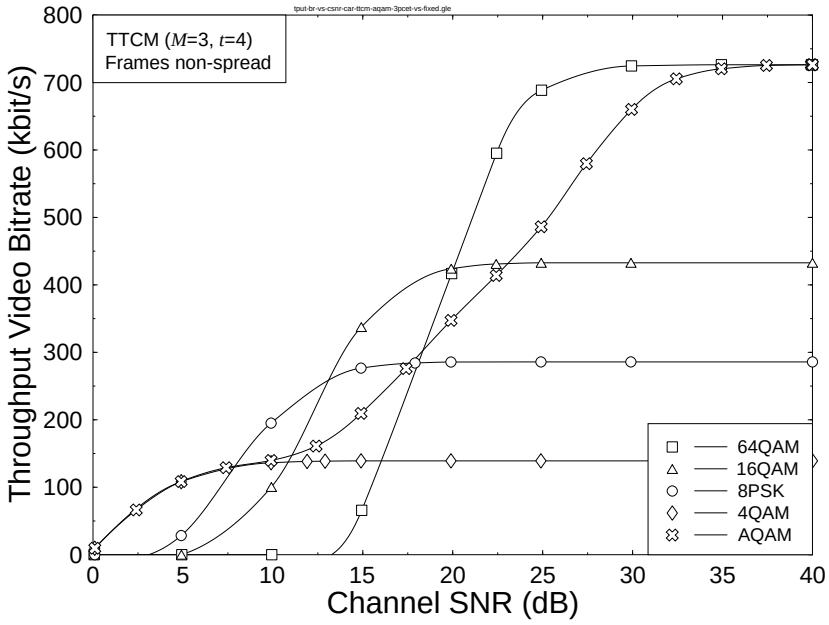

Figure 12.48: Throughput video bitrate versus channel SNR for the four fixed-modes and for the quadruple-mode TTCM AQAM scheme using the "normal" thresholds of Table 12.12, employing a code memory of $M = 3$ and $t = 4$ iterations when communicating over the COST 207 channel [407].

12.4.4.2 Performance of AQAM Using TTCM, TCC, TCM and BICM

Let us now compare the video performance of the TTCM-aided AQAM video system to that of the TCC-assisted AQAM video system of [448]. The lowest information throughput of the TTCM AQAM scheme was 1 BPS in the 4QAM mode here, while that of the TCC AQAM scheme of [448] was 0.5 BPS in the BPSK mode. Furthermore, the highest information throughput of the TTCM AQAM scheme was 5 BPS in the 64QAM mode here, while that of the TCC AQAM scheme of [448] was 3 BPS on the 64QAM mode. Hence we can see from Figure 12.48 that TTCM has a video bitrate of about 100 kbit/s at SNR = 5 dB and 726 kbit/s at SNR = 35 dB. By contrast, the TCC in Figure 12 of [448] has only a video throughput of 50 kbit/s at SNR = 5 dB and 409 kbit/s at SNR = 35 dB. Hence we may conclude that at the symbol-rate considered the TTCM scheme has substantially increased the achievable effective video bitrate of the TCC scheme having an identical symbol-rate and characterised in [448]. This increased effective video bitrate allows the TTCM scheme to transmit CIF video frames which are four times larger than the QCIF video frames transmitted by the TCC scheme of [448].

Let us now compare the video performance of the TTCM-aided AQAM video system to that of the TCM- and BICM-assisted AQAM video system. As it was shown in Figure 12.44, the TTCM scheme achieved the best PLR performance in a fixed modulation scenario. There-

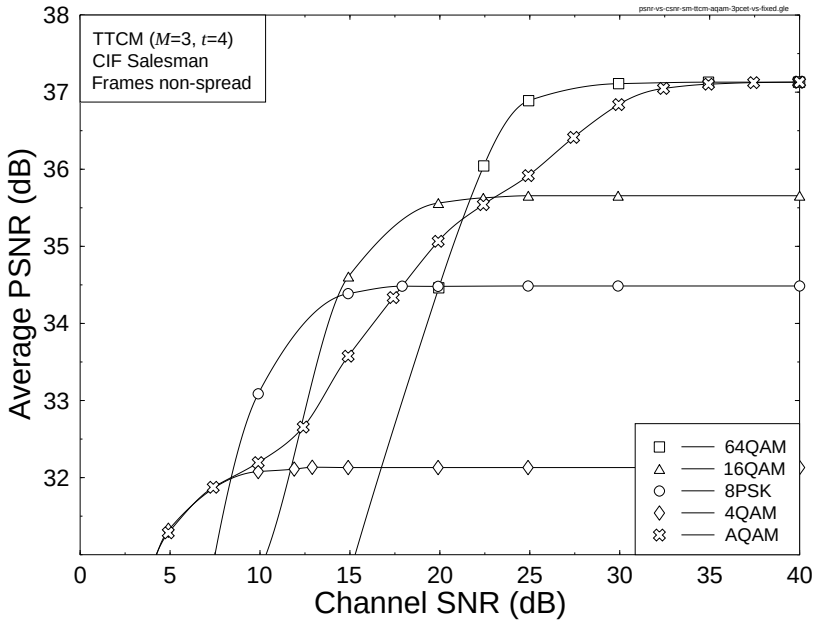

Figure 12.49: Average PSNR versus channel SNR for the four fixed TTCM modes and for the quadruple-mode TTCM AQAM scheme, using the "normal" thresholds of Table 12.12, and the CIF "Salesman" video sequence at 30 frame/s. A code memory of $M = 3$ and $t = 4$ iterations were invoked when communicating over the COST 207 channel [407].

fore – according to Table 12.12 – the AQAM switching thresholds of the TTCM scheme can then be set lower, while still achieving the required PLR performance. The lower thresholds imply that higher-order modulation modes can be used at lower channel SNRs, and hence a higher video transmission bitrate is achieved with respect to the other joint coding and modulation schemes. The PSNR video quality is closely related to the video bitrate. As shown in Figure 12.50, the TTCM-based AQAM modem exhibits the highest PSNR video quality followed by the TCM6 scheme having a code memory of $M = 6$, the TCM3 scheme having a code memory of $M = 3$, and finally, the BICM scheme having a code memory of $M = 3$.

As seen in Figure 12.50, the PSNR video performance difference of the BICM scheme compared to that of the TTCM scheme is only about 2 dBs, since the video quality improvement of TTCM is limited by the moderate turbo interleaver length of our BbB AQAM scheme. Therefore, the low complexity TCM3 scheme provides the best compromise in terms of the PSNR video performance and decoding complexity, since the BICM and TCM3 schemes are of similar complexity, but the TCM3 scheme exhibits a better video performance.

12.4.4.3 The Effect of Various AQAM Thresholds

In the previous sections we have studied the performance of AQAM using the switching thresholds of the "normal" scenario. By contrast, in this section we will study the perfor-

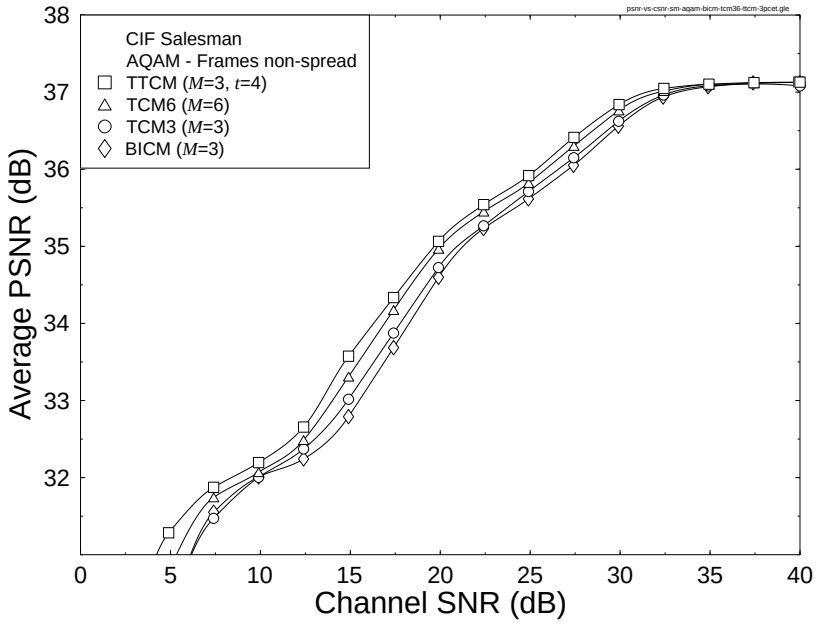

Figure 12.50: Average PSNR versus channel SNR for the quadruple-mode AQAM modems using the four joint coding/modulation schemes considered, namely BICM, TCM3, TCM6, TTCM when communicating over the COST 207 channel [407].

mance of the TTCM-aided AQAM scheme using the switching thresholds of the "conservative", "normal" and "aggressive" scenarios, which were characterised earlier in Table 12.12. Again, the "conservative", "normal" and "aggressive" thresholds sets result in a target PLR of 0.5%, 3% and 20%, respectively.

The three sets of thresholds allowed us to demonstrate, how the performance of the AQAM modem was affected, when the modem used the radio channel more 'aggressively' or more 'conservatively'. This translated in a more and less frequent employment of the higher-throughput, but more error-prone AQAM modes, respectively. Explicitly, the more aggressive switching thresholds provide a higher effective throughput at a cost of a higher PLR. The PSNR versus channel SNR performance of the three AQAM modem switching thresholds is depicted in Figure 12.51, where it is shown that the average PSNR of the AQAM modem employing "aggressive" and "normal" switching thresholds is about 4 and 2 dBs better than that employing "conservative" switching thresholds, respectively, for channel SNRs ranging from 12 to 30 dB. However, in perceptual video quality terms the best compromise was associated with the "normal" switching threshold set. This was, because the excessive PLR of the "aggressive" set inflicted noticeable channel-induced video degradations, despite the favourable video quality of the unimpaired high-throughput video packets.

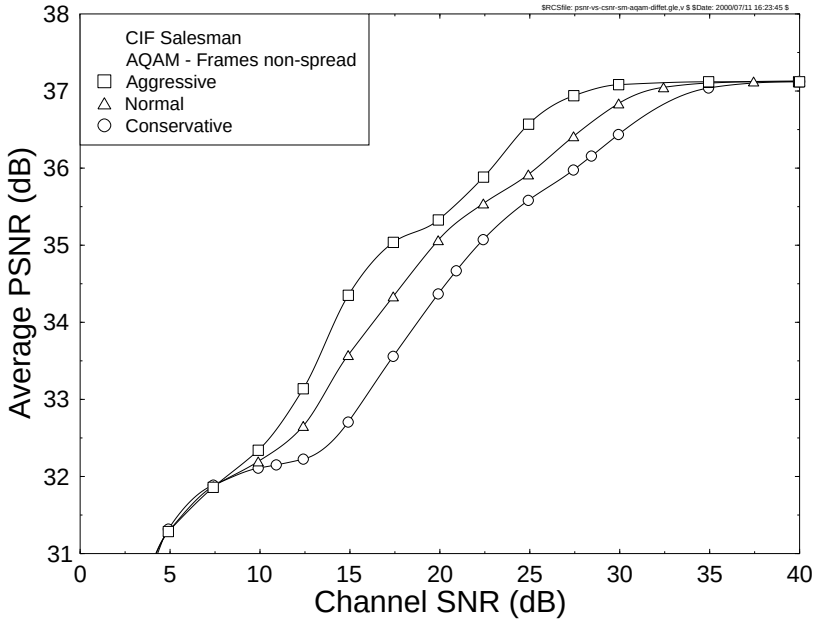

Figure 12.51: Average PSNR video quality versus channel SNR for the quadruple-mode TTCM AQAM scheme using the three different sets of switching thresholds from Table 12.12. TTCM scheme using a code of $M = 3$ and $t = 4$ iterations was used when communicating over the COST 207 channel [407].

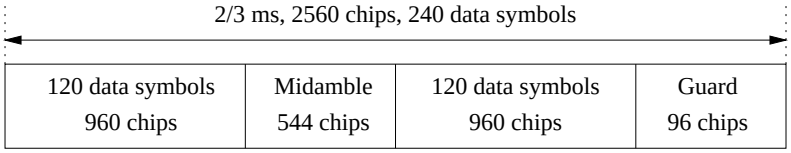

Figure 12.52: A modified UTRA Burst 1 [160] with a spreading factor of 8. The original UTRA burst has 244 data symbols.

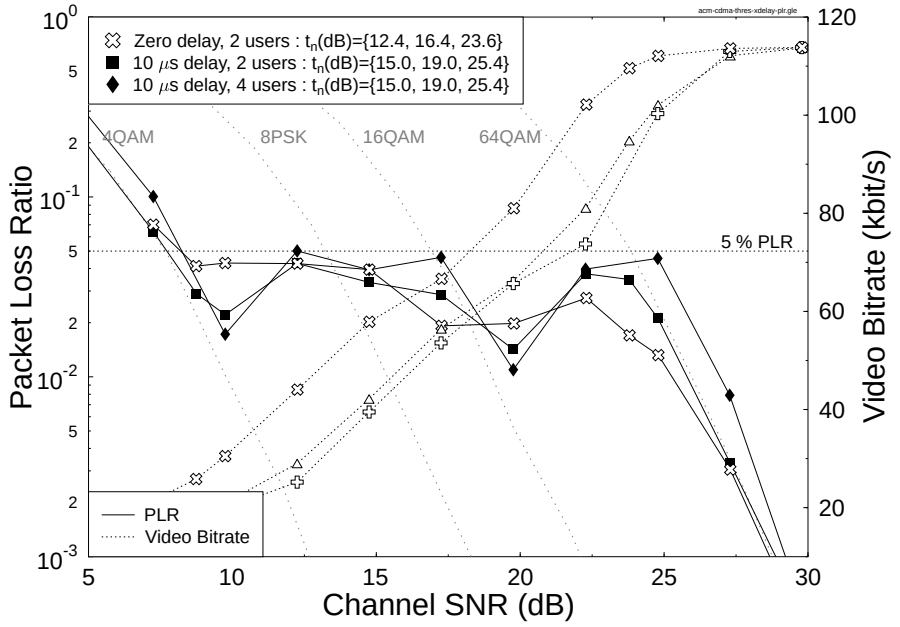

Figure 12.53: PLR and video bitrate versus channel SNR for the four fixed TTCM modes and for the quadruple-mode TTCM AQAM CDMA scheme supporting two and four users transmitting the QCIF video sequence at 30 frame/s, when communicating over the UTRA vehicular channel A [449].

12.4.5 TTCM AQAM in CDMA system

We have demonstrated that the adaptive video system aided by TTCM performs better than that aided by TCC [448], TCM and BICM in a single user scenario. We will now study the performance of the most promising TTCM AQAM scheme in the context of Direct Sequence Code Division Multiple Access (DS-CDMA), when communicating over the UTRA wideband vehicular Rayleigh fading channels [449] and supporting multiple users[9].

In order to mitigate the effects of Multiple Access Interference (MAI) and ISI, while at the same time improving the system's performance by benefiting from the multipath diversity effects of the channels, we employ the MMSE-based Block Decision Feedback Equaliser (MMSE-BDFE) for Joint Detection (JD) [202] in our system. The multiuser JD-MMSE-BDFE receivers are derivatives of the single-user MMSE-DFE [202, 438], where the MAI is equalised as if it was another source of ISI. The interested readers are referred to [202, 438] for a detailed description of the JD-MMSE-BDFE scheme.

In joint detection systems the Signal to Interference plus Noise Ratio (SINR) of each user recorded at the output of the JD-MMSE-BDFE can be calculated by using the channel

[9]**The significance of this research is that although independent adaptive coding and modulation was standardised for employment in the 3G High Speed Data Packet Access mode, this was only proposed for high-latency data transmission. By contrast, here we employ joint adaptive CM in a low-latency, real-time video context.**

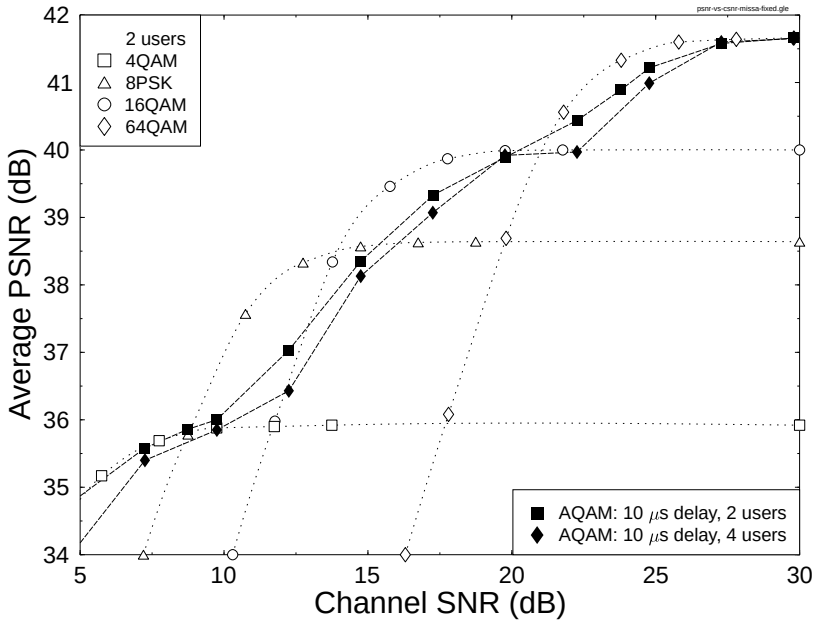

Figure 12.54: Average PSNR versus channel SNR for the four fixed TTCM modes and for the quadruple-mode TTCM AQAM CDMA scheme supporting two and four users transmitting the QCIF video sequence at 30 frame/s, when communicating over the UTRA vehicular channel A [449].

estimates and the spreading sequences of all the users. By assuming that the transmitted data symbols and the noise samples are uncorrelated, the expression used for calculating the SINR γ_o of the n-th symbol transmitted by the k-th user was given by Klein *et al.* [453] as:

$$\begin{aligned} \gamma_o(j) &= \frac{\text{Wanted Signal Power}}{\text{Res. MAI and ISI Power + Eff. Noise Power}} \\ &= g_j^2[\mathbf{D}]_{j,j}^2 - 1, \qquad \text{for} \quad j = n + N(k-1), \end{aligned} \tag{12.5}$$

where SINR is the ratio of the wanted signal power to the residual MAI and ISI power plus the effective noise power. The number of users in the system is K and each user transmits N symbols per transmission burst. The matrix $\mathbf{D}$ is a diagonal matrix that is obtained with the aid of the Cholesky decomposition [454] of the matrix used for linear MMSE equalisation of the CDMA system [202, 453]. The notation $[\mathbf{D}]_{j,j}^2$ represents the element in the j-th row and j-th column of the matrix $\mathbf{D}$ and the value g_j is the amplitude of the j-th symbol. The AQAM mode switching mechanism used for the JD-MMSE-BDFE of user k is the same as that of Equation 12.4, where γ_{DFE} of user k was used as the modulation switching metric,

which can be computed from:

$$\gamma_{DFE}(k) = \frac{1}{N} \sum_{n=1}^{N} \gamma_o(j), \quad j = n + N(k-1). \tag{12.6}$$

Again, the log-domain branch metric is computed for the CM trellis decoding scheme using the MMSE-BDFE's symbol estimate by invoking Equation 12.3.

The UTRA channel model and system parameters of the AQAM CDMA scheme are outlined as follows. Table 12.13 shows the modulation and channel parameters employed. The multi-path channel model is characterised by its discretized chip-spaced UTRA vehicular channel A [449]. The transmission burst structure of the modified UTRA Burst 1 [160] using a spreading factor of eight is shown in Figure 12.52. The number of data symbols per JD block is 20, hence the original UTRA Burst 1 was modified to host a burst of 240 data symbols, which is a multiple of 20.

The remaining system parameters are shown in Table 12.14, where there are 15 time slots in one UTRA frame and we assign one slot for one group of CDMA users. More specifically, each CDMA user group employed a similar system configuration, but communicated with the base station employing another one of the 15 different time slots.

Parameter	**Value**
Carrier Frequency	1.9GHz
Vehicular Speed	30mph
Doppler frequency	85Hz
System Baud rate	3.84 MBd
Normalised Doppler frequency	$85/(3.84 \times 10^6) = 2.21 \times 10^{-5}$
Channel type	UMTS Vehicular Channel A [449]
Number of paths in channel	6
Data modulation	Adaptive Coded Modulation (4QAM, 8PSK, 16QAM, 64QAM)
Receiver type	JD-MMSE-BDFE
No. of symbols per JD block	20

Table 12.13: Modulation and channel parameters for CDMA system.

In general, the total number of users supportable by the uplink CDMA system can be increased by using a higher spreading factor at the cost of a reduced throughput, since the system's chip rate was fixed at 3.84×10^6 chip/s, as shown in Table 12.13. Another option for increasing the number of users supported is by assigning more uplink time slots for new groups of users. In our study, we investigate the proposed system using one time slot only. Hence the data symbol rate per slot per user is 24 kBd for a spreading factor of eight. Finally, Table 12.15 shows the operational-mode specific video transceiver parameters for the TTCM AQAM video system, where the effective video bitrate of each user is ranging from 19.8 kbit/s to 113.8 kbit/s. Since the video bitrate is relatively low as a consequence of CDMA spreading, we transmitted 176x144-pixel QCIF resolution video sequences at 30 frames/s based on the H.263 video codec [160].

Features	**Value**
Multiple access	CDMA, TDD
No. of Slots/Frame	15
Spreading factor, Q	8
Frame length	10ms
Slot length	2/3ms
Data Symbols/Slot/User	240
No. of Slot/User group	1
User Data Symbol Rate (kBd)	240/10 = 24
System Data Symbol Rate (kBd)	24x15 = 360
Chips/Slot	2560
Chips/Frame	2560x15=38400
User Chip Rate (kBd)	2560/10 = 256
System Chip Rate (MBd)	38.4/10 = 3.84
System Bandwidth (MHz)	3.84 x 3/2 = 5.76
Eff. User Bandwidth (kHz)	5760/15 = 384

Table 12.14: Generic system features of the reconfigurable multi-mode video transceiver, using the spread data burst 1 of UTRA [160, 449] shown in Figure 12.52.

Features	Multi-rate System			
Mode	4QAM	8PSK	16QAM	64QAM
Transmission Symbols	240			
Bits/Symbol	2	3	4	6
Transmission bits	480	720	960	1440
Packet Rate	100/s			
Transmission bitrate (kbit/s)	48	72	96	144
Code Termination Symbols	6			
Data Symbols	234			
Coding Rate	1/2	2/3	3/4	5/6
Information Bits/Symbol	1	2	3	5
Unprotected bits	234	468	708	1170
Unprotected bitrate (kbit/s)	23.4	46.8	70.8	117.0
Video packet CRC (bits)	16			
Feedback protection (bits)	9			
Video packet header (bits)	11	12	12	13
Video bits/packet	198	431	671	1138
Effective Video-rate (kbit/s)	19.8	43.1	67.1	113.8
Video framerate (Hz)	30			

Table 12.15: Operational-mode specific transceiver parameters for TTCM in CDMA system.

12.4.5.1 Performance of TTCM AQAM in CDMA system

The PLR and video bitrate performance of the TTCM AQAM CDMA scheme designed for a target PLR of 5% and for supporting $K = 2$ and 4 users is shown in Figure 12.53. The PLR was below the target value of 5% and the video bitrate improved, as the channel SNR increased. Since we employed switching thresholds which are constant over the SNR range, in the region of SNR=10 dB the PLR followed the trend of 4QAM. Similarly, for SNRs between 17 and 20 dB the PLR-trend of 16QAM was predominantly obeyed. In both of these SNR regions a significantly lower PLR was achieved than the target value. We note, however that it is possible to increase the PLR to the value of the target PLR, in this SNR region for the sake of attaining extra throughput gains by employing a set of switching thresholds, where the thresholds are varied as a function of the SNR [455], but this design option was set aside for further research.

From Figure 12.53 we also notice that the performance difference between the $K = 2$ and 4 user scenarios is only marginal with the advent of the powerful JD-MMSE-BDFE scheme. Specifically, there was only about one dB SNR penalty, when the number of users increased from two to four for the 4QAM and 64QAM modes at both low and high SNRs, respectively. The PLR of the system supporting $K = 4$ users was still below the target PLR, when the switching thresholds derived for $K = 2$ users were employed. In terms of the video bitrate performance, the SNR penalty is less than one dB, when the number of users supported is increased from $K = 2$ to 4 users. Note that the delay spread of the chip-spaced UTRA vehicular channel A [449] is 2.51 μs corresponding to $2.51 \times 3.84 \approx 10$ chip duration for the 3.84 MBd Baud rate of our system, as seen in Table 12.13. Hence the delay spread is longer than the spreading code length ($Q = 8$ chips) used in our system and therefore the resultant ISI in the system is significantly higher, than that of the system employing a higher spreading factor, such as $Q > 10$ chips. These findings illustrated the efficiency of the JD-MMSE-BDFE scheme in combating the high ISI and MAI of the system. More importantly, the employment of the JD-MMSE-BDFE scheme in our system allowed us to generalise our results recorded for the $K = 2$ users scenario to that of a higher number of users, since the performance penalty associated with supporting more users was found marginal.

Let us also investigate the effect of mode signalling delay on the performance of the TTCM AQAM CDMA scheme in Figure 12.53. The performance of the ideal scheme, where the channel quality estimation is perfect without any signalling delay is compared to that of the proposed practical scheme, where the channel quality estimation is imperfect and outdated by the delay of one frame duration of $10\mu s$. For a target PLR of 5%, the ideal scheme exhibited a higher video bitrate than the practical scheme. More specifically, at a target PLR of 5%, about 2.5 dB SNR gain is achieved by the ideal scheme in the SNR region spanning from 8 dB to 27 dB. A channel quality signalling delay of one frame duration certainly represents the worst case scenario. In general, the shorter the signalling delay the better the performance of the adaptive system. Hence the performance of the zero-delay and one-frame delay schemes represent the lower-bound and upper-bound performance, respectively, for practical adaptive systems, although employing the channel-quality prediction schemes of [450, 451] would allow us to approximate the perfect channel estimation scenario.

Let us now evaluate the PSNR performance of the proposed practical TTCM AQAM CDMA scheme. For maintaining a target PLR of 5% in conjunction with an adaptive mode signalling delay of one UTRA frame length of 10 ms, the average PSNR versus channel SNR

performance of the quadruple-mode TTCM AQAM CDMA scheme is shown in Figure 12.54 together with that of the four fixed TTCM modes. As shown in Figure 12.54, the video performance of the TTCM AQAM CDMA scheme supporting $K = 4$ users degrades gracefully from the average PSNR of 41.5 dB to 34.2 dB, as the channel SNR degrades from 30 dB to 5 dB. Hence, an attractive subjective video performance can be obtained in the UTRA environment. Again, the PSNR performance difference between the $K = 2$ and 4 scenario is only marginal with the advent of the powerful JD-MMSE-BDFE scheme invoked [202].

12.4.6 Conclusions

In this section various BbB AQAM TCM, TTCM and BICM based video transceivers have been studied. The near-instantaneously adaptive transceiver is capable of operating in four different modulation modes, namely 4QAM, 8PSK, 16QAM and 64QAM.

The advantage of using CM schemes in our near-instantaneously adaptive transceivers is that when invoking higher-order modulation modes in case of encountering a higher channel quality, the coding rate approaches unity. This allows us to maintain as high a throughput as possible. We found that the TTCM scheme provided the best overall video performance due to its superior PLR performance. However, the lower complexity TCM3 assisted scheme provides the best compromise in terms of the PSNR performance and complexity in comparison to the TTCM, TCM6 and BICM assisted schemes.

The BbB AQAM modem guaranteed the same video performance as the lowest- and highest-order fixed-mode modulation schemes at extremely low and high channel SNRs with a minimal latency. Furthermore, in between these extreme SNRs the effective video bitrate smoothly increased, as the channel SNR increased, whilst maintaining a near-constant PLR. By controlling the AQAM switching thresholds a near-constant PLR can be maintained. We have also compared the performance of the proposed TTCM AQAM scheme to that of the TCC AQAM arrangement characterised in [448] under similar conditions and the TTCM scheme was found to be more advantageous than the TCC scheme of [448] in the context of the adaptive H.263 video system. The best TTCM AQAM arrangement was also studied in the context of a DS-CDMA system by utilising a JD-MMSE-BDFE scheme and promising results were obtained when communicating in the UTRA environment. It was also apparent from this study that, as long as the DFE or the JD-MMSE-BDFE scheme is capable of transforming the wideband Rayleigh fading channel's error statistics into 'AWGN-like' error statistics, the performance trends of the CM schemes observed in AWGN channels will be preserved in the wideband Rayleigh fading channels. Specifically, the TTCM assisted scheme, which is the best performer when communicating over AWGN channels, is also the best performer when communicating over the wideband Rayleigh fading channels, when compared to the schemes assisted by TCC, TCM and BICM. Hence it is shown that by adapting the video rate, channel coding rate and the modulation mode together according to the channel quality, the best possible source-signal representation quality is achieved efficiently in terms of bandwidth and power, on a near-instantaneous basis.

Our future research is focused on employing a similar BbB AQAM philosophy in the context of CDMA systems in conjunction with low density parity check coded modulation and the MPEG4 video codec.

12.5 Turbo-Detected MPEG-4 Video Using Multi-Level Coding, TCM and STTC[10]

12.5.1 Motivation and Background

Trellis Coded Modulation (TCM) [85, 431] constitutes a bandwidth-efficient joint channel coding and modulation scheme, which was originally designed for transmission over Additive White Gaussian Noise (AWGN) channels. By contrast, Bit-Interleaved Coded Modulation (BICM) [432] employing parallel bit-based interleavers was designed for communicating over uncorrelated Rayleigh fading channels. Therefore, TCM outperforms BICM, when communicating over AWGN channels since TCM exhibits a higher Euclidean distance. By contrast, the opposite is true, when communicating over uncorrelated Rayleigh fading channels, since BICM exhibits a higher Hamming distance. Space-Time Trellis Coding (STTC) schemes [456, 457], which employ multiple transmit and receive antennas are capable of providing both spatial diversity gain and coding gain. Note that when the spatial diversity order is sufficiently high, the channel's Rayleigh fading envelope is transformed to a Gaussian-like near-constant envelope. Hence, the benefits of a TCM scheme designed for AWGN channels will be efficiently exploited, when TCM is concatenated with STTC in comparison to BICM [458].

Multi-Level Coding (MLC) schemes [459] have been widely designed for providing unequal error protection capabilities [460]. In this section, we design a twin-class unequal protection MLC scheme by employing two different code-rate maximal minimum distance Non-Systematic Convolutional codes (NSCs) [316, p. 331] or Recursive Systematic Convolutional codes (RSCs) [85, 431] as the constituent codes. More specifically, a stronger NSC/RSC is used for protecting the more sensitive video bits, while a weaker NSC/RSC is employed for protecting the less sensitive video bits. Note that TCM employs a Set Partitioning (SP) based bit mapper [431], where the signal set is split into a number of subsets, such that the minimum Euclidean distance of the signal points in the new subset is increased at every partitioning step. Hence, the NSC/RSC encoded bits which are based on the more sensitive video bits are also mapped to the constellation subsets having the highest minimum Euclidean distance for the sake of further enhanced protection. The TCM and STTC encoders may be viewed as a 'coded mapper' for the unequal protected MLC scheme.

The MPEG-4 standard [24, 461] offers a framework for a whole range of multimedia applications, such as tele-shopping, interactive TV, Internet games or iterative mobile video telephony. *The novel contribution of this section is that the state-of-the-art MPEG-4 video codec was amalgamated with a systematically designed sophisticated turbo transceiver using MLC for providing unequal error protection, TCM for maintaining bandwidth efficiency and STTC for attaining spatial diversity. Extrinsic information was exchanged across three serially concatenated decoder stages and the decoding convergence was studied using novel three-dimensional (3D) non-binary Extrinsic Information Transfer (EXIT) charts [462]. We will refer to this unequal-protection joint MPEG-4 source-coding, channel-coding, modulation and spatial diversity aided turbo-transceiver as the STTC-TCM-2NSC or STTC-TCM-2RSC scheme. We will also investigate the STTC-BICM-2RSC scheme, where BICM is employed as the inner code for the sake of studying the performance difference between BICM and TCM*

[10] Ng, Chung and Hanzo, ©IEE 2005

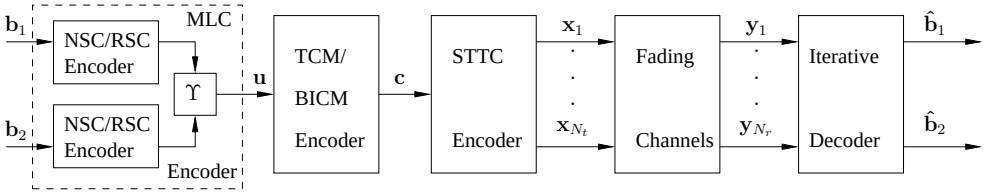

Figure 12.55: Block diagram of the serially concatenated STTC-TCM/BICM-2NSC/2RSC scheme. The notations $\mathbf{b}_i$, $\hat{\mathbf{b}}_\mathbf{i}$, $\mathbf{u}$, $\mathbf{c}$, $\mathbf{x}_j$ and $\mathbf{y}_k$ denote the vectors of the class-i video bits, the estimates of the class-i video bits, the MLC coded symbols, the TCM coded symbols (or BICM coded bits), the STTC coded symbols for transmitter j and the received symbols at receiver k, respectively. Furthermore, Υ is a bit-to-symbol converter, while N_t and N_r denote the number of transmitters and receivers, respectively. The symbol-based (or bit-based) channel interleaver between the STTC and TCM (or BICM) schemes as well as the two bit-based interleavers at the output of NSC/RSC encoders are not shown for simplicity. The iterative decoder seen at the right is detailed in Figure 12.56.

as the inner code in the STTC-based unequal-protection turbo transceiver. it is shown that significant iteration gains are attained with the aid of an efficient iterative decoding mechanism.

The rest of the section is structured as follows. In Section 12.5.2 we describe the proposed system's architecture and highlight the interactions of its constituent elements. The achievable channel capacity of the scheme is studied in Section 12.5.3, while the convergence of the iterative receiver is investigated in Section 12.5.4. We elaborate further by characterising the achievable system performance in Section 12.5.5 and conclude with a range of system design guideline in Section 12.5.6.

12.5.2 The Turbo Transceiver

The schematic of the serially concatenated STTC-TCM/BICM-2NSC/2RSC turbo scheme using a STTC, a TCM/BICM and two NSCs/RSCs as its constituent codes is depicted in Figure 12.55. The MPEG-4 codec operated at R_f=30 frames per second using the (176×144)-pixel Quarter Common Intermediate Format (QCIF) Miss America video sequence, encoded at a near-constant bitrate of R_b=69 kbps. Hence, we have $R_b/R_f = 2300$ bits per video frame. We partition the video bits into two unequal-protection classes. Specifically, class-1 and class-2 consist of 25% (which is 575 bits) and 75% (which is 1725 bits) of the total number of video bits. The more sensitive video bits constituted mainly by the MPEG-4 framing and synchronisation bits are in class-1 and they are protected by a stronger binary NSC/RSC having a coding rate of $R_1 = k_1/n_1 = 1/2$ and a code memory of $L_1 = 3$. The less sensitive video bits – predominantly signalling the MPEG-4 Discrete Cosine Transform (DCT) coefficients and motion vectors – are in class-2 and they are protected by a weaker non-binary NSC/RSC having a coding rate of $R_2 = k_2/n_2 = 3/4$ and a code memory of $L_2 = 3$. Hence, the effective code rate for the MLC scheme employing the $R_1 = 1/2$ and $R_2 = 3/4$ NSCs/RSCs is given by $R_{MLC} = (k_1 + k_2)/(n_1 + n_2) = 2/3$. Note that the number of MPEG-4 framing and synchronisation bits is only about 10% of the total number of video bits. Hence, about 25%-10%=15% of the class-1 bits are constituted by the video bits sig-

nalling the most sensitive MPEG-4 DCT coefficients. We invoke code termination bits in both NSCs/RSCs and hence the number of coded bits emerging from the $R_1 = 1/2$ binary NSC/RSC encoder is $(575 + k_1 L_1)/R_1 = 1156$ bits, while that generated by the $R_2 = 3/4$ non-binary NSC/RSC encoder is $(1725 + k_2 L_2)/R_1 = 2312$ bits.

The class-1 and class-2 NSC/RSC coded bit sequences seen in Figure 12.55 are interleaved by two separate bit interleavers of length 1156 and 2312 bits, respectively. The two interleaved bit sequences are then concatenated to form a bit sequence of $1156 + 2312 = 3468$ bits. This bit sequence is then fed to the TCM/BICM encoder of Figure 12.55 having a coding rate of $R_3 = k_3/n_3 = 3/4$ and a code memory of $L_4 = 3$. When the SP-based TCM is employed, the Most Significant Bit (MSB) of the three-bit input symbol in the rate-3/4 TCM encoder has a higher protection. Therefore, we map the interleaved bit sequence of the class-1 NSC/RSC encoder to the MSB of the TCM scheme's three-bit input symbol for the sake of further protecting the class-1 video bits. Hence the MLC encoder of Figure 12.55, which consists of two NSC/RSC encoders, can be viewed as a non-binary outer encoder providing 3-bit MLC symbols, denoted as $\mathbf{u}$ in Figure 12.55, for the rate-3/4 TCM/BICM encoder. We employ code termination also in the TCM/BICM scheme and hence at the TCM/BICM encoder's output we have $(3468 + k_3 L_3)/R_3 = 4636$ bits or 4636/4=1159 symbols. The TCM symbol sequence (or BICM bit sequence) is then symbol-interleaved (or bit-interleaved) in Figure 12.55 and fed to the STTC encoder. We invoke a 16-state STTC scheme having a code memory of $L_4 = 4$ and $N_t = 2$ transmit antennas, employing $M = 16$-level Quadrature Amplitude Modulation (16QAM). We terminate the STTC code by a 4-bit 16QAM symbol, since we have $N_t = 2$. Therefore, at each transmit antenna we have $1159 + 1 = 1160$ 16QAM symbols or $4 \times 1160 = 4640$ bits in a transmission frame. The overall coding rate is given by $R = 2300/4640 = 0.496$ and the effective throughput of the system is $\log_2(M)R = 1.98$ Bits Per Symbol (BPS). The STTC decoder employed $N_r = 2$ receive antennas and the received signals are fed to the iterative decoders for the sake of estimating the video bit sequences in both class-1 and class-2, as seen in Figure 12.55.

12.5.2.1 Turbo Decoding

The STTC-TCM-2RSC scheme's turbo decoder structure is illustrated in Figure 12.56, where there are four constituent decoders, each labelled with a round-bracketed index. Symbol-based and bit-based MAP algorithms [85] operating in the logarithmic-domain are employed by the TCM as well as the rate $R_2 = 3/4$ RSC decoders and by the $R_1 = 1/2$ RSC decoder, respectively. The notations $P(.)$ and $L(.)$ in Figure 12.56 denote the logarithmic-domain symbol probabilities and the Logarithmic-Likelihood Ratio (LLR) of the bit probabilities, respectively. The notations c, u and b_i in the round brackets $(.)$ in Figure 12.56 denote TCM coded symbols, TCM information symbols and the class-i video bits, respectively. The specific nature of the probabilities and LLRs is represented by the subscripts a, p, e and i, which denote in Figure 12.56 $a\ priori$, $a\ posteriori$, $extrinsic$ and $intrinsic$ information, respectively. The probabilities and LLRs associated with one of the four constituent decoders having a label of $\{1, 2, 3a, 3b\}$ are differentiated by the identical superscripts of $\{1, 2, 3a, 3b\}$. Note that the superscript 3 is used for representing the MLC decoder of Figure 12.56 which invokes the RSC decoders of $3a$ and $3b$.

As we can observe from Figure 12.56, the STTC decoder of block (1) benefits from the $a\ priori$ information provided by the TCM decoder of block (2), namely from $P_a^1(c) =$

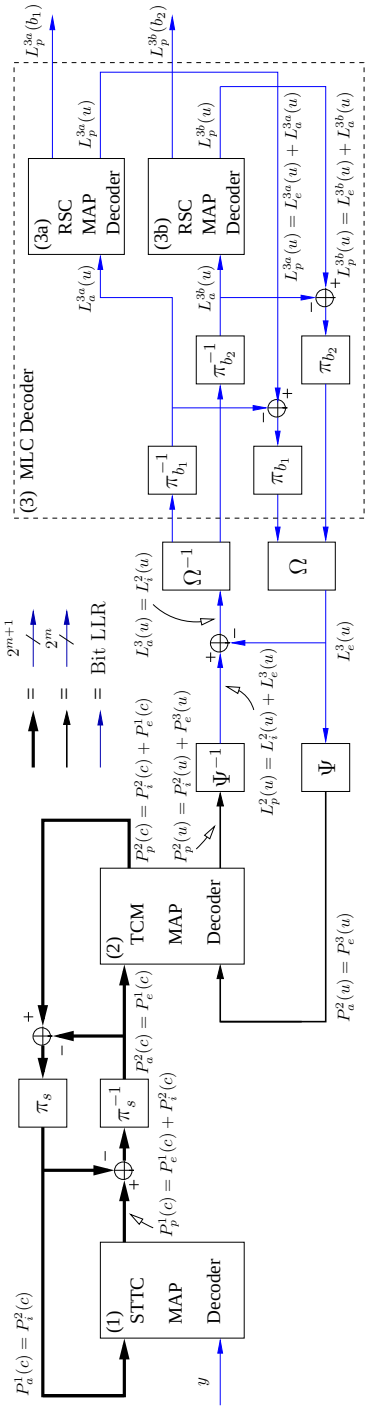

Figure 12.56: Block diagram of the STTC-TCM-2RSC turbo detection scheme. The notations $\pi_{(s,b_i)}$ and $\pi^{-1}_{(s,b_i)}$ denote the interleaver and deinterleaver, while the subscript s denotes the symbol-based interleaver of TCM and the subscript b_i denotes the bit-based interleaver for class-i RSC. Furthermore, Ψ and Ψ^{-1} denote LLR-to-symbol probability and symbol probability-to-LLR conversion, while Ω and Ω^{-1} denote the parallel-to-serial and serial-to-parallel converter, respectively. The notation m denotes the number of information bits per TCM coded symbol. The thickness of the connecting lines indicates the number of non-binary symbol probabilities spanning from a single LLR per bit to 2^m and 2^{m+1} probabilities.

$P_i^2(c)$ regarding the 2^{m+1}-ary TCM coded symbols, where m is the number of information bits per TCM coded symbol. More specifically, $P_i^2(c)$ is referred to here as the intrinsic probability of the 2^{m+1}-ary TCM coded symbols, because it contains the inseparable extrinsic information provided by the TCM decoder itself as well as the $a\ priori$ information regarding the uncoded 2^m-ary TCM input information symbols emerging from the RSC decoders of block (3), namely $P_a^2(u) = P_e^3(u)$. Hence, the STTC decoder indirectly also benefits from the $a\ priori$ information $P_a^2(u) = P_e^3(u)$ provided by the RSC decoders of block (3), potentially enhanced by the TCM decoder of block (2). Similarly, the intrinsic probability of $P_i^2(u)$ provided by the TCM decoder for the sake of the RSC decoders' benefit consists of the inseparable extrinsic information generated by the TCM decoder itself as well as of the systematic information of the STTC decoder, namely $P_a^2(c) = P_e^1(c)$. Note that after the symbol probability-to-LLR conversion, $P_i^2(u)$ becomes $L_i^2(u)$. Therefore, the RSC decoders of block (3) benefit directly from the $a\ priori$ information provided by the TCM decoder of block (2), namely from $L_a^3(u) = L_i^2(u)$ as well as indirectly from the $a\ priori$ information provided by the STTC decoder of block (1), namely from $P_a^2(c) = P_e^1(c)$. On the other hand, the TCM decoder benefits directly from the STTC and RSC decoders through the $a\ priori$ information of $P_a^2(c) = P_e^1(c)$ and $P_a^2(u) = P_e^3(u)$, respectively, as shown in Figure 12.56.

12.5.2.2 Turbo Benchmark Scheme

For the sake of benchmarking the scheme advocated, we created a powerful benchmark scheme by replacing the TCM/BICM and NSC/RSC encoders of Figure 12.55 by a single NSC codec having a coding rate of $R_0 = k_0/n_0 = 1/2$ and a code memory of $L_0 = 6$. We will refer to this benchmark scheme as the STTC-NSC arrangement. All video bits are equally protected in the benchmark scheme by a single NSC encoder and a STTC encoder. A bit-based channel interleaver is inserted between the NSC encoder and STTC encoder. Taking into account the bits required for code termination, the number of output bits of the NSC encoder is $(2300 + k_0 L_0)/R_0 = 4612$, which corresponds to 1153 16QAM symbols. Again, a 16-state STTC scheme having $N_t = 2$ transmit antennas is employed. After code termination, we have $1153 + 1 = 1154$ 16QAM symbols or $4(1154) = 4616$ bits in a transmission frame at each transmit antenna. Similar to the STTC-TCM/BICM-2NSC/2RSC scheme, the overall coding rate is given by $R = 2300/4616 = 0.498$ and the effective throughput is $\log_2(16)R = 1.99$ BPS, both of which are close to the corresponding values of the proposed scheme.

Let us define a single decoding iteration for the proposed STTC-TCM/BICM-2NSC/2RSC scheme as a combination of a STTC decoding, a TCM/BICM decoding, a class-1 NSC/RSC decoding and a class-2 NSC/RSC decoding step. Similarly, a decoding iteration of the STTC-NSC benchmark scheme is comprised of a STTC decoding and a NSC decoding step. We will quantify the decoding complexity of the proposed STTC-TCM/BICM-2NSC/2RSC scheme and that of the benchmark scheme using the number of decoding trellis states. The total number of decoding trellis states per iteration of the proposed scheme employing 2 NSC/RSC decoders having a code memory of $L_1 = L_2 = 3$, TCM/BICM having $L_3 = 3$ and STTC having $L_4 = 4$, is $S = 2^{L_1} + 2^{L_2} + 2^{L_3} + 2^{L_4} = 40$. By contrast, the total number of decoding trellis states per iteration for the benchmark scheme having a code memory of $L_0 = 6$ and STTC having $L_4 = 4$, is given by $S = 2^{L_0} + 2^{L_4} = 80$. Therefore, the complexity of the STTC-TCM-2NSC/2RSC scheme having two iterations is equivalent to that of the

benchmark scheme having a single iteration, which corresponds to 80 decoding states.

12.5.3 MIMO Channel Capacity

Let us consider a Multi-Input Multi-Output (MIMO) system employing N_t transmit antennas and N_r transmit antennas. When two-dimensional L-ary PSK/QAM is employed at each transmit antenna, the received signal vector of the MIMO system is given by:

$$\vec{\mathbf{y}} = \mathbf{H}\vec{\mathbf{x}} + \vec{\mathbf{n}} \,, \tag{12.7}$$

where $\vec{\mathbf{y}} = (\mathbf{y}_1, \ldots, \mathbf{y}_{N_r})^T$ is an N_r-element vector of the received signals, $\mathbf{H}$ is an $(N_r \times N_t)$-dimensional channel matrix, $\vec{\mathbf{x}} = (\mathbf{x}_1, \ldots, \mathbf{x}_{N_t})^T$ is an N_t-element vector of the transmitted signals and $\vec{\mathbf{n}} = (\mathbf{n}_1, \ldots, \mathbf{n}_{N_r})^T$ is an N_r-element noise vector, where each elements in $\vec{\mathbf{n}}$ is an AWGN process having a zero mean and a variance of $N_0/2$ per dimension. Note that in a MIMO system there are $M = L^{N_t}$ number of possible L-ary PSK/QAM phasor combinations in the transmitted signal vector $\vec{\mathbf{x}}$. The STTC scheme of [456] designed for attaining transmit diversity may in fact be viewed as a rate-$1/N_t$ channel code, where there are only L^1 legitimate space-time codewords out of the L^{N_t} possible phasor combinations during each transmission period. By contrast, Bell Lab's Layered Space-Time (BLAST) scheme [463] designed for attaining multiplexing gain may be viewed as a rate-1 channel code, where all L^{N_t} phasor combinations are legitimate during each transmission period. Despite having different code rates, both the STTC and BLAST schemes have the same channel capacity.

The conditional probability of receiving a signal vector $\vec{\mathbf{y}}$ given that an $M = L^{N_t}$-ary signal vector $\vec{\mathbf{x}}_m$, $m \in \{1, \ldots, M\}$, was transmitted over Rayleigh fading channels is determined by the Probability Density Function (PDF) of the noise, yielding:

$$p(\vec{\mathbf{y}}|\vec{\mathbf{x}}_m) = \frac{1}{\pi N_0} \exp\left(\frac{-||\vec{\mathbf{y}} - \mathbf{H}\vec{\mathbf{x}}_m||^2}{N_0}\right). \tag{12.8}$$

In the context of discrete-amplitude QAM [195] and PSK [464] signals, we encounter a Discrete-Input Continuous-Output Memoryless Channel (DCMC) [464]. We derived the channel capacity for a MIMO system, which uses two-dimensional M-ary signalling over the DCMC, from that of the Discrete Memoryless Channel (DMC) [465] as:

$$C_{\text{DCMC}} = \max_{p(\vec{\mathbf{x}}_1)\ldots p(\vec{\mathbf{x}}_M)} \sum_{m=1}^{M} \int_{-\infty}^{\infty} p(\vec{\mathbf{y}}|\vec{\mathbf{x}}_m) p(\vec{\mathbf{x}}_m) \log_2 \left(\frac{p(\vec{\mathbf{y}}|\vec{\mathbf{x}}_m)}{\sum_{n=1}^{M} p(\vec{\mathbf{y}}|\vec{\mathbf{x}}_n) p(\vec{\mathbf{x}}_n)}\right) d\vec{\mathbf{y}} \text{ [bit/sym]}, \tag{12.9}$$

where $p(\mathbf{x}_m)$ is the probability of occurrence for the transmitted signal $\mathbf{x}_m$. It was shown in [465, p. 94] that for a symmetric DMC, the full capacity may only be achieved by using equiprobable inputs. Hence, the right hand side of Equation (12.9), which represents the mutual information between $\vec{\mathbf{x}}$ and $\vec{\mathbf{y}}$, is maximised, when the transmitted symbols are equiprobably distributed, i.e. when we have $p(\vec{\mathbf{x}}_m) = 1/M$ for $m \in \{1, \ldots, M\}$. Hence, by using $p(\vec{\mathbf{x}}_m) = 1/M$ and after a range of mathematical manipulations, Equation (12.9) can be simplified to:

$$C_{\text{DCMC}} = \log_2(M) - \frac{1}{M} \sum_{m=1}^{M} E\left[\log_2 \sum_{n=1}^{M} \exp(\Phi_{m,n}) \,\middle|\, \vec{\mathbf{x}}_m\right] \text{ [bit/sym]}, \tag{12.10}$$

where $E[f(\vec{\mathbf{y}}|\vec{\mathbf{x}}_m)|\vec{\mathbf{x}}_m] = \int_{-\infty}^{\infty} f(\vec{\mathbf{y}}|\vec{\mathbf{x}}_m)p(\vec{\mathbf{y}}|\vec{\mathbf{x}}_m)d\vec{\mathbf{y}}$ is the expectation of the function $f(\vec{\mathbf{y}}|\vec{\mathbf{x}}_m)$ conditioned on $\vec{\mathbf{x}}_m$. The expectation in Equation (12.10) is taken over $\mathbf{H}$ and $\vec{\mathbf{n}}$, while $\Phi_{m,n}$ is given by:

$$\begin{aligned}\Phi_{m,n} &= \frac{-||\mathbf{H}(\vec{\mathbf{x}}_m - \vec{\mathbf{x}}_n) + \vec{\mathbf{n}}||^2 + ||\vec{\mathbf{n}}||^2}{N_0} , \\ &= \sum_{i=1}^{N_r} \frac{-\left|\vec{\mathbf{h}}_i(\vec{\mathbf{x}}_m - \vec{\mathbf{x}}_n) + \mathbf{n}_i\right|^2 + |\mathbf{n}_i|^2}{N_0}, \end{aligned} \tag{12.11}$$

where $\vec{\mathbf{h}}_i$ is the ith row of $\mathbf{H}$ and $\mathbf{n}_i$ is the AWGN at the ith receiver.

When the channel input is a continuous-amplitude, discrete-time Gaussian-distributed signal, we encounter a Continuous-Input Continuous-Output Memoryless Channel (CCMC) [464], where the capacity is only restricted either by the signalling energy or by the bandwidth. It was shown in [466, 467] that the MIMO capacity of the CCMC can be expressed as:

$$C_{\text{CCMC}} = E\left[WT\sum_{i=1}^{r}\log_2\left(1+\lambda_i\frac{SNR}{N_t}\right)\right] , \tag{12.12}$$

where W is the bandwidth and T is the signalling period of the finite-energy signalling waveform and r is the rank of $\mathbf{Q}$, which is defined as $\mathbf{Q} = \mathbf{H}^H\mathbf{H}$ for $N_r \geq N_t$ or $\mathbf{Q} = \mathbf{H}\mathbf{H}^H$ for $N_r < N_t$. Furthermore, λ_i is the ith eigenvalue of the matrix $\mathbf{Q}$.

However, for the special case of an orthogonal MIMO transmission system, such as the orthogonal Space Time Block Coding (STBC) scheme of [468, 469], the received signal in Equation 12.7 can be transformed into [470]:

$$\mathbf{y}_i = \sum_{j=1}^{N_t}|\mathbf{h}_{i,j}|^2\mathbf{x} + \mathbf{\Omega}_i = \chi^2_{2N_t,i}\mathbf{x} + \mathbf{\Omega}_i \ , \ i = \{1,\ldots,N_r\} , \tag{12.13}$$

where $\mathbf{y}_i$ is the received signal at receiver i in the received signal vector $\vec{\mathbf{y}}$ and $\mathbf{x}$ is the complex-valued (two-dimensional) transmitted signal, $\mathbf{h}_{i,j}$ is the complex-valued Rayleigh fading coefficient between transmitter j and receiver i, $\chi^2_{2N_t,i} = \sum_{j=1}^{N_t}|\mathbf{h}_{i,j}|^2$ represents a chi-squared distributed random variable having $2N_t$ degree of freedom at receiver i and $\mathbf{\Omega}_i$ is the ith receiver's complex-valued AWGN after transformation, which has a zero mean and a variance of $\chi^2_{2N_t,i}N_0/2$ per dimension. Due to orthogonal transmissions, the MIMO channel was transformed into a Single-Input Multi-Output (SIMO) channel, where the equivalent Rayleigh fading coefficient between the transmitter and the ith receiver is given by $\chi^2_{2N_t,i}$ and the equivalent noise at the ith receiver is given by $\mathbf{\Omega}_i$. Since the MIMO channel has now been transformed into a SIMO channel, we have $M = L^1 = L$, since there is only a single transmit antenna in a SIMO scheme. The channel capacity of STBC can be shown to be:

$$C^{\text{STBC}}_{\text{DCMC}} = \log_2(M) - \frac{1}{M}\sum_{m=1}^{M} E\left[\log_2\sum_{n=1}^{M}\exp(\Phi^{\text{STBC}}_{m,n}) \,\middle|\, \mathbf{x}_m\right] \text{ [bit/sym]}, \tag{12.14}$$

where the expectation in Equation (12.14) is taken over $\chi^2_{2N_t,i}$ and $\mathbf{\Omega}_i$, while $\Phi^{\text{STBC}}_{m,n}$ is given by:

$$\Phi^{\text{STBC}}_{m,n} = \sum_{i=1}^{N_r} \frac{-|\chi^2_{2N_t,i}(\mathbf{x}_m - \mathbf{x}_n) + \mathbf{\Omega}_i|^2 + |\mathbf{\Omega}_i|^2}{\chi^2_{2N_t,i} N_0}. \tag{12.15}$$

Furthermore, the CCMC capacity for STBC can be shown to be:

$$C^{\text{STBC}}_{\text{CCMC}} = E\left[WT \log_2(1 + \sum_{i=1}^{N_r} \chi^2_{2N_t,i} \frac{SNR}{N_t})\right] \text{ [bit/sym]}. \tag{12.16}$$

Figure 12.57 shows the MIMO channel capacity limit of STTC and STBC schemes employing 16QAM and $N_t = N_r = 2$.

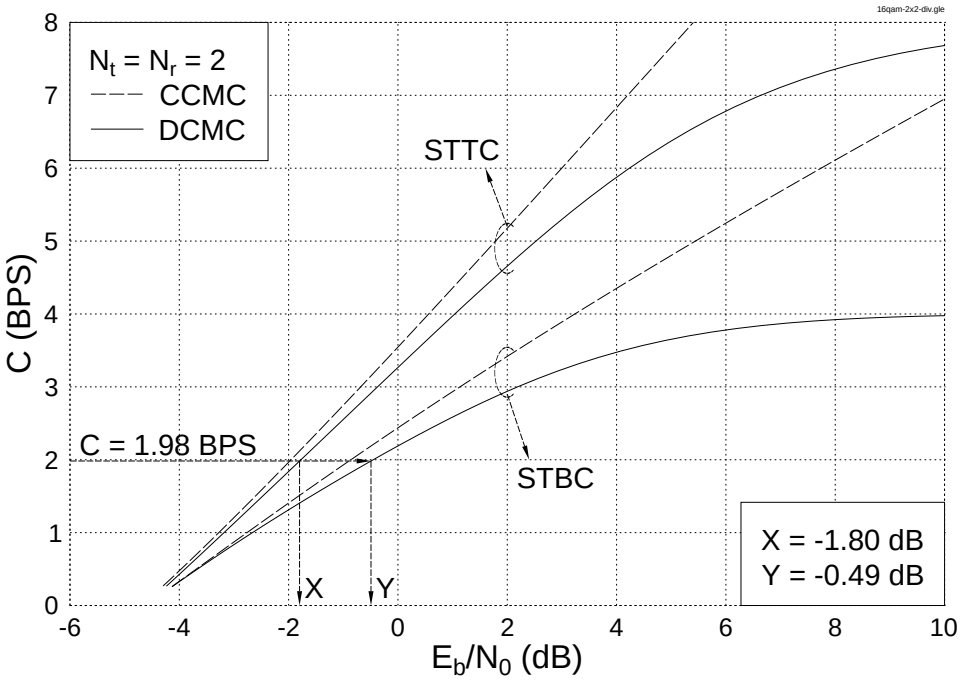

Figure 12.57: The MIMO channel capacity limit for STTC and STBC schemes employing 16QAM and $N_t = N_r = 2$.

As we can see from Figure 12.57, the channel capacity of STBC is lower than that of STTC due to employing orthogonal transmissions. Note that STBC achieves only diversity gain but no coding gain. However, the coding gain of STTC is achieved at the cost of a higher trellis-based decoding complexity. The MIMO channel capacity limit of STTC determined from Equation 12.10 at a throughput of 1.98 BPS and 1.99 BPS is E_b/N_0=-1.80 dB and -1.79 dB, respectively. The corresponding channel capacity limit of STBC evaluated from Equation 12.14 is E_b/N_0=-0.49 dB and -0.47 dB, respectively.

12.5.4 Convergence Analysis

EXIT charts [471] have been widely used for analysing the convergence behaviour of iterative decoding aided concatenated coding schemes. A specific novelty of this section is that we will employ the technique proposed in [462] for computing the *non-binary EXIT functions*, where the multidimensional histogram computation of [472, 473] is replaced by the lower-complexity averaging of the extrinsic symbol probabilities of the MAP decoders. Let us study the convergence of the proposed three-component STTC-TCM-2RSC scheme using 3D EXIT charts [474], when communicating over MIMO Rayleigh fading channels. As we can see from Figure 12.56, the TCM decoder receives inputs from and provides outputs for both the STTC and the MLC decoders of Figure 12.56. Hence we have to compute two EXIT planes, the first one corresponding to the TCM decoder's intrinsic probabilities $P_i^2(c)$ provided for the STTC decoder and the second one corresponding to $P_i^2(u)$ supplied for the MLC decoders, as shown in Figure 12.56. By contrast, the STTC decoder has a single EXIT plane characterising its extrinsic probability $P_e^1(c)$ forwarded to the TCM decoder in Figure 12.56. Similarly, the MLC decoder has one EXIT plane characterising its extrinsic probability $P_e^3(u)$ forwarded to the TCM decoder in Figure 12.56.

Let us denote the average $a\ priori$ information and the average extrinsic (or intrinsic for TCM) information as I_A and I_E, respectively. The I_A (probabilities or LLRs) and I_E (probabilities or LLRs) quantities of TCM corresponding to the links with the STTC and MLC schemes are differentiated by the subscripts 1 and 2, respectively. Similar to computing the conventional EXIT curve in a 2D EXIT chart, we have to model/provide the $a\ priori$ information I_A for each of the inputs of a constituent decoder in order to compute the EXIT plane of that constituent decoder in a 3D EXIT chart. When a long bit interleaver is used between two non-binary constituent decoders, I_A can indeed be sufficiently accurately modelled based on the assumption of having independent bits within the non-binary symbol [471]. More explicitly, for the bit-interleaved decoder, I_A can be computed based on the average mutual information obtained, when Binary Phase Shift Keying (BPSK) modulated signals are transmitted across AWGN channels. To expound further, since the MLC coded bits are bit-interleaved before feeding them to the TCM encoder, we model both the average $a\ priori$ information provided for the TCM decoder, namely I_{A2}(TCM)$= f(P_a^2(u))$ corresponding to the non-binary TCM input symbol, as well as the average $a\ priori$ information generated for the MLC decoder, namely I_A(MLC)$= f(P_i^2(c))$ corresponding to the non-binary MLC coded symbol, where $f(.)$ represents the EXIT function, by assuming that the MLC coded bits in a non-binary MLC coded symbol are independent of each other.

By contrast, the bits in a non-binary coded symbol of a symbol-interleaved concatenated coding scheme are not independent. Hence, for the symbol-interleaved links between the 16QAM-based TCM and STTC scheme, the distribution of the bits in a non-binary coded symbol cannot be sufficiently accurately modelled using independent BPSK modulation. In this scenario, we found that when the average $a\ priori$ information generated for these 4-bit TCM coded symbols is modelled based on the average mutual information obtained when 16QAM modulated signals are transmitted across AWGN channels, a good EXIT plane approximation can be obtained. Note that the average mutual information of 16QAM in AWGN channels is given by the AWGN channel's capacity computed for 16QAM (i.e. the DCMC capacity [195]) provided that all the 16QAM symbols are equiprobable. Therefore, the average $a\ priori$ information provided for the TCM decoder, namely I_{A1}(TCM)$= f(P_a^2(c))$,

and the average $a\ priori$ information for STTC decoder, namely I_A(STTC)$= f(P_a^1(c))$, are generated based on the AWGN channel's capacity determined for 16QAM.

Figures 12.58 and 12.59 illustrate the 3D EXIT charts as well as the iteration trajectories for the proposed STTC-TCM-2RSC scheme at $E_b/N_0 = -0.5$ dB, when an interleaver block length of 10000 16QAM symbols is employed, where E_b/N_0 is the Signal to Noise Ratio (SNR) per information bit.

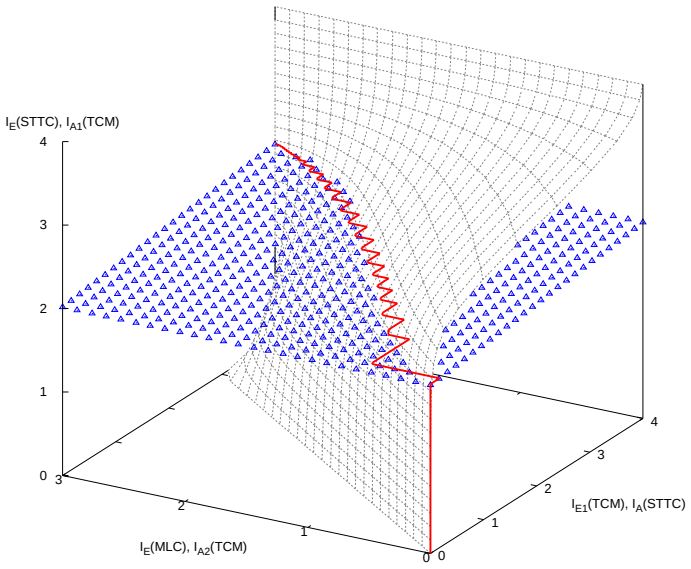

Figure 12.58: The 3D EXIT chart and the iteration trajectory between the STTC and TCM decoders at $E_b/N_0 = -0.5$dB, when a block length of 10000 16QAM symbols is used. The EXIT plane marked with triangles was computed based on the STTC decoder's output $P_e^1(c)$ and the EXIT plane drawn using lines was computed based on the TCM decoder's output $P_i^2(c)$.

Specifically, the EXIT plane marked with triangles in Figure 12.58 was computed based on the STTC decoder's output $P_e^1(c)$ at the given I_E(MLC) and I_A(STTC) abscissa values, while the EXIT plane drawn using lines in Figure 12.58 was computed based on the TCM decoder's output $P_i^2(c)$ at the given I_{A1}(TCM) and I_{A2}(TCM) value. Similarly, the EXIT plane of Figure 12.59 spanning from the vertical line [I_E(MLC)$= 0$, I_A(MLC)$= 0$, I_E(STTC)$= \{0 \rightarrow 4\}$] to the vertical line [I_E(MLC)$= 3$, I_A(MLC)$= 3$, I_E(STTC)$= \{0 \rightarrow 4\}$] was computed based on the MLC decoder's output $P_e^3(c)$ at the given I_E(STTC) and I_A(MLC). The other EXIT plane of Figure 12.59 spanning from the horizontal line [I_{A2}(TCM)$= \{0 \rightarrow 3\}$, I_{E2}(TCM)$= 0$, I_{A1}(TCM)$= 0$] to the horizontal line [I_{A2}(TCM)$= \{0 \rightarrow 3\}$, I_{E2}(TCM)$= 3$, I_{A1}(TCM)$= 4$] was computed based on the TCM decoder's output $P_i^2(u)$ at the given I_{A1}(TCM) and I_{A2}(TCM) values.

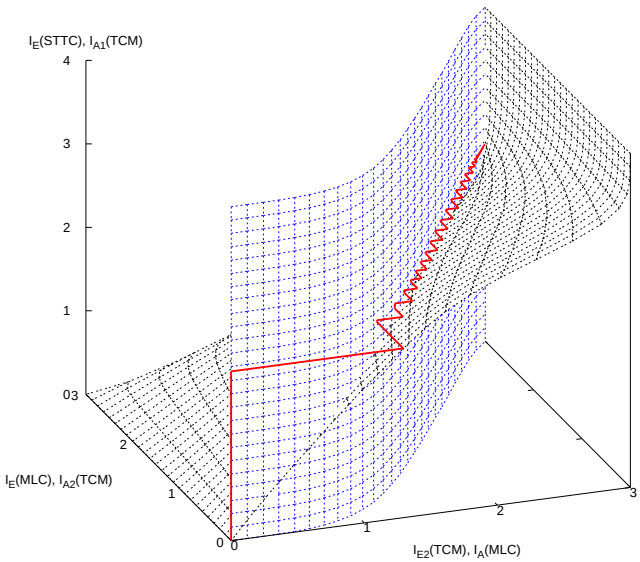

Figure 12.59: The 3D EXIT chart and the iteration trajectory between the TCM and MLC decoders at $E_b/N_0 = -0.5$dB, when a block length of 10000 16QAM symbols is used. The EXIT plane spanning from the vertical line [I_E(MLC)= 0, I_A(MLC)= 0, I_E(STTC)= $\{0 \rightarrow 4\}$] to the vertical line [I_E(MLC)= 3, I_A(MLC)= 3, I_E(STTC)= $\{0 \rightarrow 4\}$] was computed based on the MLC decoder's output $P_e^3(c)$ and the other EXIT plane was computed based on the TCM decoder's output $P_i^2(u)$.

As we can see from Figure 12.58, the iteration trajectory computed based on the average intrinsic information of the TCM decoder's output, namely I_{E1}(TCM)=$f(P_i^2(c))$, is under the STTC-EXIT plane marked with triangles and above the TCM-EXIT plane drawn using lines. Note that the approximated EXIT-planes in Figure 12.58 failed to mimic the exact distribution of the TCM coded symbols, and hence resulted in some overshooting mismatches between the EXIT-planes and the trajectory. However, as seen from Figure 12.59, the mismatch between the EXIT-planes and the trajectory computed based on the average intrinsic information of the TCM decoder's output, namely I_{E2}(TCM)=$f(P_i^2(u))$, is minimal. Explicitly, the trajectory seen in Figure 12.59 is located on the right of the MLC-EXIT plane spanning two vertical lines and on the left of the TCM-EXIT plane spanning two horizontal lines. Note from Figure 12.59 that I_{E2}(TCM) is not strictly monotonically increasing with I_E(STTC), which is in contrast to the bit-interleaved system of [474]. Hence, we cannot combine Figures 12.58 and 12.59 into a single 3D EXIT chart, as it is in [474].

As we can see from Figure 12.58, the STTC-based EXIT plane spans from the horizontal line [I_E(MLC)= $\{0 \rightarrow 3\}$, I_{E1}(TCM)=0, I_E(STTC)=2.0148] to the horizontal line [I_E(MLC)= $\{0 \rightarrow 3\}$, I_{E1}(TCM)=4, I_E(STTC)=2.3493]. Since the STTC decoder was

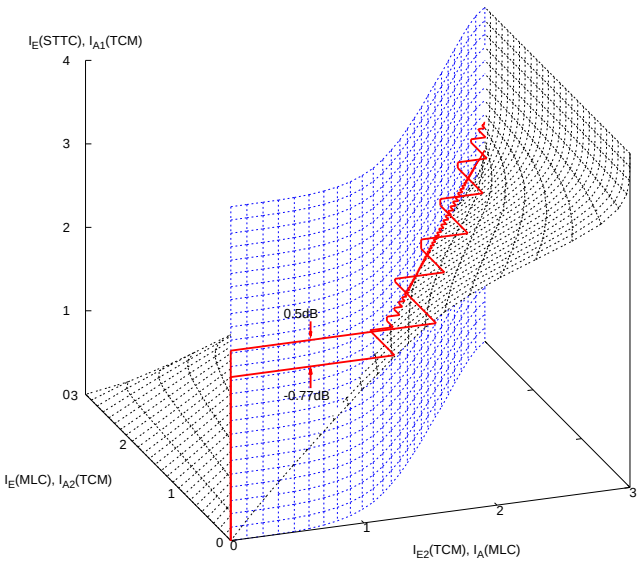

Figure 12.60: The 3D EXIT chart and the iteration trajectory between the TCM and MLC decoders at $E_b/N_0 = -0.77$dB, when a block length of 100000 16QAM symbols is used, as well as at $E_b/N_0 = 0.5$dB, when a block length of 1160 16QAM symbols is used. The EXIT plane spanning from the vertical line [I_E(MLC)= 0, I_A(MLC)= 0, I_E(STTC)= $\{0 \rightarrow 4\}$] to the vertical line [I_E(MLC)= 3, I_A(MLC)= 3, I_E(STTC)= $\{0 \rightarrow 4\}$] was computed based on the MLC decoder's output $P_e^3(c)$ and the other EXIT plane was computed based on the TCM decoder's output $P_i^2(u)$.

unable to converge to the I_E(STTC)=4 position, a two-stage concatenated scheme based on STTC, such as for example the STTC-NSC benchmark scheme, would fail to reach an error free performance at $E_b/N_0 = -0.5$ dB. However, as we can see from Figures 12.58 and 12.59, the TCM decoder's output trajectories converged to the [I_E(MLC)=3, I_{E1}(TCM)=4] and [I_E(MLC)=3, I_{E2}(TCM)=3] positions, respectively. This indicates that an error-free performance can be attained by the three-stage concatenated STTC-TCM-2RSC scheme at $E_b/N_0 = -0.5$ dB , despite employing a poorly converging STTC scheme. As we can observe from Figure 12.59, the intersection of the EXIT planes includes the vertical line at [I_E(MLC)=3, I_{E2}(TCM)=3, I_E(STTC)=$\{1.9 \rightarrow 4\}$], hence the recursive TCM decoder has in fact aided the non-recursive STTC decoder in achieving an early convergence at I_E(STTC)=1.9, rather than only at I_E(STTC)=4, when the STTC-TCM scheme is iteratively exchanging extrinsic information with the MLC decoder. This indicates that when a non-recursive STTC is employed, a three-stage concatenated coding scheme is necessary for approaching the MIMO channel's capacity. Better constituent codes may be designed for the three-stage concatenated coding scheme based on the 3D EXIT chart of Figure 12.59. More

explicitly, good constituent codes would result in two EXIT planes that intersect at as low an I_E(STTC) value in Figure 12.59, as possible. It should be noted however that such schemes may require a high number of iterations, because they may operate between the cut-off-rate and the capacity, which typically imposes a high delay and high complexity.

Figure 12.60 shows that convergence can be achieved at a low SNR value of $E_b/N_0 = -0.77$ dB, when a longer interleaver block length of 100000 16QAM symbols is employed. By contrast, convergence is only achieved at a higher SNR value of $E_b/N_0 = 0.5$ dB, when a shorter interleaver block length of 1160 16QAM symbols is used. Hence, the lower-delay STTC-TCM-2RSC scheme of Section 12.5.2 employing an interleaver length of 1160 16QAM symbols is approximately 2.3 dB away from the STTC channel capacity of -1.80 dB and 0.99 dB from the STBC channel capacity of -0.49 dB at a throughput of 1.98 BPS, according to Figure 12.57. When a longer interleaver delay of 100000 16QAM symbols can be tolerated, the effective throughput becomes approximately 2.00 BPS, since the code rate loss due to termination symbols/bits has been slightly reduced. In this case, the STTC-TCM-2RSC scheme which converged at $E_b/N_0 = -0.77$ dB is only about 1 dB away from the STTC channel capacity of -1.77 dB and it performs 0.32 dB better than the STBC channel capacity of -0.45 dB at a throughput of 2.00 BPS.

12.5.5 Simulation results

We continue our discourse by characterising the attainable performance of the proposed MPEG-4 based video telephone schemes using both the Bit Error Ratio (BER) and the average video Peak Signal to Noise Ratio (PSNR) [4].

Figures 12.61 and 12.62 depict the class-1 and class-2 BER versus E_b/N_0 performance of the 16QAM-based STTC-TCM-2NSC and STTC-TCM-2RSC schemes, respectively, when communicating over uncorrelated Rayleigh fading channels.

Specifically, the class-1 bits benefit from more than an order of magnitude lower BER at a given SNR, than the class-2 bits. Figure 12.63 compares the overall BER performance of the STTC-TCM-2NSC and STTC-TCM-2RSC schemes. More explicitly, the STTC-TCM-2RSC scheme is outperformed by the STTC-TCM-2NSC arrangement, when the number of iterations is lower than eight. At BER=10^{-4} an approximately 4 dB and 6 dB iteration gain was attained by the STTC-TCM-2NSC and STTC-TCM-2RSC schemes, respectively, when the number of iterations was increased from one to eight. Note in Figures 12.62 and 12.63 that the STTC-TCM-2RSC scheme suffers from an error floor, despite having a high iteration gain, which is due to the employment of RSC outer codes instead of the NSC outer codes.

The BER performance curves of STTC-BICM-2RSC and STTC-NSC are shown in Figure 12.64. Note that if we reduce the code memory of the NSC constituent code of the STTC-NSC benchmark scheme from L_0=6 to 3, the best possible performance becomes poorer. If we increased L_0 from 6 to 7 (or higher), the decoding complexity would be significantly increased, while the attainable best possible performance is only marginally improved. Hence, the STTC-NSC scheme having L_0=6 constitutes a powerful benchmark scheme in terms of its performance versus complexity tradeoffs. As observed in Figure 12.64, the performance of the STTC-BICM-2RSC scheme is even worse than that of the STTC-NSC benchmark scheme. More explicitly, STTC-BICM-2RSC employing eight iterations cannot outperform the STTC-NSC arrangement employing two iterations. By changing the outer code to NSC, i.e. using the STTC-BICM-2NSC scheme, the attainable performance cannot be further im-

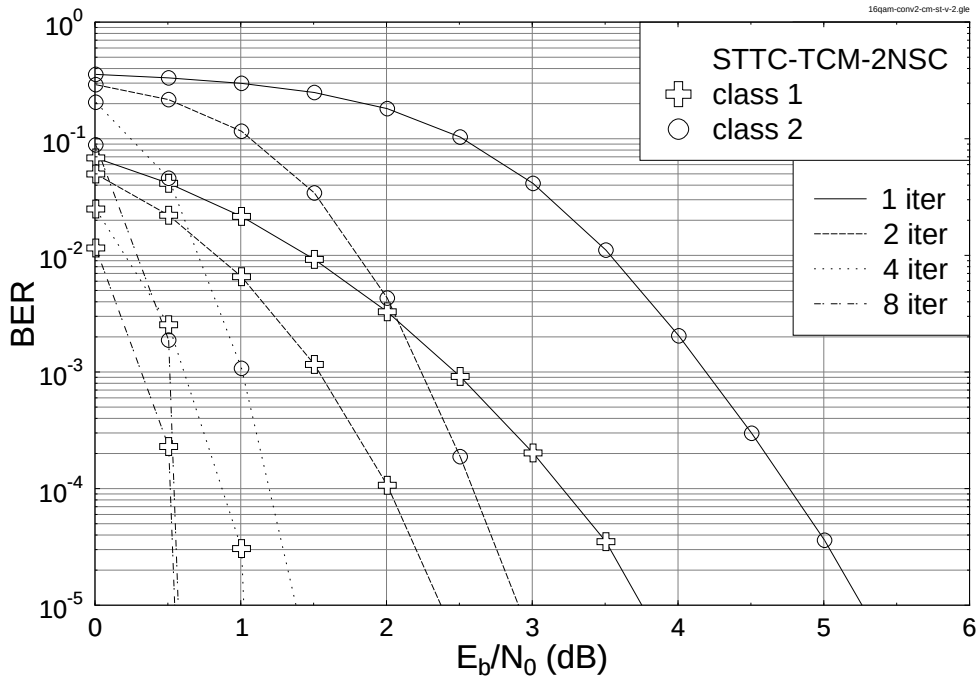

Figure 12.61: BER versus E_b/N_0 performance of the 16QAM-based STTC-TCM-2NSC assisted MPEG-4 scheme, when communicating over uncorrelated Rayleigh fading channels. The effective throughput was **1.98 BPS**.

proved. The complexity of the STTC-TCM-2NSC/2RSC arrangement having four (or eight) iterations corresponds to 160 (or 320) trellis states, which is similar to that of the STTC-NSC scheme having two (or four) iterations. Hence at a complexity of 160 (or 320) trellis states, the E_b/N_0 performance of the STTC-TCM-2NSC (or STTC-TCM-2RSC) scheme is approximately 2 dB (or 2.8 dB) better than that of the STTC-NSC benchmark scheme at BER=10^{-4}.

Let us now consider the PSNR versus E_b/N_0 performance of the systems characterised in Figures 12.65 and 12.66. The PSNR performance trends are similar to our observations made in the context of the achievable BER results. The maximum attainable PSNR is 39.7 dB. Observe in Figure 12.65 that the BER floor of the STTC-TCM-2RSC scheme resulted in a slightly lower maximum attainable PSNR value, when we had $E_b/N_0 < 6$ dB. Furthermore, when employing eight iterations at $E_b/N_0 = 0.5$ dB, the PSNR of STTC-TCM-2RSC was found to be slightly lower than that of the STTC-TCM-2NSC arrangement, although the BER of STTC-TCM-2RSC is significantly lower than that of the STTC-TCM-2NSC scheme, as it is evidenced in Figure 12.63. This is because STTC-TCM-2RSC suffers from a higher transmission frame error ratio, despite having a lower BER, in comparison to the STTC-TCM-2NSC scheme at $E_b/N_0 = 0.5$ dB.

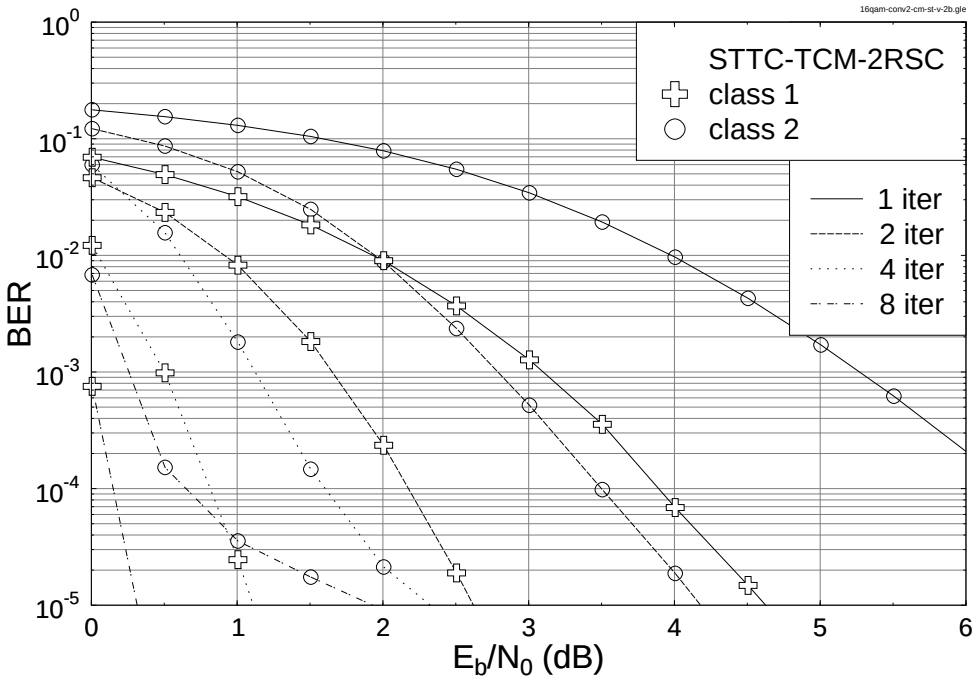

Figure 12.62: BER versus E_b/N_0 performance of the 16QAM-based STTC-TCM-2RSC assisted MPEG-4 scheme, when communicating over uncorrelated Rayleigh fading channels. The effective throughput was **1.98 BPS**.

12.5.6 Conclusions

In conclusion, a jointly optimised source-coding, outer channel-coding, inner coded modulation and spatial diversity aided turbo transceiver was studied and proposed for MPEG-4 wireless video telephony. With the aid of an MLC scheme that consists of two different-rate NSCs/RSCs the video bits were unequally protected according to their sensitivity. The employment of TCM improved the bandwidth efficiency of the system and by utilising STTC spatial diversity was attained. The performance of the proposed STTC-TCM-2NSC/STTC-TCM-2RSC scheme was enhanced with the advent of an efficient iterative decoding structure exchanging extrinsic information across three consecutive blocks. Explicitly, it was shown in Section 12.5.4 that when a non-recursive STTC decoder is employed, a three-stage concatenated iterative decoding scheme is required for approaching the MIMO channel's capacity. It was shown in Figures 12.63 and 12.65 that the STTC-TCM-2RSC scheme required E_b/N_0 = 0.5 dB in order to attain BER=10^{-4} and PSNR > 37 dB, which is 2.3 dB away from the corresponding MIMO channel's capacity. However, if the proposed STTC-TCM-2RSC scheme is used for broadcasting MPEG-4 encoded video, where a longer delay can be tolerated, the required E_b/N_0 value is only 1 dB away from the MIMO channel's capacity, as evidenced by comparing Figures 12.57 and 12.60.

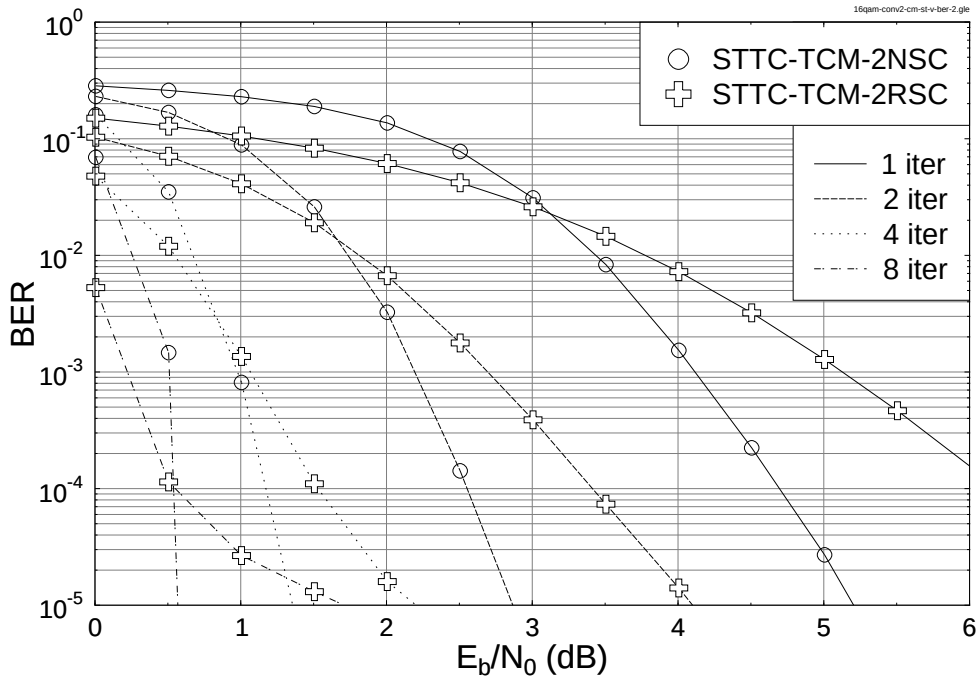

Figure 12.63: BER versus E_b/N_0 performance of the 16QAM-based STTC-TCM-2NSC and STTC-TCM-2RSC assisted MPEG-4 schemes, when communicating over uncorrelated Rayleigh fading channels. The effective throughput was **1.98 BPS**.

12.6 Near-Capacity Irregular Variable Length Codes[11]

12.6.1 Introduction

Irregular Convolutional Coding (IrCC) [475] has been proposed for employment as an outer channel codec in iteratively decoded schemes. This amalgamates a number of component Convolutional Codes (CC) having different coding rates, each of which encodes an appropriately selected fraction of the input bit stream. More specifically, the appropriate fractions may be selected with the aid of EXtrinsic Information Transfer (EXIT) chart analysis [476], in order to shape the inverted EXIT curve of the composite IrCC for ensuring that it does not cross the EXIT curve of the inner codec. In this way, an open EXIT chart tunnel may be created at low E_b/N_0 values, which implies approaching the channel's capacity bound [477]. This was demonstrated for the serial concatenation of IrCCs combined with precoded equalisation in [478], for example.

Similarly to binary Bose-Chaudhuri-Hocquenghem (BCH) codecs [479], the constituent binary CCs [479] of an IrCC codec are unable to exploit the unequal source symbol occurrence probabilities that are typically associated with audio, speech, image and video

[11] R. G. Maunder, J. Wang, S. X. Ng, L-L. Yang and L. Hanzo: On the Performance and Complexity of Irregular Variable Length Codes for Near-Capacity Joint Source and Channel Coding, submitted to IEEE Transactions on Wireless Communications

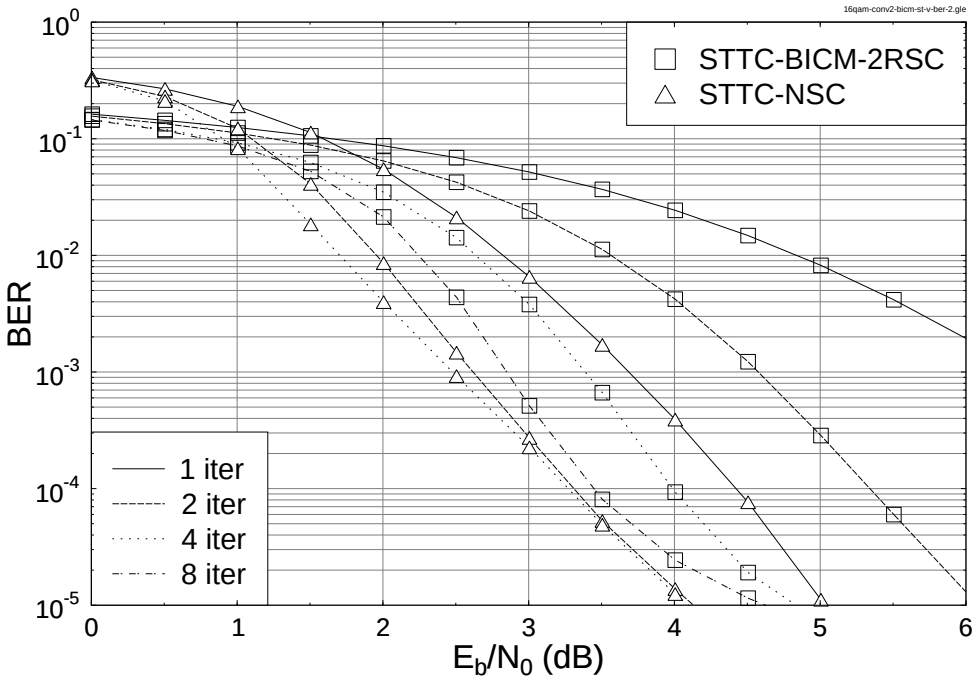

Figure 12.64: BER versus E_b/N_0 performance of the 16QAM-based STTC-BICM-2RSC and STTC-NSC assisted MPEG-4 schemes, when communicating over uncorrelated Rayleigh fading channels. The effective throughput of STTC-BICM-2RSC and STTC-NSC was **1.98 BPS** and **1.99 BPS**, respectively.

sources [391] [160]. Since the exploitation of all available redundancy is required for near-capacity operation [480], typically a Huffman source encoder [481] is employed for removing this redundancy, before channel encoding commences. However, Huffman decoding is very sensitive to bit errors, requiring the low Bit Error Ratio (BER) reconstruction of the Huffman encoded bits in order that a low Symbol Error Ratio (SER) may be achieved [482].

This motivates the application of the Variable Length Error Correction (VLEC) class of Variable Length Codes (VLCs) [482] as an alternative to the Huffman and BCH or CC coding of sequences of source symbols having values with unequal probabilities of occurrence. In VLEC coding, the source symbols are represented by binary codewords of varying lengths. Typically, the more frequently that a particular source symbol value occurs, the shorter its VLEC codeword is, resulting in a reduced average codeword length L. In order that each valid VLEC codeword sequence may be uniquely decoded, a lower bound equal to the source entropy E is imposed upon the average codeword length L. Any discrepancy between L and E is quantified by the coding rate $R = E/L \in [0, 1]$ and may be attributed to the intentional introduction of redundancy into the VLEC codewords. Naturally, this intentionally introduced redundancy imposes code constraints that limit the set of legitimate sequences of VLEC-encoded bits. Like the code constraints of CC and BCH coding [479], the VLC code constraints may be exploited for providing an additional error correcting capability during

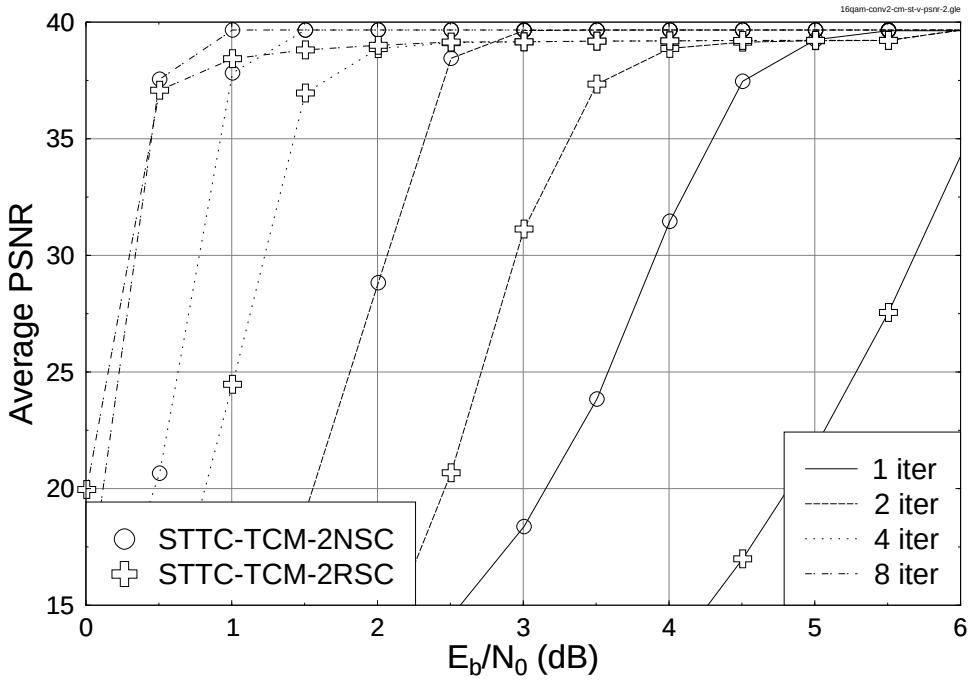

Figure 12.65: Average PSNR versus E_b/N_0 performance of the proposed 16QAM-based STTC-TCM-2NSC and STTC-TCM-2RSC assisted MPEG-4 schemes, when communicating over uncorrelated Rayleigh fading channels. The effective throughput was **1.98 BPS**.

VLEC decoding [482]. Furthermore, *unlike* in CC and BCH decoding [479], any redundancy owing to the unequal occurrence probabilities of the source symbol values may be additionally exploited during VLEC decoding [482].

Depending on the VLEC coding rate, the associated code constraints render VLEC decoding substantially less sensitive to bit errors than Huffman decoding is. Hence, a coding gain of 1 dB at an SER of 10^{-5} has been observed by employing VLEC coding having a particular coding rate instead of a concatenated Huffman and BCH coding scheme having the same coding rate [482].

This motivates the application of the irregular coding concept to VLEC coding for employment in the near-capacity joint source and channel coding of sequences of source symbols having values with unequal occurrence probabilities. More specifically, we employ a novel Irregular Variable Length Coding (IrVLC) scheme as our outer source codec, which we serially concatenate [483] [484] with an inner channel codec for the sake of exchanging extrinsic information. In analogy to IrCC, the proposed IrVLC scheme employs a number of component VLEC codebooks having different coding rates, which are used for encoding appropriately selected fractions of the input source symbol stream. In this way, the resultant composite inverted EXIT curve may be shaped for ensuring that it does not cross the EXIT curve of the inner channel codec.

The rest of this section is outlined as follows. In Section 12.6.2, we propose iteratively de-

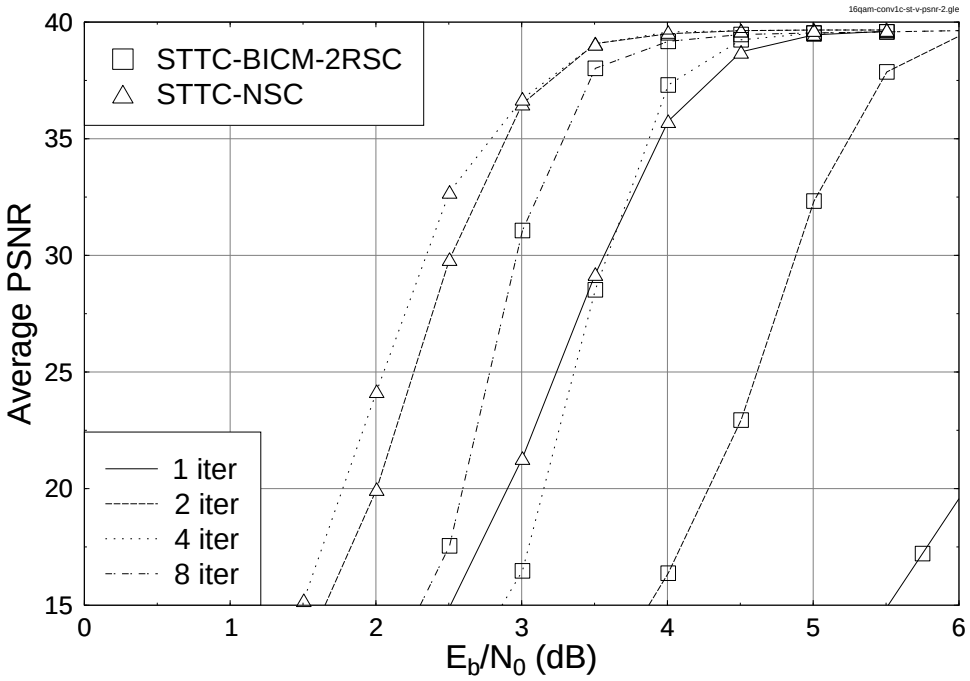

Figure 12.66: Average PSNR versus E_b/N_0 performance of the 16QAM-based STTC-BICM-2RSC and STTC-NSC assisted MPEG-4 benchmark schemes, when communicating over uncorrelated Rayleigh fading channels. The effective throughput of STTC-BICM-2RSC and STTC-NSC was **1.98 BPS** and **1.99 BPS**, respectively.

coded schemes, in which we opt for serially concatenating IrVLC with Trellis Coded Modulation (TCM). Furthermore, Section 12.6.2 additionally introduces our bench-mark schemes, where IrVLC is replaced by regular VLCs having the same coding rate. The design and EXIT chart aided characterisation of these schemes is detailed in Section 12.6.3. In Section 12.6.4, we quantify the attainable performance improvements offered by the proposed IrVLC arrangements compared to the regular VLC bench-marker schemes, as provided in [485]. Furthermore in Section 12.6.4 of this contribution, we additionally consider a Huffman coding and IrCC based bench-marker, as well as presenting significant new results pertaining to the computational complexity of the considered schemes. More specifically, we quantify the computational complexity required for achieving a range of source sample reconstruction qualities at a range of Rayleigh fading channel E_b/N_0 values. Finally, we offer our conclusions in Section 12.6.5.

12.6.2 Overview of Proposed Schemes

In this section we provide an overview of a number of serially concatenated and iteratively decoded joint source and channel coding schemes. Whilst the novel IrVLC scheme introduced in this section may be tailored for operating in conjunction with any inner channel codec, we opt for employing TCM [486] in each of our considered schemes. This provides error

protection without any bandwidth expansion or effective bit-rate reduction by accommodating the additional redundancy by transmitting more bits per channel symbol. The choice of TCM is further justified, since *A Posteriori* Probability (APP) TCM Soft-In Soft-Out (SISO) decoding, similarly to APP SISO IrVLC decoding, operates on the basis of Add-Compare-Select (ACS) operations within a trellis structure. Hence, the APP SISO IrVLC and TCM decoders can share resources in systolic-array based chips, facilitating a cost effective implementation. Furthermore, we will show that TCM exhibits attractive EXIT characteristics in the proposed IrVLC context even without requiring TTCM- or BICM-style internal iterative decoding [479].

Our considered schemes differ in their choice of the outer source codec. Specifically, we consider a novel IrVLC codec and an equivalent regular VLC-based bench-marker in this role. In both cases we employ both Symbol-Based (SB) [487] [488] and Bit-Based (BB) [489] VLC decoding, resulting in a total of four different configurations. We refer to these four schemes as the SBIrVLC-, BBIrVLC-, SBVLC- and BBVLC-TCM arrangements, as appropriate. A schematic that is common to each of these four considered schemes is provided in Figure 12.67.

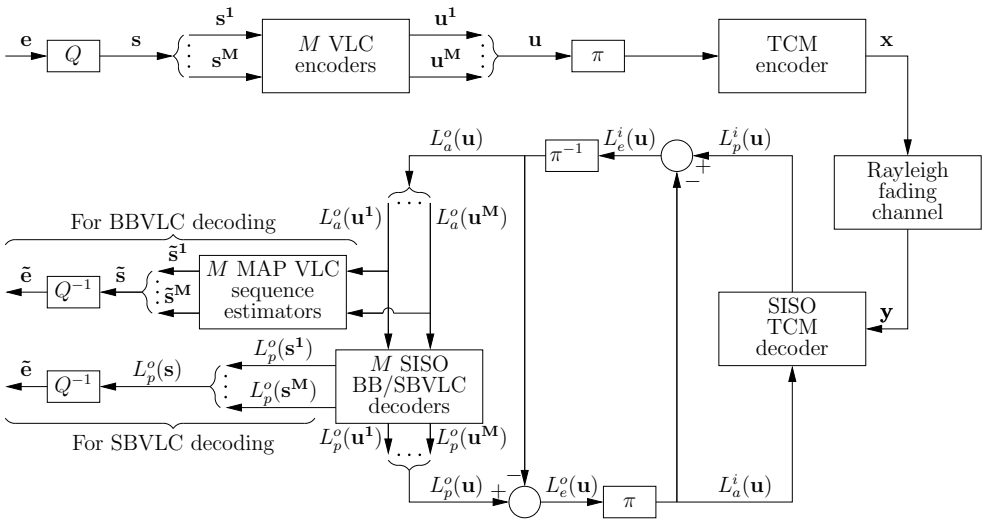

Figure 12.67: Schematic of the SBIrVLC-, BBIrVLC-, SBVLC- and BBVLC-TCM schemes. In the IrVLC schemes, the M number of VLC encoders, APP SISO decoders and MAP sequence estimators are each based upon one of N number of VLC codebooks. By contrast, in the VLC bench-markers, all of the M number of VLC encoders, decoders and sequence estimators are based upon the same VLC codebook.

12.6.2.1 Joint source and channel coding

The schemes considered are designed for facilitating the near-capacity detection of source samples received over an uncorrelated narrowband Rayleigh fading channel. We consider the case of independent identically distributed (i.i.d.) source samples, which may represent the prediction residual error that remains following the predictive coding of audio, speech, image

or video information [391] [160], for example. A Gaussian source sample distribution is assumed, since this has widespread applications owing to the wide applicability of the central limit theorem. Note however that with the aid of suitable adaptation, the techniques proposed in this treatise may be just as readily applied to arbitrary source sample distributions.

In the transmitter of Figure 12.67, the real-valued source samples are quantized to K number of quantization levels in the block Q. The resultant frame of quantized source samples is synonymously referred to as the frame of source symbols $\mathbf{s}$ here. Each source symbol in this frame indexes the particular quantization level $\tilde{e}^k$, $k \in [1 \dots K]$, that represents the corresponding source sample in the frame $\mathbf{e}$ with the minimum squared error. Owing to the lossy nature of quantization, distortion is imposed upon the reconstructed source sample frame $\tilde{\mathbf{e}}$ that is obtained by the receiver of Figure 12.67, following inverse quantization in the block Q^{-1}. The total distortion expected depends on both the original source sample distribution as well as on the number of quantization levels K. This distortion may be minimised by employing Lloyd-Max quantization [490] [491]. Here, a $K = 16$-level Lloyd-Max quantization scheme is employed, which achieves an expected Signal to Quantization Noise Ratio (SQNR) of about 20 dB for a Gaussian source [490]. Note however that with suitable adaptation, the techniques advocated in this treatise may be just as readily applied to arbitrary quantisers. Also note that Lloyd-Max quantization results in a large variation in the occurrence probabilities of the resultant source symbol values. These occurrence probabilities are given by integrating the source Probability Density Function (PDF) between each pair of adjacent decision boundaries. In the case of our $K = 16$-level quantizer, the source symbol values' occurrence probabilities vary by more than an order of magnitude between 0.0082 and 0.1019. These probabilities correspond to symbol informations spanning between 3.29 and 6.93 bits/symbol, motivating the application of VLC and giving a source entropy of $E = 3.77$ bits/symbol.

In the transmitter of the proposed scheme, the Lloyd-Max quantized source symbol frame $\mathbf{s}$ is decomposed into $M = 300$ sub-frames $\{\mathbf{s^m}\}_{m=1}^{M}$, as shown in Figure 12.67. In the case of the SBIrVLC- and SBVLC-TCM schemes, this decomposition is necessary for the sake of limiting the computational complexity of VLC decoding, since the number of transitions in the symbol-based VLC trellis is inversely proportional to the number of sub-frames in this case [487]. We opt for employing the same decomposition of the source symbol frames into sub-frames in the case of the BBIrVLC- and BBVLC-TCM schemes for the sake of ensuring that we make a fair comparison with the SBIrVLC- and SBVLC-TCM schemes. This is justified, since the decomposition considered benefits the performance of the BBIrVLC- and BBVLC-TCM schemes, as will be detailed below. Each source symbol sub-frame $\mathbf{s^m}$ comprises $J = 100$ source symbols. Hence, the total number of source symbols in a source symbol frame becomes $M \cdot J = 30,000$. As described above, each Lloyd-Max quantized source symbol in the sub-frame $\mathbf{s^m}$ has a K-ary value $s_j^m \in [1 \dots K]$, where we have $j \in [1 \dots J]$.

As described in Section 12.6.1, we employ N number of VLC codebooks to encode the source symbols, where we opted for $N = 15$ for the SBIrVLC and BBIrVLC schemes and $N = 1$ for the regular SBVLC and BBVLC schemes. Each Lloyd-Max quantized source symbol sub-frame $\mathbf{s^m}$ is VLC-encoded using a single VLC codebook $\mathbf{VLC}^n$, where we have $n \in [1 \dots N]$. In the case of the SBIrVLC and BBIrVLC schemes, the particular fraction C^n of the set of source symbol sub-frames that is encoded by the specific VLC codebook $\mathbf{VLC}^n$ is fixed and will be derived in Section 12.6.3. The specific Lloyd-Max quantized source symbols having the value of $k \in [1 \dots K]$ and encoded by the specific VLC codebook

$\mathbf{VLC}^n$ are represented by the codeword $\mathbf{VLC}^{n,k}$, which has a length of $I^{n,k}$ bits. The $J = 100$ VLC codewords that represent the $J = 100$ Lloyd-Max quantized source symbols in each source symbol sub-frame $\mathbf{s^m}$ are concatenated to provide the transmission sub-frame $\mathbf{u^m} = \{\mathbf{VLC}^{n,s_j^m}\}_{j=1}^{J}$.

Owing to the variable lengths of the VLC codewords, each of the $M = 300$ transmission sub-frames typically comprises a different number of bits. In order to facilitate the VLC decoding of each transmission sub-frame $\mathbf{u^m}$, it is necessary to explicitly convey its length $I^m = \sum_{j=1}^{J} I^{n,s_j^m}$ to the receiver. Furthermore, this highly error sensitive side information must be reliably protected against transmission errors. This may be achieved using a low rate block code, for example. For the sake of avoiding obfuscation, this is not shown in Figure 12.67. Note that the choice of the specific number of sub-frames M in each frame constitutes a trade-off between the computational complexity of SBVLC decoding or the performance of BBVLC decoding and the amount of side information that must be conveyed. In Section 12.6.3, we shall comment on the amount of side information that is required for reliably conveying the specific number of bits in each transmission sub-frame to the decoder.

In the scheme's transmitter, the $M = 300$ number of transmission sub-frames $\{\mathbf{u^m}\}_{m=1}^{M}$ are concatenated. As shown in Figure 12.67, the resultant transmission frame $\mathbf{u}$ has a length of $\sum_{m=1}^{M} I^m$ bits.

In the proposed scheme, the VLC codec is protected by a serially concatenated TCM codec. Following VLC encoding, the bits of the transmission frame $\mathbf{u}$ are interleaved in the block π of Figure 12.67 and TCM encoded in order to obtain the channel's input symbols $\mathbf{x}$, as shown in Figure 12.67. These are transmitted over an uncorrelated narrowband Rayleigh fading channel and are received as the channel's output symbols $\mathbf{y}$, as seen in Figure 12.67.

12.6.2.2 Iterative decoding

In the receiver, APP SISO TCM- and VLC-decoding are performed iteratively, as shown in Figure 12.67. Both of these decoders invoke the Bahl-Cocke-Jelinek-Raviv (BCJR) algorithm [492] on the basis of their trellises. Symbol-based trellises are employed in the case of TCM [486], SBIrVLC and SBVLC [487] [488] decoding, whilst BBIrVLC and BBVLC decoding rely on bit-based trellises [489]. All BCJR calculations are performed in the logarithmic probability domain and using an eight-entry lookup table for correcting the Jacobian approximation in the Log-MAP algorithm [479]. The proposed approach requires only Add, Compare and Select (ACS) computational operations during iterative decoding, which will be used as our complexity measure, since it is characteristic of the complexity/area/speed trade-offs in systolic-array based chips.

As usual, extrinsic soft information, represented in the form of Logarithmic Likelihood Ratios (LLRs) [493], is iteratively exchanged between the TCM and VLC decoding stages for the sake of assisting each other's operation, as detailed in [483] and [484]. In Figure 12.67, $L(\cdot)$ denotes the LLRs of the bits concerned (or the log-APPs of the specific symbols as appropriate), where the superscript i indicates inner TCM decoding, while o corresponds to outer VLC decoding. Additionally, a subscript denotes the dedicated role of the LLRs (or log-APPs), with a, p and e indicating *a priori*, *a posteriori* and extrinsic information, respectively.

Just as $M = 300$ separate VLC encoding processes are employed in the proposed scheme's transmitter, $M = 300$ separate VLC decoding processes are employed in its receiver. In

parallel to the composition of the bit-based transmission frame $\mathbf{u}$ from its $M = 300$ sub-frames, the *a priori* LLRs $L_a^o(\mathbf{u})$ are decomposed into $M = 300$ sub-frames, as shown in Figure 12.67. This is achieved with the aid of the explicit side information that conveys the number of bits I^m in each transmission sub-frame $\mathbf{u^m}$. Each of the $M = 300$ VLC decoding processes is provided with the *a priori* LLR sub-frame $L_a^o(\mathbf{u^m})$ and in response it generates the *a posteriori* LLR sub-frame $L_p^o(\mathbf{u^m})$, $m \in [1 \dots M]$. These *a posteriori* LLR sub-frames are concatenated in order to provide the *a posteriori* LLR frame $L_p^o(\mathbf{u})$, as shown in Figure 12.67.

In the case of SBIrVLC and SBVLC decoding, each of the $M = 300$ VLC decoding processes additionally provides log-APPs pertaining to the corresponding source symbol sub-frame $L_p^o(\mathbf{s^m})$. This comprises a set of K number of log-APPs for each source symbol s_j^m in the sub-frame $\mathbf{s^m}$, where $j \in [1 \dots J]$. Each of these log-APPs provides the logarithmic probability that the corresponding source symbol s_j^m has the particular value $k \in [1 \dots K]$. In the receiver of Figure 12.67, the source symbols' log-APP sub-frames are concatenated to provide the source symbol log-APP frame $L_p^o(\mathbf{s})$. By inverse-quantising this soft information in the block Q^{-1}, a frame of Minimum Mean Squared Error (MMSE) source sample estimates $\tilde{\mathbf{e}}$ can be obtained. More specifically, each reconstructed source sample is obtained by using the corresponding set of K source symbol value probabilities to find the weighted average of the K number of quantization levels $\{\tilde{e}^k\}_{k=1}^K$.

Conversely, in the case of BBIrVLC and BBVLC decoding, no symbol-based *a posteriori* output is available. In this case, each source symbol sub-frame $\mathbf{s^m}$ is estimated from the corresponding *a priori* LLR sub-frame $L_a^o(\mathbf{u^m})$. This may be achieved by employing Maximum *A Posteriori* (MAP) sequence estimation operating on a bit-based trellis structure, as shown in Figure 12.67. Unlike in APP SISO SBIrVLC and SBVLC decoding, bit-based MAP sequence estimation cannot exploit the knowledge that each sub-frame $\mathbf{s^m}$ comprises $J = 100$ source symbols. For this reason, the resultant hard decision estimate $\tilde{\mathbf{s}}^{\mathbf{m}}$ of each source symbol sub-frame $\mathbf{s^m}$ may or may not contain $J = 100$ source symbols. In order that we may prevent the loss of synchronisation that this would imply, source symbol estimates are removed from, or appended to the end of each source symbol sub-frame estimate $\tilde{\mathbf{s}}^{\mathbf{m}}$ for ensuring that they each comprise exactly $J = 100$ source symbol estimates. Note that it is the decomposition of the source symbol frame $\mathbf{s}$ into sub-frames that provides this opportunity to mitigate the loss of synchronisation that is associated with bit-based MAP VLC sequence estimation. Hence the decomposition of the source symbol frame $\mathbf{s}$ into sub-frames benefits the performance of the BBIrVLC- and BBVLC-TCM schemes, as mentioned above.

Following MAP sequence estimation, the adjusted source symbol sub-frame estimates $\tilde{\mathbf{s}}^{\mathbf{m}}$ are concatenated for the sake of obtaining the source symbol frame estimate $\tilde{\mathbf{s}}$. This may be inverse-quantised in order to obtain the source sample frame estimate $\tilde{\mathbf{e}}$. Note that for the reconstruction of a source sample frame estimate $\tilde{\mathbf{e}}$ from a given *a priori* LLR frame $L_a^o(\mathbf{u})$, a higher level of source distortion may be expected in the BBIrVLC- and BBVLC-TCM schemes than in the corresponding SBIrVLC- and SBVLC-TCM schemes. This is due to the BBIrVLC- and BBVLC-TCM schemes' reliance on hard decisions as opposed to the soft decisions of the SBIrVLC- and SBVLC-TCM schemes. However, this reduced performance substantially benefits us in terms of a reduced complexity, since the bit-based VLC decoding trellis employed during APP SISO BBIrVLC and BBVLC decoding and MAP sequence estimation contains significantly less transitions than the symbol-based VLC decoding trellis of APP SISO SBIrVLC and SBVLC decoding.

In the next section we detail the design of our IrVLC scheme and characterise each of the SBIrVLC-, BBIrVLC-, SBVLC- and BBVLC-TCM schemes with the aid of EXIT chart analysis.

12.6.3 Parameter Design for the Proposed Schemes

12.6.3.1 Scheme hypothesis and parameters

As described in Section 12.6.1, the SBIrVLC and BBIrVLC schemes may be constructed by employing a number of VLC codebooks having different coding rates, each of which encodes an appropriately chosen fraction of the input source symbols. We opted for using $N = 15$ VLC codebooks $\mathbf{VLC}^n$, $n \in [1 \dots N]$, that were specifically designed for encoding $K = 16$-level Lloyd-Max quantized Gaussian i.i.d. source samples. These 15 VLC codebooks were selected from a large number of candidate codebooks in order to provide a suite of similarly-spaced EXIT curves. More specifically, the $N = 15$ VLC codebooks comprised 13 Variable Length Error Correcting (VLEC) designs having various so-called minimum block-, convergence- and divergence-distances as defined in [494], complemented by a symmetric- and an asymmetric- Reversible Variable Length Coding (RVLC) design [494]. In all codebooks, a free distance of at least $d_f = 2$ was employed, since this supports convergence to an infinitesimally low BER [495]. The resultant average VLC codeword lengths of $L^n = \sum_{k=1}^{K} P(k) \cdot I^{n,k}$, $n \in [1 \dots N]$, were found to range from 3.94 to 12.18 bits/symbol. When compared to the source symbol entropy of $E = -\sum_{k=1}^{K} P(k) \cdot \log_2(P(k)) = 3.77$ bits/symbol, these correspond to coding rates of $R^n = E/L^n$ spanning the range of 0.31 to 0.96.

As will be detailed below, our SBIrVLC and BBIrVLC schemes were designed under the constraint that they have an overall coding rate of $R = 0.52$. This value was chosen, since it is the coding rate of the VLC codebook $\mathbf{VLC}^{10}$, which we employ in our SBVLC and BBVLC bench-markers using $N = 1$ codebook. This coding rate results in an average interleaver length of $M \cdot J \cdot E/R = 217,500$ bits for all the schemes considered.

In-phase Quadrature-phase (IQ)-interleaved TCM having eight trellis-states per symbol along with 3/4-rate coded 16-Level Quadrature Amplitude Modulation (16QAM) is employed, since this is appropriate for transmission over uncorrelated narrowband Rayleigh fading channels. Ignoring the modest bitrate contribution of conveying the side information, the bandwidth efficiency of the schemes considered is therefore $\eta = 0.52 \cdot 0.75 \cdot \log_2(16) = 1.56$ bit/s/Hz, assuming ideal Nyquist filtering having a zero excess bandwidth. This value corresponds to the channel capacity of the uncorrelated narrowband Rayleigh fading channel at an E_b/N_0 value of 2.6 dB [496]. Given this point on the corresponding channel capacity curve, we will be able to quantify, how closely the proposed schemes may approach this ultimate limit.

Recall from Section 12.6.2 that it is necessary to convey the length of each transmission sub-frame $\mathbf{u^m}$ to the receiver in order to facilitate its VLC decoding. It was found for all considered schemes that a single 10-bit fixed-length codeword of side information is sufficient for conveying the length of each of the $M = 150$ transmission sub-frames $\mathbf{u^m}$ in each transmission frame $\mathbf{u}$. As suggested in Section 12.6.2, this error sensitive side information may be protected by a low-rate block code in order to ensure its reliable transmission. Note that since even a repetition code having a rate as low as $1/7$ encodes the side information

with only about 1% of the expected transmission frame length, we consider the overhead of conveying side information to be acceptable.

12.6.3.2 EXIT chart analysis and optimization

We now consider the EXIT characteristics of the various components of our various schemes. In all cases, EXIT curves were generated using uncorrelated Gaussian distributed *a priori* LLRs with the assumption that the transmission frame's bits have equiprobable values. This is justified, because we employ a long interleaver and because the entropy of the VLC encoded bits was found to be at least 0.99 for all considered VLC codebooks. All mutual information measurements were made using the histogram-based approximation of the LLR PDFs [476].

In Figure 12.68, we provide the EXIT curves $I_e^i(I_a^i, E_b/N_0)$ of the TCM scheme for a number of E_b/N_0 values above the channel capacity bound of 2.6 dB. The inverted EXIT curves $I_a^{o,n}(I_e^o)$ plotted for the $N = 15$ VLC codebooks, together with their coding rates R^n, are also given in Figure 12.68. Note that these curves were obtained using bit-based VLC decoding, but very similar curves may be obtained for symbol-based decoding.

The inverted EXIT curve of an IrVLC scheme $I_a^o(I_e^o)$ can be obtained as the appropriately weighted superposition of the $N = 15$ component VLC codebooks' EXIT curves,

$$I_a^o(I_e^o) = \sum_{n=1}^{N} \alpha^n I_a^{o,n}(I_e^o), \tag{12.17}$$

where α^n is the fraction of the transmission frame $\mathbf{u}$ that is generated by the specific component codebook $\mathbf{VLC}^n$. Note that the values of α^n are subject to the constraints

$$\sum_{n=1}^{N} \alpha^n = 1, \quad \alpha^n \geq 0 \; \forall \, n \in [1 \ldots N]. \tag{12.18}$$

The specific fraction of source symbol sub-frames $\mathbf{s^m}$ that should be encoded by the specific component codebook $\mathbf{VLC}^n$ in order that it generates a fraction α^n of the transmission frame $\mathbf{u}$, is given by

$$C^n = \alpha^n \cdot R^n / R, \tag{12.19}$$

where $R = 0.52$ is the desired overall coding rate. Again, the specific values of C^n are subject to the constraints

$$\sum_{n=1}^{N} C^n = \sum_{n=1}^{N} \alpha^n \cdot R^n / R = 1, \quad C^n \geq 0 \; \forall \, n \in [1 \ldots N]. \tag{12.20}$$

Beneficial values of C^n may be chosen by ensuring that there is an open EXIT tunnel between the inverted IrVLC EXIT curve and the EXIT curve of TCM at an E_b/N_0 value that is close to the channel capacity bound. This may be achieved using the iterative EXIT-chart matching process of [475] to adjust the values of $\{C^n\}_{n=1}^N$ under the constraints of (12.18) and (12.20) for the sake of minimising the error function

$$\{C^n\}_{n=1}^N = \underset{\{C^n\}_{n=1}^N}{\operatorname{argmin}} \left(\int_0^1 e(I)^2 \mathrm{d}I \right), \tag{12.21}$$

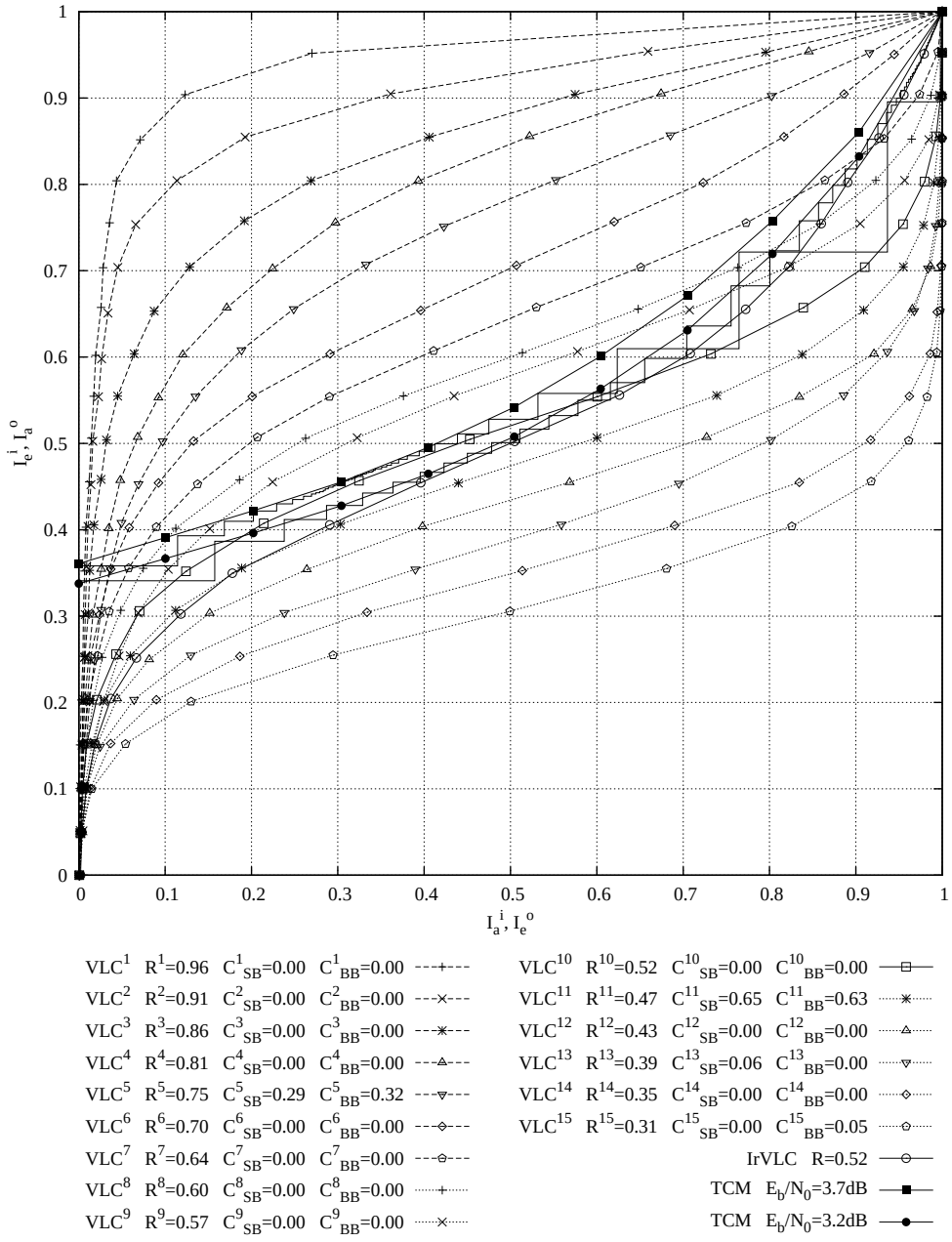

Figure 12.68: Inverted VLC EXIT curves and TCM EXIT curves.

where

$$e(I) = I_e^i(I, E_b/N_0) - I_a^o(I) \tag{12.22}$$

is the difference between the inverted IrVLC EXIT curve and the EXIT curve of TCM at a particular target E_b/N_0 value. Note that in order to ensure that the design results in an open EXIT tunnel, we must impose the additional constraint of

$$e(I) > 0 \; \forall \; I \in [0, 1]. \tag{12.23}$$

Open EXIT tunnels were found to be achievable for both the SBIrVLC- and the BBIrVLC-TCM schemes at an E_b/N_0 of 3.2 dB, which is just 0.6 dB from the channel capacity bound of 2.6 dB. The inverted BBIrVLC EXIT curve is shown in Figure 12.68, which is similar to the SBIrVLC EXIT curve not shown here for reasons of space-economy. The corresponding values of C^n are provided for both the SBIrVLC- and the BBIrVLC-TCM schemes in Figure 12.68.

By contrast, the corresponding EXIT-tunnel only becomes open for the SBVLC- and BBVLC-TCM bench-markers for E_b/N_0 values in excess of 3.7 dB, which is 1.1 dB from the channel capacity bound of 2.6 dB. We can therefore expect our SBIrVLC- and BBIrVLC-TCM schemes to be capable of operating at nearly half the distance from the channel capacity bound in comparison to our bench-markers, achieving a gain of about 0.5 dB.

12.6.4 Results

In this section, we discuss our findings when communicating over an uncorrelated narrow-band Rayleigh fading channel having a range of E_b/N_0 values above the channel capacity bound of 2.6 dB.

In addition to the proposed SBIrVLC-, BBIrVLC-, SBVLC- and BBVLC-TCM schemes, in this section we also consider the operation of an additional bench-marker which we refer to as the Huffman-IrCC-TCM scheme. In contrast to the SBIrVLC-, BBIrVLC-, SBVLC- and BBVLC-TCM schemes, in the Huffman-IrCC-TCM scheme the transmission frame $\mathbf{u}$ of Figure 12.67 is generated by both Huffman and concatenated IrCC encoding the source symbol frame $\mathbf{s}$, rather than by invoking VLC encoding. More specifically, Huffman coding is employed on a sub-frame by sub-frame basis, as described in Section 12.6.2. The resultant frame of Huffman encoded bits $\mathbf{v}$ is protected by the memory-4 17-component IrCC scheme of [497]. This was tailored to have an overall coding rate of 0.52 and an inverted EXIT curve that does not cross the TCM EXIT curve at an E_b/N_0 of 3.2 dB, just like the SBIrVLC and BBIrVLC designs detailed in Section 12.6.3. In the Huffman-IrCC-TCM receiver, iterative APP SISO IrCC and TCM decoding proceeds, as described in Section 12.6.2. Note that in addition to the *a posteriori* LLR frame $L_p^o(\mathbf{u})$ pertaining to the transmission frame $\mathbf{u}$, the APP SISO IrCC decoder can additionally provide the *a posteriori* LLR frame $L_p^o(\mathbf{v})$ pertaining to the frame of Huffman encoded bits $\mathbf{v}$. It is on the basis of this that bit-based MAP Huffman sequence estimation may be invoked on a sub-frame by sub-frame basis in order to obtain the source symbol frame estimate $\tilde{\mathbf{s}}$.

12.6.4.1 Asymptotic performance following iterative decoding convergence

For each of our schemes and for each value of E_b/N_0, we consider the reconstructed source sample frame $\tilde{\mathbf{e}}$ and evaluate the Signal to Noise Ratio (SNR) associated with the ratio of

the source signal's energy and the reconstruction error energy that may be achieved following iterative decoding convergence. This relationship is plotted for each of the SBIrVLC-, BBIrVLC-, SBVLC- and BBVLC-TCM schemes, as well as for the Huffman-IrCC-TCM scheme, in Figure 12.69.

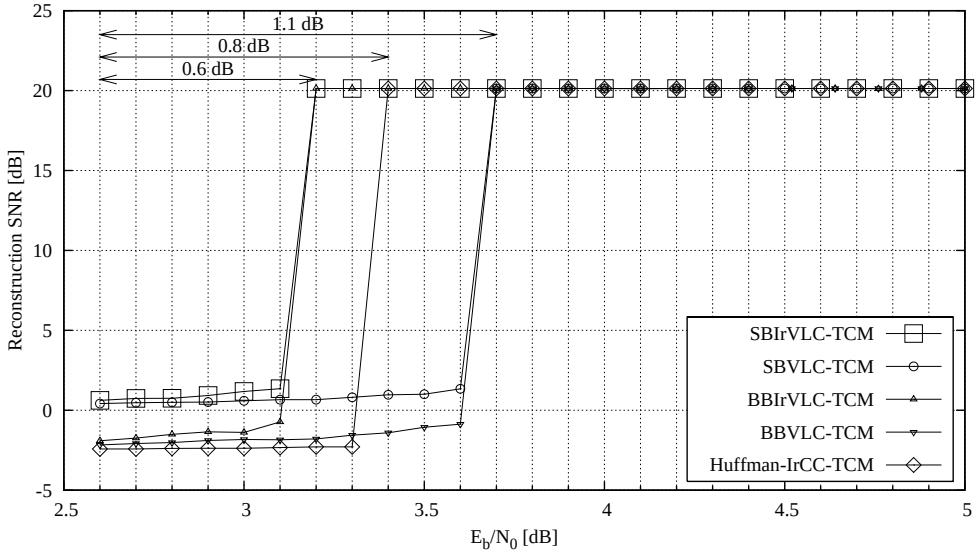

Figure 12.69: Reconstruction SNR versus E_b/N_0 for a Gaussian source using $K = 16$-level Lloyd-Max quantization for the SBIrVLC-, BBIrVLC-, SBVLC- and BBVLC-TCM schemes, as well as for the Huffman-IrCC-TCM scheme, communicating over an uncorrelated narrowband Rayleigh fading channel following iterative decoding convergence.

At sufficiently high E_b/N_0 values, all considered schemes are capable of achieving source sample reconstruction SNRs of up to 20 dB, which represents the error-free case, where only quantization noise is present, while all channel-induced errors are absent. As shown in Figure 12.69, this may be achieved by the SBIrVLC- and BBIrVLC-TCM schemes at E_b/N_0 values above 3.2 dB, which is just 0.6 dB from the channel capacity bound of 2.6 dB. This represents a 0.5 dB gain over the SBVLC- and BBVLC-TCM schemes, which require E_b/N_0 values in excess of 3.7 dB, a value that is 1.1 dB from the channel capacity bound. Additionally, the SBIrVLC- and BBIrVLC-TCM schemes can be seen to offer a 0.2 dB gain over the Huffman-IrCC-TCM scheme, which is incapable of operating within 0.8 dB of the channel capacity bound.

Note that our findings recorded in Figure 12.69 for the SBIrVLC-, BBIrVLC-, SBVLC- and BBVLC-TCM schemes confirm the EXIT chart predictions of Section 12.6.3. Figure 12.68 provides decoding trajectories for the BBIrVLC-TCM and BBVLC-TCM schemes at E_b/N_0 values of 3.2 dB and 3.7 dB, respectively. Note that owing to the sufficiently long interleaver length of $M \cdot J \cdot E/R = 217,500$ bits, correlation within the *a priori* LLR frames $L_a^i(\mathbf{u})$ and $L_a^o(\mathbf{u})$ is mitigated and the recorded trajectories exhibit a close match with the corresponding TCM and inverted IrVLC/VLC EXIT curves. In both cases, the corresponding trajectory can be seen to converge to the (1,1) mutual information point of the EXIT chart af-

ter a number of decoding iterations. Note that with each decoding iteration, a greater extrinsic mutual information is achieved, which corresponds to a greater source sample reconstruction SNR.

At low E_b/N_0 values, the corresponding TCM EXIT curves cross the inverted IrVLC or VLC EXIT curves and the open EXIT chart tunnel disappears. In these cases, iterative decoding convergence to unity mutual information cannot be achieved, resulting in the poor reconstruction quality that may be observed at low values of E_b/N_0 in Figure 12.69.

In the case of the Huffman-IrCC-TCM scheme however, poor reconstruction qualities were obtained despite the presence of an open EXIT chart tunnel for E_b/N_0 values between 3.2 dB and 3.4 dB in Figure 12.69. This surprising result may be attributed to the APP SISO IrCC decoder's relatively high sensitivity to any residual correlation within the *a priori* LLR frame $L_a^o(\mathbf{u})$ that could not be mitigated by the interleaver having an average length of 217,500 bits. As a result of this, the Huffman-IrCC-TCM EXIT trajectory does not approach the inverted IrCC EXIT curve very closely and a wide EXIT chart tunnel is required for iterative decoding convergence to the $(1, 1)$ mutual information point of the EXIT chart.

The relatively high sensitivity of APP SISO CC decoding to any correlation within the *a priori* LLR frame $L_a^o(\mathbf{u})$ as compared to VLC decoding may be explained as follows. During APP SISO CC decoding using the BCJR algorithm, it is assumed that all *a priori* LLRs that correspond to bits within each set of L consecutive codewords are uncorrelated, where L is the constraint length of the CC [479]. By contrast, during APP SISO VLC decoding using the BCJR algorithm, it is assumed that all *a priori* LLRs that correspond to bits within each *single* codeword are uncorrelated [489]. Hence, the BCJR-based APP SISO decoding of a CC scheme can be expected to be more sensitive to correlation within the *a priori* LLR frame $L_a^o(\mathbf{u})$ than that of a VLC scheme having similar codeword lengths. As a result, a longer interleaver and hence a higher latency would be required for facilitating near-capacity CC operation.

12.6.4.2 Performance during iterative decoding

The achievement of iterative decoding convergence requires the completion of a sufficiently high number of decoding iterations. Clearly, each decoding iteration undertaken is associated with a particular computational complexity, the sum of which represents the total computational complexity of the iterative decoding process. Hence, the completion of a sufficiently high number of decoding iterations in order to achieve iterative decoding convergence may be associated with a high computational complexity. In order to quantify how this computational complexity scales as iterative decoding proceeds, we recorded the total number of ACS operations performed per source sample during APP SISO decoding and MAP sequence estimation.

Furthermore, the performance of the considered schemes was also assessed *during* the iterative decoding process, not only after its completion once convergence has been achieved. This was achieved by evaluating the source sample reconstruction SNR following the completion of *each* decoding iteration. The total computational complexity associated with this SNR was calculated as the sum of the computational complexities associated with all decoding iterations completed so far during the iterative decoding process. Clearly, as more and more decoding iterations are completed, the resultant source sample reconstruction SNR can be expected to increase until iterative decoding convergence is achieved. However, the asso-

ciated total computational complexity will also increase as more and more decoding iterations are completed. Hence, this approach allows the characterisation of the tradeoff between reconstruction quality and computational complexity.

For each considered Rayleigh channel E_b/N_0 value, a set of source sample reconstruction SNRs and their corresponding computational complexities was obtained, as described above. Note that the size of these sets was equal to the number of decoding iterations required to achieve iterative decoding convergence at the particular E_b/N_0 value. It would therefore be possible to display the source sample reconstruction SNR versus both the E_b/N_0 and the computational complexity in a three-dimensional surface plot, for each of the SBIrVLC-, BBIrVLC-, SBVLC- and BBVLC-TCM schemes. For clarity however, these surfaces are projected in the direction of the source sample reconstruction SNR axis into two dimensions in Figure 12.70. We employ contours of constant source sample reconstruction SNR, namely 15 dB and 20 dB, to parameterise the relationship between the Rayleigh fading channel's E_b/N_0 value and the associated computational complexity. Note that the plot of Figure 12.69 may be thought of as a cross-section through the surfaces represented by Figure 12.70, perpedicular to the computational complexity axis at $1 \cdot 10^7$ ACS operations per source sample. Note that this particular value of computational complexity is sufficiently high to achieve iterative decoding convergence at all values of E_b/N_0, in each of the considered schemes.

Note that the SBIrVLC and SBVLC decoders have a computational complexity per source sample that depends on the number of symbols in each source symbol sub-frame $\mathbf{s^m}$, namely J. This is because the number of transitions in their symbol-based trellises is proportional to J^2 [487]. Hence the results provided in Figure 12.70 for the SBIrVLC- and SBVLC-TCM schemes are specific to the $J = 100$ scenario. By contrast, the TCM, BBIrVLC, BBVLC and IrCC decoders have a computational complexity per source sample that is independent of the number of symbols in each source symbol sub-frame $\mathbf{s^m}$, namely J. This is because the number of transitions in their trellises is proportional to J [486] [498] [479]. Hence the results for the BBIrVLC- and BBVLC-TCM schemes, as well as for the Huffman-IrCC-TCM scheme, provided in Figure 12.70 are *not* specific for the $J = 100$ case.

As shown in Figure 12.70, source sample reconstruction SNRs of up to 20 dB can be achieved within 0.6 dB of the channel's capacity bound of 2.6 dB for the SBIrVLC- and BBIrVLC-TCM schemes, within 1.1 dB for the SBVLC- and BBVLC-TCM schemes and within 0.8 dB for the Huffman-IrCC-TCM scheme. Note that these findings agree with those of the EXIT chart analysis and the asymptotic performance analysis.

12.6.4.3 Complexity analysis

We now comment on the computational complexities of the considered schemes and select our preferred arrangement.

In all considered schemes and at all values of E_b/N_0, a source sample reconstruction SNR of 15 dB can be achieved at a lower computational complexity than an SNR of 20 dB can, as shown in Figure 12.70. This is because a reduced number of decoding iterations is required for achieving the extrinsic mutual information value associated with a lower reconstruction quality, as stated above. However, for all considered schemes operating at high values of E_b/N_0, this significant 5 dB reduction in source sample reconstruction SNR facilitates only a relatively modest reduction of the associated computational complexity, which was between 9% in the case of the Huffman-IrCC-TCM scheme and 36% for the BBIrVLC-TCM scheme.

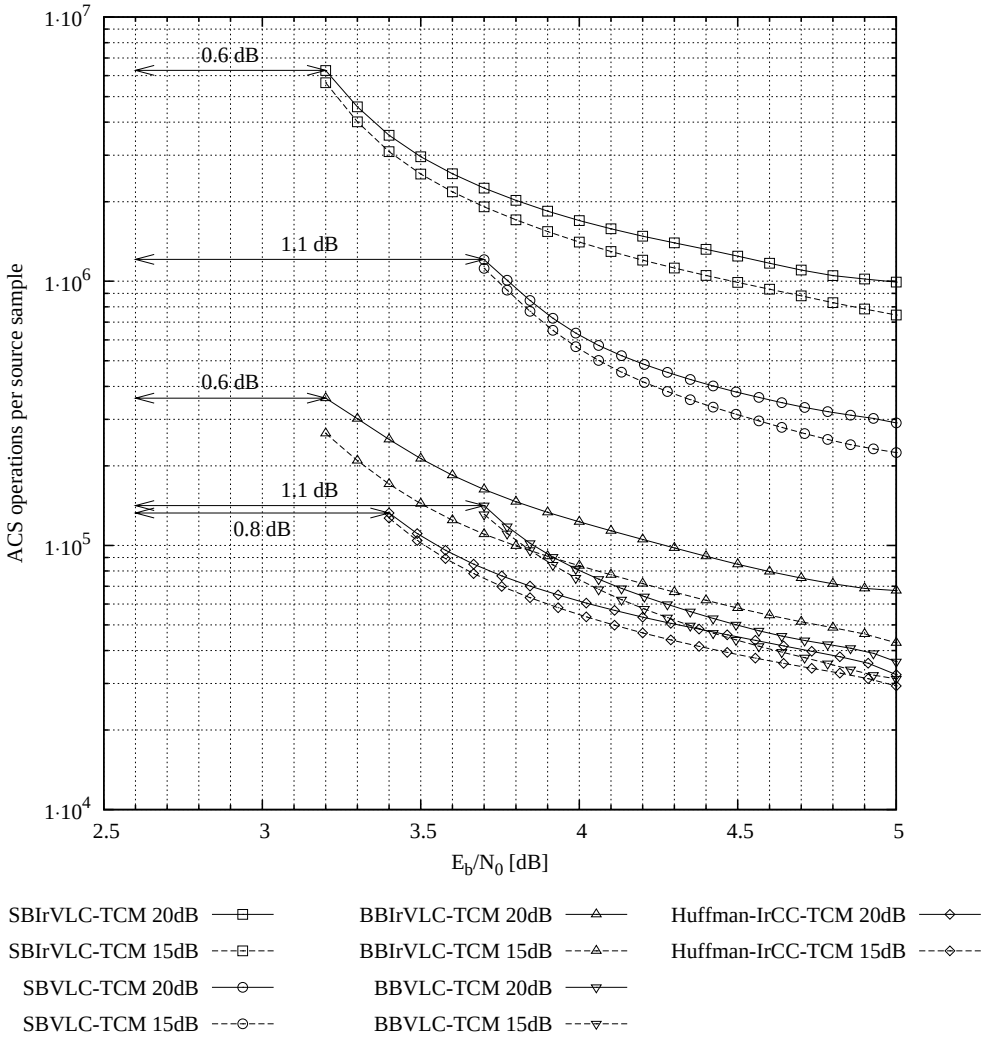

Figure 12.70: Computational complexity versus E_b/N_0 for a Gaussian source using $K = 16$-level Lloyd-Max quantization for the SBIrVLC-, BBIrVLC-, SBVLC- and BBVLC-TCM schemes, as well as for the Huffman-IrCC-TCM scheme, communicating over an uncorrelated narrowband Rayleigh fading channel, parameterised with the source sample reconstruction SNR.

Hence we may conclude that the continuation of iterative decoding until near-perfect convergence is achieved can be justified at all values of E_b/N_0.

Additionally, it may be seen that a given source sample reconstruction SNR may be achieved at a reduced computational complexity for all considered schemes as the E_b/N_0 value increases. This may be explained by the widening of the EXIT chart tunnel, as the E_b/N_0 value increases. As a result, less decoding iterations are required for reaching the extrinsic mutual information that is associated with a specific source sample reconstruction SNR considered.

In each of the considered schemes it was found that VLC and CC decoding is associated with a higher contribution to the total computational complexity than TCM decoding. Indeed, in the case of the SBIrVLC- and SBVLC-TCM schemes, it was found that VLC decoding accounts for about 97% of the numbers of ACS operations per source sample, having a complexity of about 32.3 times higher than that of TCM decoding. By contrast, in the BBIrVLC- and BBVLC-TCM schemes, VLC decoding accounts for only 70% of the operations, having a complexity of about 2.3 times that of TCM decoding. Similarly, CC decoding accounts for only 60% of the ACS operations in the Huffman-IrCC-TCM scheme, having a complexity of about 1.4 times that of TCM decoding.

The high complexity of the SBIrVLC and SBVLC decoders may be attributed to the specific structure of their trellises, which contain significantly more transitions than those of the BBIrVLC, BBVLC and IrCC decoders [487]. As a result, the SBIrVLC- and SBVLC-TCM schemes have a complexity that is about an order of magnitude higher than that of the BBIrVLC- and BBVLC-TCM schemes, as well as the Huffman-IrCC-TCM scheme, as shown in Figure 12.70. In the light of this, the employment of the SBIrVLC- and SBVLC-TCM schemes cannot be readily justified.

Observe in Figure 12.70 that at high E_b/N_0 values, the SBIrVLC- and BBIrVLC-TCM schemes have a higher computational complexity than the corresponding SBVLC- or BBVLC-TCM scheme. This is due to the influence of their low rate VLC codebook components. These codebooks comprise codewords with many different lengths, which introduce many transitions, when represented in a trellis structure. The observed computational complexity discrepancy is particularly high in the case of the schemes that employ the symbol-based VLC trellis, owing to its particular nature. For this reason, the SBIrVLC-TCM scheme has a computational complexity that is 240% higher than that of the SBVLC-TCM scheme.

By contrast, we note that at high values of E_b/N_0 the BBIrVLC-TCM scheme has only about a 60% higher computational complexity than the BBVLC-TCM scheme. Similarly, the BBIrVLC-TCM scheme has only twice the computational complexity of the Huffman-IrCC-TCM scheme. Coupled with the BBIrVLC-TCM scheme's ability to operate within 0.6 dB of the Rayleigh fading channel's capacity bound, we are able to identify this as our preferred arrangement.

12.6.5 Conclusions

In this section we have introduced a novel IrVLC design for near-capacity joint source and channel coding. In analogy to IrCC, IrVLC employs a number of component VLC codebooks having different coding rates in appropriate proportions. More specifically, with the aid of EXIT chart analysis, the appropriate fractions of the input source symbols may be chosen for directly ensuring that the EXIT curve of the IrVLC codec may be matched to that of a serially

concatenated channel codec. In this way, an open EXIT chart tunnel facilitating near-capacity high quality source sample reconstruction may be achieved.

We have detailed the construction of an IrVLC scheme that is suitable for the encoding of 16-level Lloyd-Max quantized Gaussian i.i.d. source samples and for use with IQ-interleaved TCM and 16QAM over uncorrelated narrowband Rayleigh fading channels. For the purposes of comparison, we also selected a regular VLC bench-marker, having a coding rate equal to that of our IrVLC scheme. Serially-concatenated and iteratively decoded SBIrVLC-, BBIrVLC-, SBVLC- and BBVLC-TCM schemes were characterised with the aid of EXIT chart analysis. These schemes have a bandwidth efficiency of 1.56 bits per channel symbol, which corresponds to a Rayleigh fading channel capacity bound of 2.6 dB. Using an average interleaver length of 217,500 bits, the SBIrVLC- and BBIrVLC-TCM schemes were found to offer high-quality source sample reconstruction at an E_b/N_0 value of 3.2 dB, which is just 0.6 dB from the capacity bound. This compares favourably with the SBVLC- and BBVLC-TCM bench-markers, which require an E_b/N_0 value of 3.7 dB. This also compares favourably with a Huffman-IrCC-TCM bench-marker, which requires an E_b/N_0 value of 3.4 dB owing to its slightly eroded performance when operating with the considered interleaver length. Owing to the higher computational complexity of the SBIrVLC-TCM scheme, the BBIrVLC-TCM arrangement was identified as our preferred scheme.

12.7 Digital Terrestrial Video Broadcasting for Mobile Receivers[12]

12.7.1 Background and Motivation

Following the standardization of the pan-European digital video broadcasting (DVB) systems, we have begun to witness the arrival of digital television services to the home. However, for a high proportion of business and leisure travelers, it is desirable to have access to DVB services while on the move. Although it is feasible to access these services with the aid of dedicated DVB receivers, these receivers may also find their way into the laptop computers of the near future. These intelligent laptops may also become the portable DVB receivers of wireless in-home networks.

In recent years three DVB standards have emerged in Europe for terrestrial [499], cable-based [500], and satellite-oriented [501] delivery of DVB signals. The more hostile propagation environment of the terrestrial system requires concatenated Reed–Solomon (RS) [389, 502] and rate-compatible punctured convolutional coding (RCPCC) [389, 502] combined with orthogonal frequency division multiplexing (OFDM)-based modulation [221]. By contrast, the more benign cable and satellite-based media facilitate the employment of multi-level modems using up to 256-level quadrature amplitude modulation (QAM) [221]. These schemes are capable of delivering high-definition video at bit rates of up to 20 Mbit/s in stationary broadcast-mode distributive wireless scenarios.

[12]This section is based on C. S. Lee, T. Keller, and L. Hanzo, OFDM-based turbo-coded hierarchical and non-hierarchical terrestrial mobile digital video broadcasting, *IEEE Transactions on Broadcasting*, March 2000, pp. 1-22,

Recently, a range of DVB system performance studies has been presented in the literature [503–506]. Against this background, in this contribution we have proposed turbo-coding improvements to the terrestrial DVB system [499] and investigated its performance under hostile mobile channel conditions. We have also studied various video bit-stream partitioning and channel coding schemes both in the hierarchical and nonhierarchical transceiver modes and compared their performance.

The rest of this section is divided as follows. In Section 12.7.2 the bit error sensitivity of the MPEG-2 coding parameters [507] is characterized. A brief overview of the enhanced turbo-coded and standard DVB terrestrial scheme is presented in Section 12.7.3, while the channel model is described in Section 12.7.4. Following this, in Section 12.7.5 the reader is introduced to the MPEG-2 data partitioning scheme [508] used to split the input MPEG-2 video bit-stream into two error protection classes, which can then be protected either equally or unequally. These two video bit protection classes can then be broadcast to the receivers using the DVB terrestrial hierarchical transmission format [499]. The performance of the data partitioning scheme is investigated by corrupting either the high- or low-sensitivity video bits using randomly distributed errors for a range of system configurations in Section 12.7.6, and their effects on the overall reconstructed video quality are evaluated. Following this, the performance of the improved DVB terrestrial system employing the nonhierarchical and hierarchical format [499] is examined in a mobile environment in Sections 12.7.7 and 12.7.8, before our conclusions and future work areas are presented in Section 12.7.9. We note furthermore that readers interested mainly in the overall system performance may opt to proceed directly to Section 12.7.3. Let us commence our discourse in the next section by describing an objective method of quantifying the sensitivity of the MPEG-2 video parameters.

12.7.2 MPEG-2 Bit Error Sensitivity

At this stage we again note that a number of different techniques can be used to quantify the bit error sensitivity of the MPEG-2 bits. The outcome of these investigations will depend to a degree on the video material used, the output bit rate of the video codec, the objective video-quality measures used, and the averaging algorithm employed. Perceptually motivated, subjective quality-based sensitivity testing becomes infeasible due to the large number of associated test scenarios. Hence, in this section we propose a simplified objective video-quality measure based bit-sensitivity evaluation procedure, which attempts to examine all the major factors influencing the sensitivity of MPEG-2 bits. Specifically, the proposed procedure takes into account the position and the relative frequency of the MPEG-2 parameters in the bit-stream, the number of the associated coding bits for each MPEG-2 parameter, the video bit rate, and the effect of loss of synchronization or error propagation due to corrupted bits. Nonetheless, we note that a range of similar bit-sensitivity estimation techniques exhibiting different strengths and weaknesses can be devised. No doubt future research will produce a variety of similarly motivated techniques.

In this section, we assume familiarity with the MPEG-2 standard [507, 508]. The aim of our MPEG-2 error-resilience study was to quantify the average PSNR degradation caused by each erroneously decoded video codec parameter in the bit-stream, so that appropriate protection can be assigned to each parameter. First, we define three measures, namely, the peak signal-to-noise ratio (PSNR), the PSNR degradation, and the average PSNR degradation,

which are to be used in our subsequent discussions. The PSNR is defined as follows:

$$\text{PSNR} = 10\, log_{10} \frac{\sum_{n=0}^{N} \sum_{m=0}^{M} 255^2}{\sum_{n=0}^{N} \sum_{m=0}^{M} \Delta^2}, \tag{12.24}$$

where Δ is the difference between the uncoded pixel value and the reconstructed pixel value, while the variables M and N refer to the dimension of the image. The maximum possible 8-bit pixel luminance value of 255 was used in Equation 12.24 in order to mitigate the PSNR's dependence on the video material used. The PSNR degradation is the difference between the PSNR of the decoder's reconstructed image in the event of erroneous decoding and successful decoding. The average PSNR degradation is then the mean of the PSNR degradation values computed for all the image frames of the video test sequence.

Most MPEG-2 parameters are encoded by several bits, and they may occur in different positions in the video sequence. In these different positions, they typically affect the video quality differently, since corrupting a specific parameter of a frame close to the commencement of a new picture start code results in a lesser degradation than corrupting an equivalent parameter further from the resynchronization point. Hence the sensitivity of the MPEG-2 parameters is position-dependent. Furthermore, different encoded bits of the same specific MPEG-2 parameter may exhibit different sensitivity to channel errors. Figure 12.71 shows such an example for the parameter known as intra_dc_precision [507], which is coded under the picture coding extension [508]. In this example, the PSNR degradation profiles due to bit errors being inflicted on the parameter intra_dc_precision of frame 28 showed that the degradation is dependent on the significance of the bit considered. Specifically, errors in the most significant bit (MSB) caused an approximately 3 dB higher PSNR degradation than the least significant bit (LSB) errors. Furthermore, the PSNR degradation due to an MSB error of the intra_dc_precision parameter in frame 73 is similar to the PSNR degradation profile for the MSB of the intra_dc_precision parameter of frame 28. Due to the variation of the PSNR degradation profile for the bits of different significance of a particular parameter, as well as for the same parameter at its different occurrences in the bit-stream, it is necessary to determine the *average* PSNR degradation for each parameter in the MPEG-2 bit-stream.

Our approach in obtaining the average PSNR degradation was similar to that suggested in the literature [194, 509]. Specifically, the average measure used here takes into account the significance of the bits corresponding to the MPEG-2 parameter concerned, as well as the occurrence of the same parameter at different locations in the encoded video bit-stream. In order to find the average PSNR degradation for each MPEG-2 bit-stream parameter, the different bits encoding a specific parameter, as well as the bits of the same parameter but occurring at different locations in the MPEG-2 bit-stream, were corrupted and the associated PSNR degradation profile versus frame index was registered. The observed PSNR degradation profile generated for different locations of a specific parameter was then used to compute the average PSNR degradation. As an example, we will use the PSNR degradation profile shown in Figure 12.71. This figure presents three degradation profiles. The average PSNR degradation for each profile is first computed in order to produce three average PSNR degradation values corresponding to the three respective profiles. The mean of these three PSNR averages will then form the final average PSNR degradation for the intra_dc_precision parameter. The same process is repeated for all MPEG-2 parameters from the picture layer up to the block layer. The difference with respect to the approach adopted in [194, 509] was that while in [194, 509] the average PSNR degradation was acquired for each bit of the output

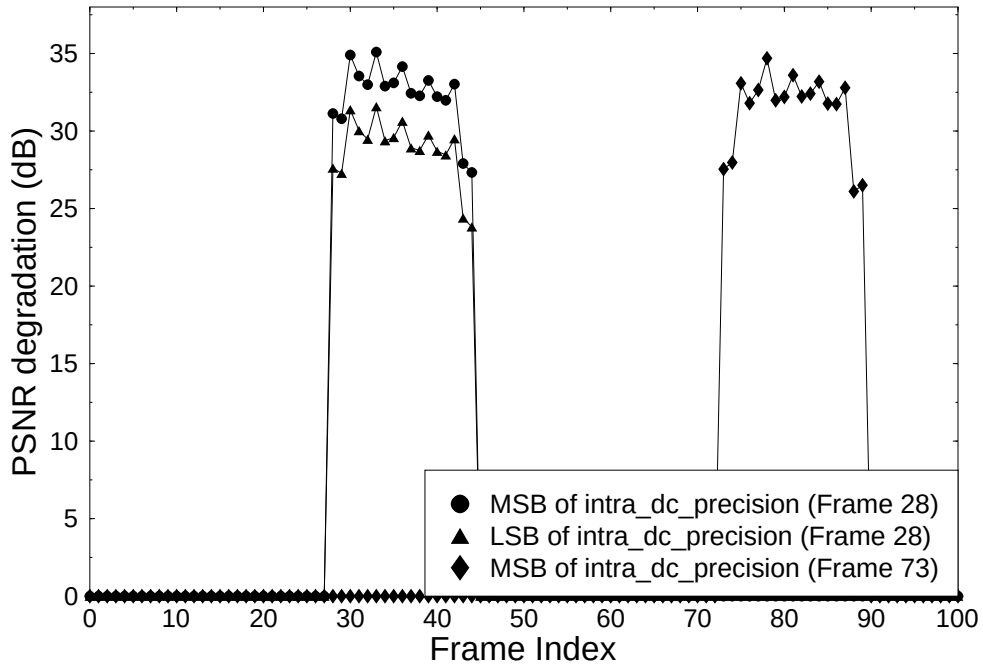

Figure 12.71: PSNR degradation profile for the different bits used to encode the intra_dc_precision parameter [507] in different corrupted video frames for the "Miss America" QCIF video sequence encoded at 30 frame/s and 1.15 Mbit/s.

bit-stream, we have adopted a simpler approach in this contribution due to the large number of different parameters within the MPEG-2 bit-stream. Figures 12.72 to 12.74 show the typical average PSNR degradations of the various MPEG-2 parameters of the picture header information, picture coding extension, slice layer macroblock layer and block layer [508], which were obtained using the 176×144 quarter common intermediate format (QCIF) "Miss America" (MA) video sequence at 30 frames/s and a high average bit rate of 1.15 Mbit/s.

The different MPEG-2 parameters or code words occur with different probabilities, and they are allocated different numbers of bits. Therefore, the average PSNR degradation registered in Figures 12.72 to 12.74 for each MPEG-2 parameter was multiplied, with the long-term probability of this MPEG-2 parameter occurring in the MPEG-2 bit-stream and with the relative probability of bits being allocated to that MPEG-2 parameter. Figures 12.75 and 12.76 show the occurrence probability of the various MPEG-2 parameters characterized in Figures 12.72 to 12.74 and the probability of bits allocated to the parameters in the picture header information, picture coding extension, as well as in the slice, macroblock, and block layers [508], respectively, for the QCIF MA video sequence encoded at 1.15 Mbit/s.

We will concentrate first on Figure 12.75(a). It is observed that all parameters — except for the full_pel_forward_vector, forward_f_code, full_pel_backward_vector, and backward_f_code — have the same probability of occurrence, since they appear once for every coded video frame. The parameters full_pel_forward_vector and forward_f_code have a higher probability of occurrence than full_pel_backward_vector and backward_f_code, since the former

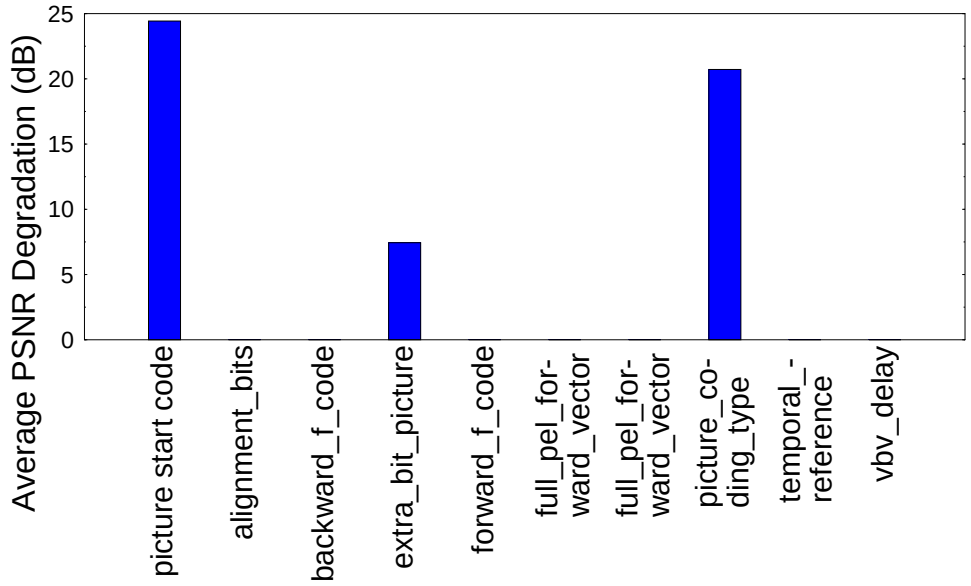

Figure 12.72: Average PSNR degradation for the various MPEG-2 parameters in picture header information for the "Miss America" QCIF video sequence encoded at 30 frame/s and 1.15 Mbit/s.

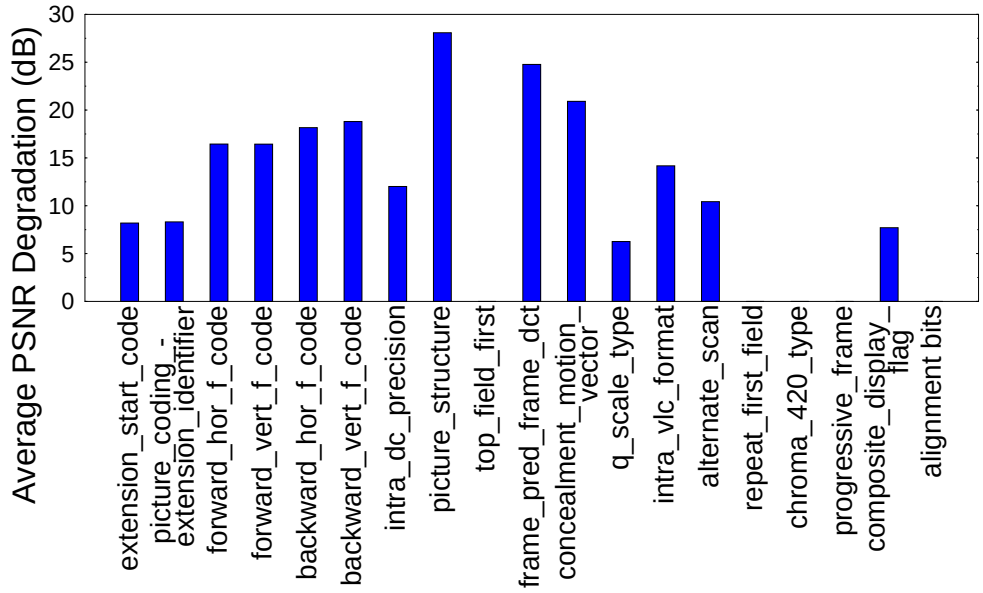

Figure 12.73: Average PSNR degradation for the various MPEG-2 parameters in picture coding extension for the "Miss America" QCIF video sequence encoded at 30 frame/s and 1.15 Mbit/s.

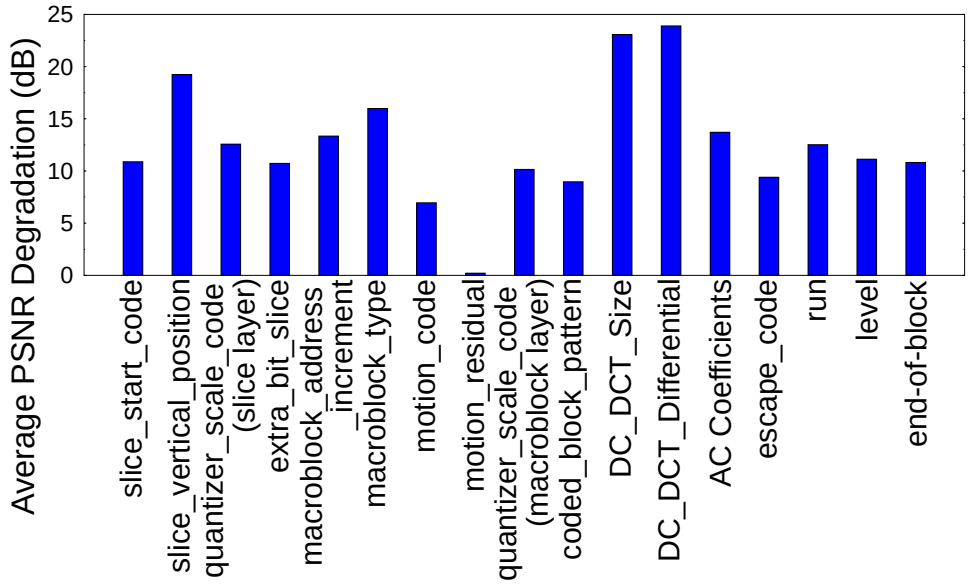

Figure 12.74: Average PSNR degradation for the various MPEG-2 parameters in slice, macroblock, and block layers for the "Miss America" QCIF video sequence encoded at 30 frame/s and 1.15 Mbit/s.

two appear in both P frames and B frames, while the latter two only occur in B frames. For our experiments, the MPEG-2 encoder was configured so that for every encoded P frame, there were two encoded B frames. However, when compared with the parameters from the slice layer, macroblock layer, and block layer, which are characterized by the bar chart of Figure 12.75(b), the parameters of the picture header information and picture coding extension appeared significantly less frequently.

If we compare the occurrence frequency of the parameters in the slice layer with those in the macroblock and block layers, the former appeared less often, since there were 11 macroblocks and 44 blocks per video frame slice for the QCIF "Miss America" video sequence were considered in our experiments. The AC discrete cosine transform (DCT) [177] coefficient parameter had the highest probability of occurrence, exceeding 80%.

Figure 12.76 shows the probability of bits being allocated to the various MPEG-2 parameters in the picture header information, picture coding extension, slice, macroblock and block layers [508]. Figure 12.77 was included to more explicitly illustrate the probability of bit allocation seen in Figure 12.76(b), with the probability of allocation of bits to the AC DCT coefficients being omitted from the bar chart. Considering Figure 12.76(a), the two dominant parameters, with the highest number of encoding bits requirement are the picture start code (PSC) and the picture coding extension start code (PCESC). However, comparing these probabilities with the probability of bits being allocated to the various parameters in the slice, macroblock, and block layers, we see that the percentage of bits allocated can still be considered minimal due to their infrequent occurrence. In the block layer, the AC DCT coefficients require in excess of 85% of the bits available for the whole video sequence. However,

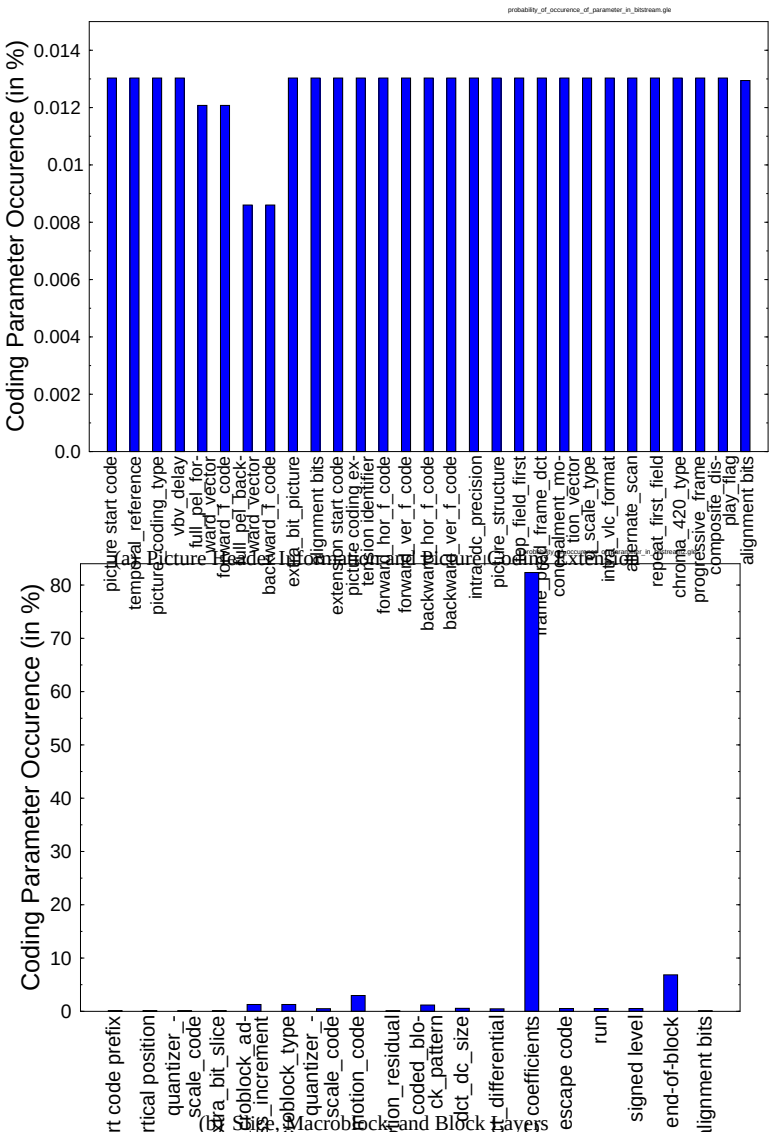

(a) Picture Header Information and Picture Coding Extension

(b) Slice, Macroblock, and Block Layers

Figure 12.75: Occurrence probabilities for the various MPEG-2 parameters characterized in Figure 12.72 to Figure 12.74. (a) Picture header information and picture coding extension. (b) Slice, macroblock, and block layers for the "Miss America" QCIF video sequence encoded at 30 frame/s and 1.15 Mbit/s.

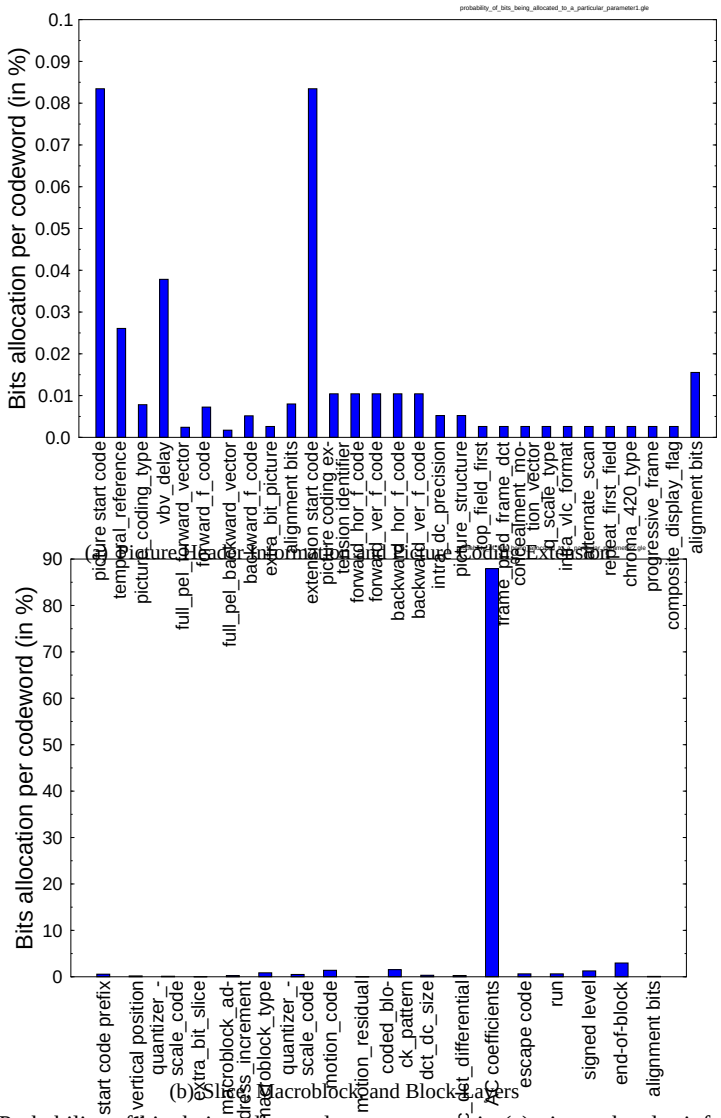

Figure 12.76: Probability of bits being allocated to parameters in (a) picture header information and picture coding extension; and (b) Slice, macroblock, and block layers for the “Miss America” QCIF video sequence encoded at 30 frame/s and 1.15 Mbit/s.

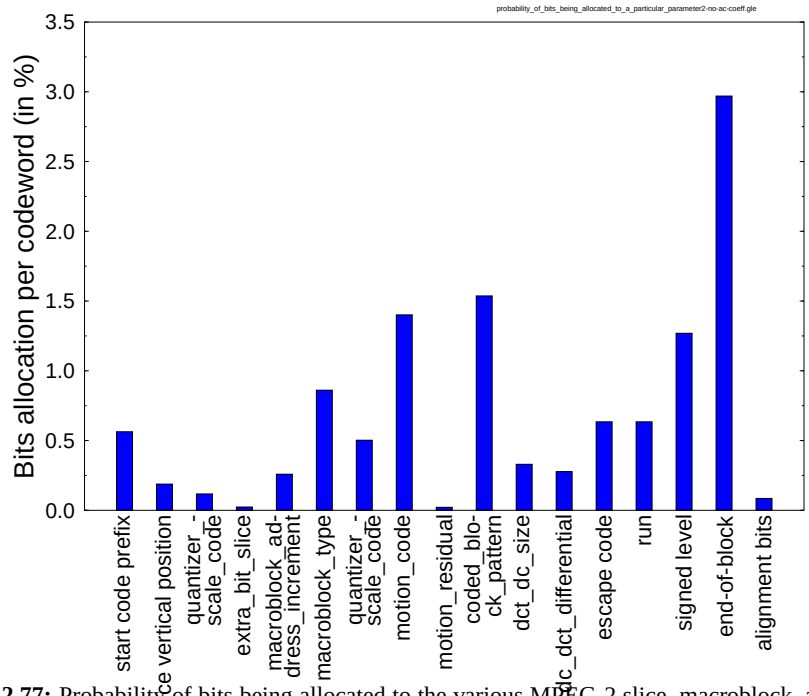

Figure 12.77: Probability of bits being allocated to the various MPEG-2 slice, macroblock, and block layer parameters, as seen in Figure 12.76(b), where the probability of bits allocated to the AC DCT coefficients was omitted in order to show the allocation of bits to the other parameters more clearly. This probability of bits allocation to the various MPEG-2 parameters is associated with the "Miss America" QCIF video sequence encoded at 30 frame/s and 1.15 Mbit/s.

at bit rates lower than 1.15 Mbit/s the proportion of AC coefficient encoding bits was significantly reduced, as illustrated by Figure 12.78. Specifically, at 30 frame/s and 1.15 Mbit/s, the average number of bits per video frame is about 38,000 and a given proportion of these bits is allocated to the MPEG-2 control header information, motion information, and the DCT coefficients. Upon reducing the total bit rate budget — since the number of control header bits is more or less independent of the target bit rate — the proportion of bits allocated to the DCT coefficients is substantially reduced. This is explicitly demonstrated in Figure 12.78 for bit rates of 1.15 Mbit/s and 240 kbit/s for the "Miss America" QCIF video sequence.

The next process, as discussed earlier, was to normalize the measured average PSNR degradation according to the occurrence probability of the respective MPEG-2 parameters in the bit-stream and the probability of bits being allocated to this parameter. The normalized average PSNR degradation caused by corrupting the parameters of the picture header information and picture coding extension [508] is portrayed in Figure 12.79(a). Similarly, the normalized average PSNR degradation for the parameters of the slice, macroblock, and block layers is shown in Figure 12.79(b). In order to visually enhance Figure 12.79(b), the normalized average PSNR degradation for the AC DCT coefficients was omitted in the bar chart shown in Figure 12.80.

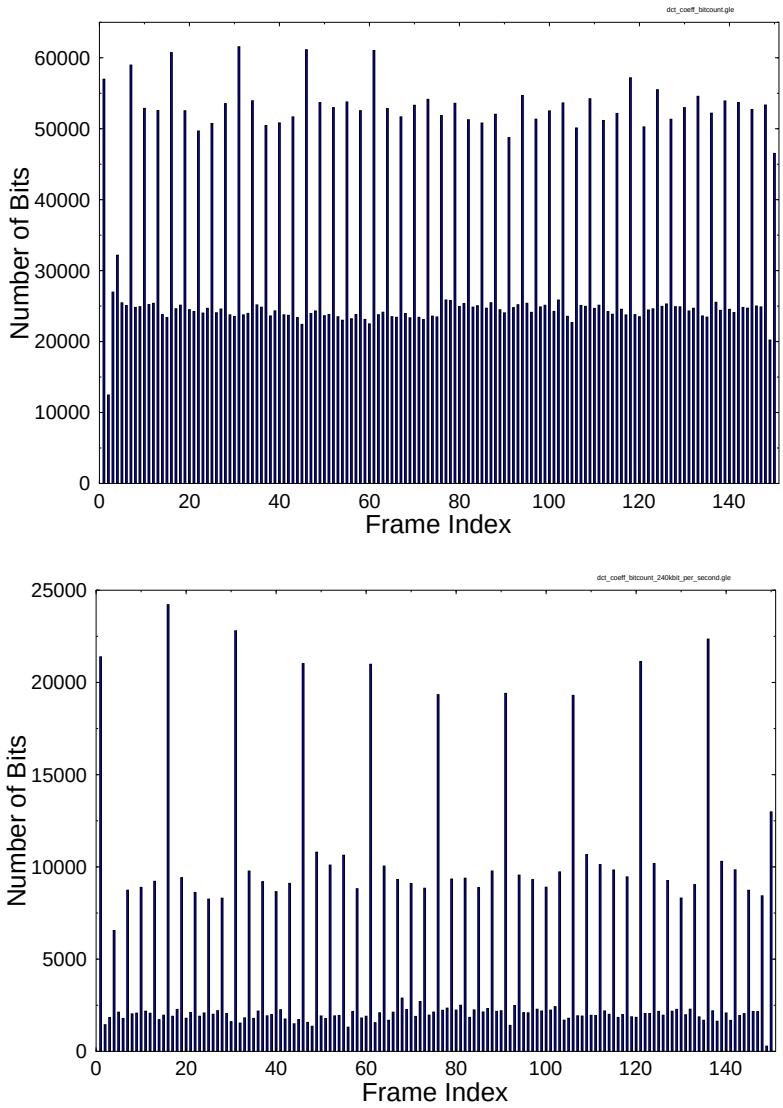

Figure 12.78: Profile of bits allocated to the DCT coefficients, when the 30 frame/s QCIF "Miss America" video sequence is coded at (a) 1.15 Mbit/s (top) and (b) 240 kbit/s (bottom). The sequence of frames is in the order I B B, P B B, P B B, P B B, and so on.

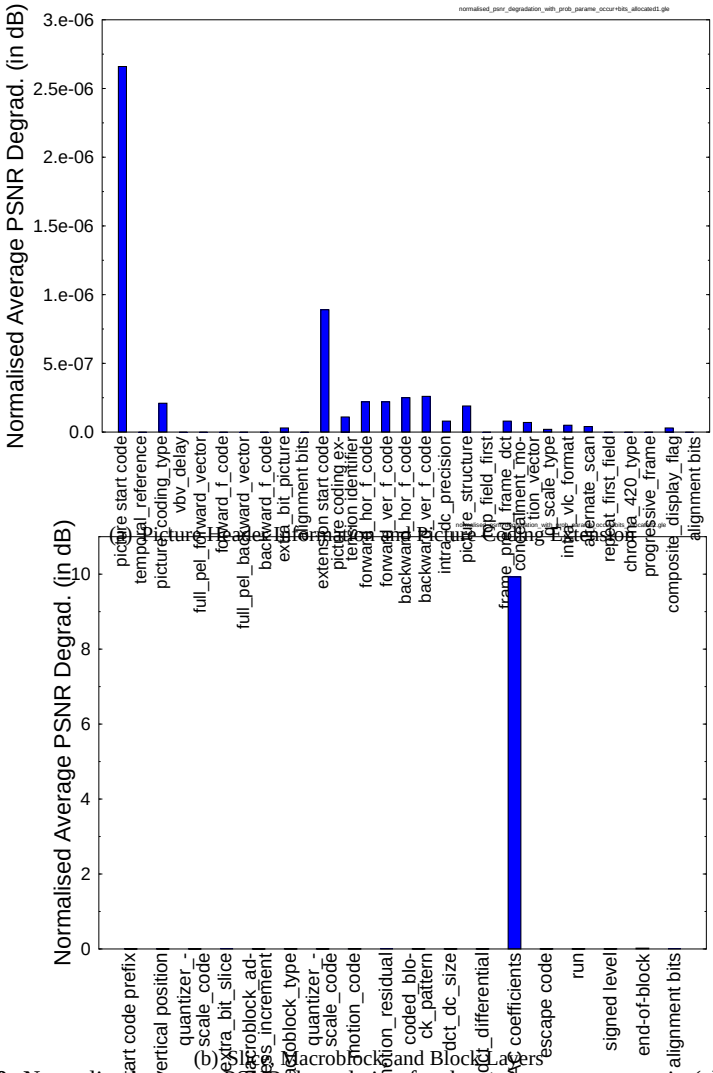

(a) Picture Header Information and Picture Coding Extension

(b) Slice, Macroblock and Block Layers

Figure 12.79: Normalized average PSNR degradation for the various parameters in (a) picture header information and picture coding extension (b) slice, macroblock, and block layers, normalized to the occurrence probability of the respective parameters in the bit-stream and the probability of bits being allocated to the parameter for the "Miss America" QCIF video sequence encoded at 30 frame/s and 1.15 Mbit/s.

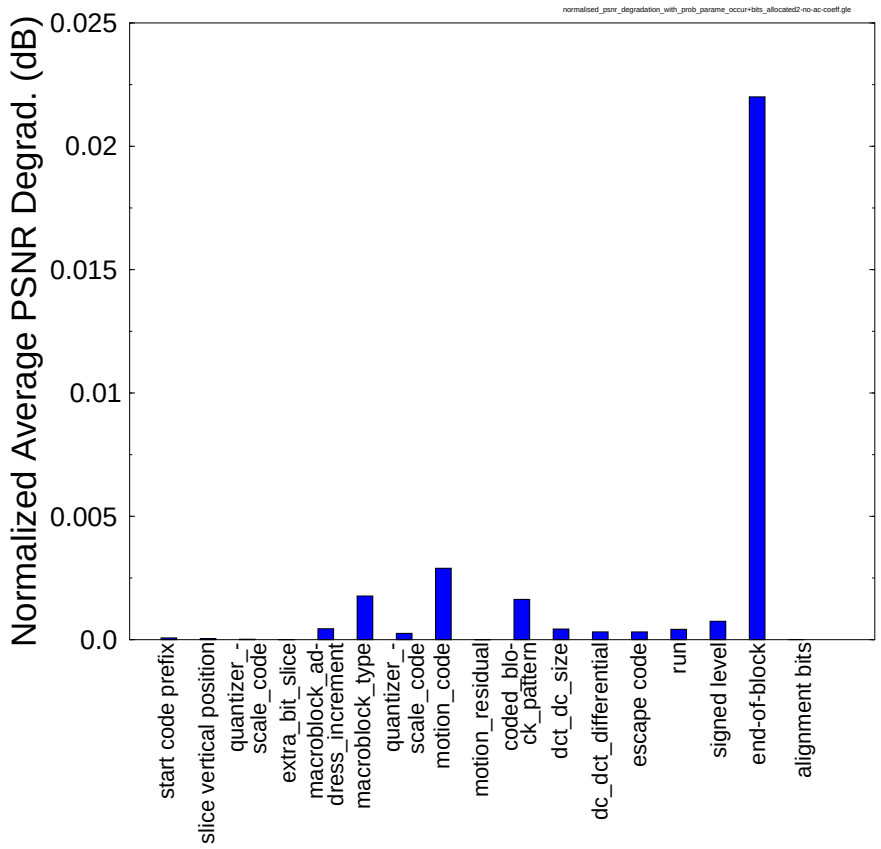

Figure 12.80: This bar chart is the same as Figure 12.79(b), although the normalized average PSNR degradation for the AC DCT coefficients was omitted in order to show the average PSNR degradation of the other parameters. This bar chart is presented for the "Miss America" QCIF video sequence encoded at 30 frame/s and 1.15 Mbit/s case.

The highest PSNR degradation was inflicted by the AC DCT coefficients, since these parameters occur most frequently and hence are allocated the highest number of bits. When a bit error occurs in the bit-stream, the AC DCT coefficients have a high probability of being corrupted. The other parameters, such as DC_DCT_size and DC_DCT_differential, exhibited high average PSNR degradations when corrupted, but registered low normalized average PSNR degradations since their occurrence in the bit-stream is confined to the infrequent intra-coded frames.

The end-of-block MPEG-2 parameter exhibited the second highest normalized average PSNR degradation in this study. Although the average number of bits used for the end-of-block is only approximately 2.17 bits, the probability of occurrence and the probability of bits being allocated to it are higher than for other parameters, with the exception of the AC DCT coefficients. Furthermore, in general, the parameters of the slice, macroblock, and block layers exhibit higher average normalized PSNR degradations due to their more frequent

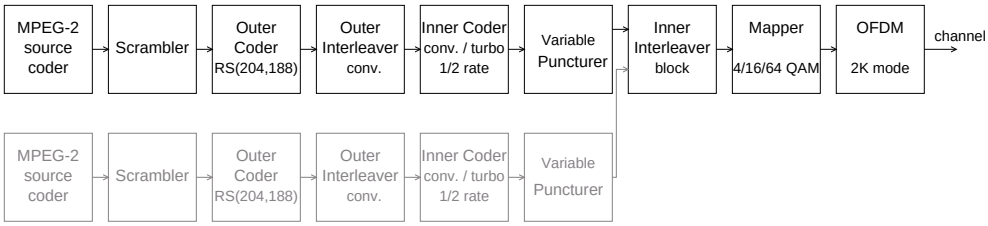

Figure 12.81: Schematic of the DVB terrestrial transmitter functions.

occurrence in the bit-stream compared to the parameters that belong to the picture header information and to the picture coding extension. This also implies that the percentage of bits allocated to these parameters is higher.

Comparing the normalized average PSNR degradations of the parameters in the picture header information and picture coding extension, we observe that the picture start code (PSC) exhibits the highest normalized average PSNR degradation. Although most of the parameters here occur with equal probability as seen in Figure 12.75(a), the picture start code requires a higher portion of the bits compared to the other parameters, with the exception of the extension start code. Despite having the same probability of occurrence and the same allocation of bits, the extension start code exhibits a lower normalized PSNR degradation than the picture start code, since its average unnormalized degradation is lower, as shown in Figure 12.72 to Figure 12.74.

In Figures 12.79 and 12.80, we observed that the video PSNR degradation was dominated by the erroneous decoding of the AC DCT coefficients, which appeared in the MPEG-2 video bit-stream in the form of variable-length codewords. This suggests that unequal error protection techniques be used to protect the MPEG-2 parameters during transmission. In a low-complexity implementation, two protection classes may be envisaged. The higher priority class would contain all the important header information and some of the more important low-frequency variable-length coded DCT coefficients. The lower priority class would then contain the remaining less important, higher frequency variable-length coded DCT coefficients. This partitioning process will be detailed in Section 12.7.5 together with its associated performance in the context of the hierarchical DVB [499] transmission scheme in Section 12.7.8. Let us, however, first consider the architecture of the investigated DVB system in the next section.

12.7.3 DVB Terrestrial Scheme

The block diagram of the DVB terrestrial (DVB-T) transmitter [499] is shown in Figure 12.81, which consists of an MPEG-2 video encoder, channel-coding modules, and an orthogonal frequency division multiplex (OFDM) modem [221, 510]. The bitstream generated by the MPEG-2 encoder is packetized into frames 188 bytes long. The video data in each packet is then randomized by the scrambler of Figure 12.81. The specific details concerning the scrambler have not been included in this chapter since they may be obtained from the DVB-T standard [499].

Because of the poor error resilience of the MPEG-2 video codec, powerful concatenated

Convolutional Coder Parameters	
Code rate	$1/2$
Constraint length	7
n	2
k	1
Generator polynomials (octal format)	171, 133

Table 12.16: Parameters of the $CC(n, k, K)$ Convolutional Inner Encoder of the DVB-T Modem

channel coding is employed. The concatenated channel codec of Figure 12.81 comprises a shortened Reed–Solomon (RS) outer code and an inner convolutional encoder. The 188-byte MPEG-2 video packet is extended by the Reed–Solomon encoder [389, 502], with parity information to facilitate error recovery in order to form a 204-byte packet. The Reed–Solomon decoder can then correct up to 8 erroneous bytes for each 204-byte packet. Following this, the RS-coded packet is interleaved by a convolutional interleaver and further protected by a half-rate inner convolutional encoder using a constraint length of 7 [389, 502].

Furthermore, the overall code rate of the concatenated coding scheme can be adapted by variable puncturing that supports code rates of $1/2$ (no puncturing) as well as $2/3$, $3/4$, $5/6$, and $7/8$. The parameters of the convolutional encoder are summarized in Table 12.16.

If only one of the two branches of the transmitter in Figure 12.81 is utilized, the DVB-T modem is said to be operating in its nonhierarchical mode. In this mode, the modem can have a choice of QPSK, 16QAM, or 64QAM modulation constellations [221].

A second video bit-stream can also be multiplexed with the first one by the inner interleaver, when the DVB modem is in its hierarchical mode [499]. The choice of modulation constellations in this mode is between 16QAM and 64QAM. We employ this transmission mode when the data partitioning scheme of Section 12.7.5 is used to split the incoming MPEG-2 video bit-stream into two video bit-protection classes, with one class having a higher grade of protection or priority than the other one. The higher priority video bits will be mapped to the MSBs of the modulation constellation points and the lower priority video bits to the LSBs of the QAM-constellation [221]. For 16QAM and 64QAM, the two MSBs of each 4-bit or 6-bit QAM symbol will contain the more important video data. The lower priority video bits will then be mapped to the lower significance 2 bits and 4 bits of 16QAM and 64QAM, respectively [221].

These QPSK, 16QAM, or 64QAM symbols are then distributed over the OFDM carriers [221]. The parameters of the OFDM system are presented in Table 12.17.

Besides implementing the standard DVB-T system as a benchmark, we have improved the system by replacing the convolutional coder with a turbo codec [401, 402]. The turbo codec's parameters used in our investigations are displayed in Table 12.18. The block diagram of the turbo encoder is shown in Figure 12.82. The turbo encoder is constructed of two component encoders. Each component encoder is a half-rate convolutional encoder whose parameters are listed in Table 12.18. The two-component encoders are used to encode the same input bits, although the input bits of the second component encoder are interleaved before encoding. The output bits of the two-component codes are punctured and multiplexed in order to form a single-output bit-stream. The component encoder used here is known as a half-rate recursive systematic convolutional encoder (RSC) [511]. It generates one parity bit and one systematic

OFDM Parameters	
Total number of subcarriers	2048 (2 K mode)
Number of effective subcarriers	1705
OFDM symbol duration T_s	224 μs
Guard interval	$T_s/4 = 56\mu$s
Total symbol duration (inc. guard interval)	280 μs
Consecutive subcarrier spacing $1/T_s$	4464 Hz
DVB channel spacing	7.61 MHz
QPSK and QAM symbol period	7/64 μs

Table 12.17: Parameters of the OFDM Module Used in the DVB-T Modem [499]

Turbo Coder Parameters	
Turbo code rate	$1/2$
Input block length	17, 952 bits
Interleaver type	Random
Number of turbo-decoder iterations	8
Turbo Encoder Component Code Parameters	
Component code encoder type	Recursive Systematic Convolutional (RSC)
Component code decoder type	log-MAP [452]
Constraint length	3
n	2
k	1
Generator polynomials (octal format)	7, 5

Table 12.18: Parameters of the Inner Turbo Encoder Used to Replace the DVB-T System's $K = 7$ Convolutional Encoder of Table 12.16 (RSC: recursive systematic code)

output bit for every input bit. In order to provide an overall coding rate of $R = 1/2$, half the output bits from the two encoders must be punctured. The puncturing arrangement used in our work is to transmit all the systematic bits from the first encoder and every other parity bit from both encoders [512]. We note here that one iteration of the turbo decoder involves two Logarithmic Maximum A-Posteriori (log-MAP) [452] decoding operations, which we repeated for the eight iterations. Hence, the total turbo decoding complexity is about 16 times higher than a constraint length $K = 3$ constituent convolutional decoding. Therefore, the turbo decoder exhibits a similar complexity to the $K = 7$ convolutional decoder.

In this section, we have given an overview of the standard and enhanced DVB-T system, which we have used in our experiments. Readers interested in further details of the DVB-T system are referred to the DVB-T standard [499]. The performance of the standard DVB-T system and the turbo-coded system is characterized in Sections 12.7.7 and 12.7.8 for nonhierarchical and hierarchical transmissions, respectively. Let us now briefly consider the

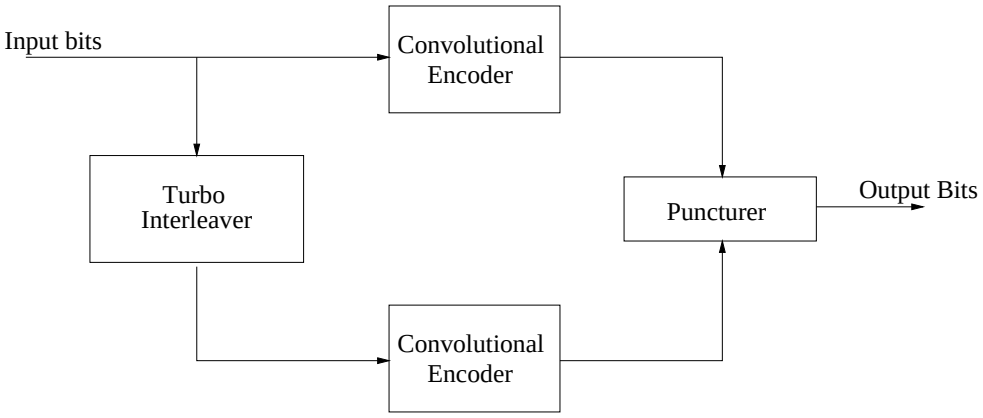

Figure 12.82: Block diagram of turbo encoder

multipath channel model used in our investigations.

12.7.4 Terrestrial Broadcast Channel Model

The channel model employed in this study was the 12-path COST 207 [513] hilly terrain (HT) type impulse response, with a maximal relative path delay of 19.9 μs. This channel was selected in order to provide a worst-case propagation scenario for the DVB-T system employed in our study.

In the system described here, we have used a carrier frequency of 500 MHz and a sampling rate of 7/64 μs. Each of the channel paths was faded independently obeying a Rayleigh-fading distribution, according to a normalized Doppler frequency of 10^{-5} [389]. This corresponds to a worst-case vehicular velocity of about 200 km/h. The unfaded impulse response is depicted in Figure 12.83. For the sake of completeness we note that the standard COST 207 channel model was defined in order to facilitate the comparison of different GSM implementations [389] under identical conditions. The associated bit rate was 271 kbit/s, while in our investigations the bit rate of DVB-quality transmissions can be as high as 20 Mbit/s, where a higher number of resolvable multipath components within the dispersion-range is considered. However, the performance of various wireless tranceivers is well understood by the research community over this standard COST 207 channel. Hence, its employment is beneficial in benchmarking terms. Furthermore, since the OFDM modem has 2048 subcarriers, the subcarrier signaling rate is effectively 2000-times lower than our maximum DVB-rate of 20 Mbit/s, corresponding to 10 kbit/s. At this subchannel rate, the individual subchannel can be considered nearly frequency-flat. In summary, in conjunction with the 200 km/h vehicular speed the investigated channel conditions constitute a pessimistic scenario.

In order to facilitate unequal error protection, the data partitioning procedure of the MPEG-2 video bit-stream is considered next.

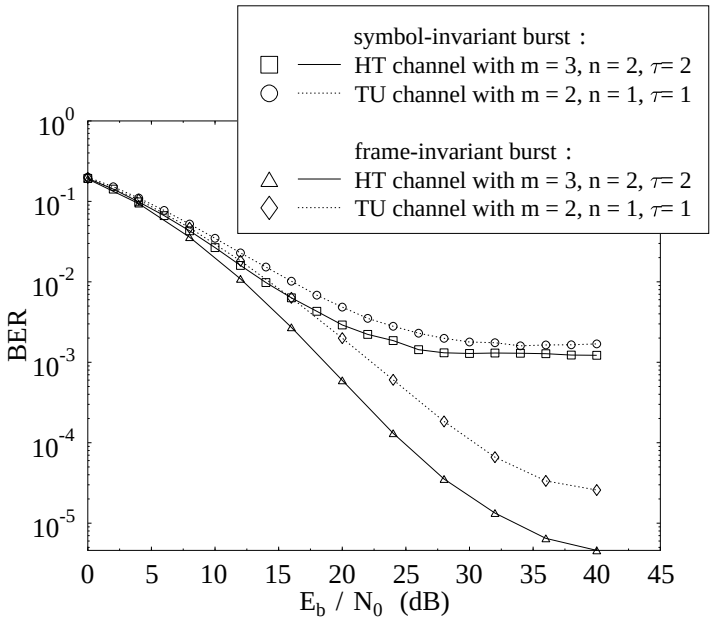

Figure 12.83: COST 207 hilly terrain (HT) type impulse response.

12.7.5 Data Partitioning Scheme

Efficient bit-stream partitioning schemes for H.263-coded video were proposed, for example, by Gharavi and Alamouti [514], and were evaluated in the context of the third-generation mobile radio standard proposal known as IMT-2000 [389]. As portrayed in Figures 12.79 and 12.80, the corrupted variable-length coded DCT coefficients produce a high video PSNR degradation. Assuming that all MPEG-2 header information is received correctly, the fidelity of the reconstructed images at the receiver is dependent on the number of correctly decoded DCT coefficients. However, the subjective effects of losing higher spatial frequency DCT coefficients are less dramatic compared to those of the lower spatial frequency DCT coefficients. The splitting of the MPEG-2 video bit-stream into two different integrity bit-streams is termed data partitioning [508]. Recall from Section 12.7.3 that the hierarchical 16-QAM and 64-QAM DVB-T transmission scheme enables us to multiplex two unequally protected MPEG-2 video bit-streams for transmission. This section describes the details of the MPEG-2 data partitioning scheme [508].

Figure 12.84 shows the block diagram of the data partitioning scheme, which splits an MPEG-2 video bit-stream into two resultant bit-streams. The position at which the MPEG-2 bit-stream is split is based on a variable referred to as the priority breakpoint (PBP) [508]. The PBP can be adjusted at the beginning of the encoding of every MPEG-2 image slice, based on the buffer occupancy or fullness of the two output buffers. For example, if the high-priority buffer is 80% full and the low-priority buffer is only 40% full, the rate-control module will

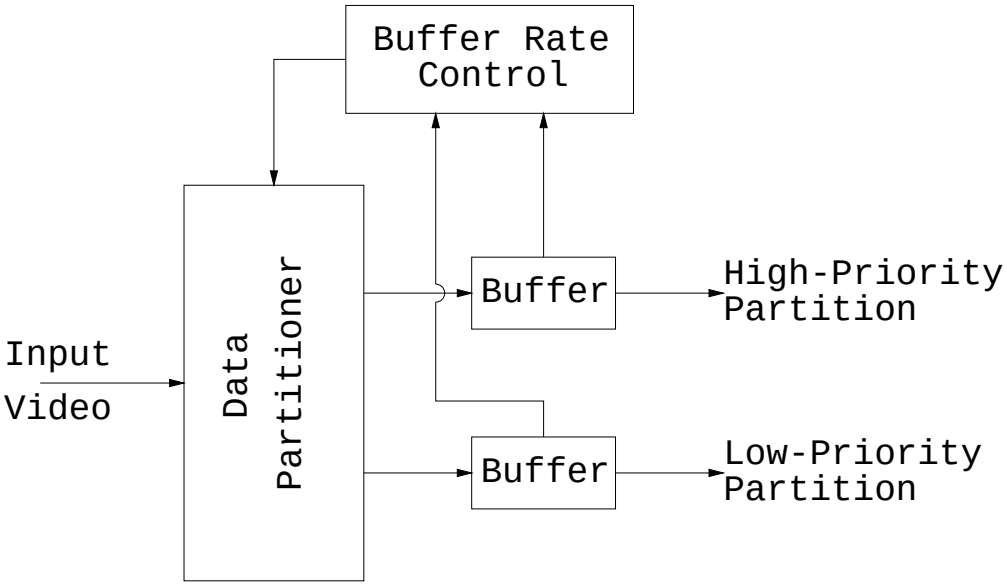

Figure 12.84: Block diagram of the data partitioner and rate controller.

PBP	Syntax Elements in High-Priority Partition
0	Low-priority partition always has its PBP set to 0.
1	Sequence, GOP, picture and slice layer information up to extra bit slice.
2	Same as above and up to macroblock address increment.
3	Same as above plus including macroblock syntax elements but excluding coded block pattern.
4 – 63	Reserved for future use.
64	Same as above plus including DC DCT coefficient and the first run-length coded DCT coefficient.
65	Same as above and up to the second run-length coded DCT coefficient.
64 + x	Same as above and up to x run-length coded DCT coefficient.
127	Same as above and up to 64 run-length coded DCT coefficient.

Table 12.19: Priority breakpoint values and the associated MPEG-2 parameters that will be directed to the high-priority partition [508]. A higher PBP directs more parameters to the high-priority partition. By contrast, for the low-priority partition a higher PBP implies obtaining less data

have to adjust the PBP so that more data is directed to the low-priority partition. This measure is taken to avoid high-priority buffer overflow and low-priority buffer underflow events. The values for the MPEG-2 PBP are summarized in Table 12.19 [508].

There are two main stages in updating the PBP. The first stage involves the rate-control module of Figure 12.84 in order to decide on the preferred new PBP value for each partition based on its individual buffer occupancy and on the current value of the PBP. The second stage then combines the two desired PBPs based on the buffer occupancy of both buffers in

order to produce a new PBP.

The updating of the PBP in the first stage of the rate control module is based on a heuristic approach, similar to that suggested by Aravind *et al.* [515]. The update procedure is detailed in Algorithm 1, which is discussed below and augmented by a numerical example at the end of this section.

The variable "sign" is used in Algorithm 1, in order to indicate how the PBP has to be adjusted in the high- and low-priority MPEG-2 partitions, so as to arrive at the required target buffer occupancy. More explicitly, the variable "sign" in Algorithm 1 is necessary because the MPEG-2 PBP values [508] shown in Table 12.19 indicate the amount of information that should be directed to the high-priority partition. Therefore, if the low-priority partition requires more data, then the new PBP must be lower than the current PBP. By contrast, for the high-priority partition a higher PBP implies obtaining more data.

Once the desired PBPs for both partitions have been acquired with the aid of Algorithm 1, Algorithm 2 is used to compute the final PBP for the current MPEG-2 image slice. The inner workings of these algorithms are augmented by a numerical example at the end of this section. There are two main cases to consider in Algorithm 2. The first one occurs when both partitions have a buffer occupancy of less than 50%. By using the reciprocal of the buffer occupancy in Algorithm 2 as a weighting factor during the computation of the PBP adjustment value "delta," the algorithm will favor the new PBP decision of the less occupied buffer in order to fill the buffer with more data in the current image slice. This is simply because the buffer is closer to underflow; hence, increasing the PBP according to its instructions will assist in preventing the particular buffer from underflowing. On the other hand, when both buffers experience a buffer occupancy of more than 50%, the buffer occupancy itself is used as a weighting factor instead. Now the algorithm will instruct the buffer having a higher occupancy to adjust its desired PBP so that less data is inserted into it in the current MPEG-2 image slice. Hence, buffer overflow problems are alleviated with the aid of Algorithm 1 and Algorithm 2.

The new PBP value is then compared to its legitimate range tabulated in Table 12.19. Furthermore, we restricted the minimum PBP value so that I-, P-, and B-pictures have minimum PBP values of 64, 3, and 2, respectively. Since B-pictures are not used for future predictions, it was decided that their data need not be protected as strongly as the data for I- and P-pictures. As for P-pictures, Ghanbari and Seferidis [323] showed that correctly decoded motion vectors alone can still provide a subjectively pleasing reconstruction of the image, even if the DCT coefficients were discarded. Hence, the minimum MPEG-2 bit-stream splitting point or PBP for P-pictures has been set to be just before the coded block pattern parameter, which would then ensure that the motion vectors would be mapped to the high-priority partition. Upon receiving corrupted DCT coefficients, they would be set to zero, which corresponds to setting the motion-compensated error residual of the macroblock concerned to zero. For I-pictures, the fidelity of the reconstructed image is dependent on the number of DCT coefficients that can be decoded successfully. Therefore, the minimum MPEG-2 bit-stream splitting point or PBP was set to include at least the first run-length-coded DCT coefficient.

Below we demonstrate the operation of Algorithm 1 and Algorithm 2 with the aid of a simple numerical example. We will assume that the PBP prior to the update is 75 and that the buffer occupancy for the high- and low-priority partition buffers is 40% and 10%, respectively. Considering the high-priority partition, according to the buffer occupancy of 40% Algorithm 1 will set the desired PBP update difference denoted by "diff" for the PBP

Algorithm 1 Computes the desired PBP update for the high- and low-priority partitions which is then passed to Algorithm 2, in order to determine the PBP to be set for the current image slice.

Step 1: Initialize parameters
  if High Priority Partition **then**
    sign := +1
  else
    sign := −1
  end if

Step 2:
  if buffer occupancy ≥ 80% **then**
    diff := 64 − PBP
  end if

  if buffer occupancy ≥ 70% **and** buffer occupancy < 80% **then**
    if PBP ≥ 100 **then**
      diff := −9
    end if
    if PBP ≥ 80 **and** PBP < 100 **then**
      diff := −5
    end if
    if PBP ≥ 64 **and** PBP < 80 **then**
      diff := −2
    end if
  end if

  if buffer occupancy ≥ 50% **and** buffer occupancy < 70% **then**
    diff := +1
  end if

  if buffer occupancy < 50% **then**
    if PBP ≥ 80 **then**
      diff := +1
    end if
    if PBP ≥ 70 **and** PBP < 80 **then**
      diff := +2
    end if
    if PBP ≥ 2 **and** PBP < 70 **then**
      diff := +3
    end if
  end if

Step 3:
  diff := sign × diff
  Return diff

Algorithm 2 Computes the new PBP for the current image slice based on the current buffer occupancy of both partitions

Step 1:

if $\text{Occupancy}_{HighPriority} < 50\%$ **and** $\text{Occupancy}_{LowPriority} < 50\%$
or $\text{Occupancy}_{HighPriority} = 50\%$ **and** $\text{Occupancy}_{LowPriority} < 50\%$
or $\text{Occupancy}_{HighPriority} < 50\%$ **and** $\text{Occupancy}_{LowPriority} = 50\%$
or $\text{Occupancy}_{HighPriority} < 25\%$ **and** $50\% < \text{Occupancy}_{LowPriority} < 70\%$
or $50\% < \text{Occupancy}_{HighPriority} < 70\%$ **and** $\text{Occupancy}_{LowPriority} < 25\%$

then

$$\text{delta} := \frac{\text{Occupancy}_{HighPriority}^{-1} \times \text{diff}_{HighPriority} + \text{Occupancy}_{LowPriority}^{-1} \times \text{diff}_{LowPriority}}{\text{Occupancy}_{HighPriority}^{-1} + \text{Occupancy}_{LowPriority}^{-1}}$$

else

$$\text{delta} := \frac{\text{Occupancy}_{HighPriority} \times \text{diff}_{HighPriority} + \text{Occupancy}_{LowPriority} \times \text{diff}_{LowPriority}}{\text{Occupancy}_{HighPriority} + \text{Occupancy}_{LowPriority}}$$

end if

Step 2:

New_PBP := Previous_PBP + $\lceil$delta$\rceil$ where $\lceil\rceil$ means rounding up to the nearest integer
Return New_PBP

to $+2$. This desired update is referred to as $\text{diff}_{HighPriority}$ in Algorithm 2. For the low-priority partition, according to the buffer occupancy of 10%, Algorithm 1 will set the desired update for the PBP to -2, since the sign of diff is changed by Algorithm 1. The desired PBP update for the low-priority partition is referred to as $\text{diff}_{LowPriority}$ in Algorithm 2. Since the occupancy of both partition buffers' is less than 50%, Algorithm 2 will use the reciprocal of the buffer occupancy as the weighting factor, which will then favor the desired update of the low-priority partition due to its 10% occupancy. The final update value, which is denoted by delta in Algorithm 2, is equal to -2 (after being rounded up). Hence, according to Step 2 of Algorithm 2, the new PBP is 73. This means that for the current MPEG-2 image slice more data will be directed into the low-priority partition in order to prevent buffer underflow since PBP was reduced from 75 to 73 according to Table 12.19.

Apart from adjusting the PBP values from one MPEG-2 image slice to another to avoid buffer underflow or overflow, the output bit rate of each partition buffer must be adjusted so that the input bit rate of the inner interleaver and modulator in Figure 12.81 is properly matched between the two partitions. Specifically, in the 16QAM mode the two modem subchannels have an identical throughput of 2 bits per 4-bit symbol. By contrast, in the 64QAM mode there are three 2-bit subchannels per 6-bit 64QAM symbol, although the standard [499] recommends using a higher-priority 2-bit and a lower-priority 4-bit subchannels. Hence, it is imperative to take into account the redundancy added by forward error correction (FEC), especially when the two partitions' FECs operate at different code rates. Figure 12.85 shows a block diagram of the DVB-T system operating in the hierarchical mode and receiving its input from the video partitioner. The FEC module represents the concatenated coding system,

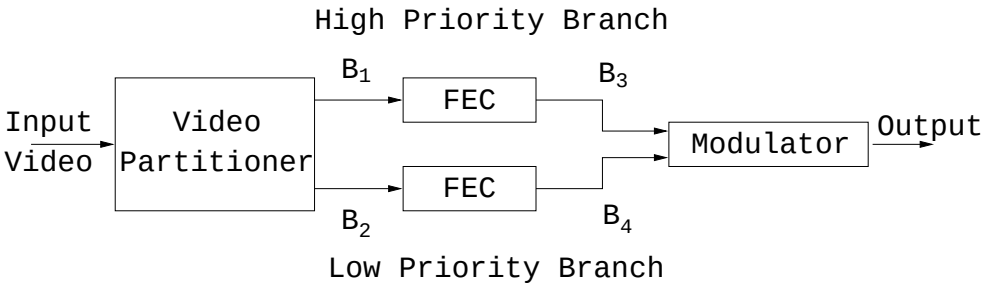

Figure 12.85: Video partitioning for the DVB-T system operating in hierarchical mode

Modulation	Conv. Code Rate (High Priority)	Conv. Code Rate (Low Priority)	Ratio (High - B1 : Low - B2)
16QAM	1/2	1/2	1 : 1
	1/2	2/3	3 : 4
	1/2	3/4	2 : 3
	1/2	5/6	3 : 5
	1/2	7/8	4 : 7
	2/3	1/2	4 : 3
64QAM	1/2	1/2	1 : 2
	1/2	2/3	3 : 8
	1/2	**3/4**	**1 : 3**
	1/2	5/6	3 : 10
	1/2	7/8	2 : 7
	2/3	1/2	2 : 3

Table 12.20: The Bit Rate Partitioning Ratios Based on the Modulation Mode and Code Rates Selected for the DVB-T Hierarchical Mode. The Line in Bold Corresponds to our Worked Example

consisting of a Reed–Solomon codec [389] and a convolutional codec [389]. The modulator can invoke both 16QAM and 64QAM [221]. We shall now use an example to illustrate the choice of the various partitioning ratios summarized in Table 12.20.

We shall assume that 64QAM is selected and the high-and low-priority video partitions employ $\frac{1}{2}$ and $\frac{3}{4}$ convolutional codes, respectively. This scenario is portrayed in the third line of the 64QAM section of Table 12.20. We do not have to take the Reed–Solomon code rate into account, since both partitions invoke the same Reed–Solomon codec. Based on these facts and on reference to Figure 12.85, the input bit rates B_3 and B_4 of the modulator must be in the ratio 1:2, since the two MSBs of the 64-QAM constellation are assigned to the high-priority video partition and the remaining four bits to the low-priority video partition.

At the same time, the ratio of B_3 to B_4 is related to the ratio of B_1 to B_2 with the FEC

	Modulation	Conv. Code Rate (High Prior. – B1)	Conv. Code Rate (Low Prior. – B2)	Ratio (High : Low) (B1 : B2)
Scheme 1	16QAM	1/2	1/2	1 : 1
Scheme 2	16QAM	1/3	2/3	1 : 2
Scheme 3	16QAM	2/3	1/3	2 : 1

Table 12.21: Summary of the Three Schemes Employed in our Investigations into the Performance of the Data Partitioning Scheme. The FEC-coded High-priority Video Bit-Stream B3, as Shown in Figure 12.85, was Mapped to the High-priority 16QAM Subchannel, while the Low-priority B4-stream to the Low Priority 16QAM Subchannel.

redundancy taken into account, requiring

$$\begin{aligned} \frac{B_3}{B_4} &= \frac{2\times B_1}{\frac{4}{3}\times B_2} \overset{64-QAM}{=} \frac{1}{2} \\ &= \frac{3}{2}\cdot\frac{B_1}{B_2} \overset{64-QAM}{=} \frac{1}{2} \\ \frac{B_1}{B_2} &= \frac{1}{2}\times\frac{2}{3} \\ &= \frac{1}{3}. \end{aligned} \tag{12.25}$$

If, for example, the input video bit rate of the data partitioner module is 1 Mbit/s, the output bit rate of the high- and low-priority partition would be $B_1 = 250$ kbit/s and $B_2 = 750$ kbit/s, respectively, according to the ratio indicated by Equation 12.25.

In this section, we have outlined the operation of the data partitioning scheme which we used in the DVB-T hierarchical transmission scheme. Its performance in the context of the overall system will be characterized in Section 12.7.8. Let us, however, first evaluate the BER sensitivity of the partitioned MPEG-2 bit-stream to randomly distributed bit errors using various partitioning ratios.

12.7.6 Performance of the Data Partitioning Scheme

Let us consider the 16QAM modem and refer to the equally split rate $\frac{1}{2}$ convolutional coded high- and low-priority scenario as Scheme 1. Furthermore, the 16QAM rate $\frac{1}{3}$ convolutional coded high priority data and rate $\frac{2}{3}$ convolutional coded low-priority data-based scenario is referred to here as Scheme 2. Lastly, the 16QAM rate $\frac{2}{3}$ convolutional coded high-priority data and rate $\frac{1}{3}$ coded low-priority databased partitioning scheme is termed Scheme 3. We then programmed the partitioning scheme of Figure 12.85 for maintaining the required splitting ratio B_1/B_2, as seen in Table 12.21. This was achieved by continuously adjusting the PBP using Algorithms 1 and 2. The 704×576-pixel "Football" high-definition television (HDTV) video sequence was used in these investigations.

Figures 12.86 to 12.88 show the relative frequency at which a particular PBP value occurs for each image of the "Football" video sequence for the three different schemes of Table 12.21 mentioned earlier. The reader may recall from Table 12.19 that the PBP values indicate the proportion of encoded video parameters, which are to be directed into the high-priority partition. As the PBP value increases, the proportion of video data mapped to the high-priority partition increases and vice versa. Comparing Figures 12.86 to 12.88, we observe

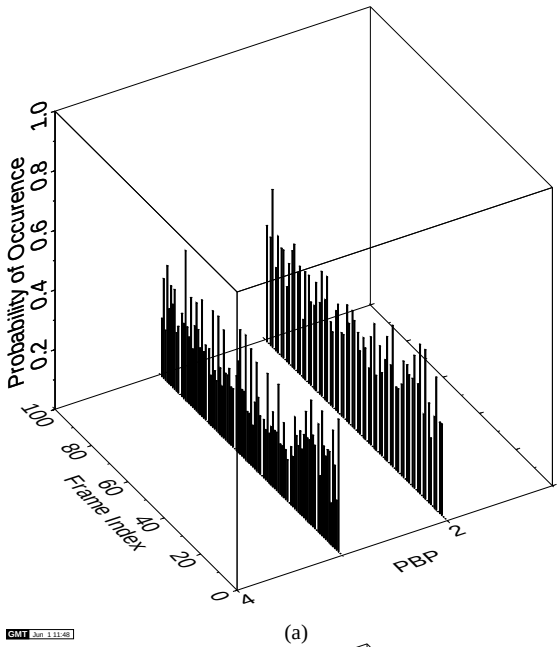

(a)

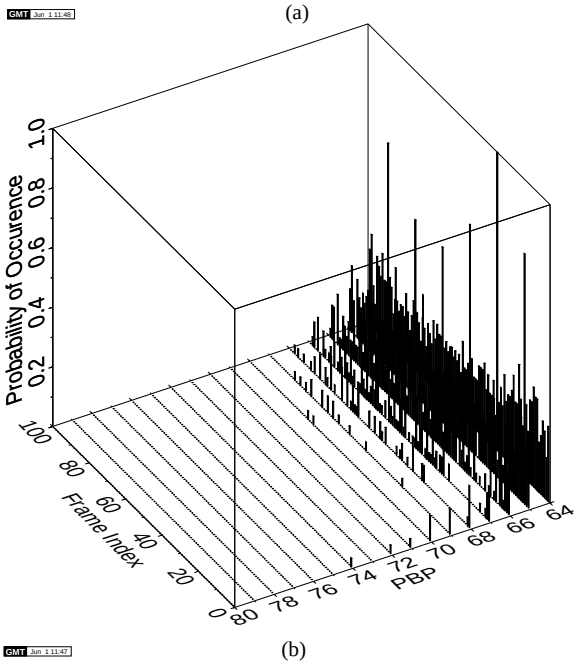

(b)

Figure 12.86: Evolution of the probability of occurrence of PBP values from one picture to another of the 704×576-pixel "Football" video sequence for Scheme 1 of Table 12.21.

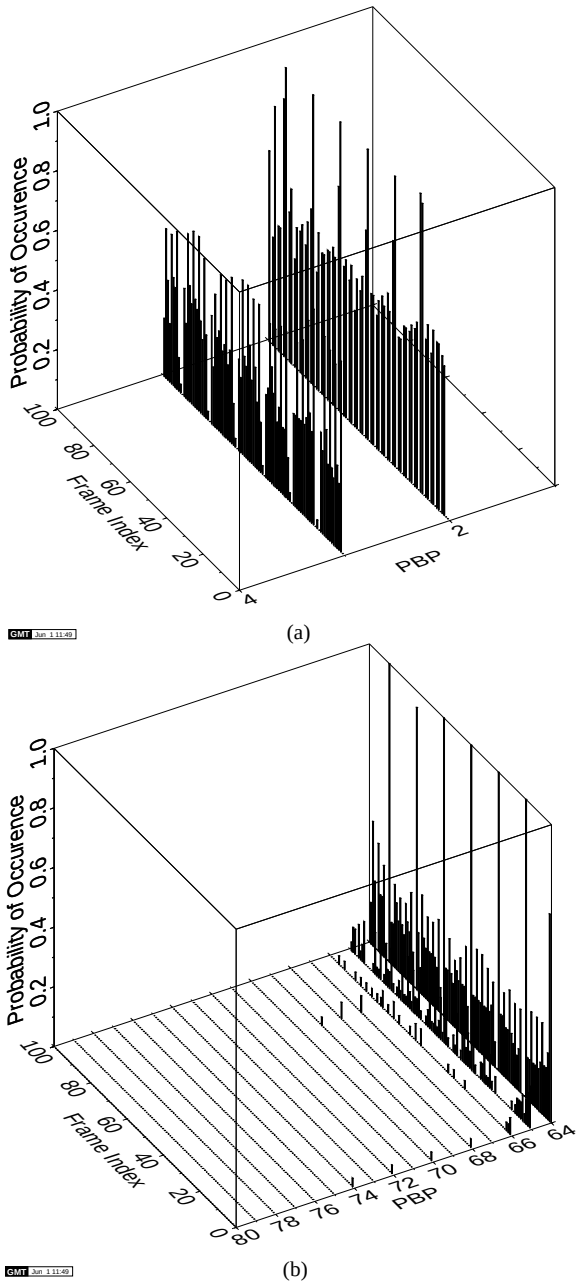

Figure 12.87: Evolution of the probability of occurrence of PBP values from one picture to another of the 704×576-pixel "Football" video sequence for Scheme 2 of Table 12.21.

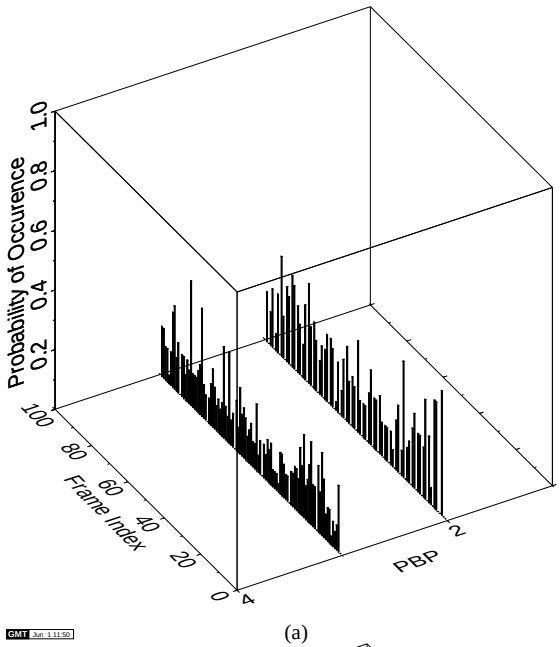

(a)

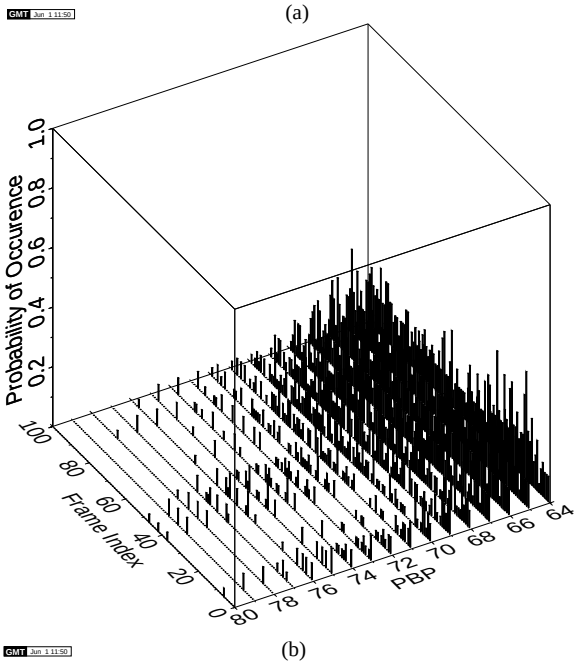

(b)

Figure 12.88: Evolution of the probability of occurrence of PBP values from one picture to another of the 704×576-pixel "Football" video sequence for Scheme 3 of Table 12.21.

that Scheme 3 has the most data in the high-priority partition associated with the high PBPs of Table 12.19, followed by Scheme 1 and Scheme 2. This observation can be explained as follows. We shall consider Scheme 3 first. In this scheme, the high-priority video bits are protected by a rate $\frac{2}{3}$ convolutional code and mapped to the higher integrity 16QAM subchannel. By contrast, the low-priority video bits are encoded by a rate $\frac{1}{3}$ convolutional code and mapped to the lower integrity 16QAM subchannel. Again, assuming that 16QAM is used in our experiment according to line 3 of Table 12.21, $\frac{2}{3}$ of the video bits will be placed in the high-priority 16QAM partition and the remaining video bits in the low-priority 16QAM partition, following the approach of Equation 12.25. The BER difference of the 16QAM subchannels depend on the channel error statistics, but the associated BERs are about a factor of 2–3 different [221]. In contrast to Scheme 3, Scheme 2 will have $\frac{1}{3}$ of the video bits placed in the high-priority 16QAM partition, and the remaining $\frac{2}{3}$ of the video bits mapped to the low-priority 16QAM partition, according to line 2 of Table 12.21. Lastly, Scheme 1 will have half of the video bits in the high- and low-priority 16QAM partitions, according to line 1 of Table 12.21. This explains our observation in the context of Scheme 3 in Figure 12.88, where a PBP value as high as 80 is achieved in some image frames. However, each PBP value encountered has a lower probability of being selected, since the total number of 3600 occurrences associated with investigated 3600 MPEG-2 video slices per 100 image frames is spread over a higher variety of PBPs. Hence, Scheme 3 directs about $\frac{2}{3}$ of the original video bits after $\frac{2}{3}$ rate coding to the high-priority 16QAM subchannel. This observation is in contrast to Scheme 2 of Figure 12.87, where the majority of the PBPs selected are only up to the value of 65. This indicates that about $\frac{2}{3}$ of the video bits are concentrated in the lower priority partition, as indicated in line 2 of Table 12.21.

Figures 12.89(a) to 12.91(a) show the average probability at which a particular PBP value is selected by the rate control scheme, as discussed in Section 12.7.5, during the encoding of the video sequence. Again, we observe that Scheme 3 encounters the widest range of PBP values, followed by Scheme 1 and Scheme 2, respectively. According to Table 12.21, these schemes map a decreasing number of bits to the high-priority partition in this order.

We then quantified the error sensitivity of the partitioning Schemes 1 to 3 characterized in Table 12.21, when each partition was subjected to randomly distributed bit errors, although in practice the error distribution will depend on the fading channel's characteristics. Specifically, the previously defined average PSNR degradation was evaluated for given error probabilities inflicting random errors imposed on one of the partitions, while keeping the other partition error-free. These results are portrayed in Figures 12.89(b), 12.90(b) and 12.91(b) for Schemes 1 to 3, respectively.

Comparing Figures 12.89(b) to 12.91(b), we observe that the average PSNR degradation exhibited by the three schemes of Table 12.21, when only their high-priority partitions are corrupted, is similar. The variations in the average PSNR degradation in these cases are caused by the different quantity of sensitive video bits, which resides in the high priority partition. If we compare the performance of the schemes summarized in Table 12.21 at a BER of 2×10^{-3}, Scheme 3 experienced approximately 8.8 dB average video PSNR degradation, while Schemes 1 and 2 exhibited approximately 5 dB degradation. This trend was expected, since Scheme 3 had the highest portion of the video bits, namely, $\frac{2}{3}$ residing in the high-priority partition, followed by Scheme 1 hosting $\frac{1}{2}$ and Scheme 2 having $\frac{1}{3}$ of the bits in this partition.

On the other hand, we can observe a significant difference in the average PSNR degrada-

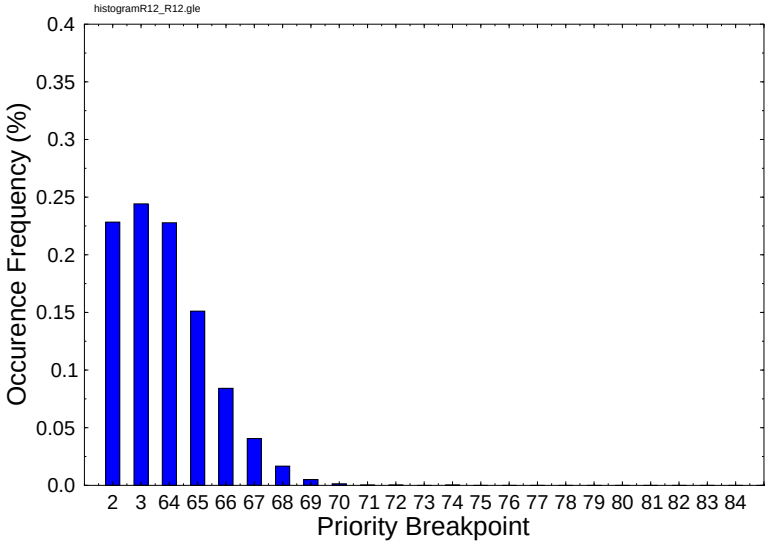

(a)

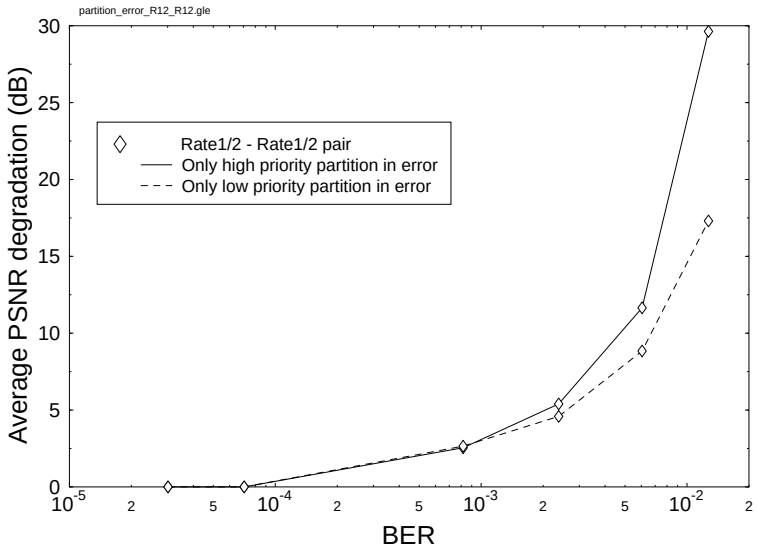

(b)

Figure 12.89: (a) Histogram of the probability of occurrence for various priority breakpoints and (b) average PSNR degradation versus BER for rate 1/2 convolutional coded high- and low-priority data in Scheme 1 of Table 12.21.

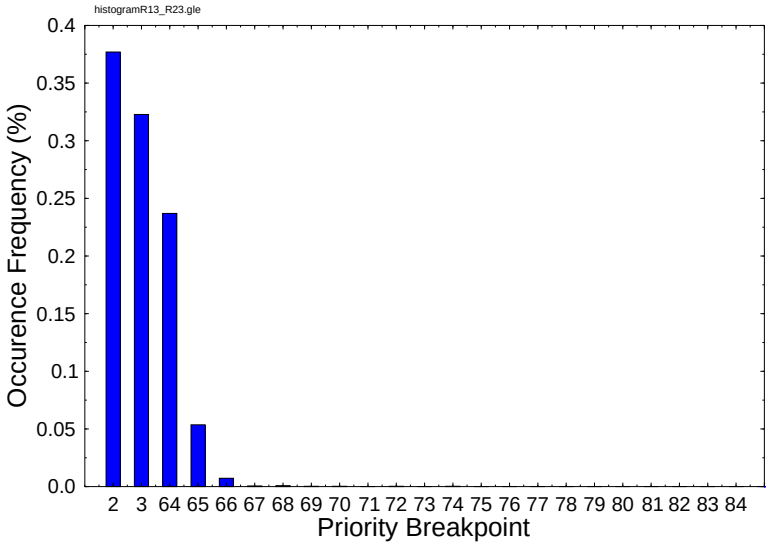

(a)

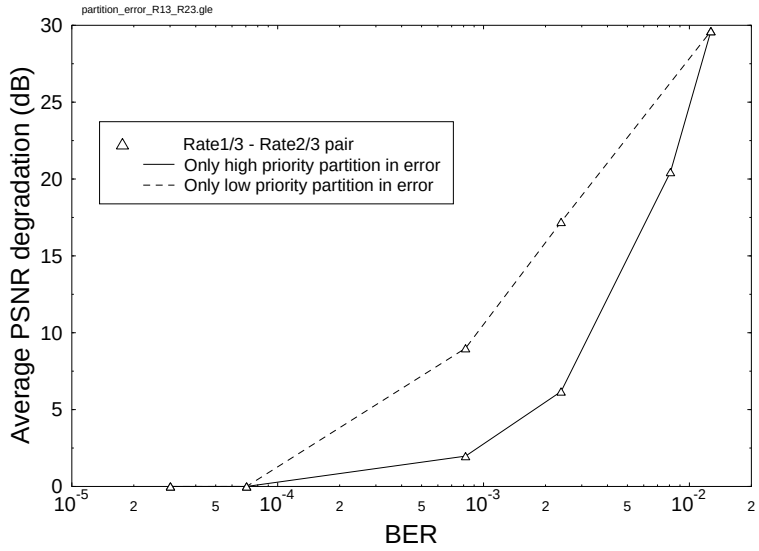

(b)

Figure 12.90: (a) Histogram of the probability of occurrence for various priority breakpoints and (b) average PSNR degradation versus BER for the rate 1/3 convolutional coded high-priority data and rate 2/3 convolutional coded low-priority data in Scheme 2 of Table 12.21.

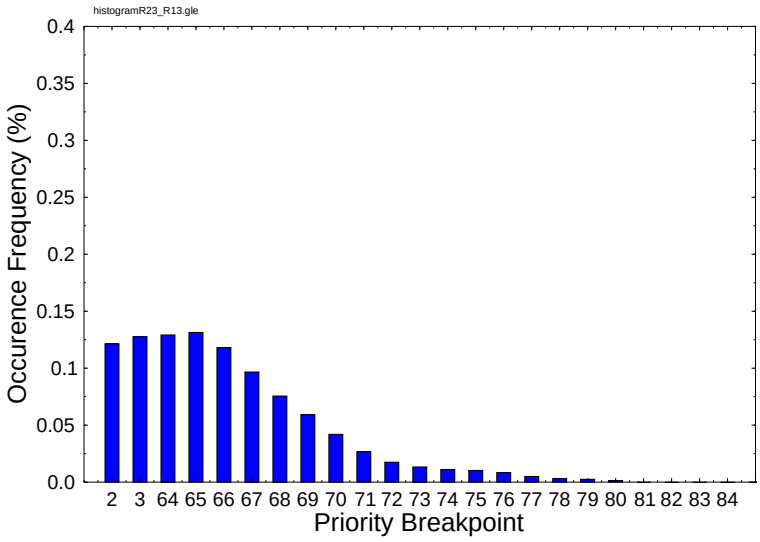

(a)

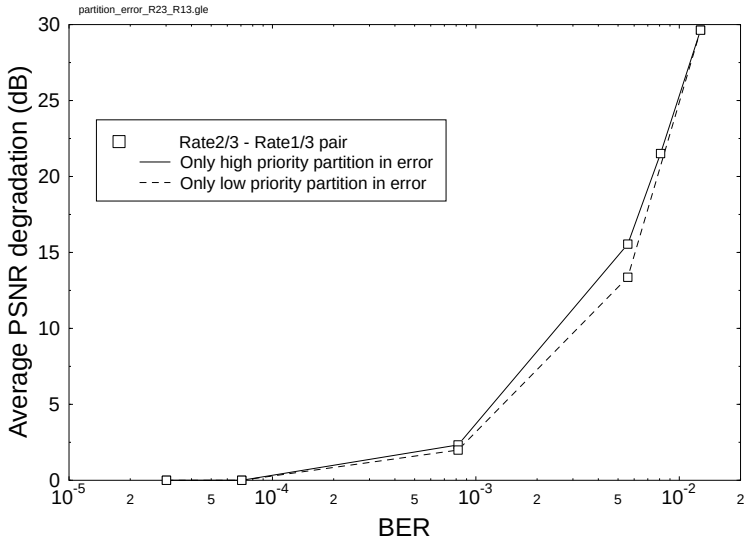

(b)

Figure 12.91: (a) Histogram of the probability of occurrence for various priority breakpoints and (b) average PSNR degradation versus BER for the rate 2/3 convolutional coded high-priority data and rate 1/3 convolutional coded low-priority data in Scheme 3 of Table 12.21.

tion measured for Schemes 1 to 3 of Table 12.21, when only the low priority partitions are corrupted by comparing the curves shown as broken lines in Figures 12.89(b) to 12.91(b). Under this condition, Scheme 2 experienced approximately 16 dB average video PSNR degradation at a BER of 2×10^{-3}. By contrast, Scheme 1 exhibited an approximately 4 dB average video PSNR degradation, while Scheme 3 experienced about 7.5 dB degradation at this BER. The scheme with the highest portion of video bits in the lower priority partition (i.e., Scheme 2) experienced the highest average video PSNR degradation. This observation correlates well with our earlier findings in the context of the high-priority partition scenario, where the partition holding the highest portion of the video bits in the error-impaired partition exhibited the highest average PSNR degradation.

Having discussed our observations for the three schemes of Table 12.21 from the perspective of the relative amount of video bits in one partition compared to the other, we now examine the data partitioning process further in order to relate them to our observations. Figure 12.92 shows a typical example of an MPEG-2 video bit-stream both prior to and after data partitioning. There are two scenarios to be considered here, namely, intra-frame and inter-frame coded macroblock partitioning. We have selected the PBP value of 64 from Table 12.19 for the intra-frame coded macroblock scenario and the PBP value of 3 for the inter-frame coded macroblock scenario, since these values have been selected frequently by the rate-control arrangement for Schemes 1 and 2. This is evident from Figures 12.86 and 12.87 as well as from Figures 12.89(a) and 12.90(a). With the aid of Table 12.19 and Figure 12.92, this implies that only the macroblock (MB) header information and a few low-frequency DCT coefficients will reside in the high-priority partition, while the rest of the DCT coefficients will be stored in the low-priority partition. These can be termed as base layer and enhancement layer, as seen in Figure 12.92. In the worst-case scenario, where the entire enhancement layer or low-priority partition data are lost due to a transmission error near the beginning of the associated low-priority bit stream, the MPEG-2 video decoder will only have the bits of the high-priority partition in order to reconstruct the encoded video sequence. Hence, the MPEG-2 decoder cannot reconstruct good-quality images. Although the results reported by Ghanbari and Seferidis [323] suggest that adequate video reconstruction is possible, provided that the motion vectors are correctly decoded, this observation is only true if the previous intra-coded frame is correctly reconstructed. If the previous intra-coded frame contains artifacts, these artifacts will be further propagated to forthcoming video frames by the motion vectors. By attempting to provide higher protection for the high-priority partition or base layer, we have indirectly forced the rate-control scheme of Section 12.7.5 to reduce the proportion of video bits directed into the high-priority partition under the constraint of a given fixed bit rate, which is imposed by the 16QAM subchannels.

In order to elaborate a little further, at a BER of 2×10^{-3}, Scheme 1 in Figure 12.89(a) exhibited a near-identical PSNR degradation for the high- and low-priority video bits. When assigning more bits to the low-priority partition, in order to accommodate a stronger FEC code in the high-priority partition, an increased proportion of error-impaired bits is inflicted in the low-priority partition. This is the reason for the associated higher error sensitivity seen in Figure 12.90(b). As such, there is a trade-off between the amount of video data protected and the code rate of the channel codec. As a comparison to the above scenarios in the context of Schemes 1 and 2, we shall now examine Scheme 3. In this scheme, more video data — namely, half the bits — can be directed into the high-priority partition, as demonstrated by Figure 12.88 due to encountering higher PBPs. This can also be confirmed with reference

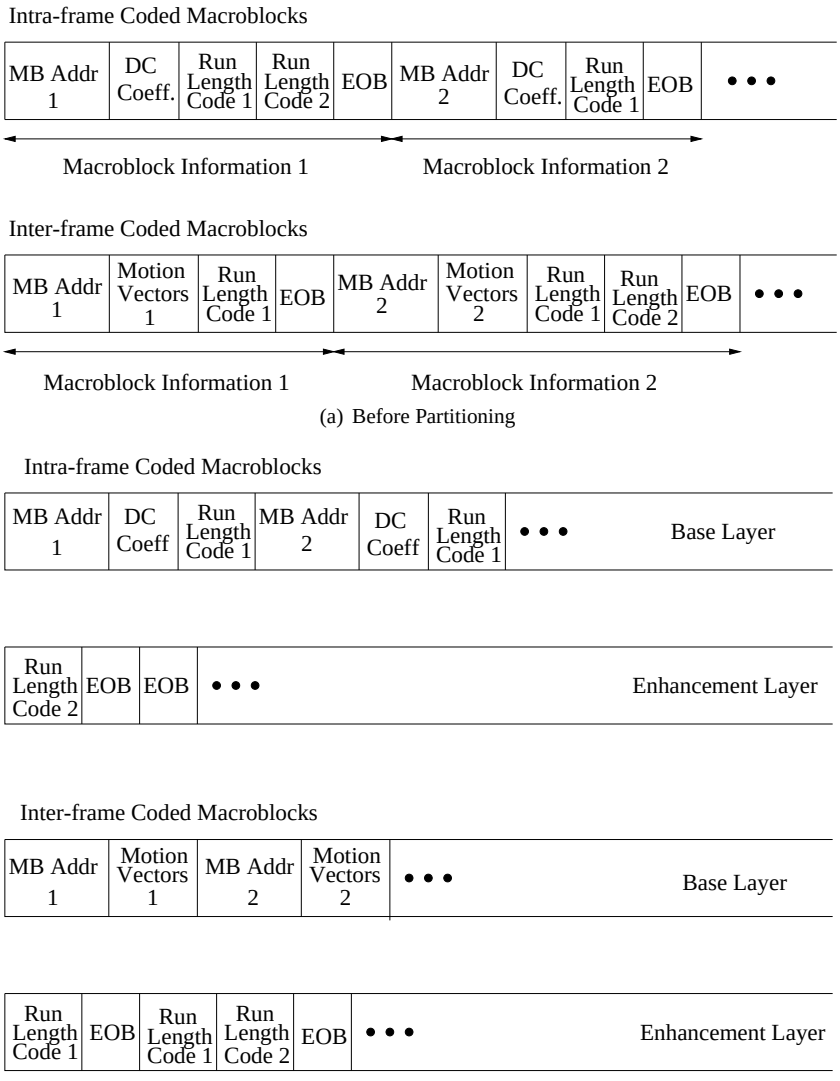

Figure 12.92: Example of video bit stream (a) before data partitioning and (b) after data partitioning for intra-frame coded macroblocks (MB) assuming a PBP of 64 and for inter-frame coded macroblocks assuming a PBP of 3.

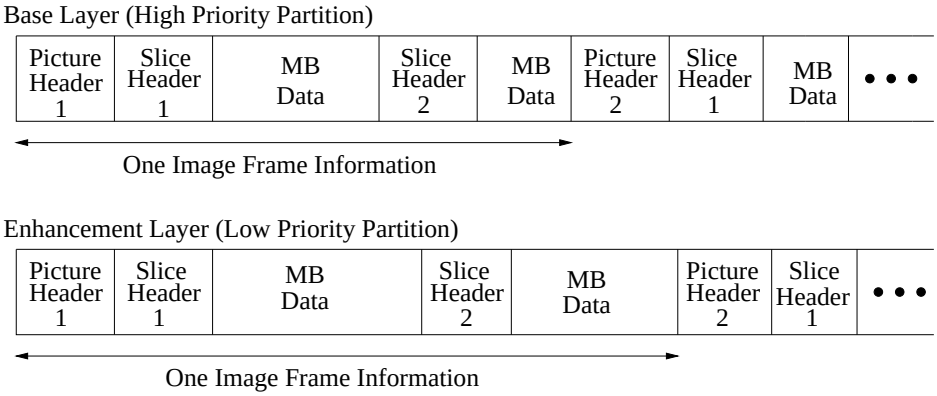

Figure 12.93: Example of high-level bit-stream syntax structure of a data partitioned MPEG-2 video bit stream. The "MB data" shown in the diagram refers to the macroblock header information and to the variable-length coded DCT coefficients, which have been partitioned as shown in Figure 12.92.

to Figures 12.90(b) and 12.91(b) by observing the PSNR degradations associated with the curves plotted in broken lines. If the low-priority partition is lost in Scheme 3, its effect on the quality of the reconstructed images is less detrimental than that of Scheme 2, since Scheme 3 loses only half the bits rather than 2/3. Hence, it is interesting to note that Scheme 3 experiences slightly higher average PSNR degradation than Scheme 1 at a BER of 2×10^{-3}, when only the low-priority partition is lost in both cases, despite directing only $\frac{1}{3}$ rather than $\frac{1}{2}$ of the bits to the low-priority partition. This observation can be explained as follows.

Apart from partitioning the macroblock header information and the variable-length coded DCT coefficients into the high- and low-priority partitions, synchronization information such as the picture header information [508] is replicated in the enhancement layer, as suggested by Gharavi *et al.* [514] as well as the MPEG-2 standard [508]. The purpose is to enable the MPEG-2 decoder to keep the base and enhancement layers synchronized during decoding. An example of this arrangement is shown in Figure 12.93. This resynchronization measure is only effective when the picture start code of both the high- and low-priority partitions is received correctly. If the picture start code in the low-priority partition is corrupted, for example, the MPEG-2 decoder may not detect this PSC, and all the data corresponding to the current image frame in the low-priority partition will be lost. The MPEG-2 decoder will then interpret the bits received for the low-priority partition of the next frame as the low-priority data expected for the current frame. As expected, because of this synchronization problem, the decoded video would have a higher average PSNR degradation than for the case where picture start codes are unimpaired. This explains our observation of a higher average PSNR degradation for Scheme 3 when only its lower priority partition was corrupted by the transmission channel. On the other hand, in this specific experiment, Scheme 1 did not experience the loss of synchronization due to corruption of its picture start code. Viewing events from another perspective, by opting for allocating less useful video bits to the low-priority partition, the probability of transmission errors affecting the fixed-length PSC within the reduced-sized low priority partition becomes higher.

These findings will assist us in explaining our observations in the context of the hierar-

chical transmission scheme of Section 12.7.8, suggesting that the data partitioning scheme did not provide overall gain in terms of error resilience over the nonpartitioned case. Let us, however, consider first the performance of the nonhierarchical DVB-T scheme in the next section.

12.7.7 Nonhierarchical OFDM DVBP Performance

In this section, we elaborate on our findings when the convolutional code used in the standard nonhierarchical DVB scheme [499] is replaced by a turbo code. We will invoke a range of standard-compliant schemes as benchmarks. The 704×576-pixel HDTV-resolution "Football" video sequence was used in our experiments. The MPEG-2 decoder employs a simple error concealment algorithm to fill in missing portions of the reconstructed image in the event of decoding errors. The concealment algorithm will select the specific portion of the previous reconstructed image, which corresponds to the missing portion of the current image in order to conceal the errors.

In Figure 12.94(a) and (b), the bit error rate (BER) performance of the various modem modes in conjunction with our diverse channel-coding schemes are portrayed over stationary, narrowband additive white Gaussian noise channels (AWGN), where the turbo codec exhibits a significantly steeper BER reduction in comparison to the convolutionally coded arrangements.

Specifically, comparing the performance of the various turbo and convolutional codes for QPSK and 64QAM at a BER of 10^{-4}, we see that the turbo code exhibited an additional coding gain of about 2.24 dB and 3.7 dB, respectively, when using half-rate codes in Figure 12.94(a) and (b). Hence, the peak signal-to-noise ratio (PSNR) versus channel signal-to-noise ratio (SNR) graphs in Figure 12.95 demonstrate that approximately 2 dB and 3.5 dB lower channel SNRs are required in conjunction with the rate $\frac{1}{2}$ turbo codec for QPSK and 64QAM, respectively, than for convolutional coding, in order to maintain high reconstructed video quality. The term *unimpaired* as used in Figure 12.95 and Figure 12.96 refers to the condition where the PSNR of the MPEG-2 decoder's reconstructed image at the receiver is the same as the PSNR of the same image generated by the local decoder of the MPEG-2 video encoder, corresponding to the absence of channel — but not MPEG-2 coding — impairments.

Comparing the BER performance of the $\frac{1}{2}$ rate convolutional decoder in Figure 12.97(a) and the log-MAP [452] turbo decoder using eight iterations in Figure 12.97(b) for QPSK modulation over the worst-case fading mobile channel of Figure 12.83, we observe that at a BER of about 10^{-4} the turbo code provided an additional coding gain of 6 dB in comparison to the convolutional code. By contrast, for 64QAM using similar codes, a 5 dB coding gain was observed at this BER.

Similar observations were also made with respect to the average peak signal-to-noise ratio (PSNR) versus channel signal-to-noise ratio (SNR) plots of Figure 12.96. For the QPSK modulation mode and a $\frac{1}{2}$ coding rate, the turbo code required an approximately 5.5 dB lower channel SNR for maintaining near-unimpaired video quality than the convolutional code.

Comparing Figure 12.97(a) and Figure 12.98(a), we note that the Reed–Solomon decoder becomes effective in lowering the bit error probability of the transmitted data further below the BER threshold of 10^{-4}. From these figures we also observe that the rate $\frac{3}{4}$ convolutional code is unsuitable for transmission over the highly dispersive hilly terrain channel used in this experiment, when 64QAM is employed. When the rate $\frac{7}{8}$ convolutional code is used, both

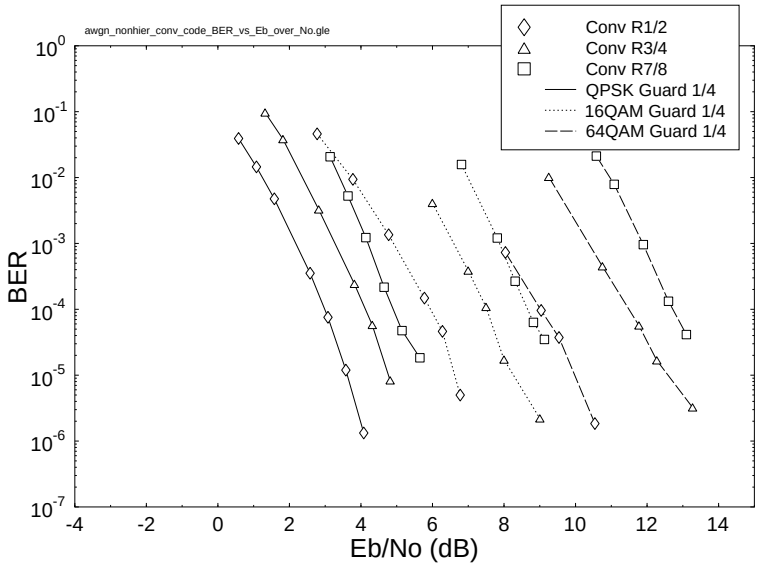

(a) Convolutional Code

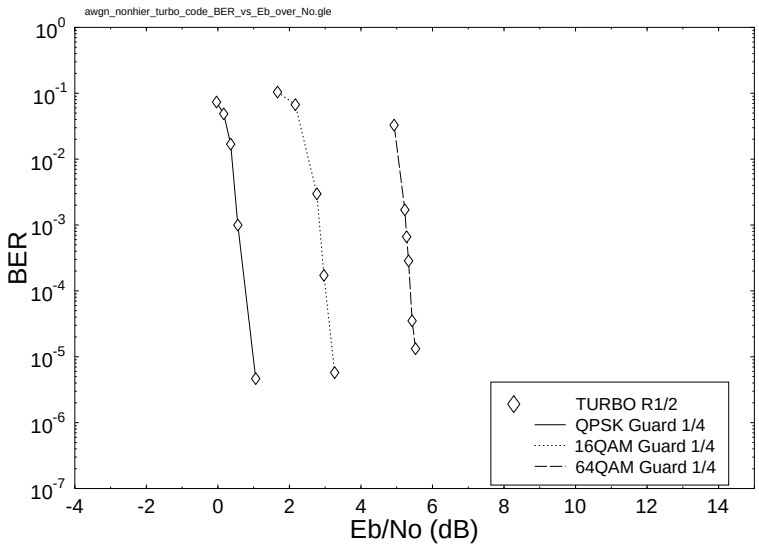

(b) Turbo Code

Figure 12.94: BER after (a) convolutional decoding and (b) turbo decoding for the DVB-T scheme over stationary nondispersive **AWGN** channels for **nonhierarchical transmission**.

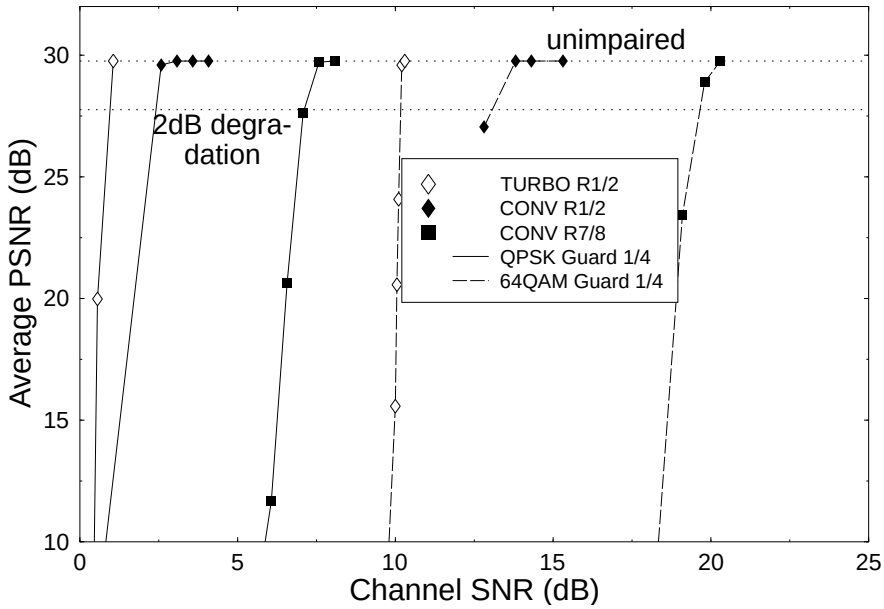

Figure 12.95: Average PSNR versus channel SNR of the DVB scheme [499] over nondispersive **AWGN** channels for **nonhierarchical transmission**.

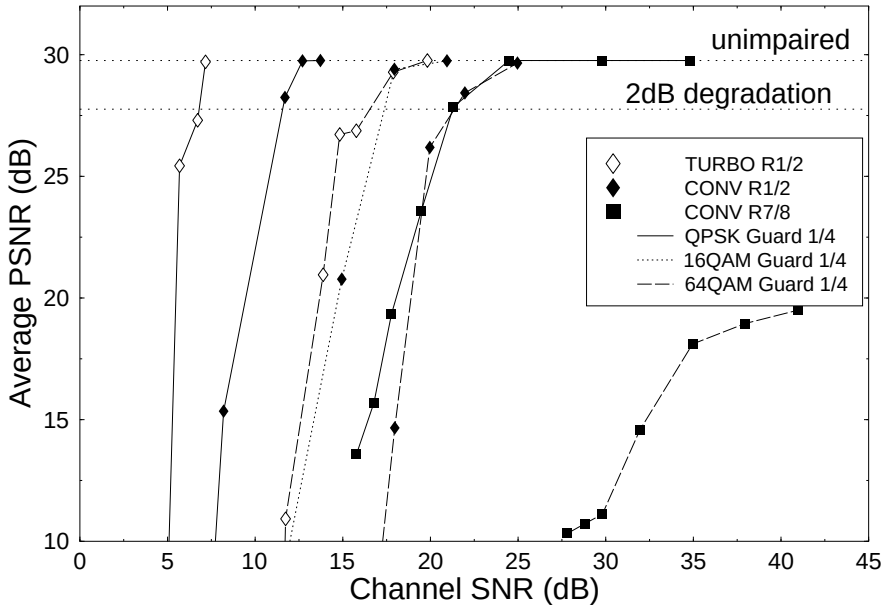

Figure 12.96: Average PSNR versus channel SNR of the DVB scheme [499] over the **wideband fading channel** of Figure 12.83 for **nonhierarchical transmission**.

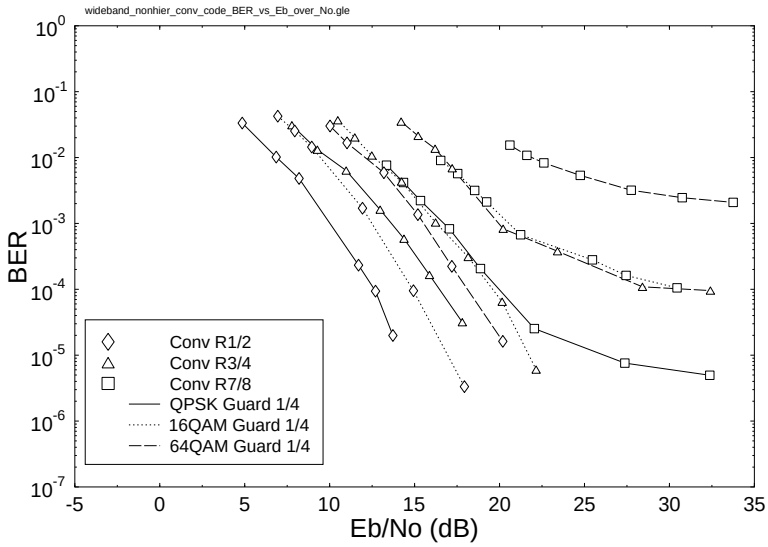

(a) Convolutional Code

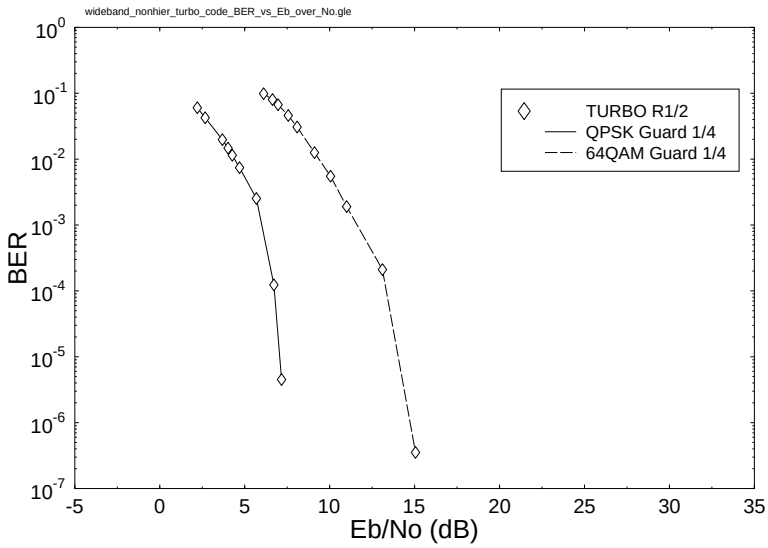

(b) Turbo Code

Figure 12.97: BER after (a) convolutional decoding and (b) turbo decoding for the DVB-T scheme over the **wideband fading channel** of Figure 12.83 for **nonhierarchical transmission**.

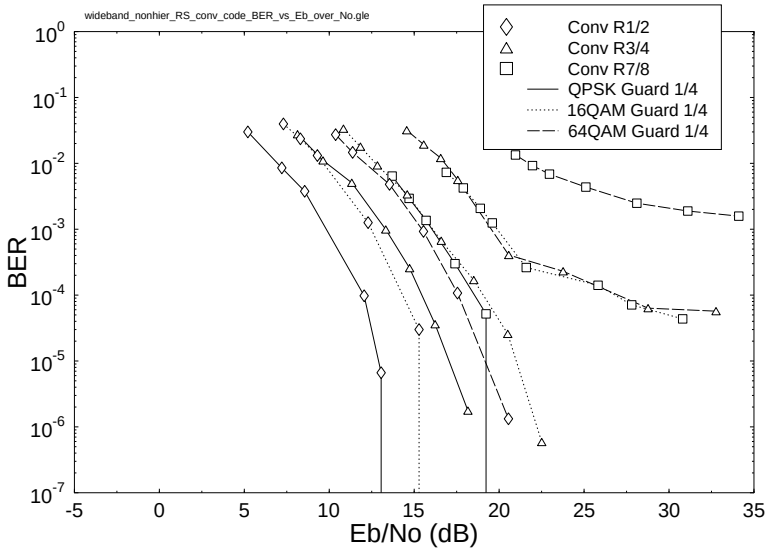

(a) RS and Convolutional Code

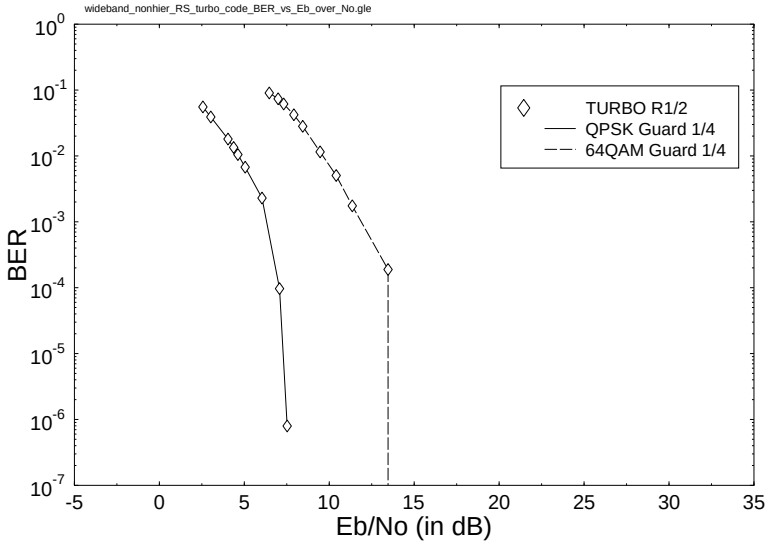

(b) RS and Turbo Code

Figure 12.98: BER after (a) RS and convolutional decoding and (b) RS and turbo decoding for the DVB-T scheme over the **wideband fading channel** of Figure 12.83 for **nonhierarchical transmission**.

Mod.	Code	CSNR (dB)	E_b/N_0	BER
QPSK	Turbo (1/2)	1.02	1.02	6×10^{-6}
64QAM	Turbo (1/2)	9.94	5.17	2×10^{-3}
QPSK	Conv (1/2)	2.16	2.16	1.1×10^{-3}
64QAM	Conv (1/2)	12.84	8.07	6×10^{-4}
QPSK	Conv (7/8)	6.99	4.56	2×10^{-4}
64QAM	Conv (7/8)	19.43	12.23	3×10^{-4}

Table 12.22: Summary of the *Nonhierarchical* Performance Results over Nondispersive *AWGN* Channels Tolerating a PSNR Degradation of 2 dB. The BER Measure Refers to BER after Viterbi or Turbo Decoding

Mod.	Code	CSNR (dB)	E_b/N_0	BER
QPSK	Turbo (1/2)	6.63	6.63	2.5×10^{-4}
64QAM	Turbo (1/2)	15.82	11.05	2×10^{-3}
QPSK	Conv (1/2)	10.82	10.82	6×10^{-4}
64QAM	Conv (1/2)	20.92	16.15	7×10^{-4}
QPSK	Conv (7/8)	20.92	18.49	3×10^{-4}

Table 12.23: Summary of the *Nonhierarchical* Performance Results over *Wideband Fading Channels* Tolerating a PSNR Degradation of 2 dB. The BER Measure Refers to BER after Viterbi or Turbo Decoding

the 16QAM and 64QAM schemes perform poorly. As for the QPSK modulation scheme, a convolutional code rate as high as $\frac{7}{8}$ can still provide a satisfactory performance after Reed–Solomon decoding.

In conclusion, Tables 12.22 and 12.23 summarize the system performance in terms of the channel SNR (CSNR) required for maintaining less than 2 dB PSNR video degradation. At this PSNR degradation, decoding errors were still perceptually unnoticeable to the viewer due to the 30 frame/s refresh rate, although the typical still frame shown in Figure 12.99 in this scenario exhibits some degradation. It is important to underline once again that the $K = 3$ turbo code and the $K = 7$ convolutional code exhibited comparable complexities. The higher performance of the turbo codec facilitates, for example, the employment of turbo-coded 16-QAM at a similar channel SNR, where convolutional-coded QPSK can be invoked. This in turn allows us to double the bit rate within the same bandwidth and thereby to improve the video quality. In the next section, we present the results of our investigations employing the DVB-T system [499] in a hierarchical transmission scenario.

12.7.8 Hierarchical OFDM DVB Performance

The philosophy of the hierarchical transmission mode is that the natural BER difference of a factor 2 to 3 of the 16QAM modem is exploited for providing unequal error protection for the FEC-coded video streams B3 and B4 of Figure 12.85 [221]. If the sensitivity of the video bits requires a different BER ratio between the B3 and B4 streams, the choice of the FEC codes protecting the video streams B1 and B2 of Figure 12.85 can be appropriately adjusted to equal out or to augment these differences.

Figure 12.99: Frame 79 of the "Football" sequence, which illustrates the visual effects of minor decoding errors at a BER of 2.10^{-4} after convolutional decoding. The PSNR degradation observed is approximately 2 dB. The sequence was coded using a rate 7/8 convolutional code and transmitted employing QPSK modulation.

Below we invoke the DVB-T hierarchical scheme in a mobile broadcasting scenario. We also demonstrate the improvements that turbo codes offer when replacing the convolutional code in the standard scheme. Hence, the convolutional codec in both the high- and low-priority partitions was replaced by the turbo codec. We have also investigated replacing only the high-priority convolutional codec with the turbo codec, pairing the $\frac{1}{2}$ rate turbo codec in the high-priority partition with the convolutional codec in the low-priority partition. Again, the "Football" sequence was used in these experiments. Partitioning was carried out using the schematic of Figure 12.85 as well as Algorithms 1 and 2. The FEC-coded high-priority video partition B3 of Figure 12.85 was mapped to the higher integrity 16QAM or 64QAM subchannel. By contrast, the low-priority partition B4 of Figure 12.85 was directed to the lower integrity 16QAM or 64QAM subchannel. Lastly, no specific mapping was required for QPSK, since it exhibits no subchannels. We note, however, that further design trade-offs become feasible when reversing the above mapping rules. This is necessary, for example, in conjunction with Scheme 2 of Table 12.21, since the high number of bits in the low-priority portion render it more sensitive than the high-priority partition. Again, the 16QAM subchannels exhibit a factor of 2 to 3 BER difference under various channel conditions, which improves the robustness of the reverse-mapped Scheme 2 of Table 12.21.

Referring to Figure 12.100 and comparing the performance of the 1/2 rate convolutional code and turbo code at a BER of 10^{-4} for the low-priority partition, we find that the turbo code, employing eight iterations, exhibited a coding gain of about 6.6 dB and 5.97 dB for 16QAM and 64QAM, respectively. When the number of turbo-decoding iterations was reduced to 4, the coding gains offered by the turbo code over that of the convolutional code were 6.23 dB and 5.7 dB for 16QAM and 64QAM, respectively. We observed that by re-

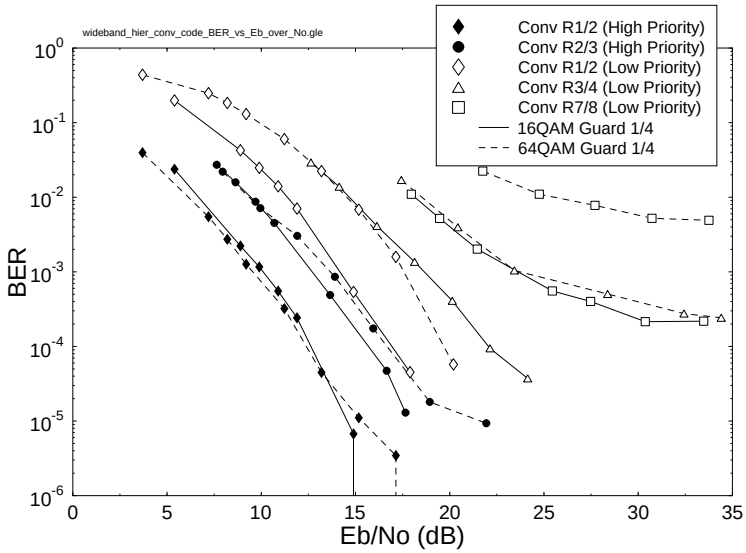

(a) Convolutional Code

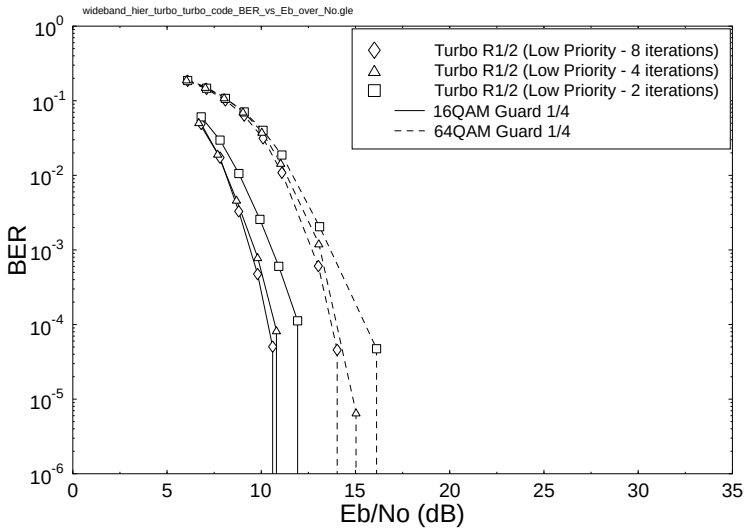

(b) Turbo Code

Figure 12.100: BER after (a) convolutional decoding and (b) turbo decoding for the **DVB-T hierarchical scheme** over the **wideband fading channel** of Figure 12.83 using the schematic of Figure 12.85 as well as Algorithms 1 and 2. In (b), the BER of the turbo- or convolutional-coded high-priority partition is not shown.

ducing the number of iterations to four halved the associated complexity, but the turbo code exhibited a coding loss of only about 0.37 dB and 0.27 dB in comparison to the eight-iteration scenario for 16QAM and 64QAM, respectively. Hence, the computational complexity of the turbo codec can be halved by sacrificing only a small amount of coding gain. The substantial coding gain provided by turbo coding is also reflected in the PSNR versus channel SNR graphs of Figure 12.101. In order to achieve transmission with very low probability of error, Figure 12.101 demonstrated that approximately 5.72 dB and 4.56 dB higher channel SNRs are required by the standard scheme compared to the scheme employing turbo coding, when using four iterations in both partitions. We have only shown the performance of turbo coding for the low-priority partition in Figures 12.100(b) and 12.102(b), since the turbo or convolutional-coded high-priority partition was received with very low probability of error after Reed–Solomon decoding for the range of SNRs used.

We also observed that the rate 3/4 and rate 7/8 convolutional codes in the low-priority partition were unable to provide sufficient protection to the transmitted video bits, as becomes evident from Figures 12.100(a) and 12.102(a). In these high coding rate scenarios, due to the presence of residual errors even after the Reed–Solomon decoder, the decoded video exhibited some decoding errors, which is evidenced by the flattening of the PSNR versus channel SNR curves in Figure 12.101(a), before reaching the error-free PSNR.

A specific problem when using the data partitioning scheme in conjunction with the high-priority partition being protected by the rate $\frac{1}{2}$ code and the low-priority partition protected by the rate $\frac{3}{4}$ and rate $\frac{7}{8}$ codes was that when the low-priority partition data was corrupted, the error-free high priority data available was insufficient for concealing the errors, as discussed in Section 12.7.6. We have also experimented with the combination of rate $\frac{2}{3}$ convolutional coding and rate $\frac{1}{2}$ convolutional coding, in order to protect the high- and low-priority data, respectively. From Figure 12.101(a) we observed that the performance of this $\frac{2}{3}$ rate and $\frac{1}{2}$ rate combination approached that of the rate $\frac{1}{2}$ convolutional code in both partitions. This was expected, since now more data can be inserted into the high-priority partition. Hence, in the event of decoding errors in the low-priority data, we had more error-free high-priority data that could be used to reconstruct the received image.

Our last combination investigated involved using rate $\frac{1}{2}$ turbo coding and convolutional coding for the high- and low-priority partitions, respectively. Comparing Figures 12.103 and 12.101(a), the channel SNRs required for achieving unimpaired video transmission were similar in both cases. This was expected, since the turbo-convolutional combination's video performance is dependent on the convolutional code's performance in the low-priority partition.

Lastly, comparing Figures 12.101 and 12.96, we found that the unimpaired PSNR condition was achieved at similar channel SNRs for the hierarchical and nonhierarchical schemes, suggesting that the data partitioning scheme had not provided sufficient performance improvements in the context of the mobile DVB scheme to justify its added complexity. Again, this was a consequence of relegating a high proportion of video bits to the low integrity partition.

12.7.9 Summary and Conclusions

In this chapter, we have investigated the performance of a turbo-coded DVB system in a mobile environment. A range of system performance results was presented based on the stan-

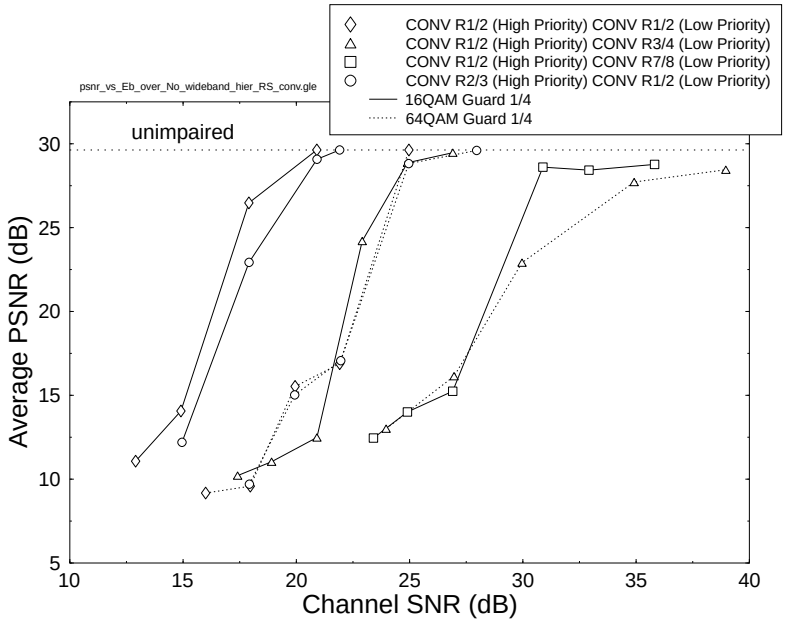

(a) Standard Scheme

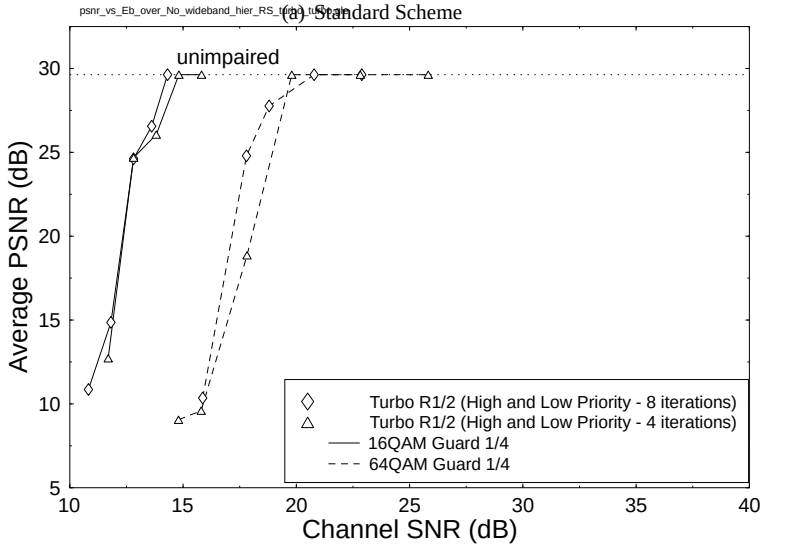

(b) Turbo Code in Both Partitions

Figure 12.101: Average PSNR versus channel SNR for (a) standard DVB scheme [499] and (b) system with turbo coding employed in both partitions, for transmission over the **wideband fading channel** of Figure 12.83 for **hierarchical transmission** using the schematic of Figure 12.85 as well as Algorithms 1 and 2.

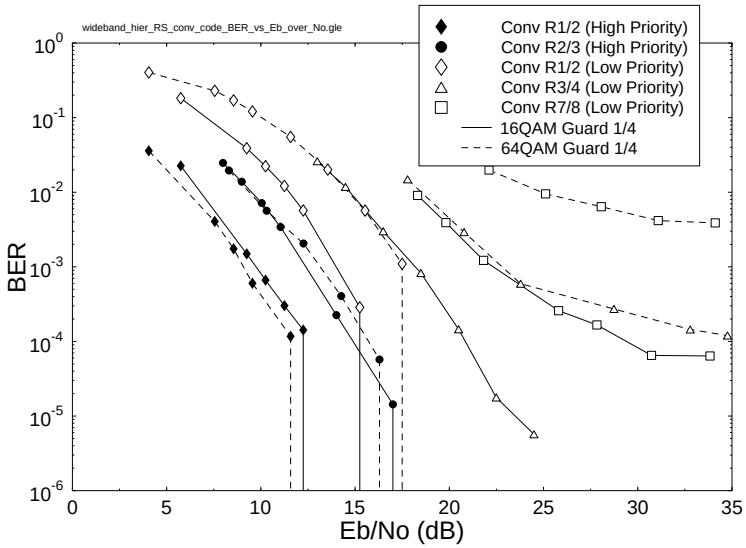

(a) RS and Convolutional Code

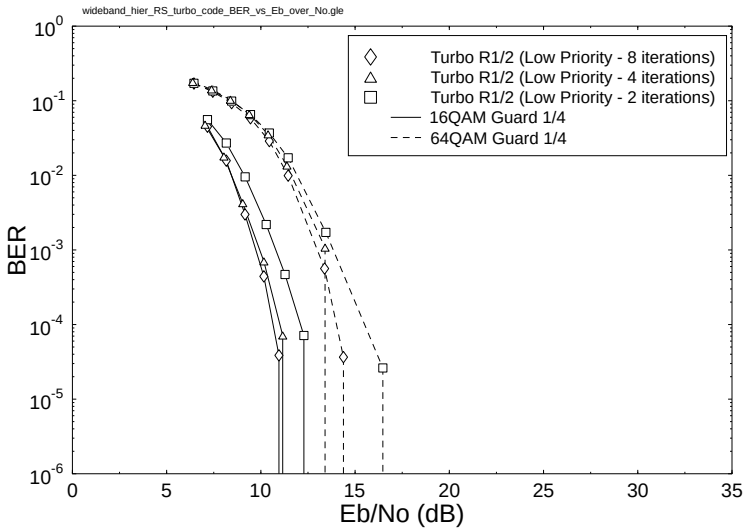

(b) RS and Turbo Code

Figure 12.102: BER after (a) RS and convolutional decoding and (b) RS and turbo decoding for the **DVB-T hierarchical scheme** over the **wideband fading channel** of Figure 12.83 using the schematic of Figure 12.85 as well as Algorithms 1 and 2. In (b), the BER of the turbo- or convolutional-coded high-priority partition is not shown.

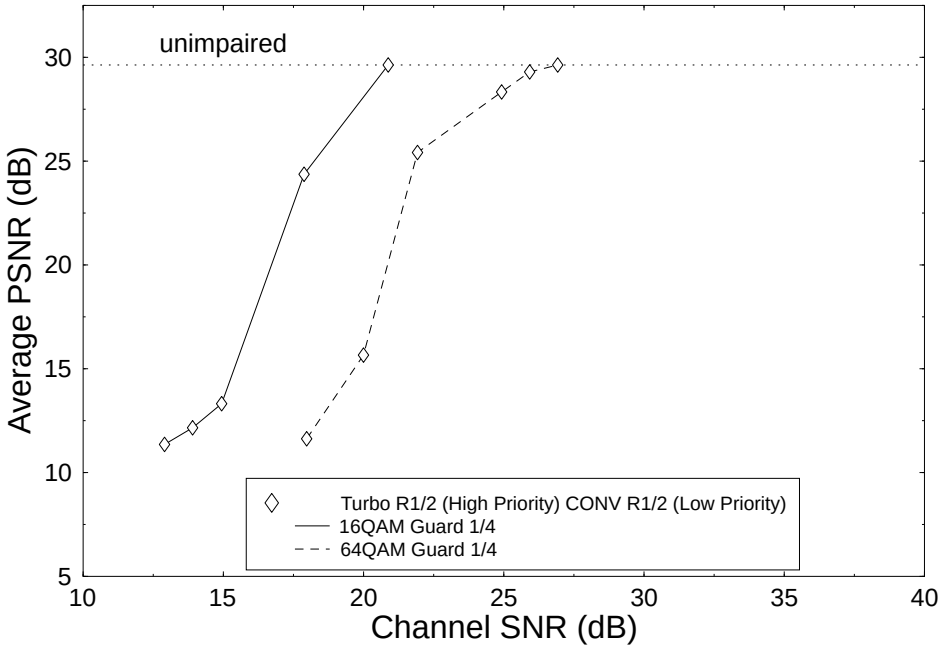

Figure 12.103: Average PSNR versus channel SNR of the DVB scheme, employing turbo coding in the high-priority partition and convolutional coding in the low-priority partition, over the **wideband fading channel** of Figure 12.83 for **hierarchical transmission** using the schematic of Figure 12.85 as well as Algorithms 1 and 2.

dard DVB-T scheme as well as on an improved turbo-coded scheme. The convolutional code specified in the standard system was replaced by turbo coding, which resulted in a substantial coding gain of around 5 dB. It is important to underline once again that the $K = 3$ turbo code and the $K = 7$ convolutional code exhibited comparable complexities. The higher performance of the turbo codec facilitates, for example, the employment of turbo-coded 16QAM at a similar SNR, where convolutional-coded QPSK can be invoked. This in turn allows us to double the video bit rate within the same bandwidth and hence to improve the video quality. We have also applied data partitioning to the MPEG-2 video stream to gauge its efficiency in increasing the error resilience of the video codec. However, from these experiments we found that the data partitioning scheme did not provide substantial improvements compared to the nonpartitioned video transmitted over the nonhierarchical DVB-T system. Our future work will focus on extending this DVB-T system study to incorporate various types of channel models, as well as on investigating the effects of different Doppler frequencies on the system. Further work will also be dedicated to trellis-coded modulation (TCM) and turbo trellis-coded modulation (TTCM) based OFDM. The impact of employing various types of turbo interleavers on the system performance is also of interest. A range of further wireless video communications issues are addressed in [160, 516]. Let us now consider a variety of satellite-based turbo-coded blind-equalized multilevel modulation-assisted video broadcasting schemes.

12.8 Satellite-Based Video Broadcasting [13]

12.8.1 Background and Motivation

In recent years, three harmonized digital video broadcasting (DVB) standards have emerged in Europe for terrestrial [499], cable-based [500], and satellite-oriented [501] delivery of DVB signals. The dispersive wireless propagation environment of the terrestrial system requires concatenated Reed–Solomon (RS) [389, 502] and rate-compatible punctured convolutional coding (RCPCC) [389, 502] combined with orthogonal frequency division multiplexing (OFDM)-based modulation [221]. The satellite-based system employs the same concatenated channel coding arrangement as the terrestrial scheme, while the cable-based system refrains from using concatenated channel coding, opting for RS coding only. The performance of both of the latter schemes can be improved upon invoking blind-equalized multilevel modems [221], although the associated mild dispersion or linear distortion does not necessarily require channel equalization. However, since we propose invoking turbo-coded 4-bit/symbol 16-level quadrature amplitude modulation (16QAM) in order to improve the system's performance at the cost of increased complexity, in this section we also invoked blind channel equalizers. This is further justified by the associated high video transmission rates, where the dispersion may become a more dominant performance limitation.

Lastly, the video codec used in all three systems is the Motion Pictures Expert Group's MPEG-2 codec. These standardization activities were followed by a variety of system performance studies in the open literature [517–520]. Against this background, we suggest turbo-coding improvements to the satellite-based DVB system [501] and present performance studies of the proposed system under dispersive channel conditions in conjunction with a variety of blind channel equalization algorithms. The transmitted power requirements of the standard system employing convolutional codecs can be reduced upon invoking more complex, but more powerful, turbo codecs. Alternatively, the standard quaternary or 2-bit/symbol system's bit error rate (BER) versus signal-to-noise ratio (SNR) performance can almost be matched by a turbo-coded 4-bit/symbol 16QAM scheme, while doubling the achievable bit rate within the same bandwidth and hence improving the associated video quality. This is achieved at the cost of an increased system complexity.

The remainder of this section is organized as follows. A succinct overview of the turbo-coded and standard DVB satellite scheme is presented in Section 12.8.2, while our channel model is described in Section 12.8.3. A brief summary of the blind equalizer algorithms employed is presented in Section 12.8.4. Following this, the performance of the improved DVB satellite system is examined for transmission over a dispersive two-path channel in Section 12.8.5, before our conclusions and future work areas are presented in Section 12.8.6.

12.8.2 DVB Satellite Scheme

The block diagram of the DVB satellite (DVB-S) system [501] is shown in Figure 12.104, which is composed of a MPEG-2 video encoder (not shown in the diagram), channel-coding

[13] This section is based on C. S. Lee, S. Vlahoyiannatos, and L. Hanzo, "Satellite based turbo-coded, blind-equalized 4QAM and 16QAM digital video broadcasting," *IEEE Transactions on Broadcasting*, March 2000, pp. 22–34,

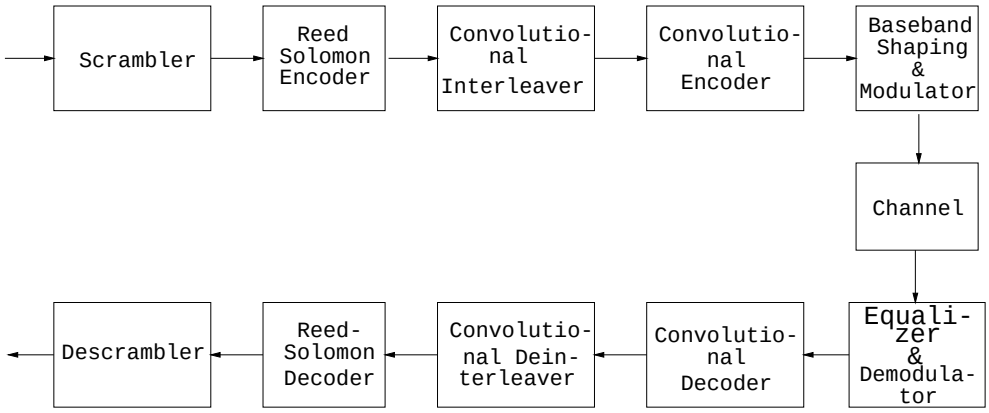

Figure 12.104: Schematic of the DVB satellite system.

Convolutional Coder Parameters	
Code rate	$1/2$
Constraint length	7
n	2
k	1
Generator polynomials (octal format)	171, 133

Table 12.24: Parameters of the $CC(n, k, K)$ Convolutional Inner Encoder of the DVB-S Modem

modules, and a quadrature phase shift keying (QPSK) modem [221]. The bit-stream generated by the MPEG-2 encoder is packetized into frames 188 bytes long. The video data in each packet is then randomized by the scrambler. The details concerning the scrambler have not been included in this chapter, since these may be obtained from the DVB-S standard [501].

Because of the poor error resilience of the MPEG-2 video codec, powerful concatenated channel coding is employed. The concatenated channel codec comprises a shortened Reed–Solomon (RS) outer code and an inner convolutional encoder. The 188-byte MPEG-2 video packet is extended by the Reed–Solomon encoder [389, 502], with parity information to facilitate error recovery to form a 204-byte packet. The Reed–Solomon decoder can then correct up to 8 erroneous bytes for each 204-byte packet. Following this, the RS-coded packet is interleaved by a convolutional interleaver and is further protected by a half-rate inner convolutional encoder with a constraint length of 7 [389, 502].

Furthermore, the overall code rate of the concatenated coding scheme can be adapted by variable puncturing, not shown in the figure, which supports code rates of $\frac{1}{2}$ (no puncturing) as well as $\frac{2}{3}$, $\frac{3}{4}$, $\frac{5}{6}$, and $\frac{7}{8}$. The parameters of the convolutional encoder are summarized in Table 12.24.

In addition to implementing the standard DVB-S system as a benchmark, we have improved the system's performance with the aid of a turbo codec [401, 402]. The block diagram of the turbo encoder is shown in Figure 12.105. The turbo encoder is constructed of two component encoders. Each component encoder is a half-rate convolutional encoder whose

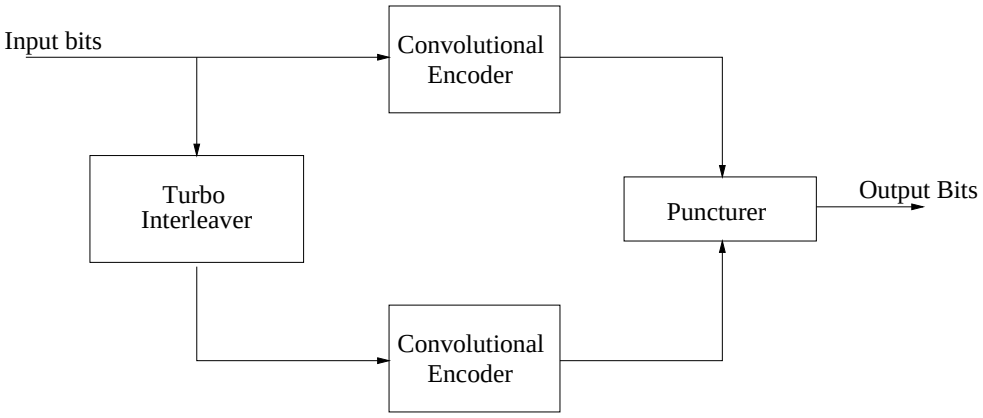

Figure 12.105: Block diagram of turbo encoder.

Turbo Coder Parameters	
Turbo code rate	$1/2$
Input block length	17 952 bits
Interleaver type	Random
Number of turbo decoder iterations	8
Turbo Encoder Component Code Parameters	
Component code encoder type	Convolutional Encoder (RSC)
Component code decoder type	log-MAP [452]
Constraint length	3
n	2
k	1
Generator polynomials (octal format)	7, 5

Table 12.25: Parameters of the Inner Turbo Encoder Used to Replace the DVB-S System's Convolutional Coder (RSC: Recursive Systematic Code)

parameters are listed in Table 12.25. The two component encoders are used to encode the same input bits, although the input bits of the second component encoder are interleaved before encoding. The output bits of the two component codes are punctured and multiplexed in order to form a single-output bit stream. The component encoder used here is known as a half-rate recursive systematic convolutional encoder (RSC) [511]. It generates one parity bit and one systematic output bit for every input bit. In order to provide an overall coding rate of one-half, half the output bits from the two encoders must be punctured. The puncturing arrangement used in our work is to transmit all the systematic bits from the first encoder and every other parity bit from both encoders.

Readers interested in further details of the DVB-S system are referred to the DVB-S standard [501]. The performance of the standard DVB-S system and the performance of the turbo-coded system are characterized in Section 12.8.5. Let us now briefly consider the multipath channel model used in our investigations.

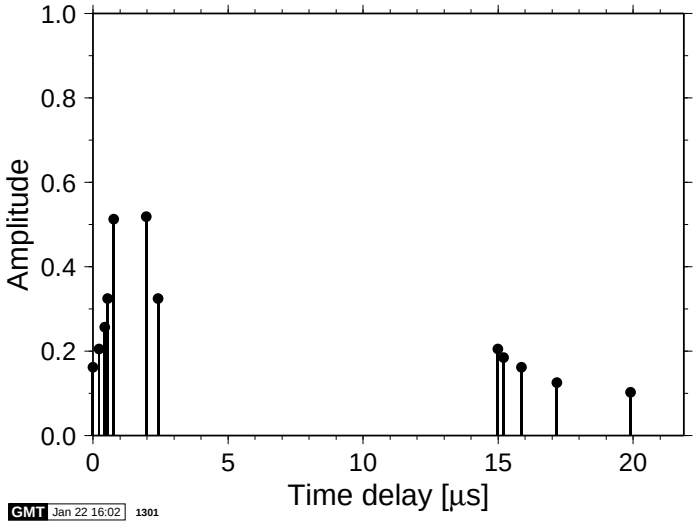

Figure 12.106: Two-path satellite channel model with either a one-symbol or two-symbol delay.

12.8.3 Satellite Channel Model

The DVB-S system was designed to operate in the 12 GHz frequency band (K-band). Within this frequency band, tropospheric effects such as the transformation of electromagnetic energy into thermal energy due to induction of currents in rain and ice crystals lead to signal attenuations [521, 522]. In the past 20 years, various researchers have concentrated on attempting to model the satellite channel, typically within a land mobile satellite channel scenario. However, the majority of the work conducted, for example, by Vogel and his colleagues [523–526] concentrated on modelling the statistical properties of a narrowband satellite channel in lower frequency bands, such as the 870 MHz UHF band and the 1.5 GHz L-band.

Our high bit-rate DVB satellite system requires a high bandwidth, however. Hence, the video bit-stream is exposed to dispersive wideband propagation conditions. Recently, Saunders *et al.* [527, 528] have proposed the employment of multipath channel models to study the satellite channel, although their study concentrated on the L-band and S-band only.

Due to the dearth of reported work on wideband satellite channel modeling in the K-band, we have adopted a simpler approach. The channel model employed in this study was the two-path (nT)-symbol spaced impulse response, where T is the symbol duration. In our studies we used $n = 1$ and $n = 2$ (Figure 12.106). This corresponds to a stationary dispersive transmission channel. Our channel model assumed that the receiver had a direct line-of-sight with the satellite as well as a second path caused by a single reflector probably from a nearby building or due to ground reflection. The ground reflection may be strong if the satellite receiver dish is only tilted at a low angle.

Based on these channel models, we studied the ability of a range of blind equalizer algorithms to converge under various path-delay conditions. In the next section, we provide a brief overview of the various blind equalizers employed in our experiments. Readers inter-

ested mainly in the system's performance may proceed directly to our performance analysis section, Section 12.8.5.

12.8.4 The Blind Equalizers

This section presents the blind equalizers used in the system. The following blind equalizers have been studied:

1. The modified constant modulus algorithm (MCMA) [529].
2. The Benveniste-Goursat algorithm (B-G) [530].
3. The stop-and-go algorithm (S-a-G) [531].
4. The per-survivor processing (PSP) algorithm [532].

We will now briefly introduce these algorithms.

First, we define the variables that we will use:

$$\mathbf{y}(n) = [y(n+N_1), \ldots, y(0), \ldots, y(n-N_2)]^T \tag{12.26}$$

$$\mathbf{c}^{(n)} = [c_{-N_1}, \ldots, c_o, \ldots, c_{N_2}]^T \tag{12.27}$$

$$z(n) = \left(\mathbf{c}^{(n)}\right)^T \mathbf{y}(n) = \mathbf{y}^T(n)\mathbf{c}^{(n)} \tag{12.28}$$

where $\mathbf{y}(n)$ is the received symbol vector at time n, containing the $N_1 + N_2 + 1$ most recent received symbols, while N_1, N_2 are the number of equalizer feedback and feedforward taps, respectively. Furthermore, $\mathbf{c}^{(n)}$ is the equalizer tap vector, consisting of the equalizer tap values, and $z(n)$ is the equalized symbol at time n, given by the convolution of the received signal with the equalizer's impulse response, while $()^T$ stands for matrix transpose. Note that the variables of Equations 12.26–12.28 assume complex values, when multilevel modulation is employed.

The **modified CMA** (MCMA) is an improved version of Godard's well-known *constant modulus algorithm (CMA)* [533]. The philosophy of the CMA is based on forcing the magnitude of the equalized signal to a constant value. In mathematical terms, the CMA is based on minimising the cost function:

$$J^{(CMA)} = E\left[\left(|z(n)|^2 - R_2\right)^2\right], \tag{12.29}$$

where R_2 is a suitably chosen constant and $E[]$ stands for the expectation. Similarly to the CMA, the MCMA, which was proposed by Wesolowsky [529], forces the real and imaginary parts of the complex signal to the constant values of $R_{2,R}$ and $R_{2,I}$, respectively, according to the equalizer tap update equation of [529]:

$$\begin{aligned}\mathbf{c}^{(n+1)} = \mathbf{c}^{(n)} - \lambda \cdot \mathbf{y}^*(n) \cdot \{&Re[z(n)] \cdot \left((Re[z(n)])^2 - R_{2,R}\right) \\ &+ jIm[z(n)] \cdot \left((Im[z(n)])^2 - R_{2,I}\right)\},\end{aligned} \tag{12.30}$$

where λ is the step-size parameter and the $R_{2,R}$, $R_{2,I}$ constant parameters of the algorithm are defined as:

$$R_{2,R} = \frac{E\left[(Re[a(n)])^4\right]}{E\left[(Re[a(n)])^2\right]} \tag{12.31}$$

$$R_{2,I} = \frac{E\left[(Im[a(n)])^4\right]}{E\left[(Im[a(n)])^2\right]}, \tag{12.32}$$

where $a(n)$ is the transmitted signal at time instant n.

The **BenvenisteGoursat** (B-G) algorithm [530] is an amalgam of the Sato's algorithm [534] and the decision-directed (DD) algorithm [221]. Strictly speaking, the decision-directed algorithm is not a blind equalization technique, since its convergence is highly dependent on the channel.

This algorithm estimates the error between the equalized signal and the detected signal as:

$$\epsilon^{DD}(n) = z(n) - \hat{z}(n), \tag{12.33}$$

where $\hat{z}(n)$ is the receiver's estimate of the transmitted signal at time instant n. Similarly to the DD algorithm's error term, the Sato error [534] is defined as:

$$\epsilon^{Sato}(n) = z(n) - \gamma \cdot csgn(z(n)), \tag{12.34}$$

where γ is a constant parameter of the Sato algorithm, defined as:

$$\gamma = \frac{E\left[\left(Re\left[a(n)\right]\right)^2\right]}{E\left[\left|Re\left[a(n)\right]\right|\right]} = \frac{E\left[\left(Im\left[a(n)\right]\right)^2\right]}{E\left[\left|Im\left[a(n)\right]\right|\right]} \tag{12.35}$$

and $csgn(x) = sign(Re\{x\}) + jsign(Im\{x\})$ is the complex sign function. The B-G algorithm combines the above two error terms into one:

$$\epsilon^{G}(n) = k_1 \cdot \epsilon^{DD}(n) + k_2 \cdot |\epsilon^{DD}(n)| \cdot \epsilon^{Sato}(n), \tag{12.36}$$

where the two error terms are suitably weighted by the constant parameters k_1 and k_2 in Equation 12.36. Using this error term, the B–G equalizer updates the equalizer coefficients according to the following equalizer tap update equations [530]:

$$\mathbf{c}^{(n+1)} = \mathbf{c}^{(n)} - \lambda \cdot \mathbf{y}^{*}(n) \cdot \epsilon^{G}(n). \tag{12.37}$$

In our investigations, the weights were chosen as $k_1 = 1$, $k_2 = 5$, so that the Sato error was weighted more heavily than the DD error.

The **stop-and-go** (S-a-G) algorithm [531] is a variant of the decision-directed algorithm [221], where at each equalizer coefficient adjustment iteration, the update is enabled or disabled depending on whether or not the update is likely to be correct. The update equations of this algorithm are given by [531]

$$\mathbf{c}^{(n+1)} = \mathbf{c}^{(n)} - \lambda \cdot \mathbf{y}^{*}(n) \cdot [f_{n,R} \cdot Re\{\epsilon^{DD}(n)\} + jf_{n,I} \cdot Im\{\epsilon^{DD}(n)\}], \tag{12.38}$$

where * stands for the complex conjugate, $\epsilon^{DD}(n)$ is the decision directed error as in Equation 12.33 and the binary functions $f_{n,R}$, $f_{n,I}$ enable or disable the update of the equalizer

	Step Size λ	No. of Equalizer Taps	Initial Tap Vector
Benveniste–Goursat	$5\text{x}10^{-4}$	10	$(1.2, 0, \cdots, 0)$
Modified CMA	$5\text{x}10^{-4}$	10	$(1.2, 0, \cdots, 0)$
Stop-and-go	$5\text{x}10^{-4}$	10	$(1.2, 0, \cdots, 0)$
PSP (1 sym delay)	10^{-2}	2	$(1.2, 0)$
PSP (2 sym delay)	10^{-2}	3	$(1.2, 0, 0)$

Table 12.26: Summary of the Equalizer Parameters Used in the Simulations. The Tap Vector $(1.2, 0, \cdots, 0)$ Indicates that the First Equalizer Coefficient is Initialized to the Value 1.2, While the Others are Initialized to 0.

according to the following rule. If the sign of the Sato error (the real or the imaginary part independently) is the same as the sign of the decision-directed error, then the update takes place; otherwise it does not.

In mathematical terms, this is equivalent to [531]:

$$f_{n,R} = \begin{cases} 1 & \text{if } sgn(Re[\epsilon^{DD}(n)]) = sgn(Re[\epsilon^{Sato}(n)]) \\ 0 & \text{if } sgn(Re[\epsilon^{DD}(n)] \neq sgn(Re[\epsilon^{Sato}(n)]) \end{cases} \tag{12.39}$$

$$f_{n,I} = \begin{cases} 1 & \text{if } sgn(Im\{\epsilon^{DD}(n)\}) = sgn(Im\{\epsilon^{Sato}(n)\}) \\ 0 & \text{if } sgn(Im\{\epsilon^{DD}(n)\}) \neq sgn(Im\{\epsilon^{Sato}(n)\}). \end{cases} \tag{12.40}$$

For a blind equalizer, this condition provides us with a measure of the probability of the coefficient update being correct.

The **PSP algorithm** [532] is based on employing convolutional coding. Hence, it is a trellis-based sequence estimation technique in which the channel is not known *a priori*. An iterative channel estimation technique is employed in order to estimate the channel jointly with the modulation symbol. In this sense, an initial channel is used, and the estimate is updated at each new symbol's arrival.

In our case, the update was based on the *least means squares (LMS)* estimates, according to the following channel-tap update equations [532]:

$$\hat{\mathbf{h}}^{(n+1)} = \hat{\mathbf{h}}^{(n)} + \lambda \cdot \hat{\mathbf{a}}^*(n) \cdot \left(y(n) - \hat{\mathbf{a}}^T(n) \hat{\mathbf{h}}^{(n)} \right), \tag{12.41}$$

where $\hat{\mathbf{h}}^{(n)} = (\hat{h}_{-L_1}^{(n)}, \ldots, \hat{h}_o^{(n)}, \ldots, \hat{h}_{L_2}^{(n)})^T$ is the estimated (for one surviving path) channel tap vector at time instant n, $\hat{\mathbf{a}}(n) = (\hat{a}(n + L_1), \ldots, \hat{a}(0), \ldots, \hat{a}(n - L_2))^T$ is the associated estimated transmitted symbol vector, and $y(n)$ is the actually received symbol at time instant n.

Each of the surviving paths in the trellis carries not only its own signal estimation, but also its own channel estimation. Moreover, convolutional decoding can take place jointly with this channel and data estimation procedure, leading to improved bit error rate (BER) performance. The various equalizers' parameters are summarized in Table 12.26.

Having described the components of our enhanced DVB-S system, let us now consider the overall system's performance.

12.8.5 Performance of the DVB Satellite Scheme

In this section, the performance of the DVB-S system was evaluated by means of simulations. Two modulation types were used, namely, the standard QPSK and the enhanced 16QAM schemes [221]. The channel model of Figure 12.106 was employed. The first channel model had a one-symbol second-path delay, while in the second one the path-delay corresponded to the period of two symbols. The average BER versus SNR per bit performance was evaluated after the equalization and demodulation process, as well as after Viterbi [389] or turbo decoding [402]. The SNR per bit or E_b/N_o is defined as follows:

$$\text{SNR per bit} = 10\ log_{10}\frac{\bar{S}}{\bar{N}} + \delta, \tag{12.42}$$

where $\bar{S}$ is the average received signal power, $\bar{N}$ is the average received noise power, and δ, which is dependent on the type of modulation scheme used and channel code rate (R), is defined as:

$$\delta = 10\ log_{10}\frac{1}{\text{R} \times \text{bits per modulation symbol}}. \tag{12.43}$$

Our results are further divided into two subsections for ease of discussion. First, we present the system performance over the one-symbol delay two-path channel in Section 12.8.5.1. Next, the system performance over the two-symbol delay two-path channel is presented in Section 12.8.5.2. Lastly, a summary of the system performance is provided in Section 12.8.5.3.

12.8.5.1 Transmission over the Symbol-Spaced Two-Path Channel

The linear equalizers' performance was quantified and compared using QPSK modulation over the one-symbol delay two-path channel model of Figure 12.107. Since all the equalizers have similar BER performance, only the modified CMA results are shown in the figure.

The equalized performance over the one symbol-spaced channel was inferior to that over the nondispersive AWGN channel. However, as expected, it was better than without any equalization. Another observation for Figure 12.107 was that the different punctured channel-coding rates appeared to give slightly different bit error rates after equalization. This was because the linear blind equalizers required uncorrelated input bits in order to converge. However, the input bits were not entirely random when convolutional coding was used. The consequences of violating the zero-correlation constraint are not generally known. Nevertheless, two potential problems were apparent. First, the equalizer may diverge from the desired equalizer equilibrium [535]. Second, the performance of the equalizer is expected to degrade, owing to the violation of the randomness requirement, which is imposed on the input bits in order to ensure that the blind equalizers will converge.

Since the channel used in our investigations was static, the first problem was not encountered. Instead, the second problem was what we actually observed. Figure 12.108 quantifies the equalizers' performance degradation due to convolutional coding. We can observe a 0.1 dB SNR degradation when the convolutional codec creates correlation among the bits for this specific case.

The average BER versus SNR curves after Viterbi or turbo decoding are shown in Figure 12.109(a). In this figure, the average BER over the nondispersive AWGN channel after turbo decoding constitutes the best-case performance, while the average BER of the one-symbol delay two-path MCMA-equalized rate 7/8 convolutionally coded scenario exhibits the

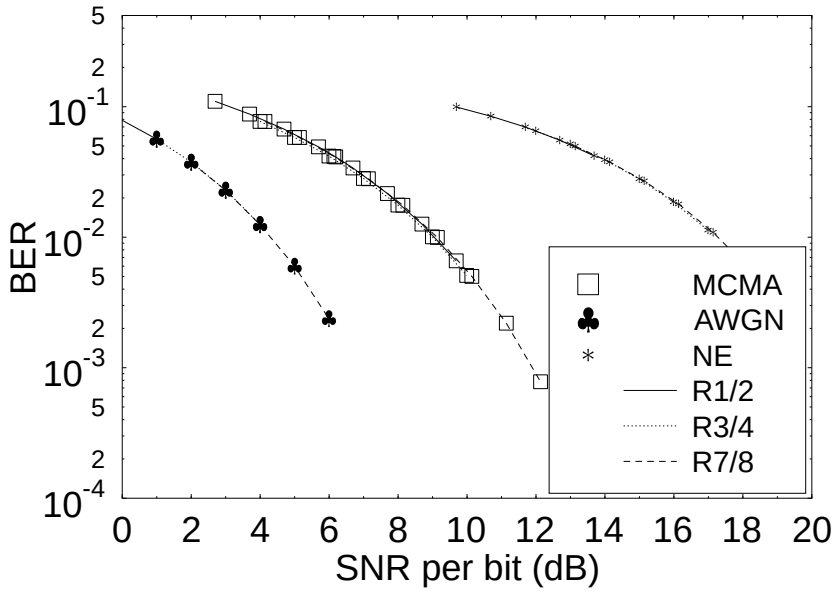

(a) After equalization and demodulation

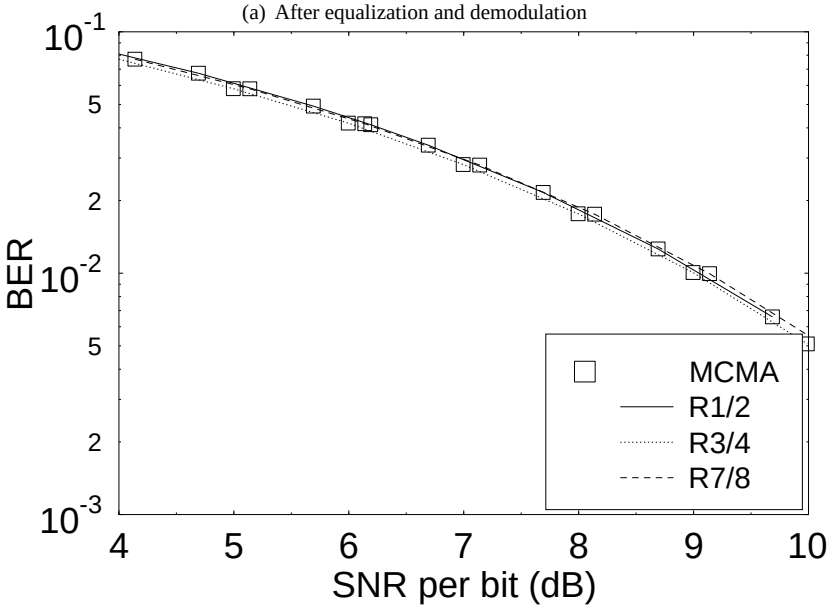

(b) Same as (a) but enlarged in order to show performance difference of the blind equalizer, when different convolutional code rates are used

Figure 12.107: Average BER versus SNR per bit performance after equalization and demodulation employing **QPSK** modulation and **one-symbol delay channel** (**NE** = nonequalized; **MCMA** = modified constant modulus algorithm).

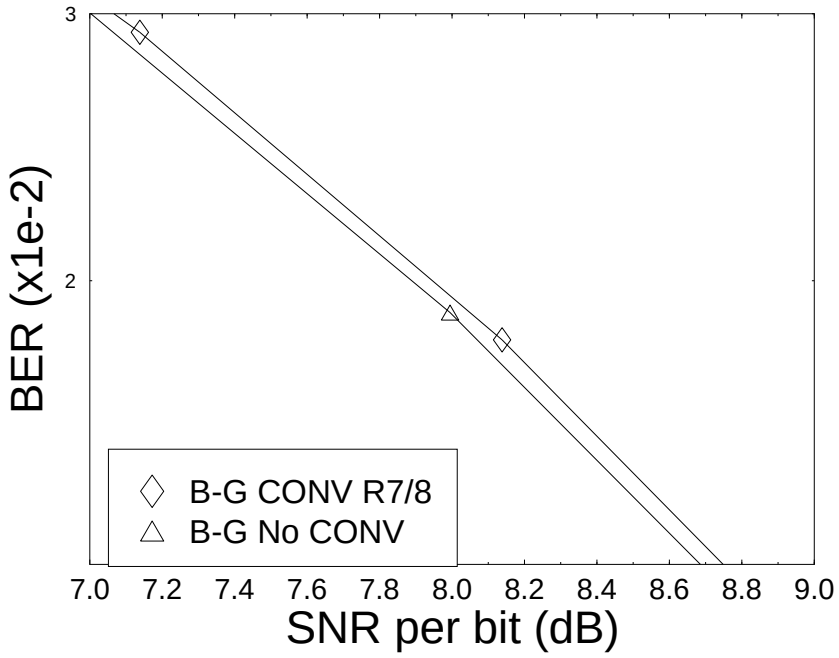

Figure 12.108: Average BER versus SNR per bit performance after equalization and demodulation employing **QPSK** modulation and the **one-symbol delay two-path channel** of Figure 12.106, for the Benveniste–Goursat algorithm, where the input bits are random (No CONV) or correlated (CONV 7/8) as a result of convolutional coding having a coding rate of 7/8.

worst-case performance. Again, in this figure only the modified CMA was featured for simplicity. The performance of the remaining equalizers was characterized in Figure 12.109(b). Clearly, the performance of all the linear equalizers investigated was similar.

As seen in Figure 12.109(a), the combination of the modified CMA blind equalizer with turbo decoding exhibited the best SNR performance over the one-symbol delay two-path channel. The only comparable alternative was the PSP algorithm. Although the performance of the PSP algorithm was better at low SNRs, the associated curves cross over and the PSP algorithm's performance became inferior below the average BER of 10^{-3}. Although not shown in Figure 12.109, the Reed–Solomon decoder, which was concatenated to either the convolutional or the turbo decoder, became effective, when the average BER of its input was below approximately 10^{-4}. In this case, the PSP algorithm performed by at least 1 dB worse in the area of interest, which is at an average BER of 10^{-4}.

A final observation in the context of Figure 12.109(a) is that when convolutional decoding was used, the associated E_b/N_o performance of the rate 1/2 convolutional coded scheme appeared slightly inferior to that of the rate 3/4 and the rate 7/8 scenarios beyond certain E_b/N_o values. This was deemed to be a consequence of the fact that the 1/2 rate encoder introduced more correlation into the bitstream than its higher rate counterparts, and this degraded the performance of the blind channel equalizers which performed best when fed with random

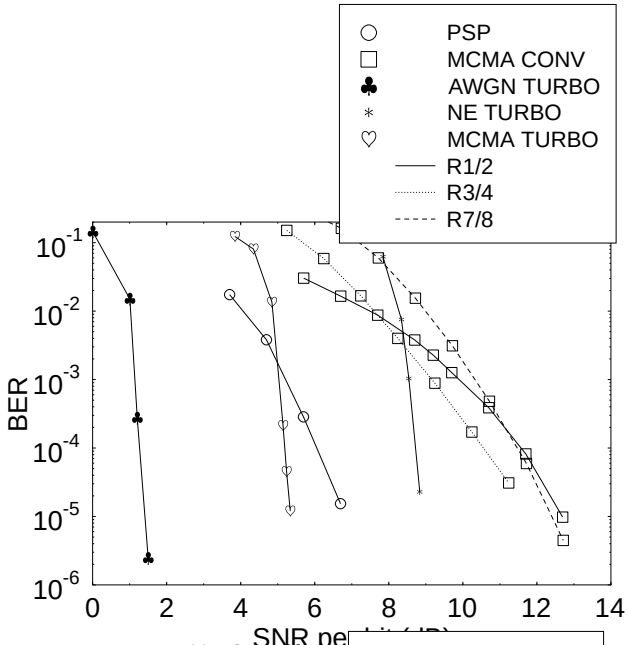

(a) PSP and linear

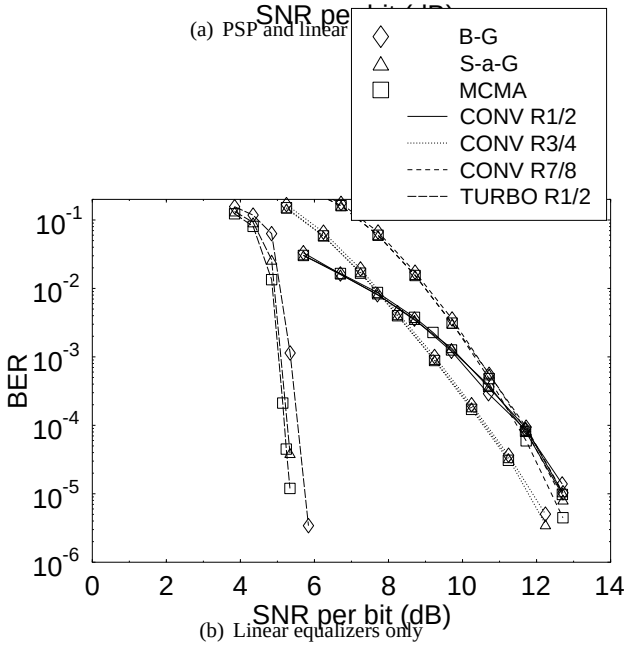

(b) Linear equalizers only

Figure 12.109: Average BER versus SNR per bit performance after convolutional or turbo decoding for **QPSK** modulation and **one-symbol delay channel** (**NE** = nonequalized; **B-G** = Benveniste–Goursat; **S-a-G** = stop-and-go; **MCMA** = modified constant modulus algorithm; **PSP** = per-survivor processing).

bits.

Having considered the QPSK case, we shall now concentrate on the enhanced system which employed 16QAM under the same channel and equalizer conditions. Figures 12.110 and 12.111 present the performance of the DVB system employing 16QAM. Again, for simplicity, only the modified CMA results are given. In this case, the ranking order of the different coding rates followed our expectations more closely in the sense that the lowest coding rate of 1/2 was the best performer, followed by rate 3/4 codec, in turn followed by the least powerful rate 7/8 codec.

The stop-and-go algorithm has been excluded from these results, because it does not converge for high SNR values. This happens because the equalization procedure is activated only when there is a high probability of correct decision-directed equalizer update. In our case, the equalizer is initialized far from its convergence point, and hence the decision directed updates are unlikely to be correct. In the absence of noise, this leads to the update algorithm being permanently deactivated. If noise is present, however, then some random perturbations from the point of the equalizer's initialization activate the stop-and-go algorithm and can lead to convergence. We made this observation at medium SNR values in our simulation study. For high SNR values, the algorithm did not converge.

It is also interesting to compare the performance of the system for the QPSK and 16QAM schemes. When the one-symbol delay two-path channel model of Figure 12.106 was considered, the system was capable of supporting the use of 16QAM with the provision of an additional SNR per bit of approximately 4–5 dB. This observation was made by comparing the performance of the DVB system when employing the modified CMA and the half-rate convolutional or turbo code in Figures 12.109 and 12.111 at a BER of 10^{-4}. Although the original DVB satellite system only employs QPSK modulation, our simulations had shown that 16QAM can be employed equally well for the range of blind equalizers that we have used in our work. This allowed us to double the video bit rate and hence to substantially improve the video quality. The comparison of Figures 12.109 and 12.111 also reveals that the extra SNR requirement of approximately 4–5 dB of 16QAM over QPSK can be eliminated by employing turbo coding at the cost of a higher implementational complexity. This allowed us to accommodate a doubled bit rate within a given bandwidth, which improved the video quality.

12.8.5.2 Transmission over the Two-Symbol Delay Two-Path Channel

In Figure 12.112 (only for the Benveniste-Goursat algorithm for simplicity) and Figure 12.113, the corresponding BER results for the two-symbol delay two-path channel of Figure 12.106 are given for QPSK. The associated trends are similar to those in Figures 12.107 and 12.109, although some differences can be observed, as listed below:

- The "crossover point" is where the performance of the PSP algorithm becomes inferior to the performance of the modified CMA in conjunction with turbo decoding. This point is now at 10^{-4}, which is in the range where the RS decoder guarantees an extremely low probability of error.
- The rate 1/2 convolutional decoding is now the best performer, when convolutional decoding is concerned, while the rate 3/4 scheme exhibits the worst performance.

Finally, in Figure 12.114, the associated 16QAM results are presented. Notice that the

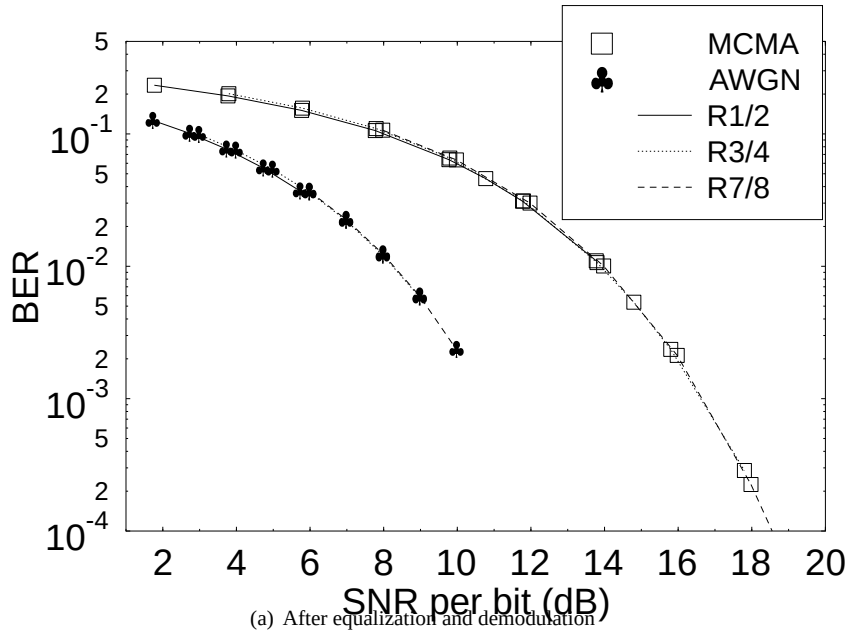

(a) After equalization and demodulation

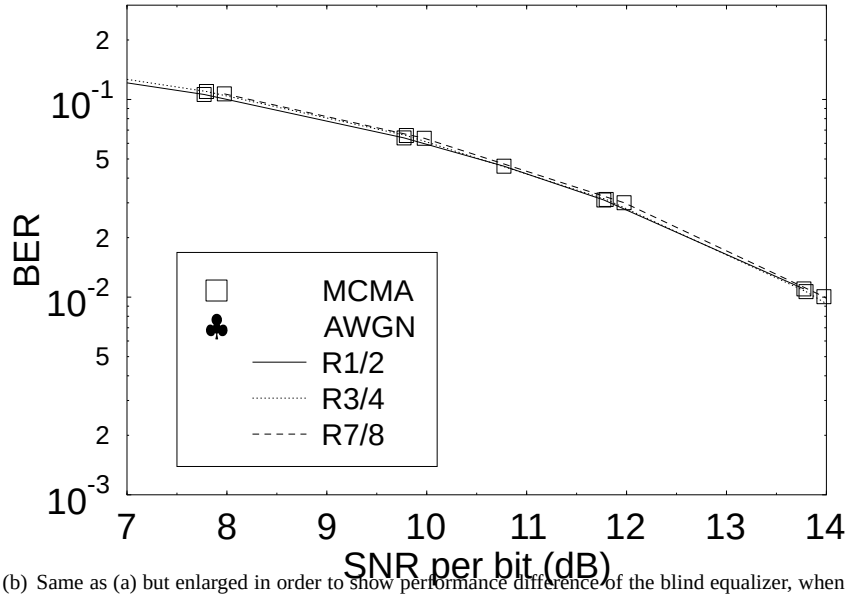

(b) Same as (a) but enlarged in order to show performance difference of the blind equalizer, when different convolutional code rates are used

Figure 12.110: Average BER versus SNR per bit after equalization and demodulation for **16QAM** over the **one-symbol delay two-path channel** of Figure 12.106 (**MCMA** = modified constant modulus algorithm).

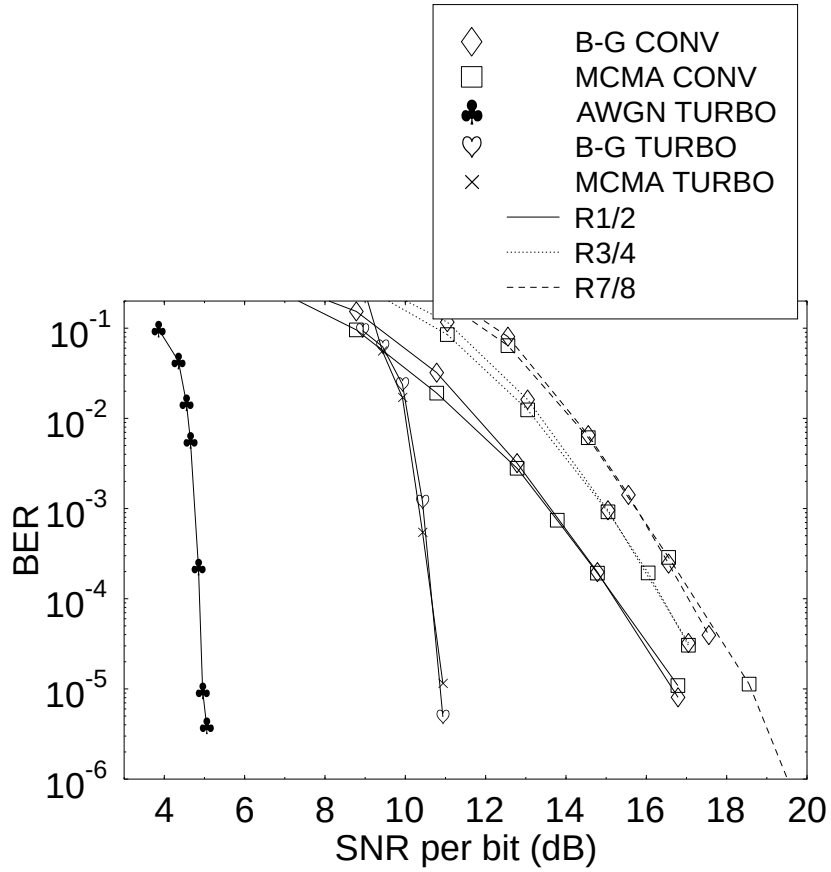

Figure 12.111: Average BER versus SNR per bit after Viterbi or turbo decoding for **16QAM** over the **one-symbol delay two-path channel** of Figure 12.106 (**B-G** = Benveniste–Goursat; **S-a-G** = stop-and-go; **MCMA** = modified constant modulus algorithm; **PSP** = per-survivor processing).

stop-and-go algorithm was again excluded from the results. Furthermore, we observe a high-performance difference between the Benveniste-Goursat algorithm and the modified CMA. In the previous cases we did not observe such a significant difference. The difference in this case is that the channel exhibits an increased delay spread. This illustrated the capability of the equalizers to cope with more widespread multipaths, while keeping the equalizer order constant at 10. The Benveniste-Goursat equalizer was more efficient than the modified CMA in this case.

It is interesting to note that in this case the performance of the different coding rates was again in the expected order: the rate $\frac{1}{2}$ scheme is the best, followed by the rate $\frac{3}{4}$ scheme and then the rate $\frac{7}{8}$ scheme.

If we compare the performance of the system employing QPSK and 16QAM over the two-symbol delay two-path channel of Figure 12.106, we again observe that 16QAM can be

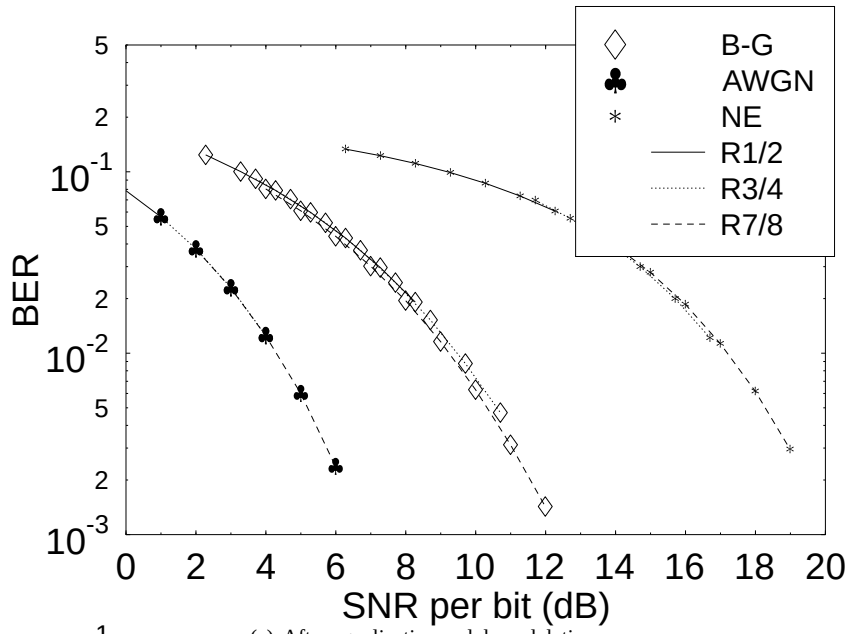

(a) After equalization and demodulation

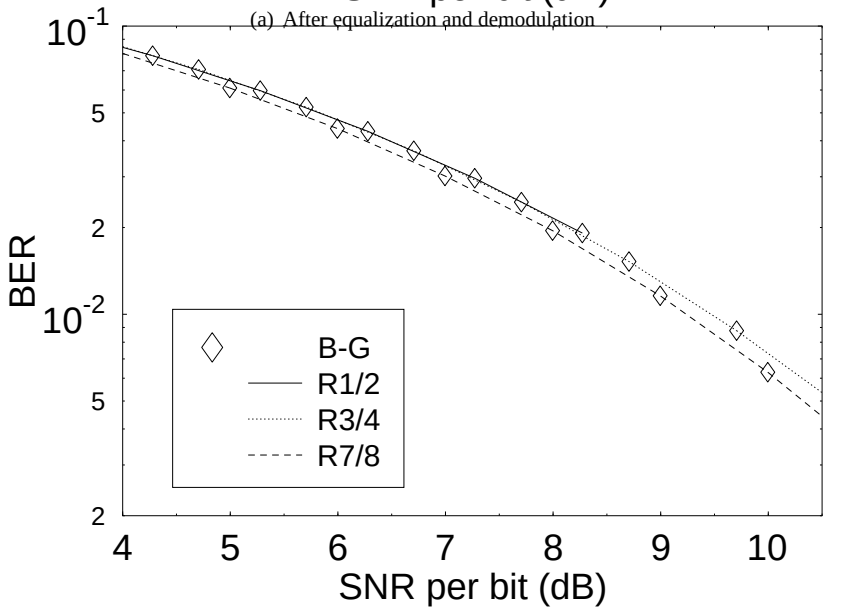

(b) Same as (a) but enlarged in order to show performance difference of the blind equalizer, when different convolutional code rates are used

Figure 12.112: Average BER versus SNR per-bit performance after equalization and demodulation for **QPSK** modulation over the **two-symbol delay two-path channel** of Figure 12.106 (**B-G** = Benveniste-Goursat).

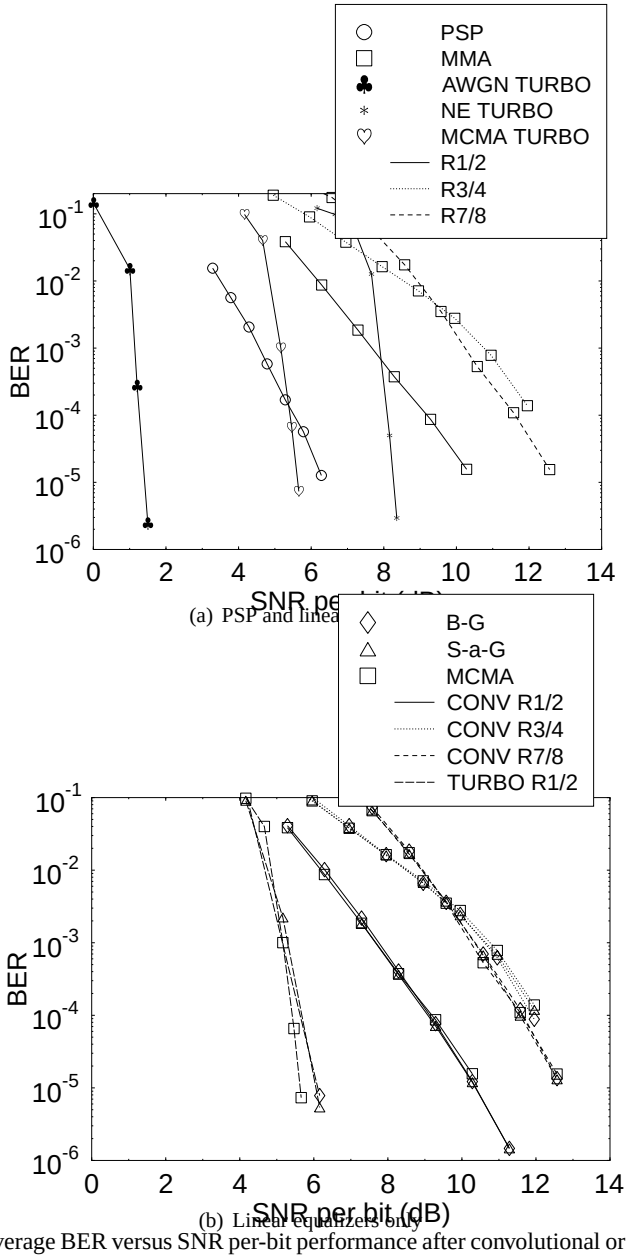

(a) PSP and linea

(b) Linear equalizers only

Figure 12.113: Average BER versus SNR per-bit performance after convolutional or turbo decoding for **QPSK** modulation over the **two-symbol delay two-path channel** of Figure 12.106 (**B-G** = Benveniste-Goursat; **S-a-G** = stop-and-go; **MCMA** = modified constant modulus algorithm; **PSP** = per-survivor processing).

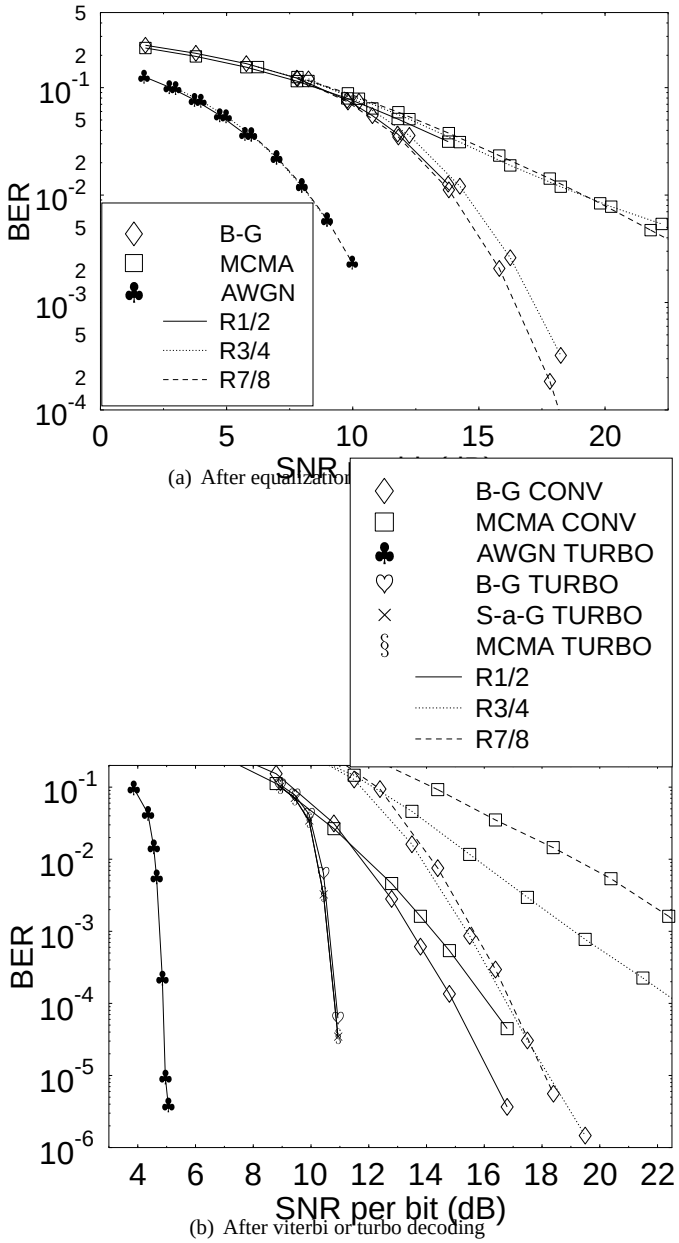

(a) After equalization

(b) After viterbi or turbo decoding

Figure 12.114: Average BER versus SNR per-bit performance (a) after equalization and demodulation and (b) after Viterbi or turbo decoding for **16QAM** over the **two-symbol delay two-path channel** of Figure 12.106 (**B–G** = Benveniste-Goursat; **S-a-G** = stop-and-go; **MCMA** = modified constant modulus algorithm; **PSP** = per-survivor processing).

	B-G	MCMA	S-a-G	PSP
QPSK 1 sym	73	161	143	0.139
QPSK 2 sym	73	143	77	0.139
16QAM 1 sym	411	645	1393	
16QAM 2 sym	359	411	1320	

Table 12.27: Equalizer Convergence Speed (in miliseconds) Measured in the Simulations, Given as an Estimate of Time Required for Convergence When 1/2 Rate Puncturing Is Used (x sym = x-Symbol Delay Two-path Channel and x Can Take Either the Value 1 or 2)

incorporated into the DVB system if an extra 5 dB of SNR per bit is affordable in power budget terms. Here, only the B-G algorithm is worth considering out of the three linear equalizers of Table 12.26. This observation was made by comparing the performance of the DVB system when employing the Benveniste-Goursat equalizer and the half-rate convolutional coder in Figures 12.113 and 12.114.

12.8.5.3 Performance Summary of the DVB-S System

Table 12.27 provides an approximation of the convergence speed of each blind equalization algorithm of Table 12.26. PSP exhibited the fastest convergence, followed by the Benveniste-Goursat algorithm. In our simulations the convergence was quantified by observing the slope of the BER curve and finding when this curve was reaching the associated residual BER, implying that the BER has reached its steady-state value. Figure 12.115 gives an illustrative example of the equalizer's convergence for 16QAM. The stop-and-go algorithm converges significantly slower than the other algorithms, which can also be seen from Table 12.27. This happens because during start-up the algorithm is deactivated most of the time. The effect becomes more severe with increasing QAM order.

Figure 12.116 portrays the corresponding reconstructed video quality in terms of the average peak signal-to-noise ratio (PSNR) versus channel SNR (CSNR) for the one-symbol delay and two-symbol delay two-path channel models of Figure 12.106. The PSNR is defined as follows:

$$\text{PSNR} = 10\, log_{10} \frac{\sum_{n=0}^{N} \sum_{m=0}^{M} 255^2}{\sum_{n=0}^{N} \sum_{m=0}^{M} \Delta^2}, \tag{12.44}$$

where Δ is the difference between the uncoded pixel value and the reconstructed pixel value. The variables M and N refer to the dimension of the image. The maximum possible 8-bit represented pixel luminance value of 255 was used in Equation 12.44 in order to mitigate the PSNR's dependence on the video material used. The average PSNR is then the mean of the PSNR values computed for all the images constituting the video sequence.

Tables 12.28 and 12.29 provide a summary of the DVB satellite system's performance tolerating a PSNR degradation of 2 dB, which was deemed to be nearly imperceptible in terms of subjective video degradations. The average BER values quoted in the tables refer to the average BER achieved after Viterbi or turbo decoding. The channel SNR is quoted in association with the 2 dB average video PSNR degradation, since the viewer will begin to perceive video degradations due to erroneous decoding of the received video around this threshold.

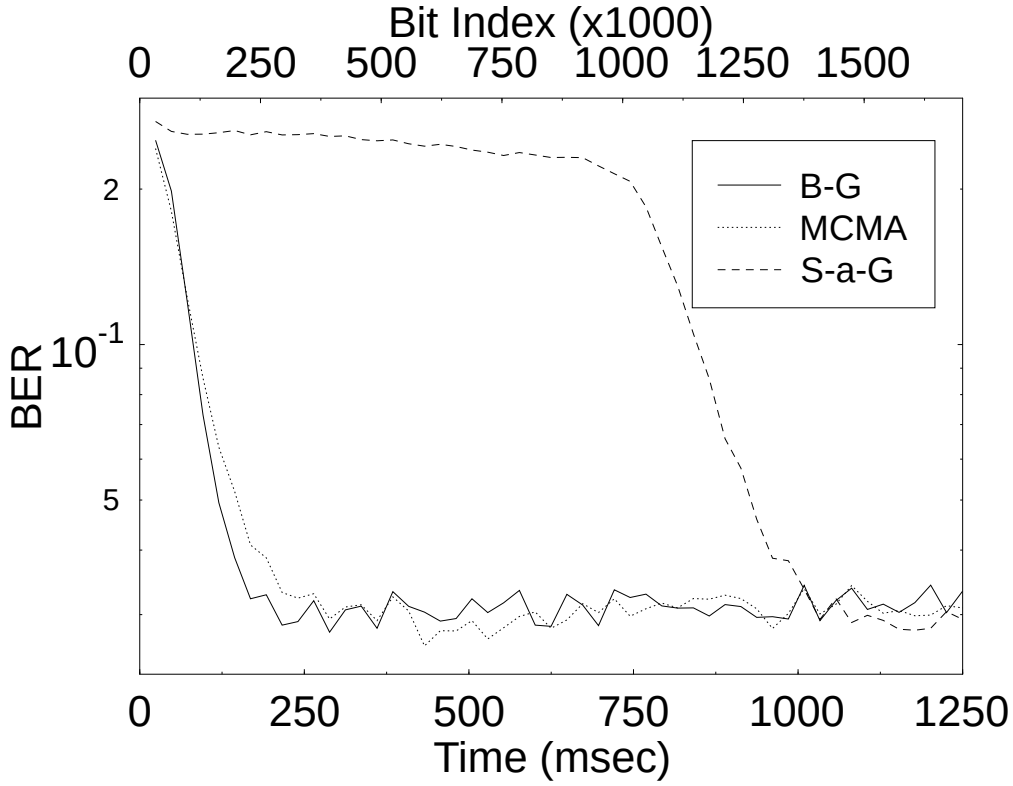

Figure 12.115: Learning curves for 16QAM, one-symbol delay two-path channel at SNR = 18 dB.

Mod.	Equalizer	Code	CSNR (dB)	E_b/N_0
QPSK	PSP	R=1/2	5.3	5.3
QPSK	MCMA	Turbo (1/2)	5.2	5.2
16QAM	MCMA	Turbo (1/2)	13.6	10.6
QPSK	MCMA	Conv (1/2)	9.1	9.1
16QAM	MCMA	Conv (1/2)	17.2	14.2
QPSK	MCMA	Conv (3/4)	11.5	9.7
16QAM	MCMA	Conv (3/4)	20.2	15.4
QPSK	B-G	Conv (7/8)	13.2	10.8
16QAM	B-G	Conv (7/8)	21.6	16.2

Table 12.28: Summary of Performance Results over the Dispersive One-symbol Delay Two-Path AWGN Channel of Figure 12.106 Tolerating a PSNR Degradation of 2 dB

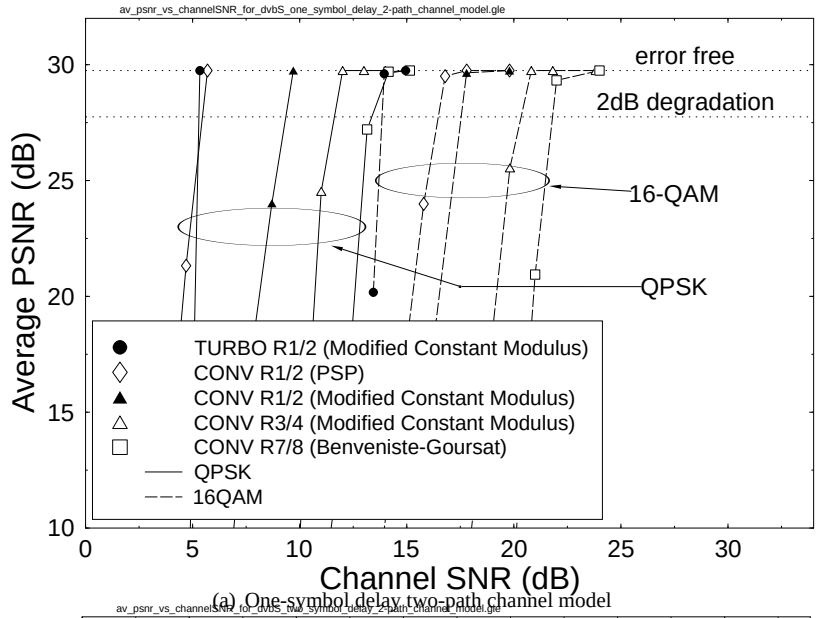

(a) One-symbol delay two-path channel model

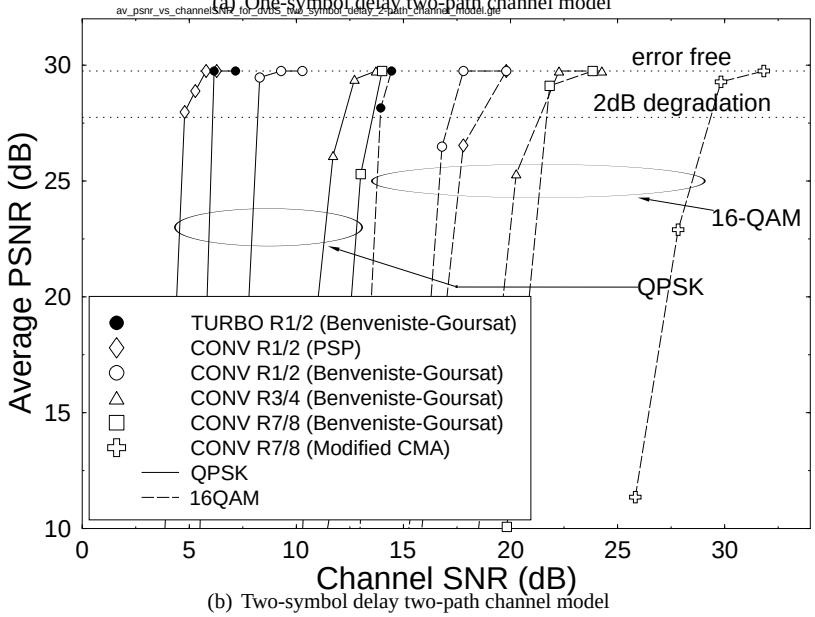

(b) Two-symbol delay two-path channel model

Figure 12.116: Average PSNR versus channel SNR for (a) the one-symbol delay two-path channel model and (b) the two-symbol delay two-path channel model of Figure 12.106 at a video bit rate of 2.5 Mbit/s using the "Football" video sequence.

Mod.	Equalizer	Code	CSNR (dB)	E_b/N_0
QPSK	PSP	R=1/2	4.7	4.7
QPSK	B-G	Turbo (1/2)	5.9	5.9
16QAM	B-G	Turbo (1/2)	13.7	10.7
QPSK	B-G	Conv (1/2)	8.0	8.0
16QAM	B-G	Conv (1/2)	17.0	14.0
QPSK	B-G	Conv (3/4)	12.1	10.3
16QAM	B-G	Conv (3/4)	21.1	16.3
QPSK	B-G	Conv (7/8)	13.4	11.0
16QAM	MCMA	Conv (7/8)	29.2	23.8

Table 12.29: Summary of Performance Results over the Dispersive Two-symbol Delay Two-path AWGN Channel of Figure 12.106 Tolerating a PSNR Degradation of 2 dB

Mod.	Equalizer	Code	E_b/N_0
QPSK	PSP	R=1/2	6.1
QPSK	MCMA	Turbo (1/2)	5.2
16QAM	MCMA	Turbo (1/2)	10.7
QPSK	MCMA	Conv (1/2)	11.6
16QAM	MCMA	Conv (1/2)	15.3
QPSK	MCMA	Conv (3/4)	10.5
16QAM	MCMA	Conv (3/4)	16.4
QPSK	B-G	Conv (7/8)	11.8
16QAM	B-G	Conv (7/8)	17.2

Table 12.30: Summary of System Performance Results over the Dispersive One-symbol Delay Two-path AWGN Channel of Figure 12.106 Tolerating an Average BER of 10^{-4}, which was Evaluated after Viterbi or Turbo Decoding but before RS Decoding

Tables 12.30 and 12.31 provide a summary of the SNR per bit required for the various system configurations. The BER threshold of 10^{-4} was selected here, because of this average BER after Viterbi or turbo decoding, the RS decoder becomes effective, guaranteeing near error-free performance. This also translates into near unimpaired reconstructed video quality.

Finally, in Table 12.32 the QAM symbol rate or baud rate is given for different puncturing rates and for different modulation schemes, based on the requirement of supporting a video bit rate of 2.5 Mbit/sec. We observe that the baud rate is between 0.779 and 2.73 MBd, depending on the coding rate and the number of bits per modulation symbol.

12.8.6 Summary and Conclusions

In this chapter, we have investigated the performance of a turbo-coded DVB system in a satellite broadcast environment. A range of system performance results was presented based

Mod.	Equalizer	Code	E_b/N_0
QPSK	PSP	R=1/2	5.6
QPSK	B-G	Turbo (1/2)	5.7
16QAM	B-G	Turbo (1/2)	10.7
QPSK	B-G	Conv (1/2)	9.2
16QAM	B-G	Conv (1/2)	15.0
QPSK	B-G	Conv (3/4)	12.0
16QAM	B-G	Conv (3/4)	16.8
QPSK	B-G	Conv (7/8)	11.7
16QAM	MCMA	Conv (7/8)	26.0

Table 12.31: Summary of System Performance Results over the Dispersive Two-symbol Delay Two-path AWGN Channel of Figure 12.106 Tolerating an Average BER of 10^{-4}, which Was Evaluated after Viterbi or Turbo Decoding but before RS Decoding

Punctured Rate	4QAM Baud Rate (MBd)	16QAM Baud Rate (MBd)
1/2	2.73	1.37
3/4	1.82	0.909
7/8	1.56	0.779

Table 12.32: The Channel Bit Rate for the Three Different Punctured Coding Rates and for the Two Modulations

on the standard DVB-S scheme, as well as on a turbo-coded scheme in conjunction with blind-equalized QPSK/16QAM. The convolutional code specified in the standard system was substituted with turbo coding, which resulted in a substantial coding gain of approximately 4–5 dB. We have also shown that 16QAM can be utilized instead of QPSK if an extra 5 dB SNR per bit gain is added to the link budget. This extra transmitted power requirement can be eliminated upon invoking the more complex turbo codec, which requires lower transmitted power for attaining the same performance as the standard convolutional codecs.

Our future work will focus on extending the DVB satellite system to support mobile users for the reception of satellite broadcast signals. The use of blind turbo equalizers will also be investigated in comparison to conventional blind equalizers. Further work will also be dedicated to trellis-coded modulation (TCM) and turbo trellis-coded modulation (TTCM)-based orthogonal frequency division multiplexed (OFDM) and single-carrier equalized modems. The impact on the system performance by employing various types of turbo interleavers and turbo codes is also of interest. A range of further wireless video communications issues are addressed in [160].

12.9 Summary and Conclusions

In this concluding chapter, we attempted to provide the reader with a system-oriented overview in the context of various adaptive and/or iterative transceivers. In all the systems investigated we have employed the H.263 video codec, but the channel coding and transmission schemes were different. The channel codecs spanned from conventional low-complexity binary BCH and nonbinary RS codes to complex iteratively decoded turbo codecs.

In Section 12.1, we investigated the feasibility of real-time wireless videotelephony over GSM/GPRS links and quantified the achievable performance advantages with the advent of turbo equalization invoking joint channel decoding and channel equalization. Interactive videotelephony is feasible over GSM/GPRS even without turbo equalization and — as expected — the attainable video performance improves when the number of GPRS time-slots is increased. Apart from the higher associated bit rate the length of the interleaver can be increased, which is also beneficial in overall error resilience terms.

HSDPA-style [197] burst-by-burst adaptive AQAM systems were also employed in conjunction with direct-sequence spreading, as it was demonstrated in Section 12.2. Explicitly, in Section 12.2 multi-user detection assisted burst-by-burst adaptive AQAM/CDMA systems were studied, which attained a near-single-user performance.

In recent years OFDM has received a tremendous attention and has been standardised for employment in a whole host of applications. Specifically, the IEEE 802.11 and the High-Performance Local Area Network standard known as HIPERLAN II employ OFDM in predominantly indoor LAN environments. Similarly, both the Pan-European terrestrial Digital Video Broadcast (DVB) system and the Digital Audio Broadcast (DAB) systems opted for advocating OFDM. Motivated by these trends, we quantified the expected video performance of a LAN-type and a cellular-type high-rate, high-quality interactive OFDM video system for transmission over strongly dispersive channels.

The concept of symbol-by-symbol adaptive OFDM systems was introduced in Section 12.3, which converted the lessons of the single-carrier burst-by-burst adaptive modems to OFDM modems. It was found that in indoor scenarios — where low vehicular/pedestrian speeds prevail and hence the channel quality does not change dramatically between the instant of channel quality estimation and the instant of invoking this knowledge at the remote transmitter — symbol-by-symbol adaptive OFDM outperforms fixed-mode OFDM. More specifically, a high-quality group of subcarriers is capable of conveying a higher number of bits per subcarrier at a given target transmission frame error ratio than the low-quality subcarrier groups. Furthermore, it was found beneficial to control the number of video bits per OFDM symbol as a function of time, since in drastically faded instances the video bit rate could be reduced and hence a less heavily loaded OFDM symbol yielded fewer transmission errors. An interesting trade-off was, however, that upon loading the OFDM symbols with more bits allowed us to use a higher turbo coding interleaver and channel interleaver, which improved the system's robustness up to a limit, resulting in an optimum OFDM symbol loading.

The last two sections of this chapter considered turbo-coded terrestrial and satellite based DVB broadcast systems, respectively. Specifically, Section 12.7 employed an OFDM-based system, while Section 12.8 used blind-equalized single-carrier modems. An interesting conclusion of our investigations was that upon invoking convolutional turbo coding — rather than the standard convolutional codecs — the system's robustness improves quite dramatically. Hence the required SNR is reduced sufficiently, in order to be able to support, for example, 4

bit/symbol transmissions, instead of 2 bit/symbol signalling. This then potentially allows us to double the associated video bit-rate within a given bandwidth at the cost of an acceptable implementational complexity increase when replacing the standard convolutional codecs by turbo channel codecs.

12.10 Wireless Video System Design Principles

We conclude that 2G and 3G interactive cordless as well as cellular wireless videophony using the H.263 ITU codec is realistic in a packet acknowledgment assisted TDMA/TDD, CDMA/TDD, or OFDM/TDD system both with and without power control following the system design guidelines summarised below:

- In time-variant wireless environments adaptive multimode transceivers are beneficial, in particular, if the geographic distribution of the wireless channel capacity — i.e., the instantaneous channel quality — varies across the cell due to path loss, slow-fading, fast-fading, dispersion, co-channel interference, etc.
- In order to support the operation of intelligent multimode transceivers a video source codec is required that is capable of conveniently exploiting the variable-rate, time-variant capacity of the wireless channel by generating always the required number of bits that can be conveyed in the current modem mode by the transmission burst. This issue was discussed throughout this chapter.
- The H.263 video codec's local and remote video reconstruction frame buffers have to be always identically updated, which requires a reliable, strongly protected acknowledgment feedback flag. The delay of this flag has to be kept as low as possible, and a convenient mechanism for its transmission is constituted by its superposition on the reverse-direction packets in TDD systems. Alternatively, the system's control channel can be used for conveying both the video packet acknowledgment flag and the transmission mode requested by the receiver. The emerging 3G CDMA systems provide a sufficiently high bitrate to convey the necessary side information. The associated timing issues were summarized in Figure 10.21.
- The acknowledgment feedback flag can be conveniently error protected by simple majority logic decoded repetition codes, which typically provide more reliable protection than more complex similar-length error correction codes.
- For multimode operation an appropriate adaptive packetization algorithm is required that controls the transmission, storage, discarding, and updating of video packets.
- For multimode operation in cellular systems an appropriate fixed FER power-control algorithm is required, that is capable of maintaining a constant transmission burst error rate, irrespective of the modulation mode used, since it is the FER, rather than the bit error rate, which determines the associated video quality.
- We emphasize again that wireless videotelephony over 2G systems is realistic using both proprietary and standard video codecs, and the same design principles can also be applied in the context of the emerging 3G CDMA systems, as it was demonstrated in the context of our JD-ACDMA design example.

- The feasibility of using similar design principles has been shown also for high-rate WATM OFDM modems in this closing chapter.

Future video transceiver performance improvements are possible, while retaining the basic system design principles itemized above. The image compression community completed the MPEG4 video standard [536–538], while the wireless communications community has commenced research toward the fourth generation of mobile radio standards. All in all, this is an exciting era for wireless video communications researchers, bringing about new standards to serve a forthcoming wireless multimedia age.

Glossary

16CIF	Sixteen Common Intermediate Format Frames are sixteen times as big as CIF frames and contain 1408 pixels vertically and 1152 pixels horizontally
2G	Second generation
3G	Third generation
3GPP	Third Generation Partnership Project
4CIF	Four Common Intermediate Format Frames are four times as big as CIF frames and contain 704 pixels vertically and 576 pixels horizontally
AB	Access burst
ACCH	Associated control channel
ACELP	Algebraic Code Excited Linear Predictive (ACELP) Speech Codec
ACF	autocorrelation function
ACL	Autocorrelation
ACO	Augmented Channel Occupancy matrix, which contains the channel occupancy for the local and surrounding base stations. Often used by locally distributed DCA algorithms to aid allocation decisions.
ACTS	Advanced Communications Technologies and Services. The fourth framework for European research (1994–98). A series of consortia consisting of universities and industrialists considering future communications systems.
ADC	Analog–to–Digital Converter
ADPCM	Adaptive Differential Pulse Coded Modulation
AGCH	Access grant control channel
AI	Acquisition Indicator
AICH	Acquisition Indicator CHannel
ANSI	American National Standards Institute
ARIB	Association of Radio Industries and Businesses
ARQ	Automatic Repeat Request, Automatic request for retransmission of corrupted data
ATDMA	Advanced Time Division Multiple Access
ATM	Asynchronous Transfer Mode

AUC Authentication center

AV.26M A draft recommendation for transmitting compressed video over error-prone channels, based on the H.263 [258] video codec

AWGN Additive White Gaussian Noise

B-ISDN Broadband ISDN

BbB Burst-by-Burst

BCCH Broadcast control channel

BCH Bose-Chaudhuri-Hocquenghem, a class of forward error correcting codes (FEC)

BCH Codes Bose-Chaudhuri-Hocquenghem (BCH) Codes

BER Bit error rate, the fraction of the bits received incorrectly

BN Bit number

BPSK Binary Phase Shift Keying

BS A common abbreviation for base station

BSIC Base station identifier code

BTC Block Truncation Coding

CBER Channel bit error rate, the bit error rate before FEC correction

CBP Coded block pattern, a H.261 video codec symbol that indicates which of the blocks in the macroblock are active

CBPB A fixed-length codeword used by the H.263 video codec to convey the coded block pattern for bidirectionally predicted (B) blocks

CBPY A variable-length codeword used by the H.263 video codec to indicate the coded block pattern for luminance blocks

CC Convolutional Code

CCCH Commom control channel

CCITT Now ITU, standardization group

CCL Cross-correlation

CD Code Division, a multiplexing technique whereby signals are coded and then combined in such a way that they can be separated using the assigned user signature codes at a later stage

CDF Cumulative density function, the integral of the probability density function (PDF)

CDMA Code Division Multiple Access

CELL_BAR_ACCESS Boolean flag to indicate whether the MS is permitted

CIF Common Intermediate Format Frames containing 352 pixels vertically and 288 pixels horizontally

CIR Carrier to Interference Ratio, same as SIR

COD A one-bit codeword used by the H.263 video codec that indicates whether the current macroblock is empty or nonempty

CPICH Common PIlot CHannel

CT2 British Second Generation Cordless Phone Standard

CWTS China Wireless Telecommunication Standard

DAB Digital Audio Broadcasting

DAC Digital-to-Analog Convertor

DAMPS	Pan-American Digital Advanced Phone System, IS-54
DB	Dummy burst
DC	Direct Current, normally used in electronic circuits to describe a power source that has a constant voltage, as opposed to AC power in which the voltage is a sine wave. It is also used to describe things that are constant, and hence have no frequency component.
DCA	Dynamic Channel Allocation
DCH	Dedicated transport CHannel
DCS1800	A digital mobile radio system standard, based on GSM but operating at 1.8 GHz at a lower power
DCT	A discrete cosine transform that transforms data into the frequency domain. Commonly used for video compression by removing high-frequency components of the video frames
DECT	A Pan-European digital cordless telephone standard
DL	Down-link
DPCCH	Dedicated Physical Control CHannel
DPCH	Dedicated Physical CHannel
DPCM	Differential Pulse Coded Modulation
DPDCH	Dedicated Physical Data CHannel
DQUANT	A fixed-length coding parameter used to differential change the current quantizer used by the H.263 video codec
DS–CDMA	Direct Sequence Code Division Multiple Access
DSMA-CD	Digital Sense Multiple Access-Collision Detection
DTTB	Digital Terrestrial Television Broadcast
DVB-T	Terrestrial Pan-European Digital Video Broadcast Standard
EIR	Equipment identity register
EMC	Electromagnetic Compatibility
EOB	An end-of-block variable-length symbol used to indicate the end of the current block in the H.261 video codec
EREC	Error-Resilient Entropy Coding. A coding technique that improves the robustness of variable-length coding by allowing easier resynchronization after errors
ERPC	Error-Resilient Position Coding, a relative of the coding scheme known as Error-Resilient Entropy Coding (EREC)
ETSI	European Telecommunications Standards Institute
EU	European Union
FA	First Available, a simple centralized DCA scheme that allocates the first channel found that is not reused within a given preset reuse distance
FACCH	Fast associated control channel
FACH	Forward Access CHannel
FAW	Frame Alignment Word
FBER	Feedback error ratio, the ratio of feedback acknowledgment messages that are received in error
FCA	Fixed Channel Allocation

FCB Frequency correction burst

FCCH Frequency Correction Channel

FD Frequency Division, a multiplexing technique whereby different frequencies are used for each communications link

FDD Frequency-Division Duplex, a multiplexing technique whereby the forward and reverse links use a different carrier frequency

FDM Frequency Division Multiplexing

FDMA Frequency Division multiple access, a multiple access technique whereby frequency division (FD) is used to provide a set of access channels

FEC Forward Error Correction

FEF Frame Error Flag

FER Frame error rate

FH Frequency hopping

FIFO First-In First-Out, a queuing strategy in which elements that have been in the queue longest are served first

FN TDMA frame number

FPLMTS Future Public Land Mobile Telecommunication System

fps Frames per second

FRAMES Future Radio Wideband Multiple Access System

GBSC Group of blocks (GOB) start code, used by the H.261 and H.263 video codecs to regain synchronization, playing a similar role to PSC

GEI Functions similar to PEI but in the GOB layer of the H.261 video codec

GFID A fixed-length codeword used by H.263 video codec to aid correct resynchronization after an error

GMSK Gaussian Mean Shift Keying, a modulation scheme used by the Pan-European GSM standard by virtue of its spectral compactness

GN Group of blocks number, an index number for a GOB used by the H.261 and H.263 video codecs

GOB Group of blocks, a term used by the H.261 and H.263 video codecs, consisting of a number of macroblocks

GOS Grade of Service, a performance metric to describe the quality of a mobile radio network

GP Guard Period

GPS Global Positioning System

GQUANT Group of blocks quantizer, a symbol used by the H.261 and H.263 video codecs to modify the quantizer used for the GOB

GSM A Pan-European digital mobile radio standard, operating at 900MHz

GSPARE Functions similar to PSPARE but in the GOB layer of the H.261 video codec

H.261 A video coding standard [257], published by the ITU in 1990

H.263 A video coding standard [258], published by the ITU in 1996

HC Huffman Coding

HCA Hybrid Channel Allocation, a hybrid of FCA and DCA

HCS Hierarchical Cell Structure

HDTV	High-Definition Television
HLR	Home location register
HO	Handover
HTA	Highest interference below Threshold Algorithm, a distributed DCA algorithm also known as MTA. The algorithm allocates the most interfered channel, whose interference is below the maximum tolerable interference threshold.
IF	Intermediate Frequency
IMSI	International mobile subscriber identity
IMT-2000	International Mobile Telecommunications-2000
IMT2000	Intelligent Mobile Telecommunications in the Year 2000, Japanese Initiative for 3rd Generation Cellular Systems
IS-54	Pan-American Digital Advanced Phone System, IS-54
IS-95	North American mobile radio standard, that uses CDMA technology
ISDN	Integrated Services Digital Network, digital replacement of the analogue telephone network
ISI	Intersymbol Interference, Inter-Subcarrier Interference
ITU	International Telecommunications Union, formerly the CCITT, standardization group
ITU-R	International Mobile Telecommunication Union – Radiocommunication Sector
JDC	Japanese Digital Cellular Standard
JPEG	"Lossy" DCT-based Still Picture Coding Standard
LFA	Lowest Frequency below threshold Algorithm, a distributed DCA algorithm that is a derivative of the LTA algorithm, the difference being that the algorithm attempts to reduce the number of carrier frequencies being used concurrently
LIA	Least Interference Algorithm, a distributed DCA algorithm that assigns the channel with the lowest measured interference that is available.
LODA	Locally Optimized Dynamic Assignment, a centralized DCA scheme, which bases its allocation decisions on the future blocking probability in the vicinity of the cell
LOLIA	Locally Optimized Least Interference Algorithm, a locally distributed DCA algorithm that allocates channels using a hybrid of the LIA and an ACO matrix
LOMIA	Locally Optimized Most Interference Algorithm, a locally distributed DCA algorithm that allocates channels using a hybrid of the MTA and an ACO matrix
LP filtering	Low-pass filtering
LP-DDCA	Local Packing Dynamic Distributed Channel Assignment, a locally distributed DCA algorithm that assigns the first channel available that is not used by the surrounding base stations, whose information is contained in an ACO matrix
LPF	Low-pass filter
LSB	Least significant bit
LSR	Linear Shift Register
LTA	Least interference below Threshold Algorithm, a distributed DCA algorithm that allocates the least interfered channel, whose interference is below a preset maximum tolerable interference level
LTI	Linear Time-invariant

MA Abbreviation for Miss America, a commonly used head and shoulders video sequence referred to as Miss America

Macroblock A grouping of 8 by 8 pixel blocks used by the H.261 and H.263 video codecs. Consists of four luminance blocks and two chrominance blocks

MAI Multiple Access Interference

MAP Maximum–A–Posteriori

MB Macroblock

MBA Macroblock address symbol used by the H.261 video codec, indicating the position of the macroblock in the current GOB

MBS Mobile Broadband System

MC Motion Compensation

MCBPC A variable-length codeword used by the H.263 video codec to convey the macroblock type and the coded block pattern for the chrominance blocks

MCER Motion Compensated Error Residual

MDM Modulation Division Multiplexing

MF-PRMA Multi-Frame Packet Reservation Multiple Access

MFlop Mega Flop, 1 million floating point operations per second

MODB A variable-length coding parameter used by the H.263 video codec to indicate the macroblock mode for bidirectionally predicted (B) blocks

MPEG Motion Picture Expert Group, also a video coding standard designed by this group that is widely used

MPG Multiple Processing Gain

MQUANT A H.261 video codec symbol that changes the quantizer used by current and future macroblocks in the current GOB

MS A common abbreviation for Mobile Station

MSC Mobile switching center

MSE Mean Square Error

MSQ Mean Square centralized DCA algorithm that attempts to minimize the mean square distance between cells using the same channel

MTA Most interference below Threshold Algorithm, a distributed DCA algorithm also known as HTA. The algorithm allocates the most interfered channel, whose interference is below the maximum tolerable interference level.

MTYPE H.261 video codec symbol that contains information about the macroblock, such as coding mode, and flags to indicate whether optional modes are used, like motion vectors, and loop filtering

MV Motion vector, a vector to estimate the motion in a frame

MVD Motion vector data symbol used by H.261 and H.263 video codecs

MVDB A variable-length codeword used by the H.263 video codec to convey the motion vector data for bidirectionally predicted (B) blocks

NB Normal burst

NCC Normalized Channel Capacity

NLF Nonlinear filtering

NMC Network management center

NN	Nearest-Neighbor centralized DCA algorithm; allocates a channel used by the nearest cell, which is at least the reuse distance away
NN+1	Nearest-Neighbor-plus-one centralized DCA algorithm; allocates a channel used by the nearest cell, which is at least the reuse distance plus one cell radius away
OFDM	Orthogonal Frequency Division Multiplexing
OMC	Operation and maintenance center
OVSF	Orthogonal Variable Spreading Factor
P-CCPCH	Primary Common Control Physical CHannel
PCH	Paging CHannel
PCM	Pulse code modulation
PCN	Personal Communications Network
PCPCH	Physical Common Packet CHannel
PCS	Personal Communications System, a term used to describe third-generation mobile radio systems in North America
PDF	Probability Density Function
PDSCH	Physical Down-link Shared CHannel
PEI	Picture layer extra insertion bit, used by the H.261 video codec, indicating that extra information is to be expected
PFU	Partial Forced Update
PGZ	Peterson-Gorenstein-Zierler (PGZ) Decoder
PHP	Japanese Personal Handyphone Phone System
PI	Page Indicator
PICH	Page Indicator CHannel
PLMN	Public land mobile network
PLMN_PERMITTED	Boolean flag to indicate, whether the MS is permitted
PLMR	Public Land Mobile Radio
PLR	Packet-Loss Ratio
PP	Partnership Project
PQUANT	A fixed-length codeword used by the H.263 video codec to indicate the quantizer to use for the next frame
PRACH	Physical Random Access CHannel
PRMA	Packet Reservation Multiple Access, a statistical multiplexing arrangement contrived to improve the efficiency of conventional TDMA systems, by detecting inactive speech segments using a voice activity detector, surrendering them and allocating them to subscribers contending to transmit an active speech packet
PRMA++	PRMA System allowing contention only in the so-called contention slots, which protect the information slots from contention and collisions
PSAM	Pilot symbol-assisted modulation, a technique whereby known symbols (pilots) are transmitted regularly. The effect of channel fading on all symbols can then be estimated by interpolating between the pilots.
PSC	Picture start code, a preset sequence used by the H.261 and H.263 video codecs, that can be searched for to regain synchronization after an error
PSD	Power Spectral Density

PSNR Peak Signal to Noise Ratio, noise energy compared to the maximum possible signal energy. Commonly used to measure video image quality

PSPARE Picture layer extra information bits, indicated by a PEI symbol in H.261 video codec

PSTN Public switched telephone network

PTYPE Picture layer information, used by H.261 and H.263 video codecs to transmit information about the picture, e.g. Resolution, etc.

QAM Quadrature Amplitude Modulation

QCIF Quarter Common Intermediate Format Frames containing 176 pixels vertically and 144 pixels horizontally

QMF Quadrature Mirror Filtering

QN Quater bit number

QoS Quality of Service

QT Quad-Tree

RACE Research in Advanced Communications Equipment Programme in Europe, from June 1987 to December 1995

RACH Random Access CHannel

RC filtering Raised-cosine filtering

RF Radio frequency

RFCH Radio frequency channel

RFN Reduced TDMA frame number in GSM

RING A centralized DCA algorithm that attempts to allocate channels in one of the cells, which is at least the reuse distance away that forms a “ring” of cells

RLC Run-Length Coding

RPE Regular pulse excited

RS Codes Reed-Solomon (RS) codes

RSSI Received Signal Strength Indicator, commonly used as an indicator of channel quality in a mobile radio network

RTT Radio Transmission Technology

RXLEV Received signal level: parameter used in hangovers

RXQUAL Received signal quality: parameter used in hangovers

S-CCPCH Secondary Common Control Physical CHannel

SAC Syntax-based arithmetic coding, an alternative to variable-length coding, and a variant of arithmetic coding

SACCH Slow associated control channel

SB Synchronization burst

SCH Synchronization CHannel

SCS Sequential Channel Search distributed DCA algorithm that searches the available channels in a predetermined order, picking the first channel found, which meets the interference constraints

SDCCH Stand-alone dedicated control channel

SF Spreading Factor

SINR	Signal-to-Interference plus Noise ratio, same as signal-to-noise ratio (SNR) when there is no interference.
SIR	Signal-to-Interference ratio
SNR	Signal-to-Noise Ratio, noise energy compared to the signal energy
SPAMA	Statistical Packet Assignment Multiple Access
SQCIF	Sub-Quarter Common Intermediate Format Frames containing 128 pixels vertically and 96 pixels horizontally
SSC	Secondary Synchronization Codes
TA	Timing advance
TB	Tailing bits
TC	Trellis Coded
TCH	Traffic channel
TCH/F	Full-rate traffic channel
TCH/F2.4	Full-rate 2.4 kbps data traffic channel
TCH/F4.8	Full-rate 4.8 kbps data traffic channel
TCH/F9.6	Full-rate 9.6 kbps data traffic channel
TCH/FS	Full-rate speech traffic channel
TCH/H	Half-rate traffic channel
TCH/H2.4	Half-rate 2.4 kbps data traffic channel
TCH/H4.8	Half-rate 4.8 kbps data traffic channel
TCM	Trellis code modulation
TCOEFF	An H.261 and H.263 video codec symbol that contains the transform coefficients for the current block
TD	Time Division, a multiplexing technique whereby several communications links are multiplexed onto a single carrier by dividing the channel into time periods, and assigning a time period to each communications link
TDD	Time-Division Duplex, a technique whereby the forward and reverse links are multiplexed in time.
TDMA	Time Division Multiple Access
TFCI	Transport-Format Combination Indicator
TIA	Telecommunications Industry Association
TN	Time slot number
TPC	Transmit Power Control
TR	Temporal reference, a symbol used by H.261 and H.263 video codecs to indicate the real-time difference between transmitted frames
TS	Technical Specifications
TTA	Telecommunications Technology Association
TTC	Telecommunication Technology Committee
TTIB	Transparent tone in band
UHF	Ultra high frequency
UL	Up-link

UMTS	Universal Mobile Telecommunications System, a future Pan-European third-generation mobile radio standard
UTRA	Universal Mobile Telecommunications System Terrestrial Radio Access
VA	Viterbi Algorithm
VAD	Voice activity detection
VAF	Voice activity factor, the fraction of time the voice activity detector of a speech codec is active
VE	Viterbi equalizer
VL	Variable length
VLC	Variable-length coding/codes
VLR	Visiting location register
VQ	Vector Quantization
W-CDMA	Wideband Code Division Multiple Access
WARC	World Administrative Radio Conference
WATM	Wireless Asynchronous Transfer Mode (ATM)
WLAN	Wireless Local Area Network
WN	White noise
WWW	World Wide Web, the name given to computers that can be accessed via the Internet using the HTTP protocol. These computers can provide information in a easy-to-digest multimedia format using hyperlinks.

Bibliography

[1] R. M. Fano, "Transmission of Information," in *M.I.T. Press*, (Cambridge, Mass), 1949.

[2] J. B. Connell, "A Huffman-Shannon-Fano code," *Proceedings of the IEEE*, vol. 61, pp. 1046–1047, 1973.

[3] D. A. Huffman, "A method for the construction of minimum-redundancy codes," *Proceedings of IRE*, vol. 20, 9, pp. 1098–1101, September 1952.

[4] L. Hanzo, P. J. Cherriman and J. Street, *Wireless Video Communications: Second to Third Generation Systems and Beyond*. NJ, USA : IEEE Press., 2001.

[5] V. Baskaran and K. Konstantinides, *Image and Video Compression Standards*. Boston: Kluwer Academic Publishers, 1995.

[6] J. L. Mitchell, W. B. Pennebaker, C. E. Fogg and D. J. LeGall, *MPEG Video Compression Standard*. New York: Chapman & Hall, 1997.

[7] B. G. Haskell, A. Puri and A. N. Netravali, *Digital Video: An Introduction to MPEG-2*. New York: Chapman & Hall, 1997.

[8] J. R. Jain, *Fundamentals of Digital Image Processing*. Englewood Cliffs, NJ: Prentice-Hall, 1989.

[9] A. Jain, *Fundamentals of Digital Image Processing*. Englewood Cliffs, NJ: Prentice-Hall, 1989.

[10] R. W. Burns, *A History of Television Broadcasting*. IEE History of Technology Series, Number 7, 1986.

[11] P. Symes, *Video Compression Demystified*. McGraw-Hill, 2001.

[12] A. Habibi, "An adaptive strategy for hybrid image coding," *IEEE Transactions on Communications*, pp. 1736–1753, December 1981.

[13] K. R. Rao and P. Yip, "Discrete cosine transform - algorithms, advantages, applications," in *Academic Press*, (San Diego, CA), 1990.

[14] B. Ramamurthi and A. Gersho, "Classified vector quantization of images," *IEEE Transactions on communications*, vol. COM-34, pp. 1105–1115, November 1986.

[15] C. W. Rutledge, "Vector DPCM: vector predictive coding of color images," *Proceedings of the IEEE Global Telecommunications Conference*, pp. 1158–1164, September 1986.

[16] M. Yuen, H. R. Wu, "A survey of hybrid MC/DPCM/DCT video coding distortions," *Signal Processing*, vol. 70, pp. 247–278, July 1998.

[17] J. Zhang, M. O. Ahmad and M. N. S. Swamy, "Bidirectional variable size block motion compensation," *Electronics Letters*, vol. 34, pp. 54–53, January 1998.

[18] S.-T. Hsiang and J. W. Woods, "Invertible three-dimensional analysis/synthesis system for video coding with half-pixel-accurate motion compensation," *Proceedomgs of SPIE 3653, Visual Communications and Image Processing'99*, January 1999.

[19] G. J. Sullivan, T. Wiegand and T. Stockhammer, "Draft H.26L video coding standard for mobile applications," in *Proceedings of IEEE International Conference on Image Processing*, vol. 3, (Thessaloniki, Greece), pp. 573–576, October 2001.

[20] A. Alatan, L. Onural, M. Wollborn, R. Mech, E. Tuncel, and T. Sikora, "Image sequence analysis for emerging interactive multimedia servicesłThe European COST211 framework," *IEEE Communications Letters*, vol. 8, pp. 802–813, November 1998.

[21] CCITT/SG XV, "Codecs for videoconferencing using primary digital group transmission," in *Recommendation H.120, CCITT (currently ITU-T)*, (Geneva), 1989.

[22] G. K. Wallace, "The JPEG still picture compression standard," *Communications of the Association for Computing Machinery*, vol. 34, no. 4, pp. 30–44, 1991.

[23] ITU-T/SG16/Q15, "Video coding for low bitrate communication," in *ITU-T Recommendation H.263, Version 2 (H.263+), ITU-T*, (Geneva), 1998.

[24] ISO/IEC JTC1/SC29/WG11, "Information technology - Generic coding of audio-visual objects.," in *Part 2: Visual. Draft ISO/IEC 14496-2 (MPEG-4), version 1, ISO/IEC*, (Geneva), 1998.

[25] ITU-T/SG16/Q15, "Draft for "H.263++" annexes U, V, and W to recommendation H.263," in *Draft, ITU-T*, (Geneva), 2000.

[26] Joint Video Team (JVT) of ISO/IEC MPEG and ITU-T VCEG, "Joint Final Committee Draft (JFCD) of joint video specification (ITU-T Rec. H.264 ł ISO/IEC 14496-10 AVC)," August 2002.

[27] ITU-T/SG15, "Video coding for low bitrate communication," in *ITU-T Recommendation H.263, Version 1, ITU-T*, (Geneva), 1996.

[28] CCITT H.261, "Video Codec for audiovisual services at px64 kbit/s," 1990.

[29] ISO/IEC JTC1/SC29/WG11, "Information technology - coding of moving pictures and associated audio for digital storage media at up to about 1.5 Mbits/s. ," in *Part 2: Video. Draft ISO/IEC 11172-2 (MPEG-1), ISO/IEC*, (Geneva), 1991.

[30] ISO/IEC JTC1/SC29/WG11, "Information technology - Generic coding of moving pictures and associated audio.," in *Part 2: Video. Draft ISO/IEC 13818-2 (MPEG-2) and ITU-T Recommendation H.262, ISO/IEC amd ITU-T*, (Geneva), 1994.

[31] ITU-T Experts Group on very low Bitrate Visual Telephony, "ITU-T Recommendation H.263:Video coding for low bitrate communication," December 1995.

[32] MPEG Video Group, "Report of ad-hoc group on the evaluation of tools for nontested functionalities of video submissions to MPEG-4," *Munich meeting, document ISO/IEC/JTC1/SC29/WG11 N0679*, Jan. 1996.

[33] D. E. Pearson, "Developments in model-based video coding," *Proceedings of the IEEE*, vol. 83, pp. 892–906, 5–9 December 1995.

[34] B. Liu and A. Zaccarin, "New fast algorithms for the estimation of block motion vectors," *IEEE Transactions on Circuits and Systems for Video Technology*, vol. 3, pp. 148–157, April 1993.

[35] ITU-R Recommendation BT.601-5 (10/95), "Studio encoding parameters of digital television for standard 4:3 and wide-screen 16:9 aspect tatios," .

[36] AT&T, "History of AT&T: Milestone in AT&T history. Online document available at URL:http://www.att.com/history/milestones.html."

[37] D. Cohen, "Specifications for the Network Voice Protocol (NVP)," *Internet Engineering Task Force, RFC 741*, November 1977.

[38] R. Cole, "PVP - A Packet Video Protocol," *Internal Document, USC/ISI*, July 1981.

[39] E. M. Schooler, "A distributed architecture for multimedia conference control," *ISI research report ISI/RR-91-289*, November 1991.

[40] ITU-T Recommendation H.320, "Narrowband ISDN Visual telephone systems and terminal equipment," 1995.

[41] V. JACOBSON, "DARTNET planning and review meeting," December 1991.

[42] T. Dorcey, "CU-SeeMe Desktop VideoConferencing Software," *Connexions*, vol. 9, March 1995.

[43] T. Turletti, "H.261 software codec for videoconferencing over the Internet," in *Rapports de Recherche 1834, Institut National de Recherche en Informatique et en Automatique (INRIA)*, (Sophia-Antipolis, France), January 1993.

[44] T. Dorcey, "CU-SeeMe Desktop Videoconferencing Software," *CONNEXIONS*, pp. 42–45, March 1995.

[45] H. Schulzrinne, "RTP: The real-time transport protocol," in *MCNC 2nd Packet Video Workshop*, vol. 2, (Research Triangle Park, NC), December 1992.

[46] Cornell University, "The CU-SeeMe home page, URL: http://cu-seeme.cornell.edu/."

[47] G. Venditto, "Internet phones - the future is calling," *Internet World*, pp. 40–52, 1996.

[48] Vocaltec Communications Ltd., "The Vocaltec Telephony Gateway. Online document available at URL:http://www.vocaltec.com/products/products.htm."

[49] ITU-T Recommendation H.324, "Terminal for Low Bitrate multimedia communication," 1995.

[50] ITU-T Recommendation T.120, "Data protocols for multimedia conferencing," July 1996.

[51] ITU-T Recommendation H.323, "Visual telephone systems and equipment for LAN which provide a non-guaranteed quality of service," November 1996.

[52] CERN, "Caltech and HP open scientific datacenter," November 1997.

[53] R. Braden et al., "Resource Reservation Protocol (RSVP)," September 1997.

[54] ITU-T Recommendation H.323 Version 2, "Packet-based multimedia communication systems," January 1998.

[55] J. Lennox, J. Rosenberg, H. Schulzrinne, "Common gateway interface for SIP," June 2000.

[56] ITU-T Recommendation H.450.4, "Call hold supplementary service for H.323, Series H: Audiovisual and Multimedia Sytems," May 1999.

[57] ITU-T Recommendation H.323 Version 4, "Packet-based multimedia communication systems," November 2000.

[58] S. Emani and S. Miller, "DPCM picture transmission over noisy channels with the aid of a markov model," *IEEE Transactions on Image Processing*, vol. 4, pp. 1473–1481, November 1995.

[59] M. Chan, "The performance of DPCM operating on lossy channels with memory," *IEEE Transactions on Communications*, vol. 43, pp. 1686–1696, April 1995.

[60] CCITT/SG XV, "Video codec for audiovisual services at $p \times 64$ kbit/s," in *Recommendation H.120, CCITT (currently ITU-T)*, (Geneva), 1993.

[61] ISO/IEC JTC1, "Coding of audio-visual objects - Part2: Visual," April 1999.

[62] ITU-T Recommendation H.263, Version 2., "Video coding for low bitrate communication. International Telecommunications Union, Geneva," January 1998.

[63] M. R. Civanlar, A. Luthra, S. Wenger and W. Zhu, "Special issue on streaming video," *IEEE Transactions on Circuits and Systems for Video Technology*, vol. 11, March 2001.

[64] C.W. Chen, P. Cosman, N. Kingsbury, J. Liang and J.W. Modestino, "Special issue on error resilient image and video transmission," *IEEE Journal on Selected Area in Communications*, vol. 18, June 2001.

[65] P. List, A. Joch, J. Lainema, G. Bjontegaard and M. Karczewicz, "Adaptive deblocking filter," *IEEE Transaction on Circuits and Systems for Video Technology*, vol. 13, pp. 614–619, July 2003.

[66] Y. Wang and Q.-F. Zhu, "Error control and concealment for video communications: A review," *Proceedings of the IEEE*, vol. 86, pp. 974–997, May 1998.

[67] S. Aign and K. Fazel, "Temporal and spatial error concealment techniques for hierarchical MPEG-2 video codec," in *in Proceedings IEEE International Conference on Communications ICC 95*, (Seattle, WA), pp. 1778–1783, June 1995.

[68] Y. Wang, Q.-F. Zhu and L. Shaw, "Maximally smooth image recovery in transform coding," *IEEE Transactions on Communications*, vol. 41, pp. 1544–1551, October 1993.

[69] S. S. Hemami and T. H.-Y. Meng, "Transform coded image reconstruction exploiting interblock correlation," *IEEE Transactions on Image Processing*, vol. 4, pp. 1023–1027, July 1995.

[70] W.-M. Lam and A.R. Reibman, "An error concealment algorithm for images subject to channel errors," *IEEE Transactions on Image Processing*, vol. 4, pp. 533–542, May 1995.

[71] H. Sun, K. Challapali and J. Zdepski, "Error concealment in digital simulcast AD-HDTV decoder," *IEEE Transactions on Consumer Electronics*, vol. 38, pp. 108–118, August 1992.

[72] R. Aravind, M.R. Civanlar and A.R. Reibman, "Packet loss resilience of MPEG-2 scalable video coding algorithms," *IEEE Transactions on Circuits and Systems for Video Technology*, vol. 6, pp. 426–435, October 1996.

[73] W.-J. Chu and J.-J. Leou, "Detection and concealment of transmission errors in H.261 images," *IEEE Transactions on Circuits and Systems for Video Technology*, vol. 8, pp. 78–84, February 1998.

[74] J. Apostolopoulos, "Error-resilient video compression via multiple state streams," *IProceedings IEEE International Workshop on Very Low Bit Rate Video Coding*, pp. 168–171, October 1999.

[75] Q.-F. Zhu, Y. Wang and L. Shaw, "Coding and cell-loss recovery in DCT based packet video," *IEEE Transactions on Circuits and Systems for Video Technology*, vol. 3, pp. 248–258, June 1993.

[76] B. Haskell and D. Messerschmitt, "Resynchronization of motion compensated video affected by ATM cell loss," *Proceedings IEEE International Conference on Acoustics, Speech and Signal Processing, ICASSP 93*, pp. 545–548, March 1992.

[77] A. Narula and J.S. Lim, "Error concealment techniques for an all-digital highdefinition television system," *Proceedings of the SPIE*, vol. 2094, pp. 304–318, November 1993.

[78] W. M. Lam, A. R. Reibman and B. Liu, "Recovery of lost or erroneously received motion vectors," *Proceedings IEEE International Conference on Acoustics, Speech and Signal Processing, ICASSP 93*, vol. 5, pp. 417–420, April 1993.

[79] J. Lu, M. L. Lieu, K. B. Letaief and J. C.-I. Chuang, "Error resilient transmission of H.263 coded video over mobile networks," *Proceedings IEEE International Symposium on Circuits and Systems*, vol. 4, pp. 502–505, June 1998.

[80] M. Ghanbari and V. Seferidis, "Cell-loss concealment in ATM video codecs," *IEEE Transactions on Circuits and Systems for Video Technology*, vol. 3, pp. 238–247, June 1993.

[81] L. H. Kieu and K. N. Ngan, "Cell-loss concealment techniques for layered video codecs in an ATM network," *IEEE Transactions on Image Processing*, vol. 3, pp. 666–677, September 1994.

[82] L. Hanzo, L. L. Yang, E. L. Kuan and K. Yen, *Single- and Multi-Carrier CDMA*. Chichester, UK: John Wiley-IEEE Press, 2003.

[83] L. Hanzo, W. Webb and T. Keller, *Single- and Multi-Carrier Quadrature Amplitude Modulation: Principles and Applications for Personal Communications, WLANs and Broadcasting*. Piscataway, NJ, USA: IEEE Press, 2000.

[84] L. Hanzo, C. H. Wong, and M. S. Yee, *Adaptive Wireless Tranceivers*. Chichester, UK: John Wiley-IEEE Press, 2002.

[85] L. Hanzo, T. H. Liew and B. L. Yeap, *Turbo Coding, Turbo Equalisation and Space Time Coding for Transmission over Wireless channels*. New York, USA: John Wiley-IEEE Press, 2002.

[86] P. Jung and J. Blanz, "Joint detection with coherent receiver antenna diversity in CDMA mobile radio systems," *IEEE Transactions on Vehicular Technology*, vol. 44, pp. 76–88, February 1995.

[87] L. Hanzo, Müenster ,Choi and Keller, *OFDM and MC-CDMA*. Chichester, UK: John Wiley and IEEE Press., 2003.

[88] E. Steinbach, N. Färber and B. Girod, "Adaptive playout for low-latency video streaming," in *IEEE International Conference on Image Processsing ICIP-01*, (Thessaloniki, Greece), pp. 962–965, October 2001.

[89] M. Kalman, E. Steinbach and B. Girod, "Adaptive playout for real-time media streaming," in *IEEE International Symposium on Circuits and Systems*, vol. 1, (Scottsdale, AZ), pp. 45–48, May 2002.

[90] S. Wenger, G. D. Knorr, J. Ott and F. Kossentini, "Error resilience support in H.263+," *IEEE Transactions on Circuits and Systems for Video Technology*, vol. 8, pp. 867–877, November 1998.

[91] R. Talluri, "Error-resilient video coding in the ISO MPEG-4 standard," *IEEE Communications Magazine*, vol. 2, pp. 112–119, June 1998.

[92] N. Färber, B. Girod and J. Villasenor, "Extension of ITU-T Recommendation H.324 for error-resilient video transmission," *IEEE Communications Magazine*, vol. 2, pp. 120–128, June 1998.

[93] E. Steinbach, N. Färber and B. Girod, "Standard compatible extension of H.263 for robust video transmission in mobile environments," *IEEE Transactions on Circuits and Systems for Video Technology*, vol. 7, pp. 872–881, December 1997.

[94] B. Girod and N. Färber, "Feedback-based error control for mobile video transmission," *Proceedings of the IEEE*, vol. 87, pp. 1707–1723, October 1999.

[95] G. J. Sullivan and T. Wiegand, "Rate-distortion optimization for video compression," *IEEE Signal Processing Magazine*, vol. 15, pp. 74–90, November 1998.

[96] A. Ortega and K. Ramchandran, "From rate-distortion theory to commercial image and video compression technology," *IEEE Signal Processing Magazine*, vol. 15, pp. 20–22, November 1998.

[97] T. Wiegand, X. Zhang and B. Girod, "Long-term memory motion-compensated prediction," *IEEE Transactions on Circuits and Systems for Video Technology*, vol. 9, pp. 70–84, February 1999.

[98] T. Wiegand, N. Färber and B. Girod, "Error-resilient video transmission using long-term memory motion-compensated prediction," *IEEE Journal on Selected Areas in Communications*, vol. 18, pp. 1050–1062, June 2000.

[99] P. A. Chou, A. E. Mohr, A. Wang and S. Mehrotra, "Error control for receiver-driven layered multicast of audio and video," *IEEE Transactions on Multimedia*, vol. 3, pp. 108–122, March 2001.

[100] G. Cote and F. Kossentini, "Optimal intra coding of blocks for robust video communication over the Internet," *Signal Processing: Image Communication*, vol. 15, pp. 25–34, September 1999.

[101] R. Zhang, S. L. Regunathan and K. Rose, "Video coding with optimal inter/intra-mode switching for packet loss resilience," *IEEE Journal on Selected Areas in Communications*, vol. 18, pp. 966–976, June 2000.

[102] R. Zhang, S. L. Regunathan and K. Rose, "Optimal estimation for error concealment in scalable video coding," in *Proceedings of Thirty-Fourth Asilomar Conference on Signals, Systems and Computers*, vol. 2, (Pacific Grove, CA), pp. 1974–1978, 2000.

[103] R. Zhang, S.L. Regunathan and K. Rose, "Robust video coding for packet networks with feedback," in *Proceedings of Thirty-Fourth Asilomar Conference on Signals, Systems and Computers*, (Snowbird, UT), pp. 450–459, 2000.

[104] W. Tan and A. Zakhor, "Video multicast using layered FEC and scalable compression," *IEEE Transactions on Circuits and Systems for Video Technology*, vol. 11, pp. 373–387, March 2001.

[105] P. C. Cosman, J. K. Rogers, P.G. Sherwood and K. Zeger, "Image transmission over channels with bit errors and packet erasures," in *Proceedings of Thirty-Fourth Asilomar Conference on Signals, Systems and Computers*, (Pacific Grove, CA), pp. 1621–1625, 1998.

[106] S. Lee and P. Lee, "Cell loss and error recovery in variable rate video," *Journal of Visual Communication and Image Representation*, vol. 4, pp. 39–45, March 1993.

[107] B. Girod, K. Stuhlmüller, M. Link and U. Horn, "Packet loss resilient Internet video streaming," in *Proceedings of Visual Communications and Image Processing VCIP-99*, (San Jose, CA), pp. 833–844, January 1999.

[108] M. Khansari and M. Vetterli, "Layered transmission of signals over powerconstrained wireless channels," in *Proc. of the IEEE International Conference on Image Processing (ICIP)*, vol. 3, (Washington, DC), pp. 380–383, October 1995.

[109] R. Puri and K. Ramchandran, "Multiple description source coding using forward error correction codes," in *Proc. Asilomar Conference on Signals, Systems and Computers*, (Pacific Grove, CA,), pp. 342–346, November 1999.

[110] R. Puri, K. Ramchandran, K. W. Lee and V. Bharghavan, "Forward error correction (FEC) codes based multiple description coding for Internet video streaming and multicast," *Signal Processing: Image Communicationn*, vol. 16, pp. 745–762, May 2001.

[111] P. A. Chou and K. Ramchandran, "Clustering source/channel rate allocations for receiver-driven multicast under a limited number of streams," in *Proceedings of the IEEE International Conference on Multimedia and Expo (ICME)*, vol. 3, (New York, NY), pp. 1221–1224, July 2000.

[112] K. Stuhlmüller, N. Farber, M. Link and B. Girod, "Analysis of video transmission over lossy channels," *IEEE Journal on Selected Areas in Communications*, vol. 18, pp. 1012–1032, June 2000.

[113] Y. J. Liang, J. G. Apostolopoulos and B. Girod, "Model-based delay-distortion optimization for video streaming using packet interleaving," in *Proceedings of the 36th Asilomar Conference on Signals, Systems and Computers*, (Pacific Grove, CA), November 2002.

[114] S. Wicker, *Error Control Systems for Digital Communication and Storage*. Prentice-Hall, 1995.

[115] B. Dempsey, J. Liebeherr and A. Weaver, "On retransmission-based error control for continuous media traffic in packet-switching networks," *Computer Networks and ISDN Systems Journal*, vol. 28, pp. 719–736, March 1996.

[116] H. Liu and M. E. Zarki, "Performance of H.263 video transmission over wireless channels using hybrid ARQ," *IEEE Journal on Selected Areas in Communications*, vol. 15, pp. 1775–1786, December 1999.

[117] C. Papadopoulos and G. M. Parulkar, "Retransmission-based error control for continuous media applications," in *Proc. Networkand Operating System Support for Digital Audio and Video (NOSSDAV)*, (Zushi, Japan), pp. 5–12, April 1996.

[118] G. J. Conklin, G. S. Greenbaum, K. O. Lillevold, A. F. Lippman and Y. A. Reznik, "Video coding for streaming media delivery on the Internet," *IEEE Transactions on Circuits and Systems for Video Technology*, vol. 11, pp. 269–281, March 2001.

[119] Y.-Q. Zhang, Y.-J. Liu and R. L. Pickholtz, "Layered image transmission over cellular radio channels," *IEEE Transactions on Vehicular Technology*, vol. 43, pp. 786–794, August 1994.

[120] B. Girod, N. Färber and U. Horn, "Scalable codec architectures for Internet video-on-demand," in *Proceedings of the Thirty-First Asilomar Conference on Signals, Systems and Computers*, (Pacific Grove, CA), pp. 357–361, November 1997.

[121] A. Puri, L. Yan and B. G. Haskell, "Temporal resolution scalable video coding," in *Proc. of the IEEE International Conference on Image Processing (ICIP)*, vol. 2, (Austin, TX), pp. 947–951, November 1994.

[122] K. M. Uz, M. Vetterli, and D. J. LeGall, "Interpolative multiresolution coding of advance television with compatible subchannels," *IEEE Transactions on Circuits and Systems for Video Technology*, vol. 1, pp. 88–99, March 1991.

[123] S. Zafar, Y.-Q. Zhang and B. Jabbari, "Multiscale video representation using multiresolution motion compensation and wavelet decomposition," *IEEE Journal on Selected Areas in Communications*, vol. 11, pp. 24–35, January 1993.

[124] U. Horn, K. Stuhlmüller, M. Link and B. Girod, "Robust Internet video transmission based on scalable coding and unequal error protection," *Signal Processing: Image Communication*, vol. 15, pp. 77–94, September 1999.

[125] B. Girod and U. Horn, "Scalable codec for Internet video streaming," in *Proceedings of the International Conference on Digital Signal Processing*, (Piscataway, NJ), pp. 221–224, July 1997.

[126] M. Khansari, A. Zakauddin, W.-Y. Chan, E. Dubois and P. Mermelstein, "Approaches to layered coding for dual-rate wireless video transmission," *Proceedings of the IEEE International Conference on Image Processing (ICIP)*, pp. 285–262, November 1994.

[127] G. Karlsson and M. Vetterli, "Subband coding of video for packet networks," *Optical Engineering*, vol. 27, pp. 574–586, July 1998.

[128] D. Quaglia and J. C. De Martin, "Delivery of MPEG video streams with constant perceptual quality of service," *Proceedings of the IEEE International Conference on Multimedia and Expo (ICME)*, vol. 2, pp. 85–88, August 2002.

[129] E. Masala, D. Quaglia and J. C. De Martin, "Adaptive picture slicing for distortion-based classification of video packets," *Proceedings of the IEEE Fourth Workshop on Multimedia Signal Processing*, pp. 111–116, October 2001.

[130] J. Shin, J. W. Kim and C. C. J. Kuo, "Quality-of-service mapping mechanism for packet video in differentiated services network," *IEEE Transactions on Multimedia*, vol. 3, pp. 219–231, June 2001.

[131] J. Shin, J. Kim and C. C. J. Kuo, "Relative priority based QoS interaction between video applications and differentiated service networks," in *Proceedings of the IEEE International Conference on Image Processing*, (Vancouver, BC, Canada), pp. 536–539, September 2000.

[132] S. Regunathan, R. Zhang and K. Rose, "Scalable video coding with robust mode selection," *Signal Processing: Image Communication*, vol. 16, pp. 725–732, May 2001.

[133] H. Yang, R. Zhang and K. Rose, "Drift management and adaptive bit rate allocation in scalable video coding," in *Proceedings of the IEEE International Conference on Image Processing (ICIP)*, vol. 2, (Rochester, NY), pp. 49–52, September 2002.

[134] S. Dogan, A. Cellatoglu, M. Uyguroglu, A. H. Sadka and A. M. Kondoz, "Error-resilient video transcoding for robust Internetwork communications using GPRS," *IEEE Transactions on Circuits and Systems for VideoTechnology - Special Issue on Wireless Video*, vol. 12, pp. 453–464, July 2002.

[135] H. G. Musmann, P. Pirsch and H. J. Grallert, "Advances in picture coding," *Proceedings of the IEEE*, vol. 73, pp. 523–548, April 1985.

[136] M. Flierl and B. Girod, "Generalized B pictures and the draft H.264/AVC video-compression standard," *IEEE Transaction on Circuits and Systems for Video Technology*, vol. 13, pp. 587–597, July 2003.

[137] T. Shanableh and M. Ghanbari, "Loss Concealment Using B-Pictures Motion Information," *IEEE Transaction on Multimedia*, vol. 5, pp. 257–266, June 2003.

[138] M. Al-Mualla, N. Canagarajah and D. Bull, "Simplex minimization for single- and multiple reference motion estimation," *IEEE Transactions on Circuits and Systems for Video Technology*, vol. 11, pp. 1029–1220, December 2001.

[139] A. Luthra, G. J. Sullivan and T. Wiegand, "Special issue on the H.264/AVC video coding standard," *IEEE Transactions on Circuits and Systems for Video Technology*, vol. 13, July 2003.

[140] S. Wenger, "H.264/AVC Over IP," *IEEE Transactions on Circuits and Systems for Video Technology*, vol. 13, pp. 587–597, July 2003.

[141] T. Stockhammer, M. M. Hannuksela and T. Wiegand, "H.264/AVC in wireless environments," *IEEE Transactions on Circuits and Systems for Video Technology*, vol. 13, pp. 587–597, July 2003.

[142] A. Arumugam, A. Doufexi, A. Nix and P. Fletcher, "An investigation of the coexistence of 802.11g WLAN and high data rate Bluetooth enabled consumer electronic devices in indoor home and office environments," *IEEE Transactions on Consumer Electronics*, vol. 49, pp. 587–596, August 2003.

[143] R. Thobaben and J. Kliewer, "Robust decoding of variable-length encoded Markov sources using a three-dimensional trellis," *IEEE communications letters*, vol. 7, pp. 320–322, July 2003.

[144] A. Murad and T. Fuja, "Joint source-channel decoding of variable-length encoded sources," in *IEEE Information Theory Workshop*, (Killarney, Ireland), pp. 94–95, June 1998.

[145] M. Barnsley, "A better way to compress images," *BYTE*, pp. 215–222, January 1988.

[146] J. Beaumont, "Image data compression using fractal techniques," *BT Technology*, vol. 9, pp. 93–109, October 1991.

[147] A. Jacquin, "Image coding based on a fractal theory of iterated contractive image transformations," *IEEE Transactions on Image Processing*, vol. 1, pp. 18–30, January 1992.

[148] D. Monro and F. Dudbridge, "Fractal block coding of images," *Electronic Letters*, vol. 28, pp. 1053–1055, May 1992.

[149] D. Monro, D. Wilson, and J. Nicholls, "High speed image coding with the bath fractal transform," in Damper *et al.* [544], pp. 23–30.

[150] J. Streit and L. Hanzo, "A fractal video communicator," in *Proceedings of IEEE VTC '94* [549], pp. 1030–1034.

[151] W. Welsh, "Model based coding of videophone images," *Electronic and Communication Engineering Journal*, pp. 29–36, February 1991.

[152] J. Ostermann, "Object-based analysis-synthesis coding based on the source model of moving rigid 3D objects," *Signal Processing: Image Communication*, vol. 6, pp. 143–161, 1994.

[153] M. Chowdhury, "A switched model-based coder for video signals," *IEEE Transactions on Circuits and Systems*, vol. 4, pp. 216–227, June 1994.

[154] G. Bozdagi, A. Tekalp, and L. Onural, "3-D motion estimation and wireframe adaptation including photometric effects for model-based coding of facial image sequences," *IEEE Transactions on circuits and Systems for Video Technology*, vol. 4, pp. 246–256, June 1994.

[155] Q. Wang and R. Clarke, "Motion estimation and compensation for image sequence coding," *Signal Processing: Image Communications*, vol. 4, pp. 161–174, 1992.

[156] H. Gharavi and M. Mills, "Blockmatching motion estimation algorithms — new results," *IEEE Transactions on Circuits and Systems*, vol. 37, pp. 649–651, May 1990.

[157] J. Jain and A. Jain, "Displacement measurement and its applications in inter frame image coding," *IEEE Transactions on Communications*, vol. 29, December 1981.

[158] B. Wang, J. Yen, and S. Chang, "Zero waiting-cycle hierarchical block matching algorithm and its array architectures," *IEEE Transactions on Circuits and Systems for Video Technology*, vol. 4, pp. 18–27, February 1994.

[159] P. Strobach, "Tree-structured scene adaptive coder," *IEEE Transactions on Communications*, vol. 38, pp. 477–486, April 1990.

[160] L. Hanzo and P. Cherriman and J. Streit, *Video Compression and Communications over Wireless Channels: From Second to Third Generation Systems, WLANs and Beyond*. IEEE Press, 2001. IEEE Press, 2001 (For detailed contents please refer to http://www-mobile.ecs.soton.ac.uk.).

[161] B. Liu and A. Zaccarin, "New fast algorithms for the estimation of block motion vectors," *IEEE Transactions on Circuits and Systems*, vol. 3, pp. 148–157, April 1993.

[162] R. Li, B. Zeng, and N. Liou, "A new three step search algorithm for motion estimation," *IEEE Transactions on Circuits and Systems*, vol. 4, pp. 439–442, August 1994.

[163] L. Lee, J. Wang, J. Lee, and J. Shie, "Dynamic search-window adjustment and interlaced search for block-matching algorithm," *IEEE Transactions on Circuits and Systems for Video Technology*, vol. 3, pp. 85–87, February 1993.

[164] B. Girod, "Motion-compensating prediction with fractional-pel accuracy," *IEEE Transactions on Communications*, vol. 41, pp. 604–611, April 1993.

[165] J. Huang et al, "A multi-frame pel-recursive algorithm for varying frame-to-frame displacement estimation," in *Proceedings of International Conference on Acoustics, Speech, and Signal Processing, ICASSP'92* [548], pp. 241–244.

[166] N. Efstratiadis and A. Katsaggelos, "Adaptive multiple-input pel-recursive displacement estimation," in *Proceedings of International Conference on Acoustics, Speech, and Signal Processing, ICASSP'92* [548], pp. 245–248.

[167] C. Huang and C. Hsu, "A new motion compensation method for image sequence coding using hierarchical grid interpolation," *IEEE Transactions on Circuits and Systems for Video Technology*, vol. 4, pp. 42–51, February 1994.

[168] J. Nieweglowski, T. Moisala, and P. Haavisto, "Motion compensated video sequence iinterpolation using digital image warping," in *Proceedings of the IEEE International Conference on Acoustics, Speech and Signal Processing (ICASSP'94)* [546], pp. 205–208.

[169] C. Papadopoulos and T. Clarkson, "Motion compensation using second-order geometric transformations," *IEEE Transactions on Circuits and Systems for Video Technology*, vol. 5, pp. 319–331, August 1995.

[170] C. Papadopoulos, *The use of geometric transformations for motion compensation in video data compression*. PhD thesis, University of London, 1994.

[171] M. Hoetter, "Differential estimation based on object oriented mapping parameter estimation," *Signal Processing*, vol. 16, pp. 249–265, March 1989.

[172] S. Karunaserker and N. Kingsbury, "A distortion measure for blocking artifacts in images based on human visual sensitivity," *IEEE Transactions on Image Processing*, vol. 6, pp. 713–724, June 1995.

[173] D. Pearson and M. Whybray, "Transform coding of images using interleaved blocks," *IEE Proceedings*, vol. 131, pp. 466–472, August 1984.

[174] J. Magarey and N. Kingsbury, "Motion estimation using complex wavelets," in *Proceedings of the IEEE International Conference on Acoustics, Speech and Signal Processing (ICASSP'96)* [547], pp. 2371–2374.

[175] R. Young and N. Kingsbury, "Frequency-domain motion estimation using a complex lapped transform," *IEEE Transactions on Image Processing*, vol. 2, pp. 2–17, January 1993.

[176] R. Young and N. Kingsbury, "Video compression using lapped transforms for motion estimation/compensation and coding," in *Proceedings of the SPIE Communication and Image Processing Conference*, (Boston, MA), pp. 1451–1463, SPIE, November 1992.

[177] K. Rao and P. Yip, *Discrete Cosine Transform: Algorithms, Advantages and Applications*. New York: Academic Press Ltd., 1990.

[178] A. Sharaf, *Video coding at very low bit rates using spatial transformations*. PhD thesis, Department of Electronic and Electrical Engineering, Kings College, London, 1997.

[179] R. Clarke, *Transform Coding of Images*. New York: Academic Press, 1985.

[180] A. Palau and G. Mirchandani, "Image coding with discrete cosine transforms using efficient energy-based adaptive zonal filtering," in *Proceedings of the IEEE International Conference on Acoustics, Speech and Signal Processing (ICASSP'94)* [546], pp. 337–340.

[181] H. Yamaguchi, "Adaptive DCT coding of video signals," *IEEE Transactions on Communications*, vol. 41, pp. 1534–1543, October 1993.

[182] K. Ngan, "Adaptive transform coding of video signals," *IEE Proceedings*, vol. 129, pp. 28–40, February 1982.

[183] R. Clarke, "Hybrid intra-frame transform coding of image data," *IEE Proceedings*, vol. 131, pp. 2–6, February 1984.

[184] F.-M. Wang and S. Liu, "Hybrid video coding for low bit-rate applications," in *Proceedings of the IEEE International Conference on Acoustics, Speech and Signal Processing (ICASSP'94)* [546], pp. 481–484.

[185] M. Ghanbari and J. Azari, "Effect of bit rate variation of the base layer on the performance of two-layer video codecs," *IEEE Transactions on Communications for Video Technology*, vol. 4, pp. 8–17, February 1994.

[186] N. Jayant and P. Noll, *Digital Coding of Waveforms, Principles and Applications to Speech and Video*. Englewood Cliffs, NJ: Prentice-Hall, 1984.

[187] N. Cheng and N. Kingsbury, "The ERPC: an efficient error-resilient technique for encoding positional information of sparse data," *IEEE Transactions on Communications*, vol. 40, pp. 140–148, January 1992.

[188] M. Narasimha and A. Peterson, "On the computation of the discrete cosine transform," *IEEE Transactions on Communications*, vol. 26, pp. 934–936, June 1978.

[189] L. Hanzo, F. Somerville, and J. Woodard, "Voice and audio compression for wireless communications: Principles and applications for fixed and wireless channels." 2007 (For detailed contents, please refer to http://www-mobile.ecs.soton.ac.uk.).

[190] R. M. Pelz, "An un-equal error protected px8 kbit/s video transmission for DECT," in *Proceedings of IEEE VTC '94* [549], pp. 1020–1024.

[191] L. Hanzo, R. Stedman, R. Steele, and J. Cheung, "A portable multimedia communicator scheme," in Damper *et al*. [544], pp. 31–54.

[192] R. Stedman, H. Gharavi, L. Hanzo, and R. Steele, "Transmission of subband-coded images via mobile channels," *IEEE Transactions on Circuits and Systems for Video Technology*, vol. 3, pp. 15–27, February 1993.

[193] L. Hanzo and J. Woodard, "An intelligent multimode voice communications system for indoor communications," *IEEE Transactions on Vehicular Technology*, vol. 44, pp. 735–748, November 1995.

[194] L. Hanzo and J. Streit, "Adaptive low-rate wireless videophone systems," *IEEE Transactions on Circuits and Systems for Video Technology*, vol. 5, pp. 305–319, August 1995.

[195] L. Hanzo, S. X. Ng, W. Webb and T.Keller, *Quadrature Amplitude Modulation: From Basics to Adaptive Trellis-Coded, Turbo-Equalised and Space-Time Coded OFDM, CDMA and MC-CDMA Systems*. New York, USA : John Wiley and Sons, 2000.

[196] ETSI, *GSM Recommendation 05.05, Annex 3*, November 1988.

[197] Harri Holma and Anti Toskala, *HSDPA/HSUPA for UMTS*. Chichester, UK : John Wiley and Sons, 2006.

[198] G. Djuknic and D. Schilling, "Performance analysis of an ARQ transmission scheme for meteor burst communications," *IEEE Transactions on Communications*, vol. 42, pp. 268–271, February/March/April 1994.

[199] L. de Alfaro and A. Meo, "Codes for second and third order GH-ARQ schemes," *IEEE Transactions on Communications*, vol. 42, pp. 899–910, February–April 1994.

[200] T.-H. Lee, "Throughput performance of a class of continuous ARQ strategies for burst-error channels," *IEEE Transactions on Vehicular Technology*, vol. 41, pp. 380–386, November 1992.

[201] S. Lin, D. Constello Jr., and M. Miller, "Automatic-repeat-request error-control schemes," *IEEE Communications Magazine*, vol. 22, pp. 5–17, December 1984.

[202] L. Hanzo and L-L. Yang, E. L. Kuan and K. Yen, *Single- and Multi-Carrier CDMA*. New York, USA: John Wiley, IEEE Press, 2003.

[203] A. Gersho and R. Gray, *Vector Quantization and Signal Compression*. Dordrecht: Kluwer Academic Publishers, 1992.

[204] L. Torres, J. Casas, and S. deDiego, "Segmetation based coding of textures using stochastic vector quantization," in *Proceedings of the IEEE International Conference on Acoustics, Speech and Signal Processing (ICASSP'94)* [546], pp. 597–600.

[205] M. Jaisimha, J. Goldschneider, A. Mohr, E. Riskin, and R. Haralick, "On vector quantization for fast facet edge detection," in *Proceedings of the IEEE International Conference on Acoustics, Speech and Signal Processing (ICASSP'94)* [546], pp. 37–40.

[206] P. Yu and A. Venetsanopoulos, "Hierarchical finite-state vector quantisation for image coding," *IEEE Transactions on Communications*, vol. 42, pp. 3020–3026, November 1994.

[207] C.-H. Hsieh, K.-C. Chuang, and J.-S. Shue, "Image compression using finite-state vector quantization with derailment compensation," *IEEE Transactions on Circuits and systems for Video Technology*, vol. 3, pp. 341–349, October 1993.

[208] N. Nasrabadi, C. Choo, and Y. Feng, "Dynamic finite-state vector quantisation of digital images," *IEEE Transactions on Communications*, vol. 42, pp. 2145–2154, May 1994.

[209] V. Sitaram, C. Huang, and P. Israelsen, "Efficient codebooks for vector quantisation image compression with an adaptive tree search algorithm," *IEEE Transactions on Communications*, vol. 42, pp. 3027–3033, November 1994.

[210] W. Yip, S. Gupta, and A. Gersho, "Enhanced multistage vector quantisation by joint codebook design," *IEEE Transactions on Communications*, vol. 40, pp. 1693–1697, November 1992.

[211] L. Po and C. Chan, "Adaptive dimensionality reduction techniques for tree-structured vector quantisation," *IEEE Transactions on Communications*, vol. 42, pp. 2246–2257, June 1994.

[212] L. Lu and W. Pearlman, "Multi-rate video coding using pruned tree-structured vector quantization," in *Proceedings of the IEEE International Conference on Acoustics, Speech and Signal Processing (ICASSP'93)*, vol. 5, (Minneapolis, MN), pp. 253–256, IEEE, 27–30 April 1993.

[213] F. Bellifemine and R. Picco, "Video signal coding with DCT and vector quantisation," *IEEE Transactions on Communications*, vol. 42, pp. 200–207, February 1994.

[214] K. Ngan and K. Sin, "HDTV coding using hybrid MRVQ/DCT," *IEEE Transactions on Circuits and Systems for Video Technology*, vol. 3, pp. 320–323, August 1993.

[215] D. Kim and S. Lee, "Image vector quantiser based on a classification in the DCT domain," *IEEE Transactions on Communications*, pp. 549–556, April 1991.

[216] L. Torres and J. Huguet, "An improvement on codebook search for vector quantisation," *IEEE Transactions on Communications*, vol. 42, pp. 208–210, February 1994.

[217] W. Press, S. Teukolsky, W. Vetterling, and B. Flannery, *Numerical Recipes in C*. Cambridge: Cambridge University Press, 1992.

[218] J. Streit and L. Hanzo, "Dual-mode vector-quantised low-rate cordless videophone systems for indoors and outdoors applications," *IEEE Transactions on Vehicular Technology*, vol. 46, pp. 340–357, May 1997.

[219] Telcomm. Industry Association (TIA), Washington, DC, *Dual-mode subscriber equipment — Network equipment compatibility specification, Interim Standard IS-54*, 1989.

[220] Research and Development Centre for Radio Systems, Japan, *Public Digital Cellular (PDC) Standard, RCR STD-27*.

[221] L. Hanzo, W. Webb, and T. Keller, *Single- and Multi-Carrier Quadrature Amplitude Modulation: Principles and Applications for Personal Communications, WLANs and Broadcasting*. IEEE Press, 2000.

[222] C. E. Shannon, "A Mathematical Theory of Communication," *The Bell system Technical Journal*, vol. 27, pp. 379–656, July 1948.

[223] L. Hanzo, P. J. Cherriman and J. Street, *Wireless Video Communications: Second to Third Generation Systems and Beyond*. New York, USA: IEEE Press, 2001.

[224] S. X. Ng, R. G. Maunder, J. Wang, L-L. Yang and L. Hanzo, "Joint Iterative-Detection of Reversible Variable-Length Coded Constant Bit Rate Vector-Quantized Video and Coded Modulation," in *European Signal Processing Conference (EUSIPCO)*, (Vienna, Austria), pp. 2231–2234, September 2004.

[225] ISO/IEC 14496-2:2004, *Information Technology – Coding of Audio-Visual Objects – Part 2: Visual*.

[226] S. X. Ng, J. Y. Chung, F. Guo and L. Hanzo, "A Turbo-Detection Aided Serially Concatenated MPEG-4/TCM Videophone Transceiver," in *IEEE Vehicular Technology Conference (VTC)*, (Los Angeles, USA), September 2004.

[227] Q. Chen and K. P. Subbalakshmi, "Joint source-channel decoding for MPEG-4 video transmission over wireless channels," *IEEE Journal on Selected Areas in Communications*, vol. 21, no. 10, pp. 1780–1789, 2003.

[228] S. Benedetto, D. Divsalar, G. Montorsi and F. Pollara, "Serial Concatenation of Interleaved Codes: Performance Analysis, Design and Iterative Decoding," *IEEE Transactions on Information Theory*, vol. 44, pp. 909–926, May 1998.

[229] J. Hagenauer and N. Görtz, "The Turbo Principal in Joint Source-Channel Coding," in *Proceedings of the IEEE Information Theory Workshop*, (Paris, France), pp. 275–278, March 2003.

[230] S. X. Ng and L. Hanzo, "Space-Time IQ-Interleaved TCM and TTCM for AWGN and Rayleigh Fading Channels," *IEE Electronics Letters*, vol. 38, pp. 1553–1555, November 2002.

[231] R. Bauer and J. Hagenauer, "Symbol-by-Symbol MAP Decoding of Variable Length Codes," in *ITG Conference on Source and Channel Coding*, (Munich, Germany), pp. 111–116, January 2000.

[232] M. W. Marcellin and T. R. Fischer, "Trellis Coded Quantization of Memoryless and Gauss-Markov Sources," *IEEE Transactions on Communications*, vol. 38, pp. 82–93, January 1990.

[233] L. R. Bahl, J. Cocke, F. Jelinek and J. Raviv, "Optimal decoding of linear codes for minimizing symbol error rate," *IEEE Transactions on Information Theory*, vol. 20, pp. 284–287, March 1974.

[234] J. Kliewer and R. Thobaben, "Iterative Joint Source-Channel Decoding of Variable-Length Codes Using Residual Source Redundancy," *IEEE Transactions on Wireless Communications*, vol. 4, May 2005.

[235] Joachim Hagenauer, Elke Offer and Lutz Papke, "Iterative Decoding of Binary Block and Convolutional Codes," *IEEE Transactions on Information Theory*, vol. 42, pp. 429–445, March 1996.

[236] L. Hanzo, T. H. Liew and B. L. Yeap, *Turbo Coding, Turbo Equalisation and Space Time Coding for Transmission over Wireless Channels*. Chichester, UK: Wiley, 2002.

[237] Y. Takishima, M. Wada and H. Murakami, "Reversible Variable Length Codes," *IEEE Transactions on Communications*, vol. 43, pp. 158–162, Feb/Mar/Apr 1995.

[238] D. A. Huffman, "A Method for the Construction of Minimum-Redundancy Codes," *Proceedings of the IRE*, vol. 40, no. 9, pp. 1098–1101, 1951.

[239] Y. Linde, A. Buzo and R. Gray, "An Algorithm for Vector Quantizer Design," *IEEE Transactions on Communications*, vol. 28, pp. 84–95, January 1980.

[240] P. Robertson, E. Villebrun and P. Höher, "A comparison of optimal and sub-optimal MAP decoding algorithms operating in Log domain," in *Proceedings of the International Conference on Communications*, pp. 1009–1013, June 1995.

[241] V. Franz and J. B. Anderson, "Concatenated Decoding with a Reduced-Search BCJR Algorithm," *IEEE Journal on Selected Areas in Communications*, vol. 16, pp. 186–195, February 1998.

[242] L. Hanzo, S. X. Ng, T. Keller and W. Webb, *Quadrature Amplitude Modulation*. Chichester, UK: Wiley, 2004.

[243] S. ten Brink, "Convergence Behaviour of Iteratively Decoded Parallel Concatenated Codes," *IEEE Transactions on Communications*, vol. 49, pp. 1727–1737, October 2001.

[244] "Feature topic: Software radios," *IEEE Communications Magazine*, vol. 33, pp. 24–68, May 1995.

[245] X. Zhang, M. Cavenor, and J. Arnold, "Adaptive quadtree coding of motion -compensated image sequences for use on the broadband ISDN," *IEEE Transactions on Circuits and Systems for Video Technology*, vol. 3, pp. 222–229, June 1993.

[246] J. Vaisey and A. Gersho, "Image compression with variable block size segmentation," *IEEE Transactions on Signal Processing*, vol. 40, pp. 2040–2060, August 1992.

[247] M. Lee and G. Crebbin, "Classified vector quantisation with variable block-size DCT models," *IEE Proceedings, Vision, Image and Signal Processing*, pp. 39–48, February 1994.

[248] E. Shustermann and M. Feder, "Image compression via improved quadtree decomposition algorithms," *IEEE Transactions on Image Processing*, vol. 3, pp. 207–215, March 1994.

[249] F. DeNatale, G. Desoli, and D. Giusto, "A novel tree-structured video codec," in *Proceedings of the IEEE International Conference on Acoustics, Speech and Signal Processing (ICASSP'94)* [546], pp. 485–488.

[250] M. Hennecke, K. Prasad, and D. Stork, "Using deformable templates to infer visual speech dynamics," in *Proceedings of the 28th Asilomar Conference on Signals, Systems and Computers*, vol. 1, (Pacific Grove, CA), pp. 578–582, 30 October – 2 November 1994.

[251] G. Wolf et al., "Lipreading by neural networks: Visual preprocessing, learning and sensory integration," *Proceedings of the neural information processing systems*, vol. 6, pp. 1027–1034, 1994.

[252] J. Streit and L. Hanzo, "Quad-tree based parametric wireless videophone systems," *IEEE Transactions Video Technology*, vol. 6, pp. 225–237, April 1996.

[253] E. Biglieri and M. Luise, "Coded modulation and bandwidth-efficient transmission," in *Proceedings of the Fifth Tirrenia Internatioanal Workshop*, (Netherlands), 8–12 September 1991.

[254] L.-F. Wei, "Trellis-coded modulation with multidimensional constellations," *IEEE Transactions on Information Theory*, vol. IT-33, pp. 483–501, July 1987.

[255] L. Hanzo and J. Stefanov, "The Pan-European Digital Cellular Mobile Radio System — known as GSM," in Steele and Hanzo [321], ch. 8, pp. 677–765.

[256] ITU-T, *ISO/IEC-CD-11172 — Coding of moving pictures and associated audio for digital storage*.

[257] ITU-T, *Recommendation H.261: Video codec for audiovisual services at px64 Kbit/s*, March 1993.

[258] ITU-T, "Recommendation H.263: Video Coding for Low Bitrate communication," March 1998.

[259] D. Redmill and N. Kingsbury, "Improving the error resilience of entropy encoded video signals," in *Proceedings of the Conference on Image Processing: Theory and Applications (IPTA)*, (Netherlands), pp. 67–70, Elsevier, 1993.

[260] N. Jayant, "Adaptive quantization with a one-word memory," *Bell System Technical Journal*, vol. 52, pp. 1119–1144, September 1973.

[261] L. Zetterberg, A. Ericsson, and C. Couturier, "DPCM picture coding with two-dimensional control of adaptive quantisation," *IEEE Transactions on Communications*, vol. 32, no. 4, pp. 457–642, 1984.

[262] C. Hsieh, P. Lu, and W. Liou, "Adaptive predictive image coding using local characteristics," *IEE Proceedings*, vol. 136, pp. 385–389, December 1989.

[263] P. Wellstead, G. Wagner, and J. Caldas-Pinto, "Two-dimensional adaptive prediction, smoothing and filtering," *Proceedings of the IEE*, vol. 134, pp. 253–266, June 1987.

[264] O. Mitchell, E. Delp, and S. Carlton, "Block truncation coding: A new approach to image compression," in *IEEE International Conference on Communications (ICC)*, pp. 12B.1.1–12B.1.4, 1978.

[265] E. Delp and O. Mitchell, "Image compression using block truncation coding," *IEEE Transactions on Communications*, vol. 27, pp. 1335–1342, September 1979.

[266] D. Halverson, N. Griswold, and G. Wiese, "A generalized block truncation coding algorithm for image compression," *IEEE Transactions Acoustics, Speech and Signal Processing*, vol. 32, pp. 664–668, June 1984.

[267] G. Arce and N. Gallanger, "BTC image coding using median filter roots," *IEEE Transactions on Communications*, vol. 31, pp. 784–793, June 1983.

[268] M. Noah, "Optimal Lloyd-Max quantization of LPC speech parameters," in *Proceedings of International Conference on Acoustics, Speech, and Signal Processing, ICASSP'84*, (San Diego, CA), pp. 1.8.1–1.8.4, IEEE, 19–21 March 1984.

[269] R. Crochiere, S. Webber, and J. Flangan, "Digital coding of speech in sub-bands," *Bell System Technology Journal*, vol. 52, pp. 1105–1118, 1973.

[270] R. Crochiere, "On the design of sub-band coders for low bit rate speech communication," *Bell System Technology Journal*, vol. 56, pp. 747–770, 1977.

[271] J. Woods and S. O'Neil, "Subband coding of images," *IEEE Transactions on Accoustic, Sound and Signal Processing*, vol. 34, pp. 1278–1288, October 1986.

[272] J. Woods, ed., *Subband Image Coding*. Dordrecht: Kluwer Academic Publishers, March 1991.

[273] H. Gharavi and A. Tabatabai, "Subband coding of digital images using two-dimensional quadrature mirror filtering," in *Proceedings of SPIE*, 1986.

[274] H. Gharavi and A. Tabatabai, "Subband coding of monochrome and color images," *IEEE Transactions on Circuits and Systems*, vol. 35, pp. 207–214, February 1988.

[275] H. Gharavi, "Subband coding algorithms for video applications: Videophone to HDTV-conferencing," *IEEE Transactions on Circuits and Systems for Video Technology*, vol. 1, pp. 174–183, February 1991.

[276] A. Alasmari, "An adaptive hybrid coding scheme for HDTV and digital video sequences," *IEEE Transactions on consumer electronics*, vol. 41, no. 3, pp. 926–936, 1995.

[277] K. Irie et al., "High-quality subband coded for HDTV transmission," *IEEE Transactions on Circuits and Systems for Video Technology*, vol. 4, pp. 195–199, April 1994.

[278] E. Simoncelli and E. Adelson, "Subband transforms," in Woods [272], pp. 143–192.

[279] K. Irie and R. Kishimoto, "A study on perfect reconstructive subband coding," *IEEE Transactions on Circuits and Systems for Video Technology*, vol. 1, pp. 42–48, January 1991.

[280] J. Woods and T. Naveen, "A filter based bit allocation scheme for subband compression of HDTV," *IEEE Transactions on Image Processing*, vol. 1, pp. 436–440, July 1992.

[281] D. Esteban and C. Galand, "Application of quadrature mirror filters to split band voice coding scheme," in *Proceedings of International Conference on Acoustics, Speech, and Signal Processing, ICASSP'77*, (Hartford, CT), pp. 191–195, IEEE, 9–11 May 1977.

[282] J. Johnston, "A filter family designed for use in quadrature mirror filter banks," in *Proceedings of International Conference on Acoustics, Speech, and Signal Processing, ICASSP'80*, (Denver, CO), pp. 291–294, IEEE, 9–11 April 1980.

[283] H. Nussbaumer, "Complex quadrature mirror filters," in *Proceedings of International Conference on Acoustics, Speech, and Signal Processing, ICASSP'83*, (Boston, MA), pp. 221–223, IEEE, 14–16 April 1983.

[284] C. Galand and H. Nussbaumer, "New quadrature mirror filter structures," *IEEE Transactions on Acoustic Speech Signal Processing*, vol. ASSP-32, pp. 522–531, June 1984.

[285] R. Crochiere and L. Rabiner, *Multirate Digital Processing*. Englewood Cliffs, NJ: Prentice-Hall, 1993.

[286] S. Aase and T. Ramstad, "On the optimality of nonunitary filter banks in subband coders," *IEEE Transactions on Image Processing*, vol. 4, pp. 1585–1591, December 1995.

[287] V. Nuri and R. Bamberger, "Size limited filter banks for subband image compression," *IEEE Transactions on Image Processing*, vol. 4, pp. 1317–1323, September 1995.

[288] H. Gharavi, "Subband coding of video signals," in Woods [272], pp. 229–271.

[289] O. Egger, W. Li, and M. Kunt, "High compression image coding using an adaptive morphological subband decomposition," *Proceedings of the IEEE*, vol. 83, pp. 272–287, February 1995.

[290] P. Westerink and D. Boekee, "Subband coding of color images," in Woods [272], pp. 193–228.

[291] Q. Nguyen, "Near-perfect-reconstruction pseudo-QMF banks," *IEEE Transactions on signal processing*, vol. 42, pp. 65–76, January 1994.

[292] S.-M. Phoong, C. Kim, P. Vaidyanathan, and R. Ansari, "A new class of two-channel biorthogonal filter banks and wavelet bases," *IEEE Transactions on Signal Processing*, vol. 43, pp. 649–665, March 1995.

[293] E. Jang and N. Nasrabadi, "Subband coding with multistage VQ for wireless image communication," *IEEE Transactions in Circuit and Systems for Video Technology*, vol. 5, pp. 347–253, June 1995.

[294] P. Cosman, R. Gray, and M. Vetterli, "Vector quantisation of image subbands: A survey," *IEEE Transactions on Image Processing*, vol. 5, pp. 202–225, February 1996.

[295] ITU, *Joint Photographic Experts Group ISO/IEC, JTC/SC/WG8, CCITT SGVIII. JPEG technical specifications, revision 5. Report JPEG-8-R5*, January 1990.

[296] P. Franti and O. Nevalainen, "Block truncation coding with entropy coding," *IEEE Transcations on Communications*, vol. 43, no. 4, pp. 1677–1685, 1995.

[297] V. Udpikar and J. Raina, "BTC image coding using vector quantisation," *IEEE Transactions on Communications*, vol. 35, pp. 353–359, March 1987.

[298] International Standards Organization, *ISO/IEC 11172 MPEG 1 International Standard, 'Coding of moving pictures and associated audio for digital storage media up to about 1.5 Mbit/s, Parts 1–3*.

[299] International Standards Organization, *ISO/IEC CD 13818 MPEG 2 International Standard, Information Technology, Generic Coding of Moving Video and Associated Audio Information, Parts 1–3*.

[300] Telenor Research and Development, P.O.Box 83, N-2007 Kjeller, Norway, *Video Codec Test Model 'TMN 5'*, *ITU Study Group 15, Working Party 15/1*.

[301] D. Choi, "Frame alignment in a digital carrier system — a tutorial," *IEEE Communications Magazin*, vol. 28, pp. 46–54, February 1990.

[302] ITU (formerly CCITT), *ITU Recommendation X25*, 1993.

[303] M. Al-Subbagh and E. Jones, "Optimum patterns for frame alignment," *IEE Proceedings*, vol. 135, pp. 594–603, December 1988.

[304] T. Turletti, "A H.261 software codec for videoconferencing over the internet," Tech. Rep. 1834, INRIA, 06902 Sophia-Antipolis, France, January 1993.

[305] N. Kenyon and C. Nightingale, eds., *Audiovisual Telecommunications*. London: Chapman and Hall, 1992.

[306] N. MacDonald, "Transmission of compressed video over radio links," *BT technology Journal*, vol. 11, pp. 182–185, April 1993.

[307] M. Khansari, A. Jalali, E. Dubois, and P. Mermelstein, "Robust low bit-rate video transmission over wireless access systems," in *Proceedings of International Communications Conference (ICC)*, pp. 571–575, 1994.

[308] M. Khansari, A. Jalali, E. Dubois, and P. Mermelstein, "Low bit-rate video transmission over fading channels for wireless microcellular systems," *IEEE Transactions on Circuits and Systems for Video Technology*, vol. 6, pp. 1–11, February 1996.

[309] N. Cheng, *Error resilient video coding for Noisy Channels*. PhD thesis, Department of Engineering, University of Cambridge, 1991.

[310] D. Redmill, *Image and Video Coding for Noisy Channels*. PhD thesis, Signal Processing and Communication Laboratory, Department of Engineering, University of Cambridge, November 1994.

[311] Y. Matsumura, S. Nakagawa, and T. Nakai, "Very low bit rate video coding with error resilience," in VLBV'95 [550], pp. L–1.

[312] K. Ngan and D. Chai, "Enhancement of image quality in VLBR coding," in VLBV'95 [550], pp. L–3.

[313] K. Ngan and D. Chai, "Very low bit rate video coding using H.263 coder," *IEEE Transactions on Circuits and Systems for Video Technology*, vol. 6, pp. 308–312, June 1996.

[314] W. Webb and L. Hanzo, "Square QAM," in *Modern Quadrature Amplitude Modulation: Principles and Applications for Wireless Communications* [221], ch. 5, pp. 156–169.

[315] IBM Corp., White Plains, NY, *General Information: Binary Synchronous Communication, IBM Publication GA27-3004*, 1969.

[316] S. Lin and D. Constello Jr., *Error Control Coding: Fundamentals and Applications*. Englewood Cliffs, NJ: Prentice-Hall, October 1982.

[317] S. Sampei, S. Komaki, and N. Morinaga, "Adaptive modulation/TDMA scheme for large capacity personal multi-media communication systems," *IEICE Transactions on Communications (Japan)*, vol. E77-B, pp. 1096–1103, September 1994.

[318] J. Torrance and L. Hanzo, "Upper bound performance of adaptive modulation in a slow Rayleigh fading channel," *Electronics Letters*, vol. 32, pp. 718–719, 11 April 1996.

[319] W. Webb and L. Hanzo, "Variable rate QAM," in *Modern Quadrature Amplitude Modulation: Principles and Applications for Wireless Communications* [221], ch. 13, pp. 384–406.

[320] R. Steele and W. Webb, "Variable rate QAM for data transmission over Rayleigh fading channels," in *Proceeedings of Wireless '91*, (Calgary, Alberta), pp. 1–14, IEEE, 1991.

[321] R. Steele and L. Hanzo, eds., *Mobile Radio Communications*. Piscataway, NJ: IEEE Press, 1999.

[322] P. Skelly, M. Schwartz, and S. Dixit, "A histogram-based model for video traffic behavior in a ATM multiplexer," *IEEE/ACM Transactions Networking*, vol. 1, pp. 446–459, August 1993.

[323] M. Ghanbari and V. Seferidis, "Cell-loss concealment in ATM video codecs," *IEEE Transactions on Circuits and Systems for Video Technology*, vol. 3, pp. 238–247, June 1993.

[324] W. Chung, F. Kossentini, and M. Smith, "An efficient motion estimation technique based on a rate-distortion criterion," in *Proceedings of the IEEE International Conference on Acoustics, Speech and Signal Processing (ICASSP'96)* [547], pp. 1977–1980.

[325] M. Whybray and W. Ellis, "H.263 - video coding recommendation for PSTN videophone and multimedia," in *IEE Colloquium (Digest)*, pp. 6/1–6/9, IEE, June 1995.

[326] P. Howard and J. Vitter, "Arithmetic coding for data compression," *Proceedings of the IEEE*, vol. 82, pp. 857–865, June 1994.

[327] Telenor Research and Development, P.O.Box 83, N-2007 Kjeller, Norway, *H.263 Software Codec*. `http://www.nta.no/brukere/DVC`.

[328] N. Färber, E. Steinbach, and B. Girod, "Robust H.263 video transmission over wireless channels," in *Proceedings of International Picture Coding Symposium (PCS)*, (Melbourne, Australia), pp. 575–578, March 1996.

[329] W. Ding and B. Liu, "Rate control of MPEG video coding and recording by rate-quantization modeling," *IEEE Transactions on Circuits and Systems for Video Technology*, vol. 6, pp. 12–20, February 1996.

[330] G. Schuster and A. Katsaggelos, "A video compression scheme with optimal bit allocation between displacement vector field and displaced frame difference," in *Proceedings of the IEEE International Conference on Acoustics, Speech and Signal Processing (ICASSP'96)* [547], pp. 1967–1970.

[331] F. Martins, W. Ding, and E. Feig, "Joint control of spatial quantization and temporal sampling for very low bitrate video," in *Proceedings of the IEEE International Conference on Acoustics, Speech and Signal Processing (ICASSP'96)* [547], pp. 2074–2077.

[332] T. Wiegand, M. Lightstone, and D. Mukherjee, "Rate-distortion optimized mode selection for very low bit rate video coding and the emerging H.263 standard," *IEEE Transactions on Circuits and Systems for Video Technology*, vol. 6, pp. 182–190, April 1996.

[333] K. Wong and L. Hanzo, "Channel coding," in Steele and Hanzo [321], ch. 4, pp. 347–488.

[334] A. Paulraj, "Diversity techniques," in Gibson [551], ch. 12, pp. 166–176.

[335] A. Mämmelä, *Diversity receivers in a fast fading multipath channel*. PhD thesis, Department of Electrical Engineering, University of Oulu, Finland, 1995.

[336] R. Steele, "Digital European Cordless Telecommunications (DECT) systems," in Steele and Hanzo [321], ch. 1.7.2, pp. 79–83.

[337] P. Crespo, R. M. Pelz, and J. Cosmas, "Channel error profile for DECT," *IEE Proceedings on Communications*, vol. 141, pp. 413–420, December 1994.

[338] S. Asghar, "Digital European Cordless Telephone," in Gibson [551], ch. 30, pp. 478–499.

[339] L. Chiariglione, "The development of an integrated audiovisual coding standard: MPEG," *Proceedings of the IEEE*, vol. 83, pp. 151–157, February 1995.

[340] R. Schäfer and T. Sikora, "Digital video coding standards and their role in video communications," *Proceedings of the IEEE*, vol. 83(10), pp. 907–924, June 1995.

[341] D. J. Le Gall, "The MPEG video compression algorithm," *Signal Processing: Image Communication*, vol. 4, pp. 129–140, 1992.

[342] T. Sikora, "MPEG-4 very low bit rate video," *Proceedings of IEEE ISCAS Conference, Hong Kong*, pp. 1440–1443, February 1997.

[343] T. Sikora, "The MPEG-4 video standard verification model," *IEEE Transactions on Circuit and Systems for Video Technology*, vol. 7, pp. 19–31, February 1997.

[344] ISO/IEC JTC1/SC29/WG11 N0702 Rev., "Information technology - Generic coding of moving pictures and associated audio, Recommendation H.262. Draft International Standard," vol. 83, March 1994.

[345] ISO/IEC 11172-2 Information technology, "Coding of moving pictures and associated audio for digital storage media at up to about 1.5Mbit/s - Video. Standards Organization/International Electrotechnical (in German). International Commission," 1993.

[346] MPEG AOE Group, "Proposal package description (PPD)-Revision 3," July 1995.

[347] ISO/IEC JTC1/SC29/WG11, "Information technology - Coding of moving pictures and associated audio for digital storage media at up to1.5Mbits/s. Part 2: Video. Draft ISO/IEC 11172-2 (MPEG-1)," *ISO/IEC*, 1991.

[348] ISO/IEC JTC1/SC29/WG11, "Information technology - Generic coding of moving pictures and associated audio. Part 2: Video. Draft ISO/IEC 13818-2 (MPEG-2) and ITU-T Recommendation H.262, ISO/IEC and ITU-T," *ISO/IEC*, 1994.

[349] ISO/IEC JTC1/SC29/WG11, "Information technology - Generic coding of audio-visual objects. Part 2: Visual. Draft ISO/IEC 14496-2 (MPEG-4), version 1," 1998.

[350] A. Jain, *Fundamentals of Digital Image Processing.* Wnglewood Cliffs, NJ: Prentice-Hall, 1989.

[351] O. Avaro, A. Eleftheriadis, C. Herpel, G. Rajan, L. Ward, "MPEG-4 systems: overview," *Signal Processing: Image Communication*, vol. 15, pp. 281–298, 2000.

[352] G. Franceschini, "The delivery layer in MPEG-4," in *Signal Processing: Image Communication*, vol. 15, pp. 347–363, 2000.

[353] C. Herpel, "Architectural considerations for carriage of MPEG-4 over IP network," *ISO/IEC JTC1/SC29/WG11 N2615*, December 1998.

[354] C. Herpel, A. Eleftheriadis, "MPEG-4 systems: elementary stream management," *Signal Processing: Image Communication*, vol. 15, pp. 299–320, 2000.

[355] R. Talluri, "Error-resilient video coding in the ISO MEPG-4 standard," *IEEE Communications Magazine*, pp. 112–119, June 1998.

[356] H. Schulzrinne, S. Casner, R. Frederick, V. Jacobson, "RTP: A transport protocol for real-time applications," *RFC 1889*, January 1996.

[357] L. Chiariglione, "MPEG and multimedia communications," *IEEE Transactions on Circuits and Systems for Video Technology*, vol. 7, pp. 5–18, February 1997.

[358] K. N. Ngan, T. Sikora, M.-T. Sun and S. Pamchanathan, "Segmentation, description and retrival of video content," *IEEE Transactions on Circuits and Systems for Video Technology, special issue*, vol. 8(5), pp. 521–524, September 1998.

[359] K. N. Ngan, T. Sikora, M.-T. Sun and S. Pamchanathan, "Representation and coding of images and video," *IEEE Transactions on Circuits and Systems for Video Technology, special issue*, vol. 8, pp. 797–801, November 1998.

[360] ISO/IEC 13818-2 MPEG-2 Video Coding Standard, "Information technology - Generic coding of moving pictures and associated audio information: Video," March 1995.

[361] T. Sikora and L. Chiariglione, "MPEG-4 Video and its potential for future multimedia services," *Proceedings of IEEE ISCAS Conference, Hong Kong*, vol. 2, pp. 1468–1471, June 1997.

[362] F. Bossen, T. Ebrahimi, "A simple and efficient binary shape coding technique based on bitmap representation," *Proceedings of the International Conference on Acoustics, Speech and Signal Processing (ICASSP'97), Munich, Germany*, vol. 4, pp. 3129–3132, April 1997.

[363] T. Ebrahimi, C. Horne, "MPEG-4 natural video coding - An overview," *Signal Proceesing: Image Communication*, vol. 15, no. 4, pp. 365–385, 2000.

[364] ISO/IEC JTC1/SC29/WG11 N1902, "Information technology - coding of audio visual objects: visual," October 1997.

[365] Recommendation ITU-T BT.500-11, "Methodology for the subjective assessment of the quality of television pictures," in *ITU-T*, 2002.

[366] ITU-T/SG 16/VCEG(formerly Q.15 now Q.6), "H.26L test model long term number 7 (TML-7), Doc. VCEG-M81," April 2001.

[367] Y. Zeng, L. Cheng, G. Bi and A. Kot, "Integer dcts and fast algorithms," *IEEE Transactions on Signal Processing*, vol. 49, pp. 2774–2782, November 2001.

[368] W. Choi and B. Jeon, "Dynamic UVLC codeword remapping with fixed re-association table for H.26L," in *Picture Coding Symposium(PCS)*, (Seoul, Korea), pp. 167–170, April 2001.

[369] D. Marpe, G. Blattermann, G. Heising, and T. Wiegand, "Further results for CABAC entropy coding scheme," Document VCEG-M59, ITU-T Video Coding Experts Group, Apr. 2001, http:// standards.pictel.com/ ftp/ video-site/ 0104 Aus/ VCEG-M59.doc."

[370] R. J. Clarke, "Transform coding of images," in *Microelectronics and Signal Processing. Academic Press*, (London), 1985.

[371] T. N. N. Ahmed and K. Rao, "Discrete Cosine Transform," *IEEE Transactions on Computers*, pp. 90–93, January 1974.

[372] ITU-T Rec. H.26L/ISO/IEC 11496-10, "Advanced video coding," *Final Committee Draft, Document JVT-E022*, September 2002.

[373] D. Marpe, G. Blättermann, G. Heising, and T. Wiegand, "Adaptive codes for H.26L," *ITU-T SG16/Q.6 VCEG-L-13*, January 2001.

[374] ITU-T, "Video coding for low bitrate communication," *ITU-T Recommendation H.263; version 1*, November 1995.

[375] J. Signes, Y. Fisher, and A. Eleftheriadis, "MPEG-4's binary format for scene description," in *Signal Processing: Image Communication, Special issue on MPEG-4*, vol. 15, pp. 312–345, Jannuary 2000.

[376] A.M. Tekalp and J. Ostermann, "Face and 2-D mesh animation in MPEG-4," in *Signal Processing: Image Communication, Special issue on MPEG-4*, vol. 15, pp. 387–421, Jannuary 2000.

[377] ISO/IEC JTC1/SC29/WG11 N1902, "Information technology - coding of audio visual objects: visual," November 1998.

[378] ISO/IEC JTC1/SC29/WG11, "Adhoc group on core experiments on error resilience aspects of MPEG-4 video, description of error resilience aspects of MPEG-4 video," *Description of Error Resilience Core Experiments*, November 1996.

[379] J.G. Proakis, *Digital Communication. 3rd ed.* McGraw-Hill, New York, 1995.

[380] S. B. Wicker, *Error Control Systems for Digital Communication and Storage*. Englewood Cliffs, NJ: Prentice Hall, 1994.

[381] A. Andreadis, G. Benelli, A. Garzelli, S. Susini, "FEC coding for H.263 compatible video transmission," *Proceesings of International Conference on Image Processing, Santa Barbara, CA*, pp. 579–581, October 1997.

[382] J. Wen, J. D. Villasenor, "A class of reversible variable length codes for robust image and video coding," *Proceedings 1997 IEEE International Conference on Image Processing*, vol. 2, pp. 65–68, October 1997.

[383] H. Sun, J. W. Zdepski, W. Kwok, and D. Raychaudhuri, "Error concealment for robust decoding of MPEG compressed video," in *Signal Processing: Image Communication*, vol. 10(4), pp. 249–268, September 1997.

[384] A. Li, S. Kittitornkun, Y. H. Hu, D. S. Park, and J. Villasenor, "Data partitioning and reversible variable length codes for robust video communications," in *IEEE Data Compression Conference Preceeding*, (Snowbird, Utah), pp. 460–469, March 2000.

[385] B. L. Montgomery, J. Abrahams, "Synchronization of binary source codes," in *IEEE Transactions on Information Theory*, vol. 32, pp. 849–854, November 1996.

[386] Y. Takishima, M. Wada, H. Murakami, "Reversible variable length codes," *IEEE Transections on Communications*, vol. 43, pp. 158–162, February 1995.

[387] R. Talluri, I. Moccagatta, Y. Nag, G. Cheung, "Error concelment by data partitioning," *Signal Processing Magazine*, vol. 14, pp. 505–518, May 1999.

[388] C. Bormann, L. Cline, G. Deisher, T. Gardos, C. Maciocco, D. Newell, J. Ott, G. Sullimendation, S. Wenger, C. Zhu, "RTP Payload format for the 1998 version of ITU-T recommendation H.263 video (H.263+); Request for Comments 2429l," , May 1998.

[389] R. Steele and L. Hanzo, eds., *Mobile Radio Communications*. New York: IEEE Press-John Wiley, 2nd ed., 1999.

[390] L. Hanzo, W. Webb, and T. Keller, *Single- and Multi-carrier Quadrature Amplitude Modulation*. New York: John Wiley-IEEE Press, April 2000.

[391] L. Hanzo, F. Somerville, and J. Woodard, "Voice compression and communications: Principles and applications for fixed and wireless channels." 2001 (For detailed contents, please refer to http://www-mobile.ecs.soton.ac.uk.).

[392] P. Cherriman and L. Hanzo, "Programmable H.263-based wireless video transceivers for interference-limited environments," *IEEE Transactions on Circuits and Systems for Video Technology*, vol. 8, pp. 275–286, June 1998.

[393] C. Douillard, A. Picart, M. Jézéquel, P. Didier, C. Berrou, and A. Glavieux, "Iterative correction of inter-symbol interference: Turbo-equalization," *European Transactions on Communications*, vol. 6, pp. 507–511, 1995.

[394] M. Gertsman and J. Lodge, "Symbol-by-symbol MAP demodulation of CPM and PSK signals on Rayleigh flat-fading channels," *IEEE Transactions on Communications*, vol. 45, pp. 788–799, July 1997.

[395] I. Marsland, P. Mathiopoulos, and S. Kallel, "Non-coherent turbo equalization for frequency selective Rayleigh fast fading channels," in *Proceedings of the International Symposium on Turbo Codes & Related Topics*, (Brest, France), pp. 196–199, 3–5 September 1997.

[396] Q. Dai and E. Shwedyk, "Detection of bandlimited signals over frequency selective Rayleigh fading channels," *IEEE Transactions on Communications*, pp. 941–950, February/March/April 1994.

[397] G. Bauch, H. Khorram, and J. Hagenauer, "Iterative equalization and decoding in mobile communications systems," in *European Personal Mobile Communications Conference*, pp. 301–312, 1997.

[398] M. Moher, "Decoding via cross-entropy minimization," in *Proceedings of the IEEE Global Telecommunications Conference 1993*, (Houston, TX), pp. 809–813, 29 November – 2 December 1993.

[399] G. Bauch and V. Franz, "Iterative equalisation and decoding for the GSM-system," in *Proceedings of IEEE Vehicular Technology Conference (VTC'98)* [539], pp. 2262–2266.

[400] D. Raphaeli and Y. Zarai, "Combined turbo equalization and turbo decoding," *IEEE Communications Letters*, vol. 2, pp. 107–109, April 1998.

[401] C. Berrou, A. Glavieux and P. Thitimajshima, "Near Shannon Limit Error-Correcting Coding and Decoding: Turbo Codes," in *Proceedings of the International Conference on Communications*, (Geneva, Switzerland), pp. 1064–1070, May 1993.

[402] C. Berrou and A. Glavieux, "Near optimum error correcting coding and decoding: turbo codes," *IEEE Transactions on Communications*, vol. 44, pp. 1261–1271, October 1996.

[403] K. Narayanan and G. Stuber, "A serial concatenation approach to iterative demodulation and decoding," *IEEE Transactions on Communications*, vol. 47, pp. 956–961, July 1999.

[404] B. Yeap, T. Liew, J. Hamorsky, and L. Hanzo, "Comparative study of turbo equalisers using convolutional codes and block-based turbo-codes for GMSK modulation," in *Proceeding of VTC'99 (Fall)*, (Amsterdam, Netherlands), pp. 2974–2978, IEEE, 19–22 September 1999.

[405] A. Klein, R. Pirhonen, J. Skoeld, and R. Suoranta, "FRAMES multiple access mode 1 — wideband TDMA with and without spreading," in *Proceedings of IEEE International Symposium on Personal, Indoor and Mobile Radio Communications, PIMRC'97*, vol. 1, (Marina Congress Centre, Helsinki, Finland), pp. 37–41, IEEE, 1–4 September 1997.

[406] E. Kuan and L. Hanzo, "Joint detection CDMA techniques for third-generation transceivers," in *Proceeding of ACTS Mobile Communication Summit '98* [540], pp. 727–732.

[407] "COST 207: Digital land mobile radio communications, final report." Office for Official Publications of the European Communities, 1989. Luxembourg.

[408] H. Matsuoka, S. Sampei, N. Morinaga, and Y. Kamio, "Adaptive modulation system with variable coding rate concatenated code for high quality multi-media communications systems," in *Proceedings of IEEE VTC'96* [545], pp. 487–491.

[409] S.-G. Chua and A. Goldsmith, "Variable-rate variable-power mQAM for fading channels," in *Proceedings of IEEE VTC'96* [545], pp. 815–819.

[410] J. Torrance and L. Hanzo, "Latency and networking aspects of adaptive modems over slow indoors rayleigh fading channels," *IEEE Transactions on Vehicular Technology*, vol. 48, no. 4, pp. 1237–1251, 1998.

[411] J. Torrance, L. Hanzo, and T. Keller, "Interference aspects of adaptive modems over slow rayleigh fading channels," *IEEE Transactions on Vehicular Technology*, vol. 48, pp. 1527–1545, September 1999.

[412] T. Liew, C. Wong, and L. Hanzo, "Block turbo coded burst-by-burst adaptive modems," in *Proceedings of Microcoll'99, Budapest, Hungary*, pp. 59–62, 21–24 March 1999.

[413] V. Lau and M. Macleod, "Variable rate adaptive trellis coded QAM for high bandwidth efficiency applications in rayleigh fading channels," in *Proceedings of IEEE Vehicular Technology Conference (VTC'98)* [539], pp. 348–352.

[414] A. Goldsmith and S. Chua, "Variable-rate variable-power MQAM for fading channels," *IEEE Transactions on Communications*, vol. 45, pp. 1218–1230, October 1997.

[415] C. Wong, T. Liew, and L. Hanzo, "Turbo coded burst by burst adaptive wideband modulation with blind modem mode detection," in *Proceeding of ACTS Mobile Communication Summit '99*, (Sorrento, Italy), pp. 303–308, ACTS, 8–11 June 1999.

[416] M. Yee and L. Hanzo, "Upper-bound performance of radial basis function decision feedback equalised burst-by-burst adaptive modulation," in *Proceedings of ECMCS'99*, (Krakow, Poland), 24–26 June 1999.

[417] T. Keller and L. Hanzo, "Adaptive orthogonal frequency division multiplexing schemes," in *Proceeding of ACTS Mobile Communication Summit '98* [540], pp. 794–799.

[418] E. Kuan, C. Wong, and L. Hanzo, "Burst-by-burst adaptive joint detection CDMA," in *Proceeding of VTC'99 (Spring)*, (Houston, TX), IEEE, 16–20 May 1999.

[419] A. Czylwik, "Adaptive OFDM for wideband radio channels," in *Proceeding of IEEE Global Telecommunications Conference, Globecom 96* [543], pp. 713–718.

[420] R. Fischer and J. Huber, "A new loading algorithm for discrete multitone transmission," in *Proceeding of IEEE Global Telecommunications Conference, Globecom 96* [543], pp. 713–718.

[421] P. Chow, J. Cioffi, and J. Bingham, "A practical discrete multitone transceiver loading algorithm for data transmission over spectrally shaped channels," *IEEE Transactions on Communications*, vol. 48, pp. 772–775, 1995.

[422] H. Rohling and R. Grünheid, "Peformance of an OFDM-TDMA mobile communication system," in *Proceeding of IEEE Global Telecommunications Conference, Globecom 96* [543], pp. 1589–1593.

[423] K. Fazel, S. Kaiser, P. Robertson, and M. Ruf, "A concept of digital terrestrial television broadcasting," *Wireless Personal Communications*, vol. 2, pp. 9–27, 1995.

[424] H. Sari, G. Karam, and I. Jeanclaude, "Transmission techniques for digital terrestrial TV broadcasting," *IEEE Communications Magazine*, pp. 100–109, February 1995.

[425] J. Borowski, S. Zeisberg, J. Hübner, K. Koora, E. Bogenfeld, and B. Kull, "Performance of OFDM and comparable single carrier system in MEDIAN demonstrator 60GHz channel," in *Proceeding of ACTS Mobile Communication Summit '97* [542], pp. 653–658.

[426] I. Kalet, "The multitone channel," *IEEE Transactions on Communications*, vol. 37, pp. 119–124, February 1989.

[427] P. Cherriman, T. Keller, and L. Hanzo, "Constant-rate turbo-coded and block-coded orthogonal frequency division multiplex videophony over UMTS," in *Proceeding of Globecom'98* [541], pp. 2848–2852.

[428] J. Woodard, T. Keller, and L. Hanzo, "Turbo-coded orthogonal frequency division multiplex transmission of 8 kbps encoded speech," in *Proceeding of ACTS Mobile Communication Summit '97* [542], pp. 894–899.

[429] Y. Li and N. Sollenberger, "Interference suppression in OFDM systems using adaptive antenna arrays," in *Proceeding of Globecom'98* [541], pp. 213–218.

[430] F. Vook and K. Baum, "Adaptive antennas for OFDM," in *Proceedings of IEEE Vehicular Technology Conference (VTC'98)* [539], pp. 608–610.

[431] G. Ungerboeck, "Channel coding with multilevel/phase signals," *IEEE Transactions on Information Theory*, vol. IT-28, pp. 55–67, January 1982.

[432] E. Zehavi, "8-PSK trellis codes for a Rayleigh fading channel," *IEEE Transactions on Communications*, vol. 40, pp. 873–883, May 1992.

[433] G. Caire, G. Taricco and E. Biglieri, "Bit-Interleaved Coded Modulation," *IEEE Transactions on Information Theory*, vol. IT-44, pp. 927–946, May 1998.

[434] S. L. Goff, A. Glavieux, and C. Berrou, "Turbo-codes and high spectral efficiency modulation," in *Proceedings of IEEE International Conference on Communications*, pp. 645–649, 1994.

[435] P. Robertson and T. Worz, "Bandwidth-Efficient Turbo Trellis-Coded Modulation Using Punctured Component Codes," *IEEE Journal on Selected Areas in Communications*, vol. 16, pp. 206–218, Feb 1998.

[436] U. Wachsmann and J. Huber, "Power and bandwidth efficient digital communications using turbo codes in multilevel codes," *European Transactions on Telecommunications*, vol. 6, pp. 557–567, September–October 1995.

[437] D. J. Costello, A. Banerjee, T. E. Fuja and P. C. Massey, "Some Reflections on the Design of Bandwidth Efficient Turbo Codes," in *Proceedings of 4th ITG Conference on Source and Channel Coding*, no. 170 in ITG Fachbericht, (Berlin), pp. 357–363, VDE–Verlag, 28–30 January 2002.

[438] L. Hanzo and C. H. Wong and M. S. Yee, *Adaptive Wireless Transceivers: Turbo-Coded, Turbo-Equalized and Space-Time Coded TDMA, CDMA and OFDM Systems*. New York, USA: John Wiley, IEEE Press, 2002.

[439] C. Wong and L. Hanzo, "Upper-bound performance of a wideband burst-by-burst adaptive modem," *IEEE Transactions on Communications*, vol. 48, pp. 367–369, March 2000.

[440] S. M. Alamouti and S. Kallel, "Adaptive Trellis-Coded Multiple-Phased-Shift Keying Rayleigh fading channels," *IEEE Transactions on Communications*, vol. 42, pp. 2305–2341, June 1994.

[441] K. J. Hole, H. Holm, and G. E. Oien, "Adaptive multidimensional coded modulation over flat fading channels," *IEEE Journal on Selected Areas in Communications*, vol. 18, pp. 1153–1158, July 2000.

[442] A. Goldsmith and S. Chua, "Adaptive coded modulation for fading channels," *IEEE Transactions on Communications*, vol. 46, pp. 595–602, May 1998.

[443] D. Goeckel, "Adaptive coding for fading channels using outdated fading estimates," *IEEE Transactions on Communications*, vol. 47, pp. 844–855, June 1999.

[444] V.K.N. Lau and M.D. Macleod, "Variable-Rate Adaptive Trellis Coded QAM for Flat-Fading Channels," *IEEE Transactions on Communications*, vol. 49, pp. 1550–1560, September 2001.

[445] P. Ormeci, X. Liu, D. Goeckel and R. Wesel, "Adaptive bit-interleaved coded modulation," *IEEE Transactions on Communications*, vol. 49, pp. 1572–1581, September 2001.

[446] V.K.N. Lau, "Performance analysis of variable rate: symbol-by-symbol adaptive bit interleaved coded modulation for Rayleigh fading channels," *IEEE Transactions on Vehicular Technology*, vol. 51, pp. 537–550, May 2002.

[447] S. X. Ng, C. H. Wong and L. Hanzo, "Burst-by-Burst Adaptive Decision Feedback Equalized TCM, TTCM, BICM and BICM-ID," *International Conference on Communications (ICC)*, p. check!, June 2001.

[448] P. Cherriman, C. Wong, and L. Hanzo, "Turbo- and BCH-coded wide-band burst-by-burst adaptive H.263-assisted wireless video telephony," *IEEE Transactions on Circuits and Systems for Video Technology*, vol. 10, pp. 1355–1363, December 2000.

[449] Special Mobile Group of ETSI, "UMTS: Selection procedures for the choice of radio transmission technologies of the UMTS," tech. rep., European Telecommunications Standard Institute (ETSI), France, 1998.

[450] A. Duel-Hallen, S. Hu, and H. Hallen, "Long range prediction of fading signals," *IEEE Signal Processing Magazine*, vol. 17, pp. 62–75, May 2000.

[451] L. Hanzo, M. Münster, B. J. Choi and T. Keller, *OFDM and MC-CDMA for Broadcasting Multi-User Communications, WLANs and Broadcasting*. New York, USA: John Wiley, IEEE Press, 2003.

[452] P. Robertson, E. Villebrun, and P. Hoeher, "A comparison of optimal and sub-optimal MAP decoding algorithms operating in the log domain," in *Proceedings of the International Conference on Communications*, pp. 1009–1013, June 1995.

[453] A. Klein, G. Kaleh, and P. Baier, "Zero forcing and minimum mean square error equalization for multiuser detection in code division multiple access channels," *IEEE Transactions on Vehicular Technology*, vol. 45, pp. 276–287, May 1996.

[454] G. Golub and C. van Loan, *Matrix Computations*. North Oxford Academic, 1983.

[455] B. J. Choi and L. Hanzo, "Optimum Mode-Switching-Assisted Constant-Power Single- and Multicarrier Adaptive Modulation," *IEEE Transactions on Vehicular Technology*, vol. 52, pp. 536–560, May 2003.

[456] V. Tarokh, N. Seshadri and A. R. Calderbank, "Space-time codes for high rate wireless communication: Performance analysis and code construction," *IEEE Transactions on Information Theory*, vol. 44, pp. 744–765, March 1998.

[457] M. Tao and R. S. Cheng, "Diagonal Block Space-time Code Design for Diversity and Coding Advantage over Flat Rayleigh Fading Channels," *IEEE Transactions on Signal Processing*, to appear in April 2004.

[458] S. X. Ng, F. Guo and L. Hanzo, "Iterative Detection of Diagonal Block Space Time Trellis Codes, TCM and Reversible Variable Length Codes for Transmission over Rayleigh Fading Channels," in *IEEE Vehicular Technology Conference*, (Los Angeles, USA), 26-29 September 2004.

[459] U. Wachsmann, R. F. H. Fischer, J. B. Huber, "Multilevel Codes: Theoretical Concepts and Practical Design Rules," *IEEE Transactions on Information Theory*, vol. 45, pp. 1361–1391, July 1999.

[460] R. H. Morelos-Zaragoza, M. P. C. Fossorier, L. Shu, H. Imai, "Multilevel Coded Modulation for Unequal Error Protection and Multistage Decoding – Part I: Symmetric Constellations," *IEEE Transactions on Communications*, vol. 48, pp. 204–213, February 2000.

[461] ISO/IEC JTC1/SC29/WG11 W2502, "ISO/IEC 14496-2.," in *Final Draft International Standard. Part 2: Visual*, (Atlantic City), 1998.

[462] J. Kliewer, S. X. Ng, and L. Hanzo, "Efficient Computation of EXIT Functions for Non-Binary Iterative Decoding," *To appera in IEEE Transactions on Communications*, 2005.

[463] G. J. Foschini, Jr., "Layered Space-time architecture for wireless communication in a fading environment when using multi-element antennas," *Bell Labs Tech. J.*, pp. 41–59, 1996.

[464] J. Proakis, *Digital Communications*. New York: McGraw-Hill, 1987.

[465] R. Gallager, *Information Theory and Reliable Communication*. John Wiley and Sons, 1968.

[466] E. Telatar, "Capacity of multi-antenna Gaussian channels," *European Transactions on Telecommunication*, vol. 10, pp. 585–595, Nov–Dec 1999.

[467] B. Vucetic and J. Yuan, *Space-Time Coding*. New York: John Wiley-IEEE Press, May 2003.

[468] S. M. Alamouti, "A simple transmit diversity technique for wireless communications," *IEEE Journal on Selected Areas in Communications*, vol. 16, pp. 1451–1458, October 1998.

[469] V. Tarokh, H. Jafarkhani, and A. Calderbank, "Space-time block codes from orthogonal designs," *IEEE Transactions on Information Theory*, vol. 45, pp. 1456–1467, May 1999.

[470] S. X. Ng and L. Hanzo, "Space-Time IQ-interleaved TCM and TTCM for AWGN and Rayleigh Fading Channels," *IEE Electronics Letters*, vol. 38, pp. 1553–1555, November 2002.

[471] S. ten Brink, "Convergence behaviour of iteratively decoded parallel concatenated codes," *IEEE Transactions on Communications*, vol. 49, pp. 1727–1737, October 2001.

[472] H. Chen and A. Haimovich, "EXIT charts for turbo trellis-coded modulation," *IEEE Communications Letters*, vol. 8, pp. 668–670, November 2004.

[473] A. Grant, "Convergence of non-binary iterative decoding," in *Proceedings of the IEEE Global Telecommunications Conference (GLOBECOM)*, (San Antonio TX, USA), pp. 1058–1062, November 2001.

[474] M. Tüchler, "Convergence prediction for iterative decoding of threefold concatenated systems," in *Proceedings of Global Telecommunications Conference — Globecom'02*, vol. 2, (Taipei, Taiwan), pp. 1358 – 1362, IEEE, 17–21 November 2002.

[475] M. Tüchler and J. Hagenauer, "EXIT charts of irregular codes," in *Conference on Information Sciences and Systems*, (Princeton, NJ), pp. 748–753, March 2002.

[476] ten Brink, S., "Convergence of iterative decoding," *Electronics Letters*, vol. 35, no. 10, pp. 806–808, 1999.

[477] A. Ashikhmin and G. Kramer and S. ten Brink, "Extrinsic information transfer functions: model and erasure channel properties," *IEEE Transactions on Information Theory*, vol. 50, pp. 2657–2673, November 2004.

[478] J. Wang and S. X. Ng and A. Wolfgang and L-L. Yang and S. Chen and L. Hanzo, "Near-capacity three-stage MMSE turbo equalization using irregular convolutional codes," in *International Symposium on Turbo Codes*, (Munich, Germany), April 2006. Electronic publication.

[479] L. Hanzo, T. H. Liew, and B. L. Yeap, *Turbo Coding, Turbo Equalisation and Space-Time Coding for Transmission over Fading Channels*. John Wiley-IEEE Press, 2002.

[480] C. Shannon, *Mathematical Theory of Communication*. University of Illinois Press, 1963.

[481] Huffman, D. A., "A method for the construction of minimum-redundancy codes," *Proceedings of the IRE*, vol. 40, pp. 1098–1101, September 1952.

[482] V. Buttigieg and P. G. Farrell, "Variable-length error-correcting codes," *IEE Proceedings on Communications*, vol. 147, pp. 211–215, August 2000.

[483] Benedetto, S. and Montorsi, G., "Serial concatenation of block and convolutional codes," *Electronics Letters*, vol. 32, no. 10, pp. 887–888, 1996.

[484] Benedetto, S. and Montorsi, G., "Iterative decoding of serially concatenated convolutional codes," *Electronics Letters*, vol. 32, no. 13, pp. 1186–1188, 1996.

[485] R. G. Maunder and J. Wang and S. X. Ng and L-L. Yang and L. Hanzo, "Irregular Variable Length Coding for Near-Capacity Joint Source and Channel coding." Submitted to *IEEE Workshop on Signal Processing Systems*, Shanghai, China, October 2007.

[486] Ungerboeck, G., "Channel coding with multilevel/phase signals," *IEEE Transactions on Information Theory*, vol. 28, no. 1, pp. 55–67, 1982.

[487] Bauer, R. and Hagenauer, J., "Symbol by symbol MAP decoding of variable length codes," in *3rd ITG Conference on Source and Channel Coding*, (Munich, Germany), pp. 111–116, January 2000.

[488] Kliewer, J. and Thobaben, R., "Iterative joint source-channel decoding of variable-length codes using residual source redundancy," *IEEE Transactions on Wireless Communications*, vol. 4, no. 3, pp. 919–929, 2005.

[489] V. B. Balakirsky, "Joint source-channel coding with variable length codes," in *IEEE International Symposium on Information Theory*, (Ulm, Germany), p. 419, June 1997.

[490] S. Lloyd, "Least squares quantization in PCM," *IEEE Transactions on Information Theory*, vol. 28, no. 2, pp. 129–137, 1982.

[491] J. Max, "Quantizing for minimum distortion," vol. 6, pp. 7–12, March 1960.

[492] Bahl, L. and Cocke, J. and Jelinek, F. and Raviv, J., "Optimal decoding of linear codes for minimizing symbol error rate (Corresp.)," *IEEE Transactions on Information Theory*, vol. 20, no. 2, pp. 284–287, 1974.

[493] Hagenauer, J. and Offer, E. and Papke, L., "Iterative decoding of binary block and convolutional codes," *IEEE Transactions on Information Theory*, vol. 42, no. 2, pp. 429–445, 1996.

[494] J. Wang and L-L. Yang and L. Hanzo, "Iterative construction of reversible variable-length codes and variable-length error-correcting codes," *IEEE Communications Letters*, vol. 8, pp. 671–673, November 2004.

[495] R. Thobaben and J. Kliewer, "Low-complexity iterative joint source-channel decoding for variable-length encoded Markov sources," *IEEE Transactions on Communications*, vol. 53, pp. 2054–2064, December 2005.

[496] Hanzo, L. and Ng, S. X. and Keller, T. and Webb, W., *Quadrature Amplitude Modulation*. Chichester, UK: Wiley, 2004.

[497] M. Tüchler, "Design of serially concatenated systems depending on the block length," *IEEE Transactions on Communications*, vol. 52, pp. 209–218, February 2004.

[498] Bauer, R. and Hagenauer, J., "On variable length codes for iterative source/channel decoding," in *Data Compression Conference*, (Snowbird, UT), pp. 273–282, March 2001.

[499] ETSI, *Digital Video Broadcasting (DVB); Framing structure, channel coding and modulation for digital terrestrial television*, August 1997. EN 300 744 V1.1.2.

[500] ETSI, *Digital Video Broadcasting (DVB); Framing structure, channel coding and modulation for cable systems*, December 1997. EN 300 429 V1.2.1.

[501] ETSI, *Digital Video Broadcasting (DVB); Framing structure, channel coding and modulation for 11/12 GHz Satellite Services*, August 1997. EN 300 421 V1.1.2.

[502] A. Michelson and A. Levesque, *Error Control Techniques for Digital Communication*. New York: Wiley-Interscience, 1985.

[503] S. O'Leary and D. Priestly, "Mobile broadcasting of DVB-T signals," *IEEE Transactions on Broadcasting*, vol. 44, pp. 346–352, September 1998.

[504] W.-C. Lee, H.-M. Park, K.-J. Kang, and K.-B. Kim, "Performance analysis of viterbi decoder using channel state information in COFDM system," *IEEE Transactions on Broadcasting*, vol. 44, pp. 488–496, December 1998.

[505] S. O'Leary, "Hierarchical transmission and COFDM systems," *IEEE Transactions on Broadcasting*, vol. 43, pp. 166–174, June 1997.

[506] L. Thibault and M. Le, "Performance evaluation of COFDM for digital audoo broadcasting Part I: parametric study," *IEEE Transactions on Broadcasting*, vol. 43, pp. 64–75, March 1997.

[507] B. Haskell, A. Puri, and A. Netravali, *Digital Video: An Introduction To MPEG-2*. Digital Multimedia Standards Series, London: Chapman and Hall, 1997.

[508] *ISO/IEC 13818-2: Information Technology — Generic Coding of Moving Pictures and Associated Audio Information — Part 2: Video*, March 1995.

[509] L. Hanzo and J. Woodard, "An intelligent voice communications system for indoors communications," in *Proceedings of IEEE Vehicular Technology Conference (VTC'95)*, vol. 4, (Chicago), pp. 735–749, IEEE, 15–28 July 1995.

[510] P. Shelswell, "The COFDM modulation system: the heart of digital audio broadcasting," *Electronics & Communication Engineering Journal*, vol. 7, pp. 127–136, June 1995.

[511] S. Wicker, *Error Control Systems for Digital Communication and Storage*. Englewood Cliffs, NJ: Prentice-Hall, 1994.

[512] A. Barbulescu and S. Pietrobon, "Interleaver design for turbo codes," *IEE Electronic Letters*, pp. 2107–2108, December 1994.

[513] M. Failli, "Digital land mobile radio communications COST 207," tech. rep., European Commission, 1989.

[514] H. Gharavi and S. Alamouti, "Multipriority video transmission for third-generation wireless communication system," in Gharavi and Hanzo [516], pp. 1751–1763.

[515] A. Aravind, M. Civanlar, and A. Reibman, "Packet loss resilience of MPEG-2 scalable video coding algorithms," *IEEE Transaction on Circuits And Systems For Video Technology*, vol. 6, pp. 426–435, October 1996.

[516] H. Gharavi and L. Hanzo, eds., *Proceedings of the IEEE*, vol. 87, October 1999.

[517] G. Reali, G. Baruffa, S. Cacopardi, and F. Frescura, "Enhancing satellite broadcasting services using multiresolution modulations," *IEEE Transactions on Broadcasting*, vol. 44, pp. 497–506, December 1998.

[518] Y. Hsu, Y. Chen, C. Huang, and M. Sun, "MPEG-2 spatial scalable coding and transport stream error concealment for satellite TV broadcasting using Ka-band," *IEEE Transactions on Broadcasting*, vol. 44, pp. 77–86, March 1998.

[519] L. Atzori, F. D. Natale, M. D. Gregario, and D. Giusto, "Multimedia information broadcasting using digital TV channels," *IEEE Transactions on Broadcasting*, vol. 43, pp. 383–392, December 1997.

[520] W. Sohn, O. Kwon, and J. Chae, "Digital DBS system design and implementation for TV and data broadcasting using Koreasat," *IEEE Transactions on Broadcasting*, vol. 44, pp. 316–323, September 1998.

[521] J. Griffiths, *Radio Wave Propagation and Antennas — An Introduction*. Englewood Cliffs, NJ: Prentice-Hall, 1987.

[522] M. Karaliopoulos and F.-N. Pavlidou, "Modelling the land mobile satellite channel: a review," *Electronics and Communication Engineering Journal*, vol. 11, pp. 235–248, October 1999.

[523] J. Goldhirsh and W. Vogel, "Mobile satellite system fade statistics for shadowing and multipath from roadside trees at UHF and L-band," *IEEE Transactions on Antennas and Propagation*, vol. 37, pp. 489–498, April 1989.

[524] W. Vogel and J. Goldhirsh, "Multipath fading at L band for low elevation angle, land mobile satellite scenarios," *IEEE Journal on Selected Areas in Communications*, vol. 13, pp. 197–204, February 1995.

[525] W. Vogel and G. Torrence, "Propagation measurements for satellite radio reception inside buildings," *IEEE Transactions on Antennas and Propagation*, vol. 41, pp. 954–961, July 1993.

[526] W. Vogel and U. Hong, "Measurement and modelling of land mobile satellite propagation at UHF and L-band," *IEEE Transactions on Antennas and Propagation*, vol. 36, pp. 707–719, May 1988.

[527] S. Saunders, C. Tzaras, and B. Evans, "Physical statistical propagation model for mobile satellite channel," tech. rep., European Commission, 1998.

[528] S. Saunders, *Antennas and Propagation for Wireless Communication Systems Concept and Design*. New York: John Wiley and Sons, 1999.

[529] K. Wesolowsky, "Analysis and properties of the modified constant modulus algorithm for blind equalization," *European Transactions on Telecommunication*, vol. 3, pp. 225–230, May–June 1992.

[530] M. Goursat and A. Benveniste, "Blind equalizers," *IEEE Transactions on Communications*, vol. COM–28, pp. 871–883, August 1984.

[531] G. Picchi and G. Prati, "Blind equalization and carrier recovery using a "stop–and–go" decision–directed algorithm," *IEEE Transactions on Communications*, vol. COM–35, pp. 877–887, September 1987.

[532] A. Polydoros, R. Raheli, and C. Tzou, "Per–survivor processing: a general approach to MLSE in uncertain environments," *IEEE Transactions on Communications*, vol. COM–43, pp. 354–364, February–April 1995.

[533] D. Godard, "Self–recovering equalization and carrier tracking in two–dimensional data communication systems," *IEEE Transactions on Communications*, vol. COM–28, pp. 1867–1875, November 1980.

[534] Y. Sato, "A method of self–recovering equalization for multilevel amplitude–modulation systems," *IEEE Transactions on Communications*, vol. COM–23, pp. 679–682, June 1975.

[535] Z. Ding, R. Kennedy, B. Anderson, and R. Johnson, "Ill-convergence of Godard blind equalizers in data communications systems," *IEEE Transactions on Communications*, vol. COM-39, pp. 1313–1327, September 1991.

[536] Y.-Q. Zhang, F. Pereira, T. Sikora, and C. Reader (Guest Editors), "Special issue on MPEG-4," *IEEE Transactions on Circuits and Systems for Video Technology*, vol. 7, February 1997.

[537] L. Chiariglione, "MPEG and multimedia communication," *IEEE Transaction On Circuits And Systems For Video Technology*, vol. 7, pp. 5–18, February 1997.

[538] T. Sikora, "The MPEG-4 video standard verification model," *IEEE Transaction On Circuits And Systems For Video Technology*, vol. 7, pp. 19–31, February 1997.

[539] IEEE, *Proceedings of IEEE Vehicular Technology Conference (VTC'98)*, (Ottawa, Canada), 18–21 May 1998.

[540] ACTS, *Proceeding of ACTS Mobile Communication Summit '98*, (Rhodes, Greece), 8–11 June 1998.

[541] IEEE, *Proceeding of Globecom'98*, (Sydney, Australia), 8–12 November 1998.

[542] ACTS, *Proceeding of ACTS Mobile Communication Summit '97*, (Aalborg, Denmark), 7–10 October 1997.

[543] IEEE, *Proceeding of IEEE Global Telecommunications Conference, Globecom 96*, (London), 18–22 November 1996.

[544] R. Damper, W. Hall, and J. Richards, eds., *Proceedings of IEEE International Symposium of Multimedia Technologies and Future Applications*, (London), Pentech Press, April 1993.

[545] IEEE, *Proceedings of IEEE VTC'96*, (Atlanta, GA), 28 April–1 May 1996.

[546] IEEE, *Proceedings of the IEEE International Conference on Acoustics, Speech and Signal Processing (ICASSP'94)*, (Adelaide, Australia), 19–22 April 1994.

[547] IEEE, *Proceedings of the IEEE International Conference on Acoustics, Speech and Signal Processing (ICASSP'96)*, (Atlanta, GA), 7–10 May 1996.

[548] IEEE, *Proceedings of International Conference on Acoustics, Speech, and Signal Processing, ICASSP'92*, March 1992.

[549] IEEE, *Proceedings of IEEE VTC '94*, (Stockholm, Sweden), 8–10 June 1994.

[550] *Proceedings of International Workshop on Coding Techniques for Very Low Bit-rate Video (VLBV'95)*, (Shinagawa, Tokyo, Japan), 8–10 November 1995.

[551] J. Gibson, ed., *The Mobile Communications Handbook*. Boca Raton FL: CRC Press and IEEE Press, 1996.

Author Index

C

D

E

F

G

H

I

J

K

L

M

N

O

P

Q

R

S

T

U

V

W

Y

Z